TECHNISCHE UNIVERSITÄT MÜNCHEN

Lehrstuhl für Aerodynamik und Strömungsmechanik

Ignition and Mixing in a Reacting Shock-Bubble Interaction

Felix Ralf Diegelmann

Vollständiger Abdruck der von der Fakultät für Maschinenwesen der Technischen Universität München zur Erlangung des akademischen Grades eines

Doktor-Ingenieurs

genehmigten Dissertation.

Vorsitzender:		Prof. Dr.-Ing. Oskar J. Haidn
Prüfer der Dissertation:	1.	Prof. Dr.-Ing. Nikolaus A. Adams
	2.	Prof. Dr.-Ing. habil. Stefan Hickel Delft University of Technology, The Netherlands

Die Dissertation wurde am 11.04.2017 bei der Technischen Universität München eingereicht und durch die Fakultät für Maschinenwesen am 17.12.2017 angenommen.

Felix Diegelmann
Schyrenstraße 11
81543 München
Germany

felix.diegelmann@gmail.com

Released January 23, 2018
Typesetting LaTeX

Abstract

Shock-induced mixing of high-speed reactive flows is a crucial aspect in technical environments as well as in natural phenomena. Scientific and technical applications can benefit from shock-induced mixing, e.g., in supersonic combustion engines the rapid and efficient mixing of fuel and oxidizer is crucial as the residence time of the fuel-oxidizer mixture in the combustion chamber amounts only a few milliseconds (Yang et al., 1993). Shock-induced instabilities, such as the Richtmyer-Meshkov instability, promotes mixing and thus increases the burning efficiency of supersonic combustion engines (Marble et al., 1990). In astrophysics one of the major research fields is the study of the interaction between shock waves, generated by the explosion of supernovae, and interstellar clouds (Klein et al., 2001).

In reactive flow fields a shock wave causes two essential effects: Firstly, the discontinuity induces Richtmyer-Meshkov and further secondary instabilities by passing a non-orthogonal interface, separating two fluids of different densities. These instabilities contribute significantly to the mixing process. Secondly, the sudden change in the thermodynamic properties across the shock wave leads to a rapid increase of the chemical reaction rates, which can be sufficient to ignite the reactive gas mixture. The following reaction wave influences the mixing behavior of the fluids distinctly. The interaction between shock-induced effects, hydrodynamic instabilities and chemical reaction kinetics generates a complex flow field with manifold physical phenomena, which are of highest interest in current scientific research.

In the present work the interaction between shock-induced hydrodynamic instabilities and reaction waves is examined within the generic setup of a reacting shock-bubble interaction (RSBI) with detailed hydrogen-oxygen reaction kinetics. A planar shock wave penetrates a gas bubble, filled with a reactive gas mixture. Due to the convex shape of the bubble, the shock is focused and spots of high pressure and temperature arise. Depending on the shock strength the bubble is ignited directly behind the shock wave or near the downstream pole after a distinct ignition delay time. The following reaction wave propagates either as a deflagration or detonation through the reactive bubble gas. The configuration of RSBI serves to investigate the influence of different reaction wave types on global flow field quantities, like mixing and enstrophy production, and on the spatial and temporal evolution of the bubble gas.

Three main configurations of RSBI serve to study the shock-induced ignition of a diluted stoichiometric hydrogen-oxygen gas mixture and the subsequent interaction with hydrodynamic instabilities. The first study contains a two-dimensional RSBI, which is penetrated by a shock wave at a constant shock Mach number. Different reaction wave types are triggered by the change of the initial pressure at a constant initial temperature.

A low initial pressure leads to a long ignition delay time, followed by a subsonic deflagration wave. An increase of the pressure shortens the ignition delay time and induces a supersonic detonation wave. The rapid propagation of the detonation wave leads to an intense interaction between the reaction wave and the arising hydrodynamic instabilities. Mixing is significantly reduced and the growth of secondary instabilities is decelerated. The deflagration wave is characterized by a minor influence on the flow field: Due to the low propagation velocity the mixing is less reduced and the bubble evolution is only affected in the long-term evolution.

The second study of RSBI analyzes the variation of the shock strength in a RSBI, which generates complex thermodynamic post-shock conditions. Different reaction wave types are triggered, including multiple ignitions and transition processes from deflagration to detonation. Two limiting cases are observed: The lowest shock Mach number induces deflagration near the shock-focusing point and the highest shock strength detonation directly at the upstream pole of the bubble. Besides the limiting cases two special phenomena are observed for shock Mach number in between, which have not been discussed before: The transition from deflagration to detonation (DDT) and a simultaneous double detonation. The numerical results are in very good agreement to the experimental measurements of Haehn et al. (2012), confirm their physical interpretation of a double detonation and provide a deeper insight into the gas composition of the simultaneous detonation as well as of DDT during the induction and transition process.

The third configuration deals with the first three-dimensional simulation of RSBI so far and outlines the influence of three-dimensional effects on the bubble evolution. A strong shock wave ignites the bubble gas before the shock-focusing point and induces a detonation wave. The reaction wave decelerates the growth of Richtmyer-Meshkov and Kelvin-Helmholtz instabilities and highly influences the mixing of the bubble gas with its surrounding. Three-dimensional effects, like vortex stretching and decay, as well as Widnall-type instabilities of the main vortex ring are observed and thoroughly analyzed. Both phenomena play a significant role in the long-term evolution of three-dimensional RSBI. Very good agreement with the experimental results of Haehn et al. (2012) is achieved in terms of induction time, reaction wave propagation velocity and spatial expansion of the bubble gas.

The present dissertation outlines numerical results of RSBI with detailed chemistry, including the first three-dimensional RSBI of its kind, and contributes to a deeper understanding of the interaction between hydrodynamic instabilities and shock-induced combustion processes. The comprehensive analysis of gas compositions and thermodynamic properties during the ignition and transition process and the intense study of mixing processes provide new insights and a deeper understanding in the field of shock accelerated reactive gas mixtures.

Kurzfassung

Die stoßinduzierte Durchmischung von reaktiven Gasgemischen ist ein physikalisches Phänomen, welches sowohl in technischen Anwendungen als auch in natürlichen Phänomenen auftritt und diese entscheidend beeinflussen kann. Besonders in wissenschaftlichen und technologischen Applikationen wird versucht, aus diesem physikalischen Effekt einen positiven Nutzen zu ziehen. Beispielsweise kann in Staustrahltriebwerken von Überschallflugkörpern die Durchmischung von Treibstoff und Oxidator durch gezieltes Einbringen von Stößen entscheidend verbessert werden (Yang et al., 1993). Stoßinduzierte Instabilitäten, wie die Richtmyer-Meshkov Instabilität, können Mischungsvorgänge beschleunigen und zu einer Effizienzsteigerung des Verbrennungsprozesses in Überschalltriebwerken beitragen (Marble et al., 1990). Des Weiteren spielen stoßinduzierte Vorgänge eine wichtige Rolle in der modernen Astrophysik: Stoßwellen, verursacht durch die Explosion einer Supernova, interagieren mit interstellaren Wolken und führen zu einer entscheidenen Beinflussung des Formationsprozesses von Sternen (Klein et al., 2001).

Zwei essentielle Effekte werden durch Stoßwellen in reaktiven Strömungen hervorgerufen: Erstens induziert der Verdichtungsstoß beim Passieren von nicht-orthogonalen Grenzflächen, welche zwei Fluide unterschiedlicher Dichte voneinander trennen, Richtmyer-Meshkov und sekundäre Instabilitäten. Diese tragen wesentlich zur Durchmischung der beiden Gase bei. Zweitens verursacht die sprungartige Änderung der thermodynamischen Eigenschaften der Fluide über die Stoßwelle hinweg einen deutlichen Anstieg der chemischen Aktivität. Bei einem ausreichend starken Verdichtungsstoß führt dies zur Selbstentzündung des Gasgemisches. Die darauf folgende Reaktionswelle beeinflusst den weiteren Durchmischungsvorgang der Fluide erheblich. Die Wechselwirkung zwischen den hydrodynamischen Effekten und der induzierten Reaktionskinetik ruft eine Vielzahl von physikalischen Phänomenen hervor, die Gegenstand intensiver aktueller Forschung sind.

In der vorliegenden Arbeit wird die generische Konfiguration einer reagierenden Stoß-Blasen-Interaktion (RSBI) genutzt, um die Interaktion zwischen stoßinduzierten hydrodynamischen Instabilitäten und Reaktionswellen zu untersuchen. Hierbei trifft ein planarer Verdichtungsstoß auf eine Gasblase. Durch deren konvexe Form wird der Stoß fokussiert und es bilden sich Regionen mit hohem Druck und Temperatur. Abhängig von der Verdichtungsstoßstärke wird das Gemisch entweder direkt hinter dem Stoß an der Vorderseite der Blase oder an der Hinterkante nach einer längeren Induktionszeit gezündet. Die darauffolgende Reaktionswelle breitet sich entweder als Detonation oder Deflagration durch das reaktive Gasgemisch aus und interagiert mit den Instabilitäten an den Grenzflächen. Durch die Simulation einer RSBI können der Einfluss des Reaktionswellentyps auf die räumliche und zeitliche Ausdehnung der Gasblase, die Durchmischungsvorgänge und die Beeinflussung der hydrodynamischen Instabilitäten gezielt untersucht werden.

In drei Simulationsreihen wird die stoßinduzierte Zündung eines stöchiometrischen Wasserstoff-Sauerstoff-Gemisches innerhalb der Blase in der Umgebung von Stickstoff untersucht. Zunächst wird in einer zweidimensionalen Simulation durch die Variation des initialen Druckes bei einer konstanten Stoßmachzahl eine gezielte Zündung des Gemisches hervorgerufen. Ein niedriger Initialdruck führt zu einer langen Zündverzugszeit und einer anschließenden Deflagration. Ein Anheben des Initialdruckes führt zu einer Verkürzung der Zündverzugszeit und zu einer Detonation des Gasgemisches. Die unterschiedlichen Ausbreitungsgeschwindigkeiten der Reaktionswellen führen zu einer differierenden Entwicklung der RSBI. Die Detonationswelle dämpft die Instabilitäten an den Grenzflächen und reduziert dadurch die Durchmischung mit dem Umgebungsgas deutlich. Dahingegen weist die trägere Deflagrationswelle einen wesentlich geringeren Einfluss auf die Blasenentwicklung aus, die Durchmischung ist erst in der Langzeitentwicklung gestört.

Die zweite Studie erhöht die Komplexität des Setups durch die Variation der initialen Stoßmachzahl, welche die Intensität der Reaktionskinetik bestimmt. Die niedrigste Machzahl führt zu einer Deflagration im hinteren Teil der Blase, die stärkste Stoßwelle zu einer Detonation direkt an der Vorderkante der Blase. Mittlere Stoßmachzahlen induzieren komplexere Verbrennungsvorgänge, welche detailliert analysiert werden. Zum einen wird die Transition von Deflagration zu Detonation beobachtet und zum anderen eine simultane Zündung an der Vorder- und Hinterkante der Blase. Durch diese numerischen Beobachtungen können experimentelle Ergebnisse von Haehn et al. (2012) bestätigt und ein tieferer Einblick in die Gaszusammensetzung während der Induktionsphase gegeben werden.

Die dritte Simulationsreihe umfasst dreidimensionale Simulation einer RSBI mit detaillierter Reaktionskinetik. Ein starker Stoß entzündet die Blase vor dem Fokussierungspunkt an der Hinterkante und induziert eine Detonationswelle. Diese interagiert mit den Richtmyer-Meshkov und Kelvin-Helmholtz-Instabilitäten an den Grenzflächen. Des Weiteren werden dreidimensionale Effekte, wie die Widnall-Instabilität der Wirbelringe und Wirbelstreckung, beobachtet, welche einen großen Einfluss auf die Gesamtentwicklung der Blase aufweisen. Im Vergleich zu zweidimensionalen Simulationen zeigt sich eine deutlich höhere Durchmischung, vor allem in der Langzeitentwicklung. Die Ergebnisse weisen eine sehr gute Übereinstimmung mit den experimentellen Ergebnissen von Haehn et al. (2012) auf, besonders hinsichtlich der Ausbreitungsgeschwindigkeit der Reaktionswelle und der räumlichen Ausdehnung der Blase.

Die vorliegende Dissertation präsentiert die Ergebnisse der umfangreichen Untersuchung einer RSBI mit detaillierter Reaktionskinetik. Es werden die ersten Simulationen einer dreidimensionalen RSBI präsentiert, die zu einem tieferen Verständnis der Interaktion zwischen hydrodynamischen Instabilitäten und stoßinduzierter Reaktionskinetik beitragen. Hierdurch werden neue Einblicke in dreidimensionale Instabilitäten und Mischungsvorgänge ermöglicht. Die erarbeiteten Ergebnisse tragen zu einem tieferen Verständnis der Gaszusammensetzungen während der Induktions- und Transitionsprozesse bei und beschreiben den Einfluss unterschiedlicher Reaktionswellentypen auf die Gesamtentwicklung einer Stoß-Blasen-Interaktion.

Danksagung

Die vorliegende Dissertation umfasst die Ergebnisse meiner Arbeit aus den letzten vier Jahren als wissenschaftlicher Mitarbeiter am Lehrstuhl für Aerodynamik und Strömungsmechanik der Technischen Universität München. Im Laufe dieser Zeit wurde ich von einer Vielzahl von Menschen unterstützt, die zum Gelingen dieser Arbeit ihren Beitrag geleistet haben. Diesen möchte ich an dieser Stelle danken.

Meinem Doktorvater Professor Nikolaus Adams möchte ich für die uneingeschränkte Unterstützung und Betreuung während meiner Zeit am Lehrstuhl danken. Sie haben mir stets die Möglichkeit gegeben, mich fachlich und persönlich in einem sehr angenehmen wissenschaftlichen Umfeld entfalten zu können. Ich danke und wertschätze die wissenschaftlichen Freiheiten und die Unterstützung beim Verwirklichen meiner Ideen und Projekte, die ich unter Ihrer Leitung realisieren konnte.

Professor Stefan Hickel, meinem Zweitprüfer und ehemaligen Gruppenleiter, gebührt ebenfalls großer Dank. Deine stetige Unterstützung, dein kreativer Input und INCA Support haben in großem Maße zum Gelingen meiner Arbeit beigetragen. Gerade in der Anfangszeit war dein stets zur Verfügung stehender Rat goldwert.

Am Überstehen des stetigen Wechselbades von Euphorie und Frust haben meine Freunde und Kollegen einen großen Anteil. Besonders möchte ich meine Bürokollegen Volker, Patrick, Jan und Vito hervorheben, dank Euch wird mir die Zeit am Lehrstuhl immer positiv in Erinnerung bleiben. Ein weiterer Dank geht an Jan-Niklas und meinem Arbeitswegmitstreiter Gerald. Des Weiteren möchte ich mich noch bei meinen Fahrrädern für ihren selbstlosen Einsatz bedanken, die mich bei 756 Arbeitsfahrten auf 30.996 km Arbeitsweg nie im Stich gelassen haben.

Der wichtigste Anteil am erfolgreichen Abschluss dieser Arbeit gebührt allerdings meiner Familie. Ohne die uneingeschränkte und fantastische Unterstützung meiner Eltern wäre das erfolgreiche Gelingen der Dissertation undenkbar gewesen. Ihr habt mich immer bestärkt, meinen Weg, sowohl durch das Studium als auch durch meine Promotion zu gehen. Ganz besonders möchte ich mich bei Lilo bedanken, Du hast mich in den letzten Jahren stets unterstützt, Dir geduldig jedes Problem angehört und mir motivierend zur Seite gestanden.

Table of contents

1. Introduction

The following thesis summarizes my work of the past four years at the Institute of Aerodynamics and Fluid Mechanics at the Technische Universität München. The main objective of the thesis was the detailed investigation of a reacting shock-bubble interaction (RSBI), a generic setup which serves to study the interaction between shock-induced hydrodynamic instabilities and chemical reaction kinetics. RSBI covers a large range of physical phenomena, which can be specifically triggered by the initial conditions. The thesis is divided into three work packages: The first objective covers the implementation of the numerical framework for reaction kinetics into the existing numerical flow solver INCA[1] and the validation by several test cases. The second objective comprises simulations of two-dimensional RSBI to study the early stage bubble evolution and ignition characteristic. Different initial pressures or shock Mach numbers trigger diverse reaction wave types, which highly affect the mixing processes and the spatial and temporal evolution of the flow field around the bubble. The last work package uses the experience of the two-dimensional RSBI to perform the first three-dimensional RSBI with detailed chemistry so far. Differences between two- and three-dimensional simulations of RSBI are elaborated in detail and the numerical results are compared with experimental data.

The thesis is structured as follows: The current chapter contains an introduction to hydrodynamic instabilities, shock-induced chemistry and shock-bubble interaction (SBI), including a literature overview of the state-of-the-art in SBI research. In Chapter 2 the numerical model is presented, including the governing equations and the numerical

[1] INCA is a general-purpose multi-physics CFD solver for high-fidelity DNS and LES, developed at the Institute of Aerodynamics and Fluid Mechanics at the Technische Universität München.

schemes for flux reconstruction, time integration and reaction kinetics. Chapter 3 emphasizes the main results of the thesis, including a short introduction to each publication. The key findings are summarized in Chapter 4. A full list of all publications is listed in Appendix A, the main publications in full length in Appendix B and the reaction mechanism used for the computation of H_2-O_2 reaction kinetics in Appendix C.

1.1. Hydrodynamic instabilities

Three hydrodynamic instabilities dominate shock-accelerated flow inhomogeneities: the Richtmyer-Meshkov instability (RMI), the Kelvin-Helmholtz instability (KHI) and, additionally for three-dimensional simulations, the Widnall-type instability.

RMI arises at an impulsively accelerated interface, which separates two fluids. If the interface is non-orthogonal to the shock wave or contains little perturbations, the misalignment of the pressure gradient, ∇p, associated with the shock wave and the density gradient, $\nabla \rho$, at the material interface causes baroclinic vorticity production ($(\nabla \rho \times \nabla p) \neq 0$). The baroclinic vorticity is the initial driving mechanism of RMI. The vorticity deposition leads to a growth of the initial interface perturbations. Furthermore, if the initial energy input is sufficient, the flow field can evolve into a turbulent mixing zone through nonlinear interactions of the material interface perturbations. RMI was theoretically stated by Richtmyer (1960) and experimentally verified by Meshkov (1969). It can be considered as the impulsive limit of the Rayleigh-Taylor instability (Rayleigh, 1883; Taylor, 1950). For comprehensive reviews the reader is referred to Brouillette (2002) and Zabusky (1999).

RMI plays an important role in reactive environments and occurs on a wide range of reacting flows from extremely large scales in astrophysics (Arnett, 2000), to intermediate scales in combustion (Yang et al., 1993; Khokhlov et al., 1999) down to very small scales in inertial confinement fusion (Craxton et al., 2015). RMI can, e.g., enhance mixing in high-speed reactive flows, promote turbulent mixing and thus increase the burning efficiency of supersonic combustion engines (Marble et al., 1990). Furthermore, the interaction between a shock wave and a flame can be found in several combustion systems, where the resulting instabilities show a distinct influence on the transition from deflagration to detonation (Khokhlov et al., 1999).

In the generic configuration of SBI, RMI induces velocity shear and small perturbations at the interface of the bubble, which are necessary preconditions for KHI (Drazin, 2002). The perturbations are amplified, generating vortices at the interface accompanied by the appearance of smaller scales (Brouillette, 2002). KHI drives the breakup of large-scale structures (Tritschler et al., 2013) and forces mixing (Oran and Boris, 2005). Both effects dominate the hydrodynamic evolution in SBI, especially in two-dimensional simulations. Three-dimensional SBIs reveal a third instability: An azimuthal instability (Widnall et al., 1974) destabilizes the vortex ring in the long-term evolution by azimuthal bending modes, which lead to an increase of the shock-induced mixing (Klein et al., 2003). The so-called Widnall-type instability is an important three-dimensional effect which leads to certain

discrepancies in the bubble dynamics in the long-term evolution between two- and three-dimensional simulations of SBI, as it accelerates the decay of the main vortex ring.

1.2. Shock-induced ignition and combustion

Besides the induction of hydrodynamic instabilities the shock wave causes a second essential effect in reactive gas mixtures: The shock-induced change in the thermodynamic properties across the shock wave increases the chemical reaction rates up to ignition. The following reaction wave can be classified into two categories: deflagration and detonation. Deflagration is a subsonic reaction wave that propagates through the gas mixture due to direct transfer of chemical energy from burning to unburned gas, driven by diffusion (Liberman, 2008). Detonation is driven by a fast chemical reaction and the associated large heat release within the reaction wave zone. A shock wave immediately precedes the detonation wave and preheats the gas mixture by compression (Liberman, 2008). The detonation wave propagates up to 10^8 times faster than the deflagration wave (Fickett and Davis, 2010). Due to these large discrepancies in the characteristic reaction time scales the reaction wave type is crucial for the flow evolution in SBI.

In a reactive flow field with specific thermodynamic conditions the deflagration wave can transform into a detonation wave. Deflagration-to-detonation transition (DDT) is one of

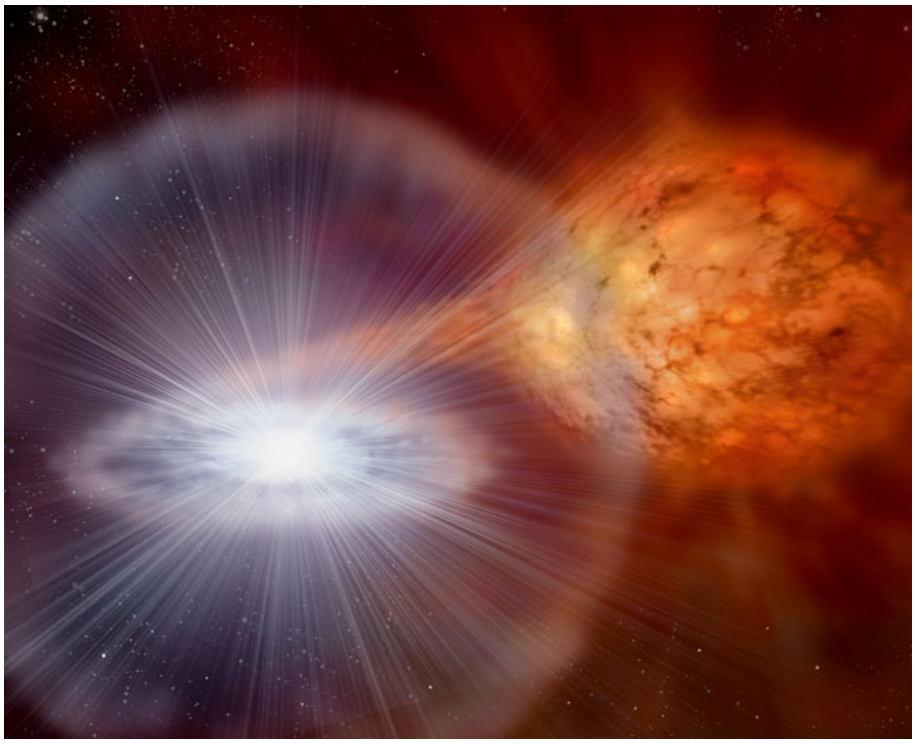

Figure 1.1.: Thermonuclear explosion of a white dwarf, which has been steadily supplied with material from a red giant companion. The reaction wave transitions from deflagration to detonation. (Artist's impression) (Hardy, 2017).

the most interesting unresolved problems in combustion theory. DDT occurs in many technical environments, like in internal combustion engines or in mines (unintended explosion), see Liberman et al. (2010). Furthermore, it plays an important role in research, like in astrophysics, where, e.g., the explosion of white dwarfs, shown Fig. 1.1, can only be explained by the occurrence of transition between deflagration and detonation, as both reaction processes individually fail to reproduce the correct light curves and nucleosynthesis during the explosion (Charignon and Chiéze, 2013).

Generally, a self-propagating deflagration wave is unstable and tends to accelerate. Under specific conditions the continuous acceleration of the deflagration wave can lead to a sudden transition into a detonation wave (Lee, 2008). There have been several attempts to explain the transition from deflagration to detonation. Zel'dovich et al. (1970) developed a gradient mechanism to explain DDT. They imposed a nonuniform distribution of the temperature gradient in a one-dimensional system, which leads to regions with shortened and regions with extended induction times. The gradient of induction time induces a spontaneous reaction wave, propagating with a velocity D_{sp}, which depends on the steepness of the gradient ($D_{sp} = (\partial\tau/\partial x)^{-1}$) (Zel'dovich, 1980), where τ is the induction time. Under specific circumstances, when D_{sp} is higher than the speed of sound and lower than the Chapman-Jouguet detonation velocity D_{CJ}, the reaction wave and the compression wave, generated by the exothermic reaction, merge and evolve into a self-sustaining detonation wave. Several numerical investigations have been carried out to explain the formation of the gradient of induction time, summarized in the review paper by Oran and Gamezo (2007). Their studies used one-step reaction mechanisms and indicated that the gradient of induction time is responsible for DDT.

However, by studying DDT with a more detailed mechanism, Kuznetsov et al. (2010) showed that the induction time is much longer than predicted by the one-step mechanisms. Real combustible gas mixtures show a significant higher induction time than simulations conducted with one-step mechanisms (Kuznetsov et al., 2009). Therefore, Liberman et al. (2010) proposed a new mechanism mainly driven by flame acceleration, which is divided into three stages. The reaction front accelerates and produces shock waves far ahead of the flame. Thereafter, the acceleration decreases, shocks are formed on the flame surface and pockets of compressed and heated unburnt gas emerge (preheat zone). In the final stage the transition to detonation occurs: The flame propagates into the preheat zone and produces a large amplitude pressure pulse. Increasing pressure enhances the reaction rates and the feedback between the pressure peak and the reaction leads to a growth of the pressure peak, which steepens into a strong shock that, coupled with the reaction zone, finally forms an overdriven detonation wave.

In shock accelerated reactive flows the transition process can be triggered by a second phenomenon. The flame front propagates into regions of gas that already have been compressed and preheated by a preceding initial shock wave and its reflections. Thus, the reaction rates and the heat release increase in these regions, which in turn enhances the pressure pulse and accelerates the transition to detonation. Hence there are two sources for DDT: (i) it develops from the preheated, compressed gas mixture between the leading shock wave and the flame or (ii) it arises from within the flame (Oran and Gamezo, 2007). The latter transition process is relevant in the setup of RSBI, as the shocked

bubble contains regions of irregular compression by the initial shock wave.

In the present thesis the reaction kinetics of hydrogen-oxygen (H_2-O_2) are studied. The limits between deflagration and detonation for a H_2-O_2 gas mixture are outlined in Fig. 1.2 as functions of temperature and pressure. In contrast to reactions of other chemical elements, H_2-O_2 is characterized by a non-linear explosion limit. Due to pressure dependent intermediate reactions, the type of ignition can change several times at constant temperature. Some intermediate products and reactions are inactive at low pressures and become active at higher pressures, which significantly affects the chemical reaction process (Oldenberg and Sommers, 1941). The chain branching exceeds the rate of chain breaking on the right side of the reversed-S curve. The solid line represents the explosion limit for a pure stoichiometric H_2-O_2 mixture. Wang and Chung (2013) diluted the stoichiometric mixture by adding an inert gas and observed a distinct shift of the explosion limit to higher temperatures. The dashed line in Fig. 1.2 shows the explosion limit for a gas mixture containing H_2, O_2 and an inert gas with a molar ratio of 2 / 1 / 4, which is similar to the bubble gas composition used in our study (H_2, O_2 and Xe with a molar ratio of 2 / 1 / 3.7).

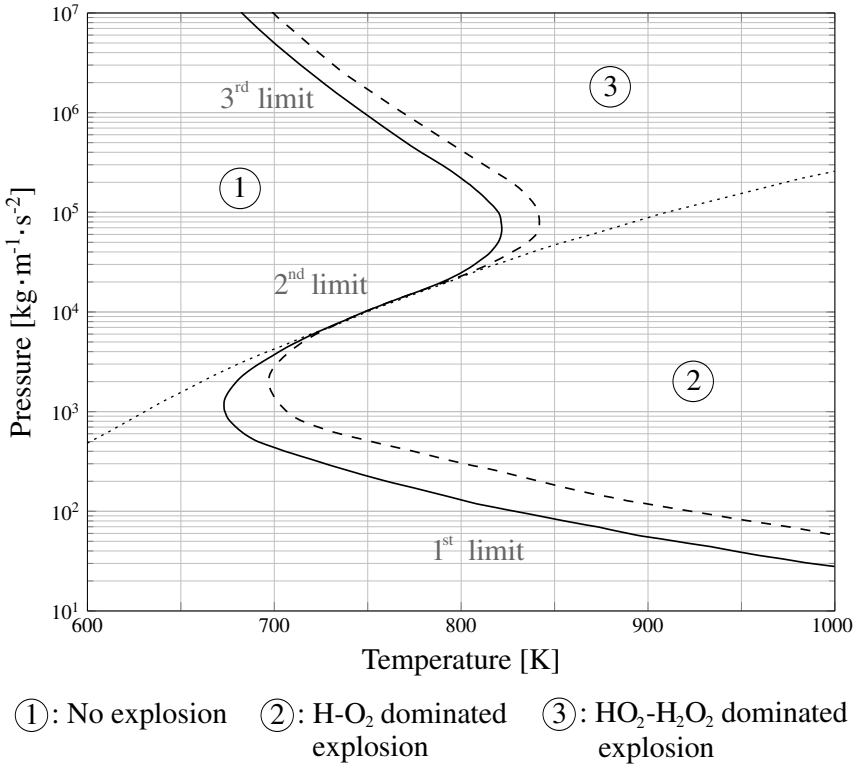

Figure 1.2.: Explosion limits for H_2-O_2 reaction. ——— : stoichiometric mixture; - - - : stoichiometric mixture, diluted by an inert gas with the molar ratio of 2 / 1 / 4; ····· : extended second explosion limit. (Based on data of Wang and Chung (2013).)

The reaction wave type in H_2-O_2 combustion depends on the temperature and pressure of the reactive gas mixture. Hence, different reaction wave types can be triggered by the variation of the initial temperature or the initial pressure as well as by the shock strength,

which determines the change of the thermodynamic properties across the shock wave. The last two configurations are applied to achieve the results of the presented work.

The general chemical reaction sequence of H_2-O_2 is outlined in the following, including the pressure dependent branching, which determines the formation of either a deflagration or a detonation wave. The reaction is initiated by the formation of hydrogen radicals

$$H_2 \longrightarrow H + H \quad . \tag{R.1}$$

The hydrogen radicals induce the subsequent chemical reactions, whereby the post-shock pressure is crucial for the following branching:

$$H + O_2 + M \quad \longrightarrow \quad HO_2 + M \quad , \tag{R.2}$$

$$H + O_2 \quad \longrightarrow \quad O + OH \quad . \tag{R.3}$$

Reaction (R.2) contains a ternary collision, which is proportional to the square of the pressure, whereas the binary collision in reaction (R.3) is only linearly proportional. The chain branching reaction (R.3) dominates at lower pressure, opening the branch that leads to deflagration, which is characterized by a high concentration of H, O and OH radicals. Higher pressures lead to an increase of the reaction rate of the ternary chain-breaking reaction (R.2). For a temperature below approximately 825 K, see Fig. 1.2, the explosion limit is crossed and the chain reaction is stopped by the destruction of H into HO_2. In the pressure range between the second and third explosion limit HO_2 is inactive, but becomes active for increasing pressure as the third explosion limit is crossed again (Oldenberg and Sommers, 1941). Higher temperatures ($T \gtrsim 825$ K) lead to a sustained chain reaction, without crossing the explosion limit. Above the third explosion limit HO_2 collides with H_2, forming either H_2O or H_2O_2 as an intermediate product that breaks down into OH:

$$HO_2 + H_2 \quad \longrightarrow \quad H_2O + OH \quad , \tag{R.4}$$

$$HO_2 + H_2 \quad \longrightarrow \quad H_2O_2 + H \quad , \tag{R.5}$$

$$H_2O_2 + M \quad \longrightarrow \quad OH + OH + M \quad . \tag{R.6}$$

The reaction chain is continued by the OH radicals

$$OH + H_2 \quad \longrightarrow \quad H_2O + H \quad . \tag{R.7}$$

The produced chain-carrying radicals accumulate due to insufficient mixing with the surrounding gas, which leads to a further increase of the reaction rate and finally to chain branching explosion (Mishra, 2013). A significant formation of HO_2 and H_2O_2, even before

the mixture ignites, characterizes the detonation above the third explosion limit.

The two different reaction branches, either dominated by reaction (R.2) or (R.3), are separated by the extended second explosion limit as illustrated in Fig. 1.2 by a dotted line. In the present investigation of RSBI the reaction wave type is determined by, whether the post-shock condition is above or below the extended second explosion limit, as all simulations involve post-shock temperatures which sustain the chain branching of H_2-O_2 reaction kinetics.

The H_2-O_2 reaction contains several more intermediate reactions, which are considered in our work, but skipped here for a better comprehension. The detailed H_2-O_2 reaction mechanism as used in the presented numerical simulations is listed in the Appendix C.

1.3. Reacting shock-bubble interaction

SBI is a generic configuration which is used to study the interaction between hydrodynamic instabilities and shock-induced combustion. A planar shock wave propagates through the domain and penetrates a bubble, filled with a gas mixture of different density. There are three main hydrodynamic phenomena in inert as well as in reacting SBI that have to be treated in detail:

Nonlinear acoustic effects arise in SBI, induced by the reflection, refraction and diffraction of the incident shock wave. Depending on the Atwood number, which describes the density ratio of the bubble gas and the surrounding gas ($A = (\rho_1 - \rho_2)/(\rho_1 + \rho_2)$), these effects have a diverse impact on the bubble evolution. For an Atwood number larger than zero the bubble acts like a converging lens, for $A < 0$ like a diverging lens (Dimotakis and Samtaney, 2006). A divergent geometry leads to a faster shock wave propagation inside the bubble. The transmitted shock wave transits the bubble and a Mach stem, a precursor shock and a triple point form outside the interface (Ranjan et al., 2011). In case of a convergent geometry (a heavy gas bubble surrounded by light ambient gas, $A > 0$) the transmitted shock wave travels more slowly than the incident shock wave outside of the bubble. At the downstream pole of the bubble the transmitted and the outer shock waves merge in the shock-focusing point.

The second aspect of SBI covers the vorticity production and transport, inducing RMI. The vorticity transport equation is given by

$$\frac{D\boldsymbol{\omega}}{Dt} = (\boldsymbol{\omega} \cdot \nabla)\boldsymbol{u} - \boldsymbol{\omega}(\nabla \cdot \boldsymbol{u}) + \frac{1}{\rho^2}(\nabla\rho \times \nabla p) + \nu\nabla^2\boldsymbol{\omega} \quad . \tag{1}$$

The first term on the right hand side, $(\boldsymbol{\omega} \cdot \nabla)\boldsymbol{u}$, represents the vortex-stretching term. It is responsible for stretching, turning and tilting of the vortex lines by velocity gradients. As $\boldsymbol{\omega}$ is perpendicular to the flow field the vortex-stretching term is absent in two dimensions, which has a certain effect on the spatial expansion in the long-term evolution (Hejazialhosseini et al., 2013). The vortex dilatation term is represented by the second term of Eq. (1), $\boldsymbol{\omega}(\nabla \cdot \boldsymbol{u})$, and is of interest for highly compressible flows (Ranjan et al.,

2011). The last term, $\nu\nabla^2\boldsymbol{\omega}$, describes the rate of change of $\boldsymbol{\omega}$ due to molecular diffusion of vorticity. It can be generally neglected because of low viscosity values of the fluid and short timescales of the simulation.

The third term in Eq. (1), $\frac{1}{\rho^2}(\nabla\rho \times \nabla p)$, is the baroclinic vorticity production term and is of high importance in SBI. The misalignment of the pressure gradient, ∇p, associated with the shock wave and the density gradient, $\nabla\rho$, at the material interface of the bubble causes baroclinic vorticity production directly after the first impact of the shock wave on the bubble ($\nabla\rho \times \nabla p \neq 0$) and drives RMI. In the generic configuration of SBI, no vorticity is initialized in the entire domain ($\boldsymbol{\omega} = 0$), which implies that the only source of vorticity is the baroclinic vorticity production term:

$$\frac{D\boldsymbol{\omega}}{Dt} = \frac{1}{\rho^2}(\nabla\rho \times \nabla p) \quad . \tag{2}$$

The magnitude of vorticity production is determined by the non-collinearity of $\nabla\rho$ and ∇p. The peak in vorticity production during the shock-wave passage is gained at the diametrical plane, where the origin of the vortex ring formation is located.

The third physical aspect can be observed during the shock-wave passage and the associated change in the thermodynamic properties. According to the Rankine-Hugoniot conditions pressure and temperature increase, whereas density decreases across the transmitted shock wave inside the bubble. This change directly affects the reaction kinetics,

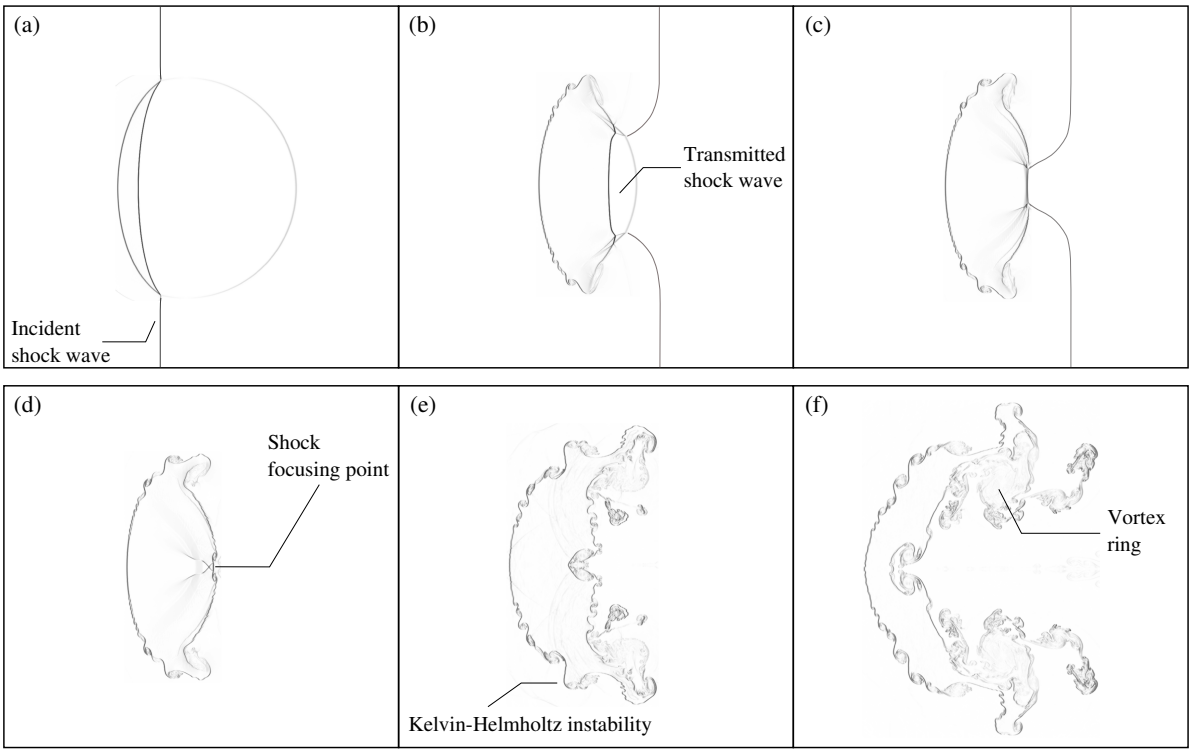

Figure 1.3.: Schematic view of a SBI with an Atwood number A $>$ 0, (convergent geometry). Gray isolines indicate the density gradients.

since higher pressures and temperatures lead to an increase of the reaction rates. If the shock wave is strong enough, the raise of the reaction rates is sufficient to induce a chain-reaction, which finally leads to an ignition of the bubble gas.

Within the scope of the present thesis SBIs with a convergent behavior ($A > 0$) are studied. Figure 1.3 outlines the general evolution of an inert convergent SBI. The first contour plots Fig. 1.3 (a) and (b) depict the SBI during the shock-wave passage, where, due to the high density of the bubble gas, the transmitted shock wave travels slower than the incident shock wave. The transmitted shock wave focuses at the downstream pole of the bubble, see Fig. 1.3 (c) and (d). As the shock wave collapses in the shock-focusing point, pressure and temperature increase, which is known as the shock-focusing phenomenon. Simultaneously, the baroclinic vorticity causes RMI to arise at the outer interface of the bubble. After the shock wave has passed the bubble, the primary vortex cores evolve and KHI arises due to shear at the material interface (Fig. 1.3 (d) and (e)). Mixing successively increases while further secondary instabilities emerge. The primary vortex cores are advected downstream and are steadily supplied by bubble gas. The last contour plot, Fig. 1.3 (f), shows a high degree of mixing between the bubble gas and the surrounding, together with the characteristic formation of the vortex core. Provided that the initial energy input is sufficient the flow develops a turbulent mixing zone through non-linear interactions of the material interface perturbations (Brouillette, 2002; Zabusky, 1999). In addition, a three-dimensional surface plot of a SBI is shown in Fig. 1.4 to illustrate the complex flow field around the shocked bubble in the long-term evolution. At this stage the bubble shows highly turbulent structures and most of the vorticity has decayed except around the main vortex core, which exhibits characteristic azimuthal instabilities.

Inert SBI have been intensively studied over the last decades. Haas and Sturtevant (1987) investigated the interaction of shock waves propagating in air with a gas bubble filled with either helium or chlorodifluoromethane (R22). Their shadow-photographs significantly contribute to a better understanding of the temporal bubble evolution under shock acceleration and established an entire new class of canonical flow configurations. Quirk and Karni (1996) performed a detailed numerical investigation of SBI problems. They complemented experimental findings by reproducing the transition from regular to irregular refraction, shock-wave focusing and the formation of a jet towards the center of the bubble. A comprehensive review on SBI is given by Ranjan et al. (2011).

The replacement of the inert gas by a reactive gas mixture adds an additional level of complexity to the setup. The increase of thermodynamic properties across the shock wave leads to a raise of chemical reaction rates, which can be sufficient to ignite the gas mixture. The propagation of the reaction wave through the bubble gas and its interaction with the hydrodynamic instabilities influence the spatial and temporal evolution of the bubble and the mixing process with the surrounding gas distinctly. In general, there exist three possible ignition scenarios: The first one consists of a strong shock wave, which is high enough to ignite the gas mixture directly behind the shock wave with a short ignition delay time, followed by a detonation wave. The second ignition case requires the pressure and temperature peak in the shock focusing point at the downstream pole for a successful ignition. The triggered reaction wave is still a detonation wave as the pressure

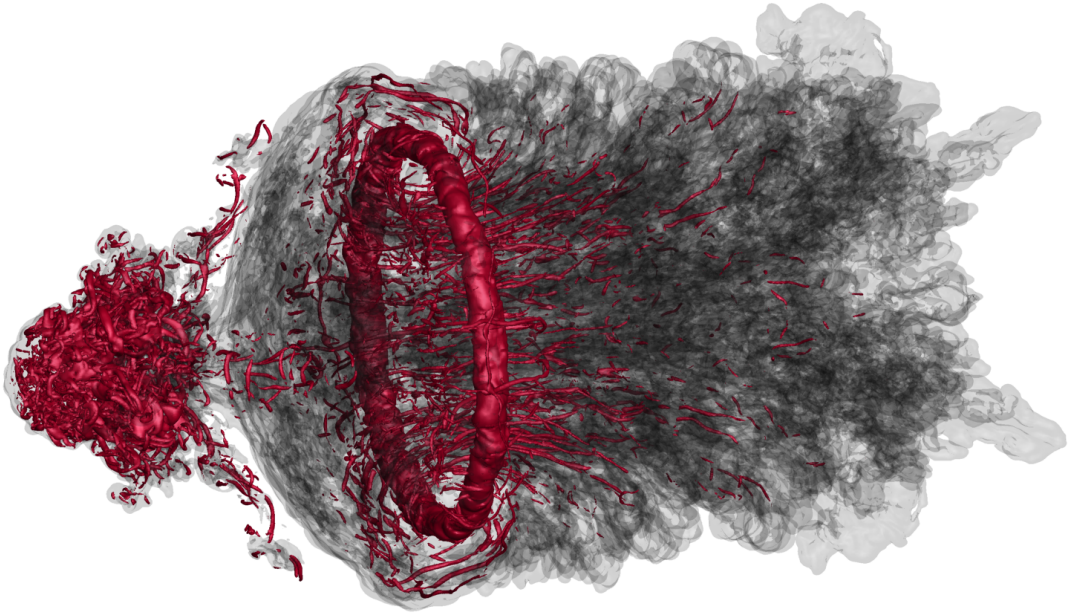

Figure 1.4.: Highly turbulent SBI in the long-term evolution ($Ma = 2.83$ at $t = 410$ µs). Gray translucent isosurface shows a specific mass fraction of xenon ($Y_{Xe} = 0.1$). The red isosurface represents a characteristic value of the vorticity magnitude ($|\omega| = 400000$ s^{-1}) to visualize the evolution of the vortex structure, including the main vortex ring.

and temperature are above the explosion limit. The third scenario is triggered by a weak shock wave and leads to a deflagration wave after a long induction time. The point of origin remains in the shock-focusing area, but the long ignition delay and the subsonic propagation velocity of the reaction wave reduce the influence of the reaction kinetics on the flow field. Maximum pressure and temperature are reached when the shock passes the bubble. Subsequently, the gas mixture expands and the two main parameters controlling the reaction rate, temperature and pressure, decrease, which reduces the chemical reactivity of the gas mixture. If the shock wave is too weak, the increase of the thermodynamic properties across the shock wave is not sufficient to ignite the gas mixture at all.

Haehn et al. (2012) performed the first experiment of RSBI by replacing the inert gas within the bubble by a reacting gas composition. In their investigation a stoichiometric gas mixture of H_2 and O_2, diluted by xenon (Xe), is compressed by a shock wave propagating at Mach numbers in the range of $Ma = 1.34$ to $Ma = 2.83$. They observed three ignition scenarios in their experiments: A low shock Mach number does not ignite the gas mixture within the experimental timeframe as the compression is not sufficiently high. An increase of the shock strength results in an ignition, followed by a deflagration reaction wave. At higher shock Mach numbers the stoichiometric mixture ignites and forms a detonation wave, even before the shock wave has reached the shock focusing point. Damköhler numbers were determined in the range from $Da = 0.25$ ($Ma = 1.65$) to $Da = 8.00$ ($Ma = 2.83$). Haehn et al. (2012) concluded that heat conduction plays an important

role at lower Mach numbers, and that the Zeldovich mechanism becomes important at higher Mach numbers. This finding is consistent with the two limiting cases of shock-induced combustion, the strong and the weak ignition (Oran and Gamezo, 2007). Strong ignition leads to a detonation mostly initiated directly by the shock wave, whereas weak ignition is characterized by the occurrence of small flames that can undergo transition into detonation waves. Haehn et al. (2012) provide several chemiluminescence exposures to depict the qualitative evolution of the bubble and the reaction processes. Moreover, they present quantitative data for the temporal evolution of the transverse diameter of the bubble as well as for the vortex ring diameter. However, the complex experimental setup of Haehn et al. (2012) implies uncertainties. For instance, the uncertainty of the Damköhler number at the highest Mach number ($Ma = 2.83$) amounts to $Da = 8 \pm 4$. At the lowest Mach number ($Ma = 1.34$) 30% of all measurements showed no ignition within the given experimental time frame. Such uncertainties underline the need for a detailed numerical investigation of RSBI.

1.4. Objectives

The fundamental objective of the present work is the implementation and validation of a reaction rate solver which provides the numerical framework for the simulation of multi-component reacting flows. Therefore, a high-order solver for stiff ordinary differential equations is coupled with the existing in-house flow solver INCA. The implementation bases on a rudimentary reaction rate solver, which was elaborated in the master's thesis of the author (Diegelmann, 2013). A comprehensive validation of the implemented solver through several test cases and comparisons with other numerical codes proved high accuracy and reliability of the newly-implemented solver. The validation campaign places special emphasis on precise ignition delay times, which are essential for accurate simulations of shock-induced chemistry.

The first numerical study of two-dimensional RSBI focuses on the variation of the initial pressure and its capability to trigger either deflagration or detonation. A constant shock wave strength of $Ma = 2.30$ ensures a similar pressure and temperature increase across the shock wave front for all initial pressures. Thus the formation of either a detonation or deflagration wave is only determined by the initial pressure. Spatial and temporal bubble evolution and mixing are studied with respect to the reaction wave type. A preceding grid resolution study shows convergence of integral quantities and the quantities of interest, like the pressure and the temperature peak across the shock wave front. The analysis of the Damköhler numbers underlines the influence of the reaction wave type.

The knowledge and results of the first study are used for the second, more comprehensive, investigation of two-dimensional RSBI. The variation of the shock Mach number ($Ma = 2.07 - 2.90$) permits a more specific control of reaction kinetics during the interaction. Besides detonation and deflagration waves, more complex effects such as DDT and simultaneous detonations are triggered and thoroughly studied. The interaction between different reaction wave types and hydrodynamic instabilities is analyzed in detail. The gas compositions of the ignition spots are examined during the induction as well as the

ignition stage to identify specific reaction branches. Furthermore, results are compared to experimental data and limitations of two-dimensional simulations are discussed.

The final objective of the present work comprises the first three-dimensional simulation of RSBI. A shock Mach number of $Ma = 2.83$ triggers ignition plainly before the shock-focusing point, followed by a detonation wave. Mixing, growth of instabilities and spatial expansion of the bubble gas, especially in the long-term evolution, are highly affected by three-dimensional effects, which are studied in detail. Discrepancies between two- and three-dimensional simulations are emphasized and examined. A grid-convergence study and comparison to experimental data underline the high-fidelity of the presented results.

2. Numerical model

In the following chapter the governing equations, consisting of the Navier-Stokes equations, caloric and transport properties as well as chemical reaction kinetics, are presented in detail. Furthermore, the numerical scheme for the flux reconstruction, time integration and the source term computation are outlined.

2.1. Governing equations

2.1.1. Navier-Stokes equations

The full set of compressible reacting multi-component Navier-Stokes equations is solved in conservative form

$$\frac{\partial \boldsymbol{U}}{\partial t} + \nabla \cdot \boldsymbol{F}(\boldsymbol{U}) = \nabla \cdot \boldsymbol{F}_\nu(\boldsymbol{U}) + \boldsymbol{S} \quad , \tag{1}$$

with

$$\boldsymbol{U} = \begin{pmatrix} \rho \\ \rho\boldsymbol{u} \\ E \\ \rho Y_i \end{pmatrix} \quad , \quad \boldsymbol{F}(\boldsymbol{U}) = \begin{pmatrix} \rho\boldsymbol{u} \\ \rho\boldsymbol{u}\boldsymbol{u} + p\boldsymbol{\delta} \\ (E+p)\boldsymbol{u} \\ \rho\boldsymbol{u}Y_i \end{pmatrix} \quad ,$$
$$\boldsymbol{F}_\nu(\mathbf{U}) = \begin{pmatrix} 0 \\ \boldsymbol{\tau} \\ \boldsymbol{\tau}\cdot\boldsymbol{u} - \boldsymbol{q_c} - \boldsymbol{q_d} \\ \boldsymbol{J_i} \end{pmatrix} \quad \text{and} \quad \boldsymbol{S} = \begin{pmatrix} 0 \\ \mathbf{0} \\ \dot{\omega}_T \\ \dot{\omega}_i \end{pmatrix} \quad , \tag{2}$$

where ρ is the mixture density and $\boldsymbol{u}$ denotes the velocity vector. The identity matrix is denoted by $\boldsymbol{\delta}$, total energy by E and pressure by p. Y_i is the mass fraction of species $i = 1, 2, ..., N$, with N being the total number of species. The source term $\boldsymbol{S}$ contains the heat release $\dot{\omega}_T$ and the species formation and destruction in terms of individual mass rates $\dot{\omega}_i$, representing the chemical reaction kinetics. The viscous stress tensor is given by, $\boldsymbol{q_c}$ denotes the heat conduction, $\boldsymbol{q_d}$ the interspecies diffusional heat flux and $\boldsymbol{J}_i$ the species diffusion.

2.1.2. Caloric and transport properties

The viscous stress tensor $\boldsymbol{\tau}$ for a Newtonian fluid is given by

$$\boldsymbol{\tau} = 2\overline{\mu}\left[\frac{1}{2}\left(\nabla\boldsymbol{u} + (\nabla\boldsymbol{u})^T\right) - \frac{1}{3}\boldsymbol{\delta}\left(\nabla\cdot\boldsymbol{u}\right)\right] \quad , \tag{3}$$

with $\overline{\mu}$ as the mixture viscosity

$$\overline{\mu} = \frac{\sum_{i=1}^{N}\mu_i Y_i/M_i^{1/2}}{\sum_{i=1}^{N} Y_i/M_i^{1/2}} \quad . \tag{4}$$

M_i is defined as the molecular mass of each species i. The calculation of the viscosity of each species μ_i is based on the Chapman-Enskog viscosity model

$$\mu_i = 2.6693\cdot 10^{-6}\frac{\sqrt{M_i T}}{\Omega_{\mu,i}\sigma_i^2} \quad , \tag{5}$$

where T is the temperature and σ_i the collision diameter. The collision integral $\Omega_{\mu,i}$ (Neufeld et al., 1972) is defined as

$$\Omega_{\mu,i} = A(T_i^*)^B + C\exp\left(DT_i^*\right) + E\exp\left(FT_i^*\right) \quad , \tag{6}$$

with $A = 1.16145$, $B = -0.14874$, $C = 0.52487$, $D = -0.7732$, $E = 2.16178$, $F = -2.43787$ and $T_i^* = T/(\epsilon/k)_i$, using the Lennard-Jones energy parameter $(\epsilon/k)_i$ for species i. According to the Fourier law, the heat conduction is defined as

$$\boldsymbol{q_c} = -\overline{\kappa}\nabla T \quad , \tag{7}$$

with $\overline{\kappa}$ denoting the mixture heat conductivity, which is calculated from Poling et al. (2001)

$$\overline{\kappa} = \frac{\sum_{i=1}^{N}\kappa_i Y_i/M_i^{1/2}}{\sum_{i=1}^{N} Y_i/M_i^{1/2}} \quad , \tag{8}$$

where κ_i is the thermal conductivity of species i. The interspecies diffusional heat flux $\boldsymbol{q_d}$ (Cook, 2009) is given by

$$\boldsymbol{q_d} = \sum_{i=1}^{N} h_i \boldsymbol{J}_i \quad , \tag{9}$$

with h_i as the individual species enthalpy. The species diffusion $\boldsymbol{J}_i$ is modeled as

$$\boldsymbol{J}_i = -\rho\left(D_i\nabla Y_i - Y_i\sum_{j=1}^{N} D_j\nabla Y_j\right) \quad . \tag{10}$$

D_i describes the effective binary diffusion coefficient of species i

$$D_i = (1 - X_i)\left(\sum_{j\neq i}^{N}\frac{X_j}{D_{ij}}\right)^{-1} \quad , \tag{11}$$

with X_i as the mole fraction of species i. Equation (11) ensures that the interspecies diffusion fluxes balance to zero. The constitutive empirical law is used to compute the mass diffusion coefficient of a binary mixture (Poling et al., 2001)

$$D_{ij} = \frac{0.0266}{\Omega_{D,ij}}\frac{T^{3/2}}{p\sqrt{M_{ij}}\sigma_{ij}^2} \quad , \tag{12}$$

where

$$M_{ij} = \frac{2}{\frac{1}{M_i} + \frac{1}{M_j}} \quad \text{and} \quad \sigma_{ij} = \frac{\sigma_i + \sigma_j}{2} \quad . \tag{13}$$

The collision integral for diffusion $\Omega_{D,ij}$ is given by

$$\begin{aligned} \Omega_{D,ij} = A^*(T_{ij}^*)^{B^*} + C^* \exp\left(D^* T_{ij}^*\right) \\ + E^* \exp\left(F^* T_{ij}^*\right) + G^* \exp\left(H^* T_{ij}^*\right) \quad . \end{aligned} \tag{14}$$

The parameters are defined as $A^* = 1.06036$, $B^* = -0.1561$, $C^* = 0.19300$, $D^* = -0.47635$, $E^* = 1.03587$, $F^* = -1.52996$, $G^* = 1.76474$, $H^* = -3.89411$, and $T_{ij}^* = T/T_{\epsilon_{ij}}$. $T_{\epsilon_{ij}}$ have been obtained from the Lennard-Jones energy parameters for species i and j as

$$T_{\epsilon_{ij}} = \sqrt{\left(\frac{\epsilon}{k}\right)_i \left(\frac{\epsilon}{k}\right)_j} \quad . \tag{15}$$

2.1.3. Equation of state

The equation of state for an ideal gas is used to close the equations

$$p(E, Y_i) = \left(\overline{\gamma} - 1\right) E \quad , \tag{16}$$

where $\overline{\gamma}$ represents the ratio of specific heats of the mixture

$$\overline{\gamma} = \frac{\overline{c_p}}{\overline{c_p} - \overline{R}} \quad , \tag{17}$$

with

$$\overline{c_p} = \sum_{i=1}^{N} Y_i c_{p,i} \quad . \tag{18}$$

The specific gas constant of the mixture is defined by $\overline{R} = \mathcal{R}/\overline{M}$, with $\mathcal{R}$ as the universal gas constant. $\overline{M}$ is the molar mass of the mixture

$$\overline{M} = \left[\sum_{i=1}^{N} \frac{Y_i}{M_i}\right]^{-1} = \sum_{i=1}^{N} X_i M_i \quad . \tag{19}$$

$c_{p,i}$ represents the specific heat coefficient of species i

$$c_{p,i} = \frac{\gamma_i}{\gamma_i - 1} R_i \quad . \tag{20}$$

R_i is defined as $R_i = \mathcal{R}/M_i$. The temperature is computed from

$$T = \frac{p}{\overline{R}\rho} \quad . \tag{21}$$

2.1.4. Chemical reaction kinetics

The chemical reaction kinetics are expressed by the heat release $\dot{\omega}_T$ and the species formation and destruction in terms of individual mass rates $\dot{\omega}_i$ in the Navier-Stokes equations (Eq. (1)). The specific heat release $\dot{\omega}_T$ is calculated from

$$\dot{\omega}_T = -\sum_{i=1}^{N} \Delta h^0_{f,i} \dot{\omega}_i \quad , \tag{22}$$

where $h^0_{f,i}$ represents the heat of formation of each species i. Mass rates $\dot{\omega}_i$ for each species are estimated by

$$\dot{\omega}_i = W_i \sum_{r=1}^{N_R} \nu_{ir} \Gamma_r \left(k_{fr} \prod_{j=1}^{N} [X_j]^{\nu'_{jr}} - k_{br} \prod_{j=1}^{N} [X_j]^{\nu''_{jr}} \right) \quad , \tag{23}$$

where N_R is the number of reactions, W_i the molecular weight, Γ_r the third body efficiency of reaction r, X_j the molar concentration, and ν'_{jr} and ν''_{jr} the molar stoichiometric coefficients of the reactant and the product of reaction r. ν_{ir} represents the net stoichiometric coefficient

$$\nu_{ir} = \nu''_{ir} - \nu'_{ir} \quad . \tag{24}$$

The Arrhenius law is used to calculate the forward and backward reaction rates k_{fr} and k_{br}. The forward reaction rates are calculated from

$$k_{fr} = A_{fr} T^{\beta_{fr}} \exp\left(\frac{E_{fr}}{RT}\right) \quad . \tag{25}$$

A_{fr} is the pre-exponential factor, E_{fr} is the activation energy and β_{fr} is the temperature exponent for each reaction r (Poinsot and Veynante, 2001). The equilibrium constant K_{cr} is required to calculate the backward reaction rates

$$k_{br} = \frac{k_{fr}}{K_{cr}} \quad , \tag{26}$$

where K_{cr} is given by

$$K_{cr} = \left(\frac{p^\circ}{RT}\right)^{\nu_r} \exp\left(\frac{\Delta S^\circ_{r,i}}{R} - \frac{\Delta H^\circ_{r,i}}{RT}\right) \quad , \tag{27}$$

with p° as a pressure of 1 atm, ν_r as the net change in the number of species in the reaction r, $\Delta S^\circ_{r,i}$ as the net change in entropy and $\Delta H^\circ_{r,i}$ as the net change in enthalpy.

Pressure dependent and duplicated reactions are considered by modifying Eq. (25). Pressure dependency is taken into account by calculating two forward reaction rates k_{fr_0} and k_{fr_∞} for the high-pressure and the low-pressure limit, respectively. A blending function composed of these high- and low-pressure Arrhenius rate parameters is applied for a smooth pressure dependence

$$k_{fr} = k_{fr_\infty} \left(\frac{p_r}{1 + p_r}\right) F \quad , \tag{28}$$

where p_r is defined as

$$p_r = \frac{k_{fr_0}\, c_r}{k_{fr_\infty}} \quad . \tag{29}$$

c_r represents the "effective" concentration of third bodies taking part in the reaction r (Kee et al., 2003). F contains a blending function, developed by Troe (1979)

$$\log_{10}\, F = \left(1 + \left[\frac{\log_{10}\, p_r + c}{n - d(\log_{10}\, p_r + c)}\right]^2\right)^{-1} \log_{10}\, F_{cent} \quad . \tag{30}$$

The constants c, n, d are defined as

$$c = -0.4 - 0.67 \log_{10} F_{cent} \quad , \tag{31}$$

$$n = 0.75 - 1.27 \log_{10} F_{cent} \quad , \tag{32}$$

$$d = 0.14 \quad . \tag{33}$$

F_{cent} contains four fitted parameters α, T^{***}, T^{*} and T^{**}

$$F_{cent} = (1-\alpha) \exp(-T/T^{***}) + \alpha \exp(-T/T^{*}) + \exp(-T^{**}/T) \quad . \tag{34}$$

The four parameters are part of the reaction mechanism and individually defined for each pressure dependent reaction. A more comprehensive review of pressure dependent reaction rates is given by Kee et al. (2003).

Furthermore, duplicated reactions are considered by extending Eq. (25) to

$$k_{fr} = \sum_{i=1}^{2} A_{fr_i} T^{\beta_{fr_i}} \exp\left(\frac{E_{fr_i}}{RT}\right) \quad . \tag{35}$$

For duplicated reactions the reaction mechanism provides two sets of Arrhenius parameters for one reaction.

There are several reaction mechanisms available to provide the parameters for the Arrhenius law. They differ in the number of reactions and species and whether third body efficiencies, duplicated and pressure dependent reaction are considered. The right choice of the reaction mechanism is essential for the accuracy of the numerical investigation. As shown in the first publication of the present thesis (Diegelmann et al., 2016a), available mechanisms show large discrepancies in terms of ignition delay and pressure sensitivity. However, the precise prediction of these parameters is essential for simulations dealing with RSBI. In particular, the precise calculation of the ignition delay time is important, as the bubble evolution and the reaction wave type highly depend on the ignition spot. It was shown that a certain number of intermediate reactions, third body efficiencies, duplicated and pressure dependent reactions is inevitable for the accurate prediction of the reaction kinetics within the wide range of pressures and temperatures considered in the presented studies.

The accurate calculation of chemical reaction kinetics is also important for the precise prediction of complex combustion phenomena, such as DDT. As shown in Section 1.2, the transition process is still in the focus of current research and not fully understood. In the beginning of the 21$^{\text{th}}$ century the common opinion was that a one-step reaction mechanism is able to resolve DDT. The review paper of Oran and Gamezo (2007) presents several studies, mainly operating with one-step chemical kinetics. DDT through the Zeldovich

gradient mechanism was observed, arising due to the gradient of induction time within the hot spots in front of the flame, where temperature varies in the range of 600 to 800 K. A precise computation of the induction time and the corresponding heat release is therefore essential for an accurate description of DDT (Liberman et al., 2010). However, it was shown in 2010 that the induction time of detailed mechanisms is larger than predicted by one-step mechanisms (Kuznetsov et al., 2010) and also greater than the time between flame initiation and transition to detonation, which marks numerical results obtained with simple mechanisms questionable. Important quantities of combustion, such as detonation initiation and induction time in chain-branching kinetics, are not correctly reproduced by one-step mechanisms (Ivanov et al., 2011). Furthermore, they reveal significant differences between the temperature gradient that leads to detonation with one-step and detailed mechanisms. For the detailed mechanism a much smaller temperature gradient is sufficient to ignite detonation, which is in accordance with the behavior of real combustible mixtures (Liberman et al., 2010).

In conclusion from the comparison of different reaction mechanisms and the requirements for the precise prediction of DDT, the reaction mechanism of Ó Conaire et al. (2004) is used to provide the reaction rate parameters for the Arrhenius law. The mechanism is valid for a wide range of pressures (0.05 to 87 atm) and temperatures (298 to 2700 K). $8 + N$ species (two reactants: H_2, O_2; 5 chain-carrying intermediates: hydrogen radical (H), oxygen radical (O), hydroxyl radical (OH), hydroperoxyl radical (HO_2), hydrogen peroxid (H_2O_2); the product: hydrogen oxide (H_2O); N inert gases) and 19 intermediate reactions are considered, including duplicated and pressure dependent reactions as well as third-body efficiencies. Third-bodies absorb energy during the two-body recombination reaction and stabilize the final combination. The available modes for energy storage control the energy absorption. The third-body efficiencies of Xe, which is used as inert gas in the present studies, are set identical to argon (Ar), which are provided by Ó Conaire et al. (2004). As the available modes of Ar and Xe are identical, the third-body efficiencies can be assumed to be comparable. Also, the steric factor for monoatomic gases, which accounts for the geometry influence on the collision between molecules, is similar (Haehn, 2012). The mechanism of Ó Conaire has been widely used in the recent years (Ferrer et al., 2014; Korobeinichev and Bol'shova, 2009). As part of a validation campaign (Diegelmann et al., 2016a), the applied reaction mechanism was compared to less complex reaction mechanisms. Accurate ignition delay times, crucial for the spatial evolution of the bubble and mixing, can only be achieved by a complex reaction mechanism, like the Ó Conaire reaction mechanism. Less complex mechanisms fail in the accurate prediction of ignition delay times and gas compositions over the wide range of pressure and temperature in RSBI.

2.2. NUMERICAL SCHEME

The Navier-Stokes equations, Eq. (1), are solved by the 2nd-order accurate Strang time splitting scheme (Strang, 1968). The Strang splitting scheme separates the stiff source term, containing the chemical reaction kinetics ($\dot{\omega}_T$ and $\dot{\omega}_i$), from the Navier-Stokes equations. This results in a system of partial differential equations (PDE) and in a stiff system of ordinary differential equations (ODE). The numerical investigations of two- and three-dimensional RSBI are achieved by a finite-volume discretization that applies a flux projection onto local characteristics for the hyperbolic part of the PDE system. This part can be considered as a Riemann problem which consists of a conservation law with piecewise constant initial condition and a single discontinuity. In the present work, Roe's approximate Riemann solver for a multi-component system is applied. The solver bases on the original formulation of Roe's approximate Riemann solver, which derives the Roe-averaged matrix for a single-component fluid (Roe, 1981).

Considering a non-linear system of hyperbolic PDE

$$\frac{\partial \boldsymbol{U}}{\partial t} + \frac{\partial \boldsymbol{F}(\boldsymbol{U})}{\partial x} = 0 \quad , \tag{36}$$

the chain rule can be used to form a set of quasi-linear hyperbolic equations

$$\frac{\partial \boldsymbol{U}}{\partial t} + \boldsymbol{A}(\boldsymbol{U})\frac{\partial \boldsymbol{U}}{\partial x} = 0 \quad . \tag{37}$$

In Eq. (37), $\boldsymbol{A}(\boldsymbol{U}) = \boldsymbol{A} = \partial \boldsymbol{F}/\partial \boldsymbol{U}$ describes the Jacobian matrix of the flux vector $\boldsymbol{F}(\boldsymbol{U})$ and has $N-1$ real eigenvalues $\lambda_i(\boldsymbol{U})$ corresponding to $N-1$ eigenvectors $R_i(\boldsymbol{U})$. By the use of Eq. (37) the hyperbolic part of the Navier-Stokes equations can be written as a quasi-linear system

$$\frac{\partial}{\partial t}\begin{pmatrix} \rho \\ \rho \boldsymbol{u} \\ E \\ \rho Y_i \end{pmatrix} + \boldsymbol{A}\frac{\partial}{\partial x}\begin{pmatrix} \rho \\ \rho \boldsymbol{u} \\ E \\ \rho Y_i \end{pmatrix} = 0 \quad . \tag{38}$$

Y_i is the mass fraction of species $i = 1, 2, ..., N-1$, with N being the total number of species. The Jacobian matrix $\boldsymbol{A}$ of a multi-component system with N species is given by (Larouturou and Fezoui, 1989)

$$\boldsymbol{A} = \begin{pmatrix} 0 & 1 & 0 & 0 & 0 & 0 & \cdots & 0 \\ -u_1^2+\frac{1}{2}(\overline{\gamma}-1)q^2+\Psi & (3-\overline{\gamma})u_1 & (1-\overline{\gamma})u_2 & (1-\overline{\gamma})u_3 & \overline{\gamma}-1 & \Psi_1 & \cdots & \Psi_{N-1} \\ -u_1u_2 & u_2 & u_1 & 0 & 0 & 0 & \cdots & 0 \\ -u_1u_3 & u_3 & 0 & u_1 & 0 & 0 & \cdots & 0 \\ u_1[\frac{1}{2}(\overline{\gamma}-1)q^2-H]+u_1\Psi & H-(\overline{\gamma}-1)u_1^2 & (1-\overline{\gamma})u_1u_2 & (1-\overline{\gamma})u_1u_3 & \overline{\gamma}u_1 & u_1\Psi_1 & \cdots & u_1\Psi_{N-1} \\ -u_1Y_1 & Y_1 & 0 & 0 & 0 & u_1 & \cdots & 0 \\ \vdots & \vdots & \vdots & \vdots & \vdots & & \ddots & \\ -u_1Y_{N-1} & Y_{N-1} & 0 & 0 & 0 & 0 & \cdots & u_1 \end{pmatrix} \quad , \tag{39}$$

with H as the enthalpy and $q = \|\boldsymbol{u}\|^2$. Ψ, respectively Ψ_i, are given by

$$\Psi = \frac{\partial \overline{\gamma}}{\partial \rho} \rho e \quad , \tag{40}$$

$$\Psi_i = \frac{\partial \overline{\gamma}}{\partial \rho Y_i} \rho e \quad \text{for} \quad i \in [1, N-1] \quad . \tag{41}$$

A flux projection on local characteristics is necessary to solve Eq. (38) numerically[2]. The Roe-averaged matrix $\tilde{\boldsymbol{A}}$ required for the projection is calculated for the full multi-species system, which yields the left and right eigenvectors, see Roe (1981). The flux is projected onto the characteristic field by the left eigenvectors. The WENO-CU6 scheme (Hu et al., 2010), presented in the next section, is applied to reconstruct numerical fluxes $f_{i\pm1/2}$ at the cell boundaries from the cell averages. These reconstructed numerical fluxes are then projected back onto the physical field using the right eigenvectors. A local switch to a Lax-Friedrichs flux is applied as entropy fix, see Toro (2009).

2.2.1. Flux reconstruction and time integration

The numerical fluxes at the cell boundaries are reconstructed from cell averages by the adaptive central-upwind 6$^{\text{th}}$-order weighted essentially non-oscillatory (WENO-CU6) scheme (Hu et al., 2010). The idea behind the WENO schemes is to choose the most appropriated stencil from a set of candidate stencils. First introduced by Harten et al. (1987) (ENO scheme), the scheme was improved by Liu et al. (1994). They presented a WENO schemes with excellent shock-capturing behavior by using a convex non-linear combination of a stencil set to reconstruct the fluxes. Non-oscillatory properties are preserved and additional orders of accuracy are added. For a comprehensive review on (W)ENO schemes the reader is referred to Shu (1997).

The applied WENO-CU6 scheme uses a non-dissipative 6$^{\text{th}}$-order central stencil in smooth flow regions and a non-linear convex combination of 3$^{\text{rd}}$-order stencils in regions with steep gradients. The scheme is characterized by further reduction of numerical dissipation compared to the classical WENO-6 scheme, while preserving the shock-capturing capabilities. Additional improvements were implemented by Hu and Adams (2011), who proposed a physically motivated scale-separation formulation to further reduce the dissipation. The WENO-CU6 scheme uses a non-linear convex combination of a set of 3$^{\text{rd}}$-order candidate stencils to reconstruct the flux at the cell boundary

$$\hat{f}_{i+1/2} = \sum_{k=0}^{3} \omega_k \hat{f}_{k,i+1/2} \quad . \tag{42}$$

[2] Only $N-1$ species are projected onto the characteristic space, whereas species N is calculated from the conservation of mass and the remaining $N-1$ species.

ω_k represents the weights of the 3$^{\text{rd}}$-order stencils $\hat{f}_{k,i+1/2}$, which are chosen to recover a non-dissipative 6$^{\text{th}}$-order central stencil in smooth flow regions and to keep non-oscillatory properties at discontinuities

$$\omega_k = \frac{\alpha_k}{\sum_{k=0}^{3} \alpha_k} \quad . \tag{43}$$

The weights ω_k are normalized by α_k, defined as

$$\alpha_k = d_k \left(C + \frac{\tau_6}{\beta_k + \epsilon \Delta x^2} \right)^q \quad . \tag{44}$$

d_k are the optimal weights with $d_k = \{1/20, 9/20, 9/20, 1/20\}$ to obtain the 6$^{\text{th}}$-order central scheme. ϵ is set to 10^{-40} to prevent division by zero. q is set to > 1 and C to $\gg 1$ to increase the contribution of optimal weights when the smoothness indicators have comparable magnitudes (Taylor et al., 2007). In regions where the fine grid is coarsen to a lower resolution the two parameters are modified to increase dissipation to avoid artificial oscillations. The accuracy of the results is not affected, as these regions have an adequate distance to the shocked bubble. τ_6 is the reference smoothness indicator,

$$\tau_6 = \beta_6 - \frac{1}{6}(\beta_0 + \beta_2 + 4\beta_1) \quad , \tag{45}$$

defined by the smoothness indicators β_k

$$\beta_k = \sum_{j=1}^{2} \Delta x^{2j-1} \int_{x-1/2}^{x+1/2} \left(\frac{d^j}{dx^j} \hat{f}_k(x) \right)^2 dx \quad , \tag{46}$$

which leads to

$$\beta_0 = \frac{1}{4}(f_{i-2} - 4f_{i-1} + 3f_i)^2 + \frac{13}{12}(f_{i-2} - 2f_{i-1} + f_i)^2 \quad , \tag{47}$$

$$\beta_1 = \frac{1}{4}(f_{i-1} - f_{i+1})^2 + \frac{13}{12}(f_{i-1} - 2f_i + f_{i+1})^2 \quad , \tag{48}$$

$$\beta_2 = \frac{1}{4}(3f_i - 4f_{i+1} + f_{i+2})^2 + \frac{13}{12}(f_i - 2f_{i+1} + f_{i+2})^2 \quad . \tag{49}$$

β_3 is identical to β_6, which bases also on Eq. (46), but with a 5$^{\text{th}}$-order polynomial

approximation for the fluxes, resulting in a 6-point stencil

$$\begin{aligned}\beta_6 = \frac{1}{10080}[&271779f_{i-2}^2 + f_{i-2}(2380800f_{i-1} + 4086352f_i - 3462252f_{i+1} \\ &+ 1458762f_{i+2} - 245620f_{i+3}) + f_{i-1}(5653317f_{i-1} - 20427884f_i \\ &+ 17905032f_{i+1} - 7727988f_{i+2} + 1325006f_{i+3}) + f_i(19510972f_i \\ &- 35817664f_{i+1} + 15929912f_{i+2} - 2792660f_{i+3}) + f_{i+1}(17195652f_{i+1} \\ &- 15880404f_{i+2} + 2863984f_{i+3}) + f_{i+2}(3824847f_{i+2} - 1429976f_{i+3}) \\ &+ 139633f_{i+3}^2] \quad .\end{aligned} \tag{50}$$

Time integration is performed by the 3rd-order strongly stable Runge-Kutta scheme of Gottlieb and Shu (1998). The method of lines approximation of the Navier-Stokes equations yields a system of ODEs

$$\frac{dy}{dt} = y_t = \mathcal{L}(y) \quad , \tag{51}$$

with $y_0 = y(t = 0)$ and $\mathcal{L}$ as the finite difference operator. The 3rd-order total variation diminishing Runge-Kutta scheme uses three substeps to compute the new solution at the next time step

$$y_{(1)} = y_n + \Delta t\mathcal{L}(y_n) \quad , \tag{52}$$

$$y_{(2)} = \frac{3}{4}y_n + \frac{1}{4}y_{(1)} + \frac{1}{4}\Delta t\mathcal{L}(y_{(1)}) \quad , \tag{53}$$

$$y_{n+1} = \frac{1}{3}y_n + \frac{2}{3}y_{(2)} + \frac{2}{3}\Delta t\mathcal{L}(y_{(2)}) \quad . \tag{54}$$

For the derivation of the used Runge-Kutta scheme and for a comprehensive review on high-order Runge-Kutta schemes in general, the reader is referred to Gottlieb and Shu (1998).

2.2.2. Source term computation

The second part of the split Navier-Stokes equations (Eq. (1)), governing the specific heat release $\dot{\omega}_T$ and the species formation and destruction in terms of individual mass rates $\dot{\omega}_i$, is solved by a variable-coefficient ODE solver (VODE) using 5^{th}-order backward differentiation formulas (BDF) (Brown et al., 1989), which is one of to the most efficient linear multistep methods (Süli and Mayers, 2003). The solver is characterized by variable-order, subcycled time-step size and fixed-leading-coefficient form and developed with special emphasis for stiff ODEs, ideal for reaction kinetics. The BDF solves the initial value problem:

$$y' = f(t, y) \quad , \quad y(t_0) = y_0 \quad . \tag{55}$$

The general formula of the linear multistep method can be written as

$$\sum_{i=0}^{k} \alpha_i y_{n-i} = h\beta_0 f(t_n, y_n) \quad . \tag{56}$$

The coefficients for 5^{th}-order BDF (k = 5) are listed in table 2.1.

k	β_0	α_0	α_1	α_2	α_3	α_4	α_5
1	1	1	-1				
2	$\frac{2}{3}$	1	$-\frac{4}{3}$	$\frac{1}{3}$			
3	$\frac{6}{11}$	1	$-\frac{18}{11}$	$\frac{9}{11}$	$-\frac{2}{11}$		
4	$\frac{12}{25}$	1	$-\frac{48}{25}$	$\frac{36}{25}$	$-\frac{16}{25}$	$\frac{3}{25}$	
5	$\frac{60}{137}$	1	$-\frac{300}{137}$	$\frac{300}{137}$	$-\frac{200}{137}$	$\frac{75}{137}$	$-\frac{12}{137}$

Table 2.1.: Coefficients for 5^{th}-order BDF (Ascher and Petzold, 1998).

The presented numerical model has been tested, validated and successfully applied for shock-induced turbulent multi-species mixing problems at finite Reynolds numbers in the work of Tritschler et al. (2013, 2014a,b,c) and for simulations of RSBI with detailed reaction kinetics by Diegelmann et al. (2016a,b, 2017).

3. Accomplishments

In the following chapter the fundamental contribution of my work and the specific accomplishments of each publication are summarized, including an overview of the current state of the art in research with special emphasis on the objectives of this thesis.

3.1. Fundamental contributions

The studies of RSBI require comprehensive preparatory work. The compressible multi-component numerical flow solver INCA is extended to handle chemical reaction kinetics. Therefore, a source term has to be added to the Navier-Stokes equations, containing the heat release and the species formation and destruction in terms of individual mass rates of each species. To solve this extended Navier-Stokes equations, 2^{nd}-order Strang splitting (Strang (1968)) is applied which separates the stiff source term from the remaining PDE. The 5^{th}-order VODE solver (Brown et al., 1989) is implemented to solve the stiffs source term, including the chemical reaction kinetics, at variable timesteps. The implementation bases on a rudimentary reaction rate solver elaborated in the master's thesis of the author (Diegelmann, 2013), which used less accurate reaction mechanisms and was not sufficiently validated. Hence, the newly achieved results are validated with the well-established Cantera software (Goodwin et al., 2014). Reactor and Sod shock tube (Sod, 1978) simulations are performed to confirm ignition characteristics, combustion temperatures and reacted gas compositions over a wide range of temperature and pressures. Furthermore, different

reaction mechanisms were compared to each other and to experimental data to ensure a high degree of accuracy, especially in terms of ignition delay time, which is essential in RSBI.

3.2. Two-dimensional reacting shock-bubble interaction

The recent studies of SBI focused on hydrodynamic effects and therefore studied the interaction between a shock wave and a bubble, filled with an inert gas mixture. SBI was intensively studied in recent years with focus on mixing processes, jet formation, uncertainty quantification, vorticity growth rate and multiple shock-accelerated bubbles.

The mixing behavior of SBI at low shock Mach numbers was investigated by Tomkins et al. (2008). Their detailed experimental measurements established three main mixing regions: The vortex core, the outer interface region containing KHI, and the bridge region, connecting the two primary vortices. The latter contributes up to 40% to the total mixing, which was confirmed in the first study of the author (Diegelmann et al., 2016a). Furthermore, scaling invariance of mixing quantities like growth rate and volume fraction in a spherical RMI was shown by Dutta et al. (2004). The study of Zhai et al. (2013) focused on the jet formation in SBI in dependence of the shock strength and the Atwood number. They underline that the pressure perturbation and the baroclinic vorticity are the main drivers of jet formation.

So (2013) also studied the jet formation in SBI as part of an uncertainty analysis and outlined that the bubble gas composition as well as the bubble shape show a large influence on the characteristic of the jet. Further uncertainty analysis has been performed by Zou et al. (2016), who studied different bubble aspect ratios in a SBI and revealed a distinct impact on the spatial bubble evolution, the vorticity production and the vortex ring diameter. Georgievskiy et al. (2015) compared spherical and slightly stretched bubbles and observed a significant influence on the thermodynamic post shock properties.

Hejazialhosseini et al. (2013) focused on the influence of the shock Mach number on the vorticity growth rates in SBI and showed that the vortex stretching term influences the bubble evolution mainly in the late stage, independent of the shock Mach number, whereas the baroclinic production term exhibits an enhanced influence on the flow field evolution for higher shock Mach numbers. Tomkins et al. (2003) studied the vortical interaction between two shocked cylinders. They observed a decrease and a non-linear threshold-type behavior of the inner vortices. Experimental and numerical studies of three shocked density inhomogeneities were performed by Kumar et al. (2007). They outline that small perturbations in the initial conditions are sufficient to influence the post-shock flow evolution distinctly. The interaction of the resulting vortical structures show a high sensitivity to the initial condition.

The second important research field involving SBI can be found in astrophysics, where laser-driven experiments and corresponding numerical simulations are used to study the interaction between shock waves and interstellar clouds (Klein et al., 2001). Klein et al.

(2003) used the NOVA laser from the Lawrence Livermore National Laboratory to generate shock waves with shock Mach numbers up to $Ma = 10$, which interact with small spherical density inhomogeneities. This configuration serves to study the interaction between shock waves, generated by the explosion of supernovae, with interstellar clouds. Most of the mass of an interstellar cloud should form stars, but observations show that only a small percentage of it does. Following the explanation of Hansen et al. (2007) one reason can be found in shock waves with high Mach numbers, which propagate through the cloud and strip its mass. They investigated interstellar clouds at high shock Mach numbers with a high resolution point-projection radiography technique and found quantitative agreement in the lengthwise growth of the bubble compared to experiments of Ranjan et al. (2005), who studied classical SBI of a gas bubble filled with argon at a shock Mach number of $Ma = 2.88$. Hence, Hansen et al. (2007) showed that the fundamental evolution of SBI outlines similarities even between astrophysical research at very high shock Mach numbers and fluid dynamical investigations at moderate shock-wave strengths.

The interaction between hydrodynamic effects and chemical reaction kinetics was left out by most of the investigations in the last decades. First experiments of a RSBI were performed by Haehn et al. (2012). Their bubble, filled with a diluted stoichiometric H_2-O_2 gas mixture, is penetrated by shock waves with Mach numbers between $Ma = 1.34$ and $Ma = 2.83$. They observed different reaction wave types and ignition spots. Low Mach numbers induce deflagration, higher Mach number detonation. Several chemiluminescence exposures depict the qualitative evolution of the bubble and the reaction processes. Besides such visualizations, they present quantitative data for the temporal evolution of the transverse diameter of the bubble as well as for the vortex ring diameter. Furthermore, Haehn et al. (2012) provide Damköhler numbers and ignition delay times for their reacting simulations. However, the complex setup reveals the limits of experimental measurement technology. Uncertainty of the Damköhler number at the highest shock Mach number ($Ma = 2.83$) amounts to $Da = 8 \pm 4$. 30% of the measurements at the lowest shock Mach number ($Ma = 1.34$) show no ignition within the given experimental time frame. Some effects, like double detonation, could not be resolved unambiguously, which underlines the need for a detailed numerical study of RSBI.

F. R. Diegelmann, V. K. Tritschler, S. Hickel and N. A. Adams (2016)
On the pressure dependence of ignition and mixing in two-dimensional reactive shock-bubble interaction
Combustion and Flame, **163**, 414-426.

The first paper of the present work (Diegelmann et al., 2016a) analyzes the pressure dependent behavior of a two-dimensional RSBI with detailed chemistry. The setup contains a gas bubble, filled with H_2, O_2 and Xe in a stoichiometric composition of 2 / 1 / 3.67 mole fractions, surrounded by pure N_2. The inert gas Xe is used to increase the density of the bubble, leading to an Atwood number of $A = 0.48$. The diameter is set to $D = 0.04$ m, initial pressure varies between $p = 0.25$ atm and $p = 0.75$ atm at a constant shock Mach number of $Ma = 2.30$. The pressure sensitivity of H_2-O_2 reaction kinetics is used to specifically trigger either a deflagration or a detonation wave. The different propagation velocities and energy releases of the reaction waves show a significant influence on the hydrodynamic evolution of the bubble and the mixing process with its surrounding.

At a low initial pressure of $p = 0.25$ atm the reaction branch producing mainly H, O, OH is dominant. The accumulation of these radicals leads to an ignition at the downstream pole of the bubble after a long ignition delay time, followed by a subsonic deflagration wave. A Damköhler number of $Da = 0.44$ indicates a flow field dominated by hydrodynamic effects, which is confirmed by the analysis of integral quantities, such as the enstrophy production or the molar mixing fraction. The reaction wave affects the enstrophy production and mixing only in the long-term evolution. Hence mixing is only reduced by about 20% compared to the inert simulation. Bubble expansion and the growth of secondary instabilities are unaffected by the reaction wave.

Higher initial pressure enhances a different branch in the chemical reaction kinetics of H_2-O_2. The production of HO_2 and H_2O_2 increases and dominates the ignition process, which finally induces a supersonic detonation wave. The Damköhler number increases to $Da > 1.30$, indicating a chemical-driven flow field. Spatial expansion enlarges due to the fast propagation of the reaction wave and the growth of the secondary instabilities, as well as the bridge region is disturbed, which decreases mixing by up to 50%. A further pressure increase has no additional influence on the flow field and the chemical reaction. The ignition delay time is slightly shortened, however, the reaction wave type and the bubble evolution are not affected.

The main contribution of the first paper is threefold: (i) Numerical simulations of RSBI with detailed chemistry are performed, which establish a numerical framework for further investigations. (ii) Demonstration of the controllability of the reaction wave type through specific triggering of different reaction branches by the variation of the initial pressure is shown. (iii) The influence of the reaction wave type on the general bubble evolution, the enstrophy production and the mixing process are shown and quantified.

My contribution to this work was the development of the concept of the investigation, including its main objectives. Based on the work done in my master's thesis (Diegelmann, 2013), I implemented the solver for chemical reaction kinetics in the in-house code INCA, tested and validated the reaction kinetics by several test cases, performed the numerical simulations and wrote major parts of the manuscript for the publication.

F. R. Diegelmann, S. Hickel and N. A. Adams (2016)
Shock Mach number influence on reaction wave types and mixing in reactive shock-bubble interaction
Combustion and Flame, **174**, 085-099.

The second paper (Diegelmann et al., 2016b) studies the shock Mach number sensitivity of H_2-O_2 reaction kinetics and the subsequent interaction between the reaction wave and hydrodynamic instabilities in RSBI. The different shock strengths are used to trigger specific post-shock conditions, which in turn lead to different characteristic shock-induced reaction phenomena. RSBI at shock Mach numbers between $Ma = 2.13$ and $Ma = 2.90$ are studied in detail. The shock strength determines the reaction wave type. A low shock Mach number of $Ma = 2.13$ ignites the mixture after a long ignition delay time in the shock focusing point, followed by a deflagration wave. The highest shock Mach number induces a detonation wave. The ignition delay time is shortened and the mixture ignites directly at the upstream pole of the bubble ($Ma = 2.90$).

Intermediate shock Mach numbers reveal further combustion phenomena: DDT is observed at a shock strength of $Ma = 2.19$. The reactive gas mixture ignites in a deflagration wave. Subsequently, the reaction front propagates through the complex post-shock pressure and temperature field inside the bubble, which influences the reaction kinetics and finally leads to transition into a detonation wave. Critical parameters like pressure, temperature and radical compositions across the reaction front are studied and exhibit the characteristic evolution during DDT. A shock Mach number of $Ma = 2.50$ shows an additional effect: The gas mixture ignites simultaneously at two different spots, followed by two detonation waves which propagate towards each other through the gas bubble.

The analysis of integral quantities shows the reaction wave sensitivity of the global bubble evolution. The detonation wave leads to a rapid expansion of the bubble gas, whereas the simulation at a low shock Mach number, which induces a deflagration wave, shows a nearly linear raise. The shock wave in front of the detonation wave induces additional vorticity and decelerates the growth of secondary instabilities. As a consequence mixing decreases by up to 50%, whereas the deflagration wave reduces mixing only by 30%. Comparison to the experimental data of Haehn et al. (2012) show very good agreement. Their observation of a double detonation was confirmed and a deeper insight into the gas composition of the two ignition spots during the induction time is given.

The main contributions of the second paper are: (i) Proof of the controllability of the reaction wave type by the variation of the initial shock Mach number is given. (ii) Mixing reduction by both reaction wave types is observed and (iii) DDT is detected and thoroughly analyzed. (iv) Insight into the gas composition of the two ignition spots of the double detonation during the induction and ignition stage is provided and (v) very good agreement to experimental results is shown.

My contribution to this work was the development of the concept of the investigation, including its main objectives. I tested and validated the implementations in the in-house code INCA, performed the numerical simulations and wrote major parts of the manuscript for the publication.

3.3. Three-dimensional reacting shock-bubble interaction

Two-dimensional simulations of RSBI have their validity, but also limitations. Important effects and physical phenomena cannot be resolved in two dimensions. There have been several studies to outline the differences between two- and three-dimensional investigations of SBI. In the early development of SBI three-dimensional effects play a subordinate role and can be neglected, if the research focus lays on these stages. Peng et al. (2003) studied vortex-accelerated secondary baroclinic vorticity deposition and showed good agreement of their two-dimensional simulations to experimental data. Klein et al. (2003) investigated the interaction between a sphere and a shock wave at high shock Mach numbers. They compared the two-dimensional results with experimental data and observed good accordance in the radial and axial width of the shocked sphere. The investigation of Miles et al. (2005) showed no significant differences of the early growth rates of shock-induced instabilities between three- and two-dimensional simulations.

Three-dimensional effects become important, if the focus of research lays on the long-term evolution of RSBI. Wang et al. (2015) studied the bubble diameter of two- and three-dimensional SBIs and measured a certain deviation. The different bubble diameters are caused by the missing vortex stretching term in the vorticity equation in two dimensions, which reduces the spanwise expansion in the long-term evolution. The influence of the vortex stretching term is confirmed by Hejazialhosseini et al. (2013). They studied the vortex dynamics in SBI and showed that the vortex stretching term plays an important role in the long-term evolution. Diegelmann et al. (2016b) confirmed these observations: The two-dimensional RSBI showed good agreement in the early stage of SBI, however it exhibits a certain deviation in the long-term evolution due to the missing vortex stretching term.

Giordano and Burtschell (2006) observed that the N_2-jet in the centerline of the bubble only occurs in two-dimensional simulations. However, the jet highly affects the bubble evolution in the late stages and therefore contributes to the deviation between two- and three-dimensional SBIs. A further important physical phenomenon, which can only be resolved by three-dimensional simulations, is the Widnall-type instability (Widnall et al., 1974). Hansen et al. (2007) and Robey et al. (2002) confirmed in their studies that two-dimensional simulations fail to predict Widnall-type instabilities. The instability affects the long-term evolution of SBI by destabilizing the main vortex ring. Three-dimensional vortex rings tend to become unstable, whereas two-dimensional vortex cores remain stable because of the missing Widnall-type instability. In addition, the vortex stretching can result in broad-band turbulence (Davidson, 2004), which in turn highly affects the mixing behavior.

The influence of three-dimensional effects on the bubble evolution in RSBI is also affected by the Atwood number. Niederhaus et al. (2008) studied the vorticity evolution in two- and three-dimensional simulations of SBI and outlined that the Atwood number is essential for the deviation in spatial and temporal evolution of SBI. For Atwood numbers

smaller than 0.2 three-dimensional effects can be neglected, even in the long-term evolution. Higher Atwood numbers lead to strong secondary diffracted and focused shocks inside the bubble, which have three-dimensional character and influence the global bubble dynamics.

The extension to three-dimensional simulations of RSBI is inevitable, when the primary focus of research lies on the long-term evolution of RSBI and the associated mixing processes. The third paper of the dissertation contains the first simulation of RSBI in a three-dimensional domain including detailed chemistry. The simulation provides new insights with respect to the interaction between hydrodynamic phenomena and reaction kinetics in a highly turbulent three-dimensional flow field.

F. R. Diegelmann, S. Hickel and N. A. Adams (2017)
Three-dimensional reacting shock-bubble interaction
Combustion and Flame, **181**, 300-314.

The third paper (Diegelmann et al., 2017) presents the first three-dimensional numerical simulation of a RSBI with detailed chemical reaction kinetics. The additional dimension reveals hydrodynamic effects that have been neglected in the previous two-dimensional studies. These effects play a significant role in the long-term evolution of RSBI and influence the spatial and temporal evolution of the gas bubble.

The interaction between a bubble, filled with H_2, O_2 and Xe in a stoichiometric composition of 2 / 1 / 3.67 mole fractions, and a shock wave with a shock strength of $Ma = 2.83$ is investigated. The sudden increase of thermodynamic properties across the shock wave is sufficient to ignite the gas mixture inside the bubble plainly upstream of the shock-focusing point at the downstream pole. The following reaction wave is identified as a detonation wave. The accuracy of the numerical results is confirmed by a detailed grid-convergence study.

The reaction wave significantly affects the spatial and temporal evolution as well as the mixing of the bubble gas. The interaction between the interface and the detonation wave induces additional vorticity while the growth of RMI and secondary instabilities is damped. The inert SBI is characterized by a highly mixed fluid, which has spread into streamwise and transverse direction. The unimpeded growth of instabilities leads to mixing of up to 90% within the simulated timeframe. The reacting SBI shows a different evolution: Large regions of unmixed gas are preserved, even in the long-term evolution, which leads to a significant lower mixing of 53%.

Three-dimensional effects play a significant role in the long-term evolution of the shocked bubble. Azimuthal instabilities along the vortex ring in the three-dimensional simulations destabilize the vortex center. Furthermore, the vortex stretching term, which is absent in two-dimensional simulations, influences the bubble evolution significantly. Both phenomena contribute to a higher spatial expansion of the bubble gas in streamwise direction and affect the mixing, which increases in both three-dimensional simulations compared to their two-dimensional counterparts. Comparison to experimental data shows very good agreement in terms of ignition delay, reaction wave propagation velocity and spatial expansion.

The main contributions of the third paper are: (i) first successful simulation of a three-dimensional RSBI with detailed chemistry, (ii) observation of distinct mixing reduction by the detonation wave, (iii) study of three-dimensional effects and their influence on the spatial expansion in the long-term evolution with main emphasis on azimuthal instabilities along the vortex rings and (iv) detailed analysis and comparison of the numerical results to two-dimensional simulations and experimental data.

My contribution to this work was the development of the concept of the study, including its main objectives. I tested and validated the implementations in the in-house code INCA, performed the numerical simulations and wrote major parts of the manuscript for the publication.

4. Conclusion

Shock-accelerated flows in reactive environments are of interest in a wide range of applications, from very small scales in inertial confinement fusion (Craxton et al., 2015; Aglitskiy et al., 2010), intermediate scales in combustion engines (Khokhlov et al., 1999; Yang et al., 1993), up to extremely large scales in astrophysics (Arnett, 2000; Hansen et al., 2007). The present thesis contains detailed numerical simulations of shock-accelerated flows in highly reactive environments. The focus lays on the interaction between shock-induced hydrodynamic instabilities and chemical reaction kinetics.

The generic setup of a reacting shock bubble interaction (RSBI) is chosen to study the interaction between hydrodynamic phenomena and hydrogen-oxygen (H_2-O_2) reaction kinetics in two- and three-dimensional simulations. The numerical investigation focuses on the influence of shock-induced chemical reactions in general and the reaction wave type in particular on the mixing process of the bubble gas with its surrounding, the spatial evolution of the bubble and the gas compositions during the induction and ignition stage. The shock-induced Richtmyer-Meshkov instability and the subsequent Kelvin-Helmholtz as well as the Widnall-type instabilities are analyzed in detail. The thesis contains three investigations of RSBI, each one focusing on a particular topic in the field of shock-accelerated flow inhomogeneities in reactive environments.

The influence of the initial pressure on the reaction kinetics and the mixing process is studied in a two-dimensional configuration of RSBI. The pressure sensitivity of H_2-O_2 chemical reaction kinetics is used to trigger either a deflagration or a detonation wave. Differences in the propagation velocity and the heat release significantly affect the bubble

evolution. The detonation wave increases the bubble expansion and decreases the mixing with its surrounding. Due to the slow propagation velocity, the deflagration wave shows a minor effect: Bubble expansion is nearly unaffected and mixing reduces only slightly in the long-term evolution.

For the investigation of more complex combustion phenomena, besides the limiting cases of deflagration and detonation, the setup of RSBI is extended. The variation of the shock Mach number induces deflagration for low and detonation for high shock Mach numbers. For intermediate shock strengths more complex combustion phenomena have been captured: deflagration-to-detonation transition (DDT) and simultaneous detonations at different spots within the gas bubble. DDT was observed near the downstream pole of the bubble, triggered by the complex pressure and temperature field inside the shocked bubble gas. Analysis of the gas composition, temperature and pressure across the reaction front lead to a clear identification of DDT. Furthermore, an intermediate shock Mach number induces a double detonation of the reactive gas mixture. Two spots, one at the upstream pole and one near the shock focusing point, ignite simultaneously. Comprehensive analysis of the two ignition spots provides a deeper understanding of the gas compositions during the induction and ignition stage. The numerical results are confirmed by a comparison with experimental measurements.

The first three-dimensional simulation of RSBI finalizes the presented numerical investigation and outlines the influence of three-dimensional effects on the long-term evolution of the shocked bubble gas. A strong shock wave ignites the bubble gas before the shock-focusing point and induces a detonation wave. The supersonic reaction wave decelerates the growth of Richtmyer-Meshkov and Kelvin-Helmholtz instabilities, which in turn reduces mixing compared to the inert SBI. Three-dimensional effects, like vortex stretching, vortex decay, and the Widnall-type instability of the vortex ring are observed and analyzed in detail. These phenomena are responsible for the divergent evolution of two- and three-dimensional RSBI in the late stage. Very good agreement with experimental results in terms of induction time, reaction wave propagation velocity and spatial expansion of the bubble gas are achieved.

The presented thesis provides a comprehensive analysis of shock-accelerated flow inhomogeneities in reactive environments. For this purpose, two- and three-dimensional simulations of RSBI are performed to study the interaction between shock-induced hydrodynamic instabilities and detailed H_2-O_2 reaction kinetics. The successive increase of complexity and the revalidation of the results in combination with excellent agreement to experimental results provides a framework for detailed numerical investigations. New insights into RSBI, with emphasis on the spatial and temporal evolution and the mixing behavior of the bubble gas, are given. A deeper understanding of the controllability of the reaction wave type and the gas composition during the reaction process are elaborated and thoroughly analyzed.

A. List of publications

A.1. Peer-reviewed journal publications

- **F. R. Diegelmann**, S. Hickel and N. A. Adams (2017). Three-dimensional reacting shock-bubble interaction. *Combustion and Flame*, 181, 300-314.

- **F. R. Diegelmann**, S. Hickel and N. A. Adams (2016). Shock Mach number influence on reaction wave types and mixing in reactive shock-bubble interaction. *Combustion and Flame*, 174, 085-099.

- **F. R. Diegelmann**, V. K. Tritschler, S. Hickel and N. A. Adams (2016). On the pressure dependence of ignition and mixing in two-dimensional reactive shock-bubble interaction. *Combustion and Flame*, 163, 414-426.

A.2. Book sections

- **F. R. Diegelmann**, V. K. Tritschler and S. Hickel (2017). Mach Number Influence on Ignition and Mixing Processes in a Reacting Shock-Bubble Interaction. in *30th International Symposium on Shock Waves 2*; G. Ben-Dor, O. Igra and O. Sadot (Eds.) Springer. ISBN 978-3-319-44864-0.

- **F. R. Diegelmann**, S. Hickel and N. A. Adams (2016). Shock Mach number influence in reactive shock-bubble interaction. in *High Performance Computing in Science and Engineering*; S. Wagner, A. Bode, H. Brüchle and M. Brehm (Eds.), Verlag der Bayerischen Akademie der Wissenschaften. ISBN 978-3-9816675-1-6.

A.3. Conferences

- S. Hickel, **F. R. Diegelmann** and V. K. Tritschler (2015). Mach Number Effects on Ignition and Mixing Processes in a Reacting Shock-Bubble Interaction. *68th Annual Meeting of the APS Division of Fluid Dynamics*, November 22 - 24, 2015, Boston, USA.

- **F. R. Diegelmann**, V. K. Tritschler and S. Hickel (2015). Mach Number Influence on Ignition and Mixing Processes in a Reacting Shock-Bubble Interaction. *30th International Symposium on Shock Waves (ISSW30)*, July 19 - 24, 2015, Tel Aviv, Israel.

- **F. R. Diegelmann**, J. Matheis, V. K. Tritschler, S. Hickel and N. A. Adams (2015). On the Influence of pressure variation on ignition and mixing processes in a reacting shock-bubble interaction. *International Symposium On Turbulence and Shear Flow Phenomena (TSFP-9)*, Juni 30 - July 03, 2015, Melbourne, Australia.

- **F. R. Diegelmann**, V. K. Tritschler, S. Hickel and N. A. Adams (2015). Ignition and mixing in shock-bubble interaction with chemical reaction. *86th Annual Meeting of the international Association of Applied Mathematics and Mechanic (GAMM86)*, March 23 - 27, 2015, Lecce, Italy.

B. Peer-reviewed journal publications

Here, the peer-reviewed journal publications of the present work are attached.

B.1. On the pressure dependence of ignition and mixing in two-dimensional reactive shock-bubble interaction

ELSEVIER LICENSE
TERMS AND CONDITIONS

Mar 21, 2017

This Agreement between Felix Diegelmann ("You") and Elsevier ("Elsevier") consists of your license details and the terms and conditions provided by Elsevier and Copyright Clearance Center.

License Number	4073570103866
License date	
Licensed Content Publisher	Elsevier
Licensed Content Publication	Combustion and Flame
Licensed Content Title	On the pressure dependence of ignition and mixing in two-dimensional reactive shock-bubble interaction
Licensed Content Author	Felix Diegelmann,Volker Tritschler,Stefan Hickel,Nikolaus Adams
Licensed Content Date	January 2016
Licensed Content Volume	163
Licensed Content Issue	n/a
Licensed Content Pages	13
Start Page	414
End Page	426
Type of Use	reuse in a thesis/dissertation
Portion	full article
Format	both print and electronic
Are you the author of this Elsevier article?	Yes
Will you be translating?	No
Order reference number	
Title of your thesis/dissertation	Ignition and Mixing in a Reacting Shock-Bubble Interaction
Expected completion date	Apr 2017
Estimated size (number of pages)	115
Elsevier VAT number	GB 494 6272 12
Requestor Location	Felix Diegelmann Schyrenstr. 11 Munich, Bavaria 81543 Germany Attn: Felix Diegelmann
Publisher Tax ID	GB 494 6272 12
Total	0.00 EUR
Terms and Conditions	

INTRODUCTION

1. The publisher for this copyrighted material is Elsevier. By clicking "accept" in connection with completing this licensing transaction, you agree that the following terms and conditions apply to this transaction (along with the Billing and Payment terms and conditions established by Copyright Clearance Center, Inc. ("CCC"), at the time that you opened your Rightslink account and that are available at any time at http://myaccount.copyright.com).

GENERAL TERMS

2. Elsevier hereby grants you permission to reproduce the aforementioned material subject to the terms and conditions indicated.
3. Acknowledgement: If any part of the material to be used (for example, figures) has appeared in our publication with credit or acknowledgement to another source, permission must also be sought from that source. If such permission is not obtained then that material may not be included in your publication/copies. Suitable acknowledgement to the source must be made, either as a footnote or in a reference list at the end of your publication, as follows:
"Reprinted from Publication title, Vol /edition number, Author(s), Title of article / title of chapter, Pages No., Copyright (Year), with permission from Elsevier [OR APPLICABLE SOCIETY COPYRIGHT OWNER]." Also Lancet special credit - "Reprinted from The Lancet, Vol. number, Author(s), Title of article, Pages No., Copyright (Year), with permission from Elsevier."
4. Reproduction of this material is confined to the purpose and/or media for which permission is hereby given.
5. Altering/Modifying Material: Not Permitted. However figures and illustrations may be altered/adapted minimally to serve your work. Any other abbreviations, additions, deletions and/or any other alterations shall be made only with prior written authorization of Elsevier Ltd. (Please contact Elsevier at permissions@elsevier.com). No modifications can be made to any Lancet figures/tables and they must be reproduced in full.
6. If the permission fee for the requested use of our material is waived in this instance, please be advised that your future requests for Elsevier materials may attract a fee.
7. Reservation of Rights: Publisher reserves all rights not specifically granted in the combination of (i) the license details provided by you and accepted in the course of this licensing transaction, (ii) these terms and conditions and (iii) CCC's Billing and Payment terms and conditions.
8. License Contingent Upon Payment: While you may exercise the rights licensed immediately upon issuance of the license at the end of the licensing process for the transaction, provided that you have disclosed complete and accurate details of your proposed use, no license is finally effective unless and until full payment is received from you (either by publisher or by CCC) as provided in CCC's Billing and Payment terms and conditions. If full payment is not received on a timely basis, then any license preliminarily granted shall be deemed automatically revoked and shall be void as if never granted. Further, in the event that you breach any of these terms and conditions or any of CCC's Billing and Payment terms and conditions, the license is automatically revoked and shall be void as if never granted. Use of materials as described in a revoked license, as well as any use of the materials beyond the scope of an unrevoked license, may constitute copyright infringement and publisher reserves the right to take any and all action to protect its copyright in the materials.
9. Warranties: Publisher makes no representations or warranties with respect to the licensed material.
10. Indemnity: You hereby indemnify and agree to hold harmless publisher and CCC, and their respective officers, directors, employees and agents, from and against any and all claims arising out of your use of the licensed material other than as specifically authorized pursuant to this license.
11. No Transfer of License: This license is personal to you and may not be sublicensed, assigned, or transferred by you to any other person without publisher's written permission.

12. No Amendment Except in Writing: This license may not be amended except in a writing signed by both parties (or, in the case of publisher, by CCC on publisher's behalf).
13. Objection to Contrary Terms: Publisher hereby objects to any terms contained in any purchase order, acknowledgment, check endorsement or other writing prepared by you, which terms are inconsistent with these terms and conditions or CCC's Billing and Payment terms and conditions. These terms and conditions, together with CCC's Billing and Payment terms and conditions (which are incorporated herein), comprise the entire agreement between you and publisher (and CCC) concerning this licensing transaction. In the event of any conflict between your obligations established by these terms and conditions and those established by CCC's Billing and Payment terms and conditions, these terms and conditions shall control.
14. Revocation: Elsevier or Copyright Clearance Center may deny the permissions described in this License at their sole discretion, for any reason or no reason, with a full refund payable to you. Notice of such denial will be made using the contact information provided by you. Failure to receive such notice will not alter or invalidate the denial. In no event will Elsevier or Copyright Clearance Center be responsible or liable for any costs, expenses or damage incurred by you as a result of a denial of your permission request, other than a refund of the amount(s) paid by you to Elsevier and/or Copyright Clearance Center for denied permissions.

LIMITED LICENSE

The following terms and conditions apply only to specific license types:
15. **Translation**: This permission is granted for non-exclusive world **English** rights only unless your license was granted for translation rights. If you licensed translation rights you may only translate this content into the languages you requested. A professional translator must perform all translations and reproduce the content word for word preserving the integrity of the article.
16. **Posting licensed content on any Website**: The following terms and conditions apply as follows: Licensing material from an Elsevier journal: All content posted to the web site must maintain the copyright information line on the bottom of each image; A hyper-text must be included to the Homepage of the journal from which you are licensing at http://www.sciencedirect.com/science/journal/xxxxx or the Elsevier homepage for books at http://www.elsevier.com; Central Storage: This license does not include permission for a scanned version of the material to be stored in a central repository such as that provided by Heron/XanEdu.
Licensing material from an Elsevier book: A hyper-text link must be included to the Elsevier homepage at http://www.elsevier.com . All content posted to the web site must maintain the copyright information line on the bottom of each image.

Posting licensed content on Electronic reserve: In addition to the above the following clauses are applicable: The web site must be password-protected and made available only to bona fide students registered on a relevant course. This permission is granted for 1 year only. You may obtain a new license for future website posting.
17. **For journal authors:** the following clauses are applicable in addition to the above:
Preprints:
A preprint is an author's own write-up of research results and analysis, it has not been peer-reviewed, nor has it had any other value added to it by a publisher (such as formatting, copyright, technical enhancement etc.).
Authors can share their preprints anywhere at any time. Preprints should not be added to or enhanced in any way in order to appear more like, or to substitute for, the final versions of articles however authors can update their preprints on arXiv or RePEc with their Accepted Author Manuscript (see below).
If accepted for publication, we encourage authors to link from the preprint to their formal publication via its DOI. Millions of researchers have access to the formal publications on ScienceDirect, and so links will help users to find, access, cite and use the best available

version. Please note that Cell Press, The Lancet and some society-owned have different preprint policies. Information on these policies is available on the journal homepage.
Accepted Author Manuscripts: An accepted author manuscript is the manuscript of an article that has been accepted for publication and which typically includes author-incorporated changes suggested during submission, peer review and editor-author communications.
Authors can share their accepted author manuscript:

- immediately
  - via their non-commercial person homepage or blog
  - by updating a preprint in arXiv or RePEc with the accepted manuscript
  - via their research institute or institutional repository for internal institutional uses or as part of an invitation-only research collaboration work-group
  - directly by providing copies to their students or to research collaborators for their personal use
  - for private scholarly sharing as part of an invitation-only work group on commercial sites with which Elsevier has an agreement
- After the embargo period
  - via non-commercial hosting platforms such as their institutional repository
  - via commercial sites with which Elsevier has an agreement

In all cases accepted manuscripts should:

- link to the formal publication via its DOI
- bear a CC-BY-NC-ND license - this is easy to do
- if aggregated with other manuscripts, for example in a repository or other site, be shared in alignment with our hosting policy not be added to or enhanced in any way to appear more like, or to substitute for, the published journal article.

Published journal article (JPA): A published journal article (PJA) is the definitive final record of published research that appears or will appear in the journal and embodies all value-adding publishing activities including peer review co-ordination, copy-editing, formatting, (if relevant) pagination and online enrichment.
Policies for sharing publishing journal articles differ for subscription and gold open access articles:
Subscription Articles: If you are an author, please share a link to your article rather than the full-text. Millions of researchers have access to the formal publications on ScienceDirect, and so links will help your users to find, access, cite, and use the best available version.
Theses and dissertations which contain embedded PJAs as part of the formal submission can be posted publicly by the awarding institution with DOI links back to the formal publications on ScienceDirect.
If you are affiliated with a library that subscribes to ScienceDirect you have additional private sharing rights for others' research accessed under that agreement. This includes use for classroom teaching and internal training at the institution (including use in course packs and courseware programs), and inclusion of the article for grant funding purposes.
Gold Open Access Articles: May be shared according to the author-selected end-user license and should contain a CrossMark logo, the end user license, and a DOI link to the formal publication on ScienceDirect.
Please refer to Elsevier's posting policy for further information.
18. **For book authors** the following clauses are applicable in addition to the above:
Authors are permitted to place a brief summary of their work online only. You are not allowed to download and post the published electronic version of your chapter, nor may you scan the printed edition to create an electronic version. **Posting to a repository:** Authors are permitted to post a summary of their chapter only in their institution's repository.

19. **Thesis/Dissertation**: If your license is for use in a thesis/dissertation your thesis may be submitted to your institution in either print or electronic form. Should your thesis be published commercially, please reapply for permission. These requirements include permission for the Library and Archives of Canada to supply single copies, on demand, of the complete thesis and include permission for Proquest/UMI to supply single copies, on demand, of the complete thesis. Should your thesis be published commercially, please reapply for permission. Theses and dissertations which contain embedded PJAs as part of the formal submission can be posted publicly by the awarding institution with DOI links back to the formal publications on ScienceDirect.

Elsevier Open Access Terms and Conditions

You can publish open access with Elsevier in hundreds of open access journals or in nearly 2000 established subscription journals that support open access publishing. Permitted third party re-use of these open access articles is defined by the author's choice of Creative Commons user license. See our open access license policy for more information.

Terms & Conditions applicable to all Open Access articles published with Elsevier:

Any reuse of the article must not represent the author as endorsing the adaptation of the article nor should the article be modified in such a way as to damage the author's honour or reputation. If any changes have been made, such changes must be clearly indicated.

The author(s) must be appropriately credited and we ask that you include the end user license and a DOI link to the formal publication on ScienceDirect.

If any part of the material to be used (for example, figures) has appeared in our publication with credit or acknowledgement to another source it is the responsibility of the user to ensure their reuse complies with the terms and conditions determined by the rights holder.

Additional Terms & Conditions applicable to each Creative Commons user license:

CC BY: The CC-BY license allows users to copy, to create extracts, abstracts and new works from the Article, to alter and revise the Article and to make commercial use of the Article (including reuse and/or resale of the Article by commercial entities), provided the user gives appropriate credit (with a link to the formal publication through the relevant DOI), provides a link to the license, indicates if changes were made and the licensor is not represented as endorsing the use made of the work. The full details of the license are available at http://creativecommons.org/licenses/by/4.0.

CC BY NC SA: The CC BY-NC-SA license allows users to copy, to create extracts, abstracts and new works from the Article, to alter and revise the Article, provided this is not done for commercial purposes, and that the user gives appropriate credit (with a link to the formal publication through the relevant DOI), provides a link to the license, indicates if changes were made and the licensor is not represented as endorsing the use made of the work. Further, any new works must be made available on the same conditions. The full details of the license are available at http://creativecommons.org/licenses/by-nc-sa/4.0.

CC BY NC ND: The CC BY-NC-ND license allows users to copy and distribute the Article, provided this is not done for commercial purposes and further does not permit distribution of the Article if it is changed or edited in any way, and provided the user gives appropriate credit (with a link to the formal publication through the relevant DOI), provides a link to the license, and that the licensor is not represented as endorsing the use made of the work. The full details of the license are available at http://creativecommons.org/licenses/by-nc-nd/4.0.

Any commercial reuse of Open Access articles published with a CC BY NC SA or CC BY NC ND license requires permission from Elsevier and will be subject to a fee.

Commercial reuse includes:

- Associating advertising with the full text of the Article
- Charging fees for document delivery or access
- Article aggregation
- Systematic distribution via e-mail lists or share buttons

Posting or linking by commercial companies for use by customers of those companies.

20. **Other Conditions**:

v1.9

Questions? customercare@copyright.com or +1-855-239-3415 (toll free in the US) or +1-978-646-2777.

Combustion and Flame 163 (2016) 414–426

Contents lists available at ScienceDirect

Combustion and Flame

journal homepage: www.elsevier.com/locate/combustflame

On the pressure dependence of ignition and mixing in two-dimensional reactive shock-bubble interaction

Felix Diegelmann[a,*], Volker Tritschler[a], Stefan Hickel[a,b], Nikolaus Adams[a]

[a] Institute of Aerodynamics and Fluid Mechanics, Technische Universität München, Garching 85748, Germany
[b] Faculty of Aerospace Engineering, TU Delft, 2629 HS Delft, Netherlands

ARTICLE INFO

Article history:
Received 10 June 2015
Revised 8 October 2015
Accepted 12 October 2015
Available online 14 November 2015

Keywords:
Shock wave
Richtmyer–Meshkov instability
Shock-bubble interaction
Detonation
Deflagration

ABSTRACT

We analyse results of numerical simulations of reactive shock-bubble interaction with detailed chemistry. The interaction of the Richtmyer–Meshkov instability and shock-induced ignition of a stoichiometric H_2-O_2 gas mixture is investigated. Different types of ignition (deflagration and detonation) are observed at the same shock Mach number of $Ma = 2.30$ upon varying initial pressure. Due to the convex shape of the bubble, shock focusing leads to a spot with high pressure and temperature. Initial pressures between $p_0 = 0.25 - 0.75$ atm exhibit low pressure reactions, dominated by H, O, OH production and high pressure chemistry driven by HO_2 and H_2O_2. Deflagration is observed for the lowest initial pressure. Increasing pressure results in smaller induction times and ignition, followed by a detonation wave. The spatial and temporal evolution of the gas bubble is highly affected by the type of ignition. The Richtmyer–Meshkov instability and the subsequent Kelvin–Helmholtz instabilities develop with a high reaction sensitivity. Mixing is significantly reduced by both reaction types. The strongest effect is observed for detonation.

1. Introduction

For high-speed reactive flows, such as supersonic combustion, the rapid and efficient mixing of fuel and oxidizer is crucial as the residence time of the fuel-oxidizer mixture in the combustion chamber is only a few milliseconds [1]. The Richtmyer–Meshkov instability (RMI) promotes mixing and thus increases the burning efficiency of supersonic combustion engines [2]. However a discontinuity in thermodynamic properties can cause reaction waves. The reacting shock-bubble interaction (RSBI) allows to investigate the interaction between the RMI and the reaction waves inside the bubble that are initiated by the shock.

1.1. Richtmyer–Meshkov instability

RMI [3,4] is a shock-induced hydrodynamic instability which occurs at the interface between two fluids of different densities. It can be considered as the impulsive limit of the Rayleigh–Taylor instability [5,6], where initial perturbations at the interface grow due to constant gravitational acceleration. In RMI, baroclinic vorticity production at the interface is caused by misalignment of pressure gradient, ∇p, associated with a shock wave and density gradient, $\nabla \rho$, at the material interface. For comprehensive reviews the reader is referred to Brouillette [7] and Zabusky [8]. RMI occurs for a wide range of physical phenomena ranging from extreme large scales in astrophysics [9], to intermediate scales in combustion [1,10] and to very small scales in inertial confinement fusion [11].

1.2. Shock-induced chemistry

A shock-induced change in thermodynamic properties can cause ignition, followed by a reaction wave where two types can be distinguished: deflagration and detonation. Deflagration is a subsonic reaction wave that propagates through the gas mixture due to direct transfer of chemical energy from burning to unburned gas, driven by diffusion [12]. Detonation is driven by a fast chemical reaction and the associated large heat release within the reaction wave. A shock wave immediately precedes the detonation wave and preheats the gas mixture by compression [12]. The detonation wave propagates up to 10^8 times faster than the deflagration wave [13]. Due to the large differences in the characteristic reaction time scales, the type of the reaction wave is crucial for flow evolution.

Limits between deflagration and detonation for a hydrogen-oxygen (H_2-O_2) gas mixture are shown in Fig. 1 as functions of temperature and pressure. The chain branching exceeds the rate of chain breaking on the right side of the reversed-S curve. Due to pressure dependent intermediate reactions, the type of ignition can change several times at constant temperature. Some intermediate products and

* Corresponding author.
E-mail address: felix.diegelmann@aer.mw.tum.de (F. Diegelmann).

http://dx.doi.org/10.1016/j.combustflame.2015.10.016
0010-2180/

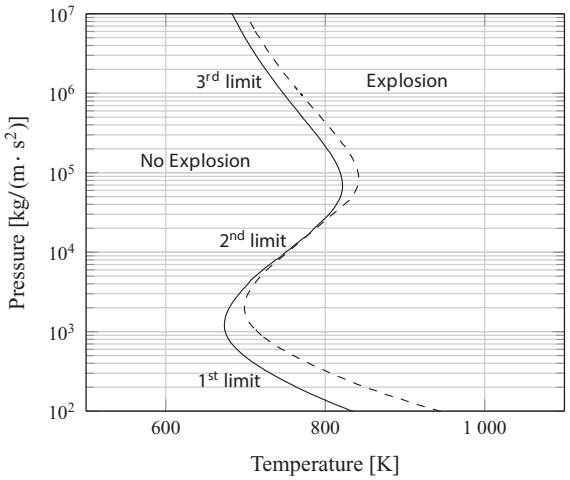

Fig. 1. Explosion limits for a stoichiometric pure hydrogen-oxygen mixture (solid line) and for a stoichiometric hydrogen-oxygen mixture with inert gas (2/1/4) (dashed lines) [15].

reactions are inactive at low pressure and become active at higher pressure, affecting the chemical reaction process significantly [14]. The solid line represents the explosion limit for a pure stoichiometric H_2-O_2 mixture. Wang and Chung [15] added an inert gas to dilute the stoichiometric mixture and observed a distinct shift of the explosion limit to higher temperatures. The dashed line shows a molar ratio of 2/1/4 (H_2/O_2/inert gas), which is close to the gas composition in this work (2/1/3.67).

1.3. Reacting shock-bubble interaction

The interaction of a shock wave with a gas bubble containing a reactive gas mixture triggers RMI simultaneously with chemical reaction processes. In classical inert shock-bubble interactions (SBI) the baroclinic vorticity production generated at the interface causes the bubble to evolve into a vortex ring. Upon contact, the incident shock wave is partially reflected and partially transmitted. In case of a convergent geometry (a heavy gas bubble surrounded by light ambient gas with an Atwood number $A = (\rho_1 - \rho_2)/(\rho_1 + \rho_2) < 1$) the transmitted shock wave travels more slowly than the incident shock wave outside of the bubble. The transmitted shock wave focuses at the downstream pole of the bubble. As the shock wave collapses in the shock-focusing point, pressure and temperature increase. This phenomenon is known as the shock-focusing phenomenon. Furthermore, vorticity deposition leads to a growth of the initial interface disturbances. Provided that the initial energy input is sufficient the flow develops a turbulent mixing zone through non-linear interactions of the material interface perturbations [7,8].

The non-reacting setup of SBI was rigorously studied over the last decades. In 1983, Haas and Sturtevant [16] investigated the interaction of shock waves propagating in air with a gas bubble filled with either helium or R_{22}. Through their shadow-photographs, Haas and Sturtevant [16] did not only significantly contribute to a better understanding of the temporal bubble evolution under shock acceleration, but also established an entire new class of canonical flow configurations. Later, Quirk and Karni [17] conducted a detailed numerical investigation of such shock-bubble interaction problems and complemented experimental findings by reproducing the transition from regular to irregular refraction, shock wave focusing and the formation of a jet towards the center of the bubble. For a comprehensive review on SBI please refer to Ranjan et al. [18].

Haehn et al. [19] extended the setup by replacing the gas within the bubble by a reactive gas mixture. As the shock wave propagates through the bubble temperature and pressure increase. This results in a raise of chemical reaction rates up to ignition of the gas mixture. In their experimental investigation, a stoichiometric gas mixture of H_2 and O_2, diluted by xenon (Xe) is compressed by a shock wave propagating at Mach numbers between $Ma = 1.34$ and $Ma = 2.83$. In general, maximum pressures and temperatures are reached when the shock passes the bubble. Subsequently, the gas mixture relaxes and the two main parameters controlling the reaction rate, temperature and pressure, decrease.

At low shock Mach numbers the gas mixture does not ignite within the experimental timeframe, as the compression is not sufficiently high. An increase of shock strength results in an ignition, followed by a deflagration reaction wave. At higher shock Mach numbers the stoichiometric mixture reacts in a detonation wave, even before the shock wave has reached the shock focusing point. Haehn et al. [19] determine Damköhler numbers in the range from 0.25 ($Ma = 1.65$) to 8.00 ($Ma = 2.83$). They conclude that heat conduction plays an important role at lower Mach numbers, and that the Zeldovich mechanism becomes important at higher Mach numbers. This finding is consistent with the two limiting cases of shock-induced combustion, the strong and the weak ignition [20]. Strong ignition leads to a detonation mostly initiated directly by the shock wave, whereas weak ignition is characterized by the occurrence of small flames that can undergo transition into detonation waves. Haehn et al. [19] provide several chemiluminescence exposures to depict the qualitative evolution of the bubble and reaction processes. Beside such visualizations, they present quantitative data for the temporal evolution of the transverse diameter of the bubble as well as for the vortex ring diameter. However, the complex experimental setup of Haehn et al. [19] implies uncertainties. For instance, the uncertainty of the Damköhler number at the highest Mach number ($Ma = 2.83$) is $Da = 8 \pm 4$. At the lowest Mach number ($Ma = 1.34$) 30% of all measurements showed no ignition within the given experimental time frame. Such uncertainties underline the need for a detailed numerical study of RSBI.

1.4. Objectives of the current investigation

The present numerical investigation complements these of Haehn et al. [19] and establishes a numerical framework for further studies. Special emphasis is given on the general temporal and spatial evolution of RSBI, the comparison with SBI, and the dependence of the bubble evolution on the reaction wave type. In our study the initial pressure is varied at a constant shock Mach number. The chemical reaction rates of most gas mixtures simply increase with pressure H_2-O_2 reactions, however, show a different behavior [21], as discussed in Section 1.2. The reaction rates are sensitive to pressure, and a variation of the initial pressure can change the entire reaction process between detonation and deflagration.

The paper is structured as follows: Section 2 outlines the governing equations. Molecular transport properties for multicomponent flows and chemical reaction kinetics, based on the Arrhenius law as well as the validation of the employed reaction mechanism are presented in detail. Section 3 outlines the computational domain and the initial condition of each simulation. Results are discussed in Section 4. First the spatial and temporal evolution of RSBI are presented. The effect of different types of reaction waves on bubble deformation are compared with each other and with their non-reacting counterparts. The chemical reaction process during shock passage until ignition is analyzed in detail. The pressure dependency of H_2-O_2 reactions enables different reaction branches and leads to different gas compositions, and this results in either deflagration or detonation waves. In the following a consistent definition of the dimensionless Damköhler number is used to evaluate if hydrodynamic or chemical reaction time scales dominate the flow field for given initial pressure. Integral quantities, such as enstrophy or the molar mixing fraction, are consulted to determine the effect of the reaction

waves on mixing of the bubble gas. Section 5 summarizes the key findings.

2. Numerical model

2.1. Governing equations

The full set of compressible reacting multicomponent Navier–Stokes equations is solved in conservative form

$$\frac{\partial \boldsymbol{U}}{\partial t} + \nabla \cdot \boldsymbol{F}(\boldsymbol{U}) = \nabla \cdot \boldsymbol{F}_v(\boldsymbol{U}) + \boldsymbol{S}, \tag{1}$$

with

$$\boldsymbol{U} = \begin{pmatrix} \rho \\ \rho \boldsymbol{u} \\ E \\ \rho Y_i \end{pmatrix}, \quad \boldsymbol{F}(\boldsymbol{U}) = \begin{pmatrix} \rho \boldsymbol{u} \\ \rho \boldsymbol{u}\boldsymbol{u} + p\boldsymbol{\delta} \\ (E+p)\boldsymbol{u} \\ \rho \boldsymbol{u} Y_i \end{pmatrix},$$

$$\boldsymbol{F}_v(\mathbf{U}) = \begin{pmatrix} 0 \\ \boldsymbol{\tau} \\ \boldsymbol{\tau}\cdot\boldsymbol{u} - \boldsymbol{q_c} - \boldsymbol{q_d} \\ \boldsymbol{J_i} \end{pmatrix} \quad \text{and} \quad \boldsymbol{S} = \begin{pmatrix} 0 \\ \mathbf{0} \\ \dot{\omega}_T \\ \dot{\omega}_i \end{pmatrix}. \tag{2}$$

ρ represents the mixture density, $\boldsymbol{u}$ the velocity vector, E the total energy, p the pressure, and Y_i the mass fraction of species $i = 1, 2, \ldots N$, with N being the total number of species. The source term $\boldsymbol{S}$ includes heat release $\dot{\omega}_T$ and species formation and destruction in terms of individual mass rates $\dot{\omega}_i$. The identity matrix is given by $\boldsymbol{\delta}$, and the viscous stress tensor $\boldsymbol{\tau}$ is defined for a Newtonian fluid as

$$\boldsymbol{\tau} = 2\overline{\mu}\left[\frac{1}{2}\left(\nabla \boldsymbol{u} + (\nabla \boldsymbol{u})^T\right) - \frac{1}{3}\boldsymbol{\delta}(\nabla \cdot \boldsymbol{u})\right], \tag{3}$$

with the mixture viscosity $\overline{\mu}$. Following the Fourier law we define the heat conduction as

$$\boldsymbol{q_c} = -\overline{\kappa}\nabla T, \tag{4}$$

where T is the temperature and $\overline{\kappa}$ the mixture heat conductivity, which is calculated from [22]

$$\overline{\kappa} = \frac{\sum_{i=1}^{N} \kappa_i Y_i / M_i^{1/2}}{\sum_{i=1}^{N} Y_i / M_i^{1/2}}, \tag{5}$$

where M_i is the molecular mass, and κ_i is given by

$$\kappa_i = c_{p_i} Y_i \frac{\mu_i}{Pr_i}, \tag{6}$$

with c_{p_i} as the specific heat coefficient and Pr_i as the specific Prandtl number of species i. The viscosity μ_i is calculated from the Chapman-Enskog viscosity model

$$\mu_i = 2.6693 \cdot 10^{-6} \frac{\sqrt{M_i T}}{\Omega_{\mu,i}\sigma_i^2}, \tag{7}$$

with σ_i as the collision diameter and $\Omega_{\mu,i}$ as the collision integral [23] defined as

$$\Omega_{\mu,i} = A(T_i^*)^B + C\exp(DT_i^*) + E\exp(FT_i^*). \tag{8}$$

The parameters are given as $A = 1.16145$, $B = -0.14874$, $C = 0.52487$, $D = -0.7732$, $E = 2.16178$ and $F = -2.43787$, it is $T_i^* = T/(\epsilon/k)_i$, using the Lennard-Jones energy parameter $(\epsilon/k)_i$ for species i.

The mass diffusion coefficient of a binary mixture is computed from the constitutive empirical law [22]

$$D_{ij} = \frac{0.0266}{\Omega_{D,ij}} \frac{T^{3/2}}{p\sqrt{M_{ij}}\sigma_{ij}^2}, \tag{9}$$

where

$$M_{ij} = \frac{2}{\frac{1}{M_i} + \frac{1}{M_j}} \quad \text{and} \quad \sigma_{ij} = \frac{\sigma_i + \sigma_j}{2}. \tag{10}$$

The collision integral for diffusion $\Omega_{D,ij}$ is defined as

$$\Omega_{D,ij} = A(T_{ij}^*)^B + C\exp(DT_{ij}^*) + E\exp(FT_{ij}^*) + G\exp(HT_{ij}^*), \tag{11}$$

with the parameters $A = 1.06036$, $B = -0.1561$, $C = 0.19300$, $D = -0.47635$, $E = 1.03587$, $F = -1.52996$, $G = 1.76474$, $H = -3.89411$, and $T_{ij}^* = T/T_{\epsilon_{ij}}$. $T_{\epsilon_{ij}}$ is obtained from of the Lennard-Jones energy parameters for species i and j as

$$T_{\epsilon_{ij}} = \sqrt{\left(\frac{\epsilon}{k}\right)_i \left(\frac{\epsilon}{k}\right)_j}. \tag{12}$$

The interspecies diffusional heat flux $\boldsymbol{q_d}$ [24] is defined as

$$\boldsymbol{q_d} = \sum_{i=1}^{N} h_i \boldsymbol{J}_i, \tag{13}$$

where h_i is the individual species enthalpy. The species diffusion $\boldsymbol{J_i}$ is

$$\boldsymbol{J_i} \approx -\rho\left(D_i \nabla Y_i - Y_i \sum_{j=1}^{N} D_j \nabla Y_j\right). \tag{14}$$

D_i indicates the effective binary diffusion coefficient of species i. The equation of state for an ideal gas is used to close the equations

$$p(\rho e, Y_i) = (\overline{\gamma} - 1)\rho e. \tag{15}$$

The ratio of specific heats of the mixture is represented by $\overline{\gamma}$ and the internal energy by e with

$$\rho e = E - \frac{\rho}{2}\boldsymbol{u}^2. \tag{16}$$

The temperature is computed from

$$T = \frac{p}{\overline{R}\rho}, \tag{17}$$

with $\overline{R}$ being the specific gas constant of the mixture. The source term $\boldsymbol{S}$ in Eq. (2), contains the specific heat release

$$\dot{\omega}_T = -\sum_{i=1}^{N} \Delta h_{f,i}^0 \dot{\omega}_i, \tag{18}$$

with $h_{f,i}^0$ being the heat of formation of each species i. The individual mass rates $\dot{\omega}_i$ for each species are

$$\dot{\omega}_i = W_i \sum_{r=1}^{N_R} \nu_{ir} \Gamma_r \left(k_{fr} \prod_{i=1}^{N} [X_i]^{\nu'_{ir}} - k_{br} \prod_{i=1}^{N} [X_i]^{\nu''_{ir}}\right). \tag{19}$$

In Eq. (19) N_R is the number of reactions, W_i is the molecular weight, Γ_r is the third body efficiency of reaction r, X_i is the molar concentration, and ν'_{ir} and ν''_{ir} are the molar stoichiometric coefficients of the reactant and the product of reaction r. ν_{ir} is the net stoichiometric coefficent

$$\nu_{ir} = \nu''_{ir} - \nu'_{ir}. \tag{20}$$

The forward and backward reaction rates k_{fr} and k_{br} are modeled according to Arrhenius law. The forward reaction rates are computed as

$$k_{fr} = A_{fr} T^{\beta_{fr}} exp\left(\frac{E_{fr}}{RT}\right), \tag{21}$$

where A_{fr} is the pre-exponential factor, E_{fr} is the activation energy, β_{fr} is the temperature exponent for each reaction r [25] and R is the universal gas constant. The backward reaction rates are calculated with the equilibrium constants K_{cr}

$$k_{br} = \frac{k_{fr}}{K_{cr}}. \tag{22}$$

K_{cr} is defined as

$$K_{cr} = \left(\frac{p^{\circ}}{RT}\right)^{\nu_r} exp\left(\frac{\Delta S^{\circ}_{r,i}}{R} - \frac{\Delta H^{\circ}_{r,i}}{RT}\right), \tag{23}$$

where p° is a pressure of 1 atm, ν_r the net change in the number of species in the reaction, $\Delta S^{\circ}_{r,i}$ the net change in entropy and $\Delta H^{\circ}_{r,i}$ the net change in enthalpy.

Furthermore pressure dependent and duplicated reactions are considered. The parameters of the reaction mechanism are discussed in Section 2.3.

2.2. Finite volume disrectization

The system of equations given by Eq. (1) is solved by the 2*nd*-order accurate Strang time splitting scheme [26]. The Strang splitting scheme separates the stiff source term from the Navier-Stokes equations, which results in a system of partial differential equations (PDE) and a system of stiff ordinary differential equations (ODE)

$$\frac{\partial \boldsymbol{U}^*}{\partial t} + \nabla \cdot \boldsymbol{F}(\boldsymbol{U}) = \nabla \cdot \boldsymbol{F}_v(\boldsymbol{U}), \tag{24}$$

$$\frac{\partial \boldsymbol{U}}{\partial t} = \frac{\partial \boldsymbol{U}^*}{\partial t} + \boldsymbol{S}(\boldsymbol{U}^*). \tag{25}$$

A 2*nd*-order time discretization is obtained by solving Eq. (25) before and after Eq. (24) with half the time step of Eq. (24), see [26]. For the PDE system, Eq. (24), we use a finite-volume discretization scheme that applies a flux projection onto local characteristics for the hyperbolic part. The Roe matrix required for the projection is calculated for the full multi-species system [27,28]. The numerical fluxes at the cell faces are reconstructed from cell averages by the adaptive central-upwind 6*th*-order weighted essentially non-oscillatory (WENO-CU6) scheme [29]. The fundamental idea of the WENO-CU6 scheme is to use a non-dissipative 6th-order central stencil in smooth flow regions and a non-linear convex combination of 3*rd*-order stencils in regions with steep gradients. The scheme shows excellent shock-capturing properties with very low numerical diffusion in smooth flow regions [29]. Time integration is performed with the 3rd-order total variation diminishing Runge–Kutta scheme, developed by Gottlieb and Shu [30]. With respect to the objective in this paper, the numerical model has been tested and validated for shock induced turbulent multi-species mixing problems at finite Reynolds numbers [31–33]. The accurate calculation of ignition delay times and gas compositions has been validated with Cantera [34]. The stiff ODE, Eq. (25), is solved separately by the variable-coefficient ODE solver using 5th-order backward differentiation formulas [35]. The present approach with 2nd-order Strang splitting is state-of-the-art in combustion and reactive flow simulations [36].

2.3. Ó Conaire reaction mechanism

The reaction rate parameters for the Arrhenius law are provided by the Ó Conaire [37] reaction mechanism, which is valid for a wide range of pressures (0.05 to 87 atm) and temperatures (298–2700 K). The mechanism considers $8 + N$ species (two reactants: H_2, O_2; 5 chain-carrying intermediates: hydrogen radical (H), oxygen radical (O), hydroxyl radical (OH), hydroperoxyl radical (HO_2), hydrogen peroxid (H_2O_2); the product: hydrogen oxide (H_2O); N inert gases) and 19 intermediate reactions. This mechanism has been used widely during the recent years [38,39]. The 3rd-body efficiencies of *Xe* are set as the same as for argon (*Ar*), which are given by Ó Conaire. 3rd-bodies absorb energy during the two-body recombination reaction and stabilize the final combination. The available modes for energy storage control the energy absorption. As the available modes of *Ar* and *Xe* are identical, the 3rd-body efficiencies can be assumed to be comparable. Also the steric factor for monoatomic gases, accounting for the geometry influence on the collision between molecules, is similar [40].

Table 1
Overview of the reaction mechanisms used for the simulation of the ignition delay time; N = Number of species, N_R = Number of reactions, *TBE* = Third body efficiencies, *PD* = pressure dependency.

Mechanism	*N*	N_R	*TBE*	*PD*
Ó Conaire	9	19	✓	✓
Jachimowski	9	19	✓	
reduced Jachimowksi	7	7	✓	
Bane	3	1		

2.4. Model validation

An accurate prediction of the ignition delay times is crucial for the simulation of shock-induced ignition. Petersen et al. [41] provide experimental data for stoichiometric H_2-O_2 mixtures, highly diluted with *Ar* (97–99.85%) at pressures between 33 and 64 atm. For validation, results for the Ó Conaire mechanism are compared with results obtained by three other reaction mechanisms (Jachimowksi [42], reduced Jachimowksi [42] and Bane et al. [43] mechanisms) and with the experimental data of Petersen et al. [41]. The reaction mechanisms differ by the number of species N and reactions N_R, whether third body efficiencies (TBE) are considered or whether the reactions are pressure dependent (PD) or not. Table 1 summarizes the reaction mechanisms applied in this paper.

Figure 2 shows the Arrhenius plot of the normalized ignition delay time over the inverse temperature for initial pressures of $p_0 = 33$ and 64 atm. Petersen et al. [41] define the ignition delay time as elapsed time from the shock passage until the time when the maximum rate in the *OH*-signal is reached ($\{d[OH]/dt\}_{max}$). We used the same definition, except for the Bane [43] mechanism which considers only three species (H_2, O_2 and H_2O). For this case the ignition delay time is defined as the time until a temperature increase of $\Delta T = 20K$ is reached. From Fig. 2 it becomes clear that accuracy of the results benefits from the more complex reaction mechanism. The mechanism of Bane [43] shows a large discrepancy for the ignition delay time. It overpredicts the delay time by two orders of magnitude, and the temperature sensitivity is weaker than observed in the experiments. The more complex reduced Jachimowski mechanism [42] shows good agreement with the experimental results at higher temperatures but still lacks accuracy at lower temperatures. The correct temperature sensitivity is achieved only by the mechanisms of Jachimowski [42] and Ó Conaire [37], using 19 reactions and nine species. The Jachimowski mechanism overpredicts the ignition delay time over the entire range of initial temperatures. The Ó Conaire mechanism exhibits the best overall agreement with the experimental data. The superior accuracy of the Ó Conaire mechanism is achieved by considering fall-off reactions. These reactions not only depend on temperature but also include a pressure dependence between an Arrhenius high-pressure and low-pressure limit. A blending function composed of the high and low pressure Arrhenius rate parameters is applied for a smooth pressure dependence. For more details on fall-off reactions the reader is referred to Troe [44].

The Ó Conaire mechanism has been validated also for a wide range of initial conditions. Adachi et al. [45] showed that the mechanism

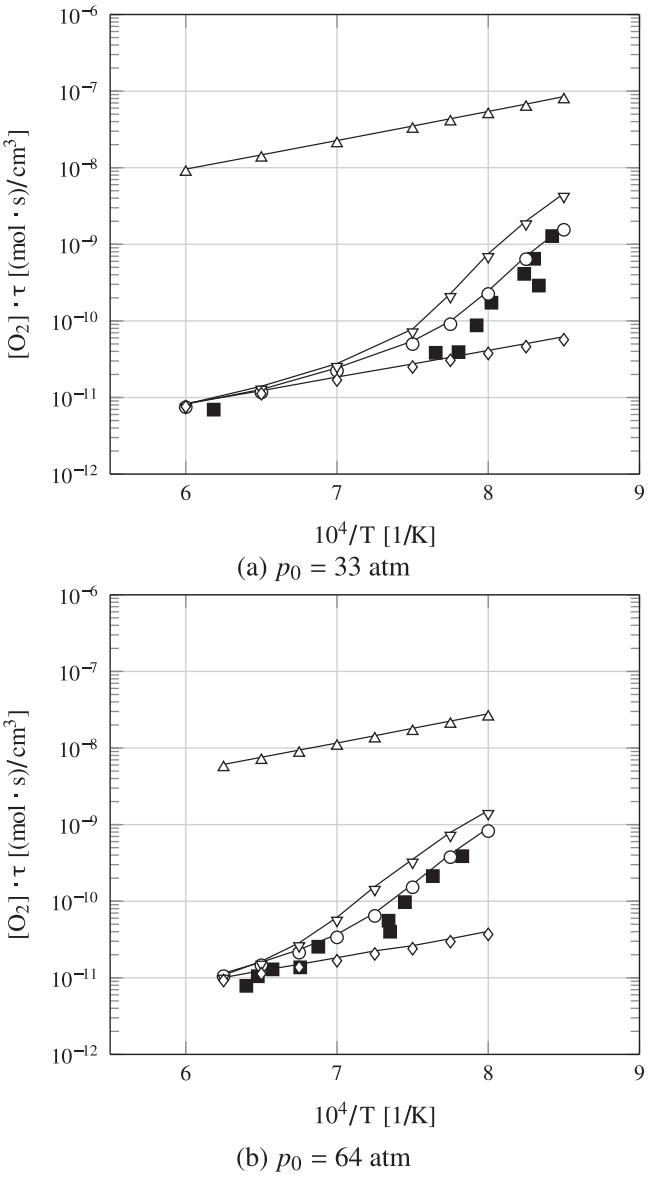

Fig. 2. Ignition delay times of stoichiometric $H_2/O_2/Ar$ (2/1/97 mole fractions) gas mixture at different initial pressures using four different reaction mechanisms: ■ Experimental data of Petersen [41], ○ Ó Conaire mechanism [37], ▽ Jachimowski mechanism [42], ◇ reduced Jachimowski mechanism [42] and △ Bane mechanism [43].

can predict detonation of an H_2-O_2 mixture at high pressures. In addition, Ströhle and Myhrvold [46] underline the good agreement of the Ó Conaire mechanism with experimental data upon comparison with even more complex reaction mechanisms such as GRI-Mech [47]. Weydahl et al. [48] confirm these results by comparing the Ó Conaire mechanism and six other mechanisms over a wide range of pressures and temperatures with experimental data.

3. Setup

3.1. Testcase and initial conditions

Based on the setup of Haehn et al. [19], the bubble diameter is set to $D = 2r = 0.04$ m. The bubble gas contains H_2, O_2 and Xe in a stoichiometric composition of 2/1/3.67 molar fractions, surrounded by pure N_2. The inert gas Xe increases the density of the bubble, leading to an Atwood number of $A = 0.476$. The interface between the bubble gas mixture and N_2 is defined by an interface equation, in terms of the molar fraction

$$X_{N_2} = \frac{\tanh\left((\sqrt{x^2+y^2} - r)\xi\right) + 1}{2}, \tag{26}$$

where r is the radius of the bubble and ξ the sharpness coefficient, with $\xi = 20.000$. The molar fraction $(X = 1 - X_{N_2})$ inside the bubble is distributed among the three gases, ensuring a stoichiometric mixture with a relative composition of 2/1/3.67 ($H_2/O_2/Xe$).

The shock wave is initialized on the left side of the bubble. The pre-shock state is defined by $T_0 = 350$ K and three different initial pressures $p_0 = 0.25/0.50/0.75$ atm. The post-shock thermodynamics state is given by standard Rankine–Hugoniot conditions

$$\rho'_{N_2} = \rho_{N_2} \frac{(\gamma_{N_2}+1)Ma^2}{2 + (\gamma_{N_2}-1)Ma^2}, \tag{27}$$

$$u'_{N_2} = Ma\, c_{N_2}\left(1 - \frac{\rho_{N_2}}{\rho'_{N_2}}\right), \tag{28}$$

$$p'_{N_2} = p_0\left(1 + 2\frac{\gamma_{N_2}}{\gamma_{N_2}+1}(Ma^2 - 1)\right), \tag{29}$$

with $c_{N_2} = \sqrt{\gamma_{N_2} p_0/\rho_{N_2}}$. Variables marked with a prime indicate post-shock conditions.

3.2. Computational setup

The RSBI is studied within a two-dimensional rectangular domain with a symmetry plane at the center axis of the bubble, see Fig. 5. We impose inflow boundary conditions at the left domain boundary and outflow boundary conditions at the right and upper boundaries. The initial bubble radius is denoted by r, and the domain size ($32.5\ r \times 8\ r$) is chosen sufficiently large as to avoid artifacts due to shock reflections. Computational costs are reduced by refining the Cartesian grid near the bubble by a factor of 25 compared to the coarse resolution outer grid. Four grid resolutions with cell sizes of $\Delta_{xy} = 234$ μm, 117 μm, 59 μm and 29 μm are used on the different grids respectively in the high resolution part of the domain, corresponding to a total number of 0.15, 0.6, 2.4 and 9.7 million cells. The simulations are performed at a CFL-number of 0.3 on 1054 cores for the coarser resolutions and on 4216 cores for the finest grid. Figure 3 shows con-

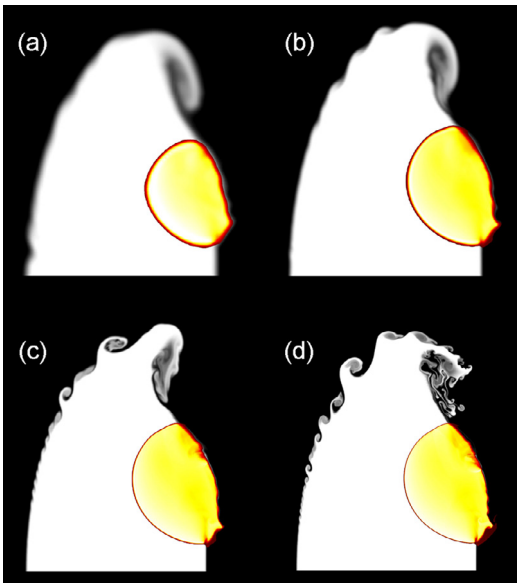

Fig. 3. Contour plots shortly after ignition for $p_{2_0} = 0.50$ atm, gray scale: mass fraction of Xe, color scale: temperature; cell sizes Δ_{xy}: (a) 234 μm, (b) 117 μm, (c) 59 μm and (d) 29 μm.

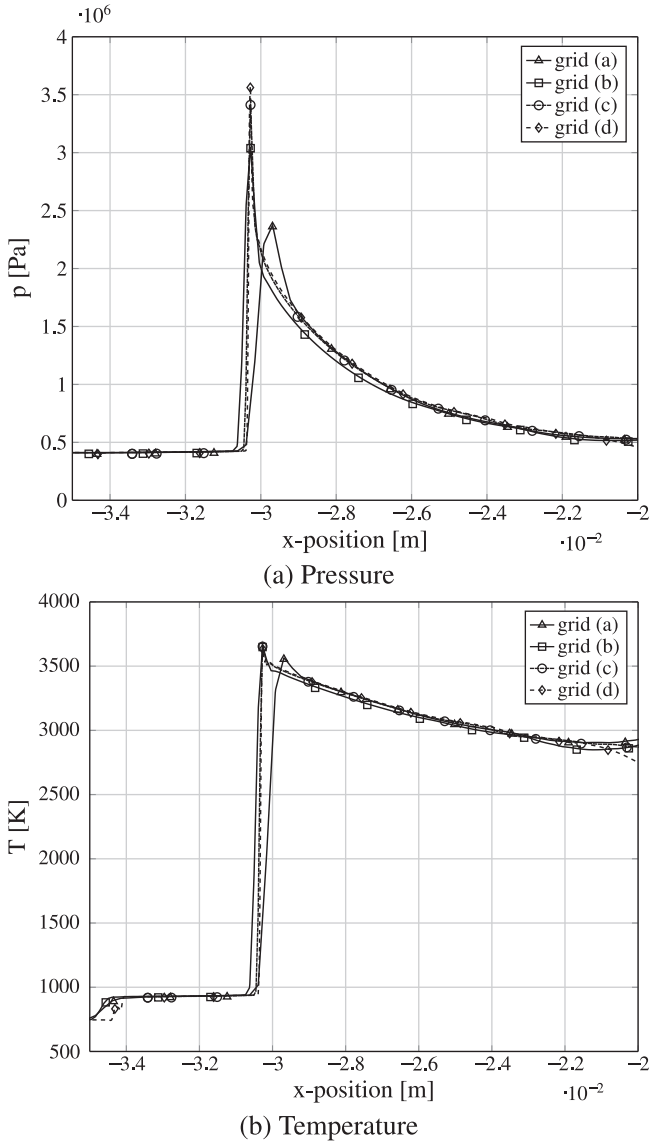

Fig. 4. Plots of the pressure and temperature over a characteristic cross-section of the bubble at a time instant when the reaction wave propagates through the bubble gas. Four different grid resolutions are shown, with grid (a) as the coarsest up to the finest grid (d). Initial pressure $p_0 = 0.50$ atm.

tours of mass fraction and temperature shortly after ignition for the four different grids, verifying that results presented in this work are, in terms of huge-scale structures, independent of the grid resolution. Although the interface representation and small flow scales still depend on the grid resolution, results at all three grid resolutions are in good overall agreement. On the two coarsest grids, Fig. 3 (a) and (b), the interface is smeared out and small scale Kelvin–Helmholtz instabilities (KHI) are suppressed, whereas on the finer grids, Fig. 3 (c) and (d) more small scale structures and KHI develop. Additionally we inspect pressure and temperature along a cross-section of the bubble at a time instant when the reaction wave propagates through the bubble gas. Figure 4 (a) shows as quantities of interest (QoI) the pressure and Fig. 4 (b) the temperature evolution across the reaction wave for a simulation with an initial pressure of $p_0 = 0.50$ atm. We observe grid-convergence, as in particular the rapid temperature increase over the reaction wave is sharply resolved by the three higher resolutions. The pressure peak over the detonation front increases as expected with higher grid resolution and state of the two finest grids are almost indistinguishable. As both QoI are important for a correct prediction of the reaction front in terms of propagation and burned gas composition we can conclude, that the second finest grid resolution is sufficient to capture the essential properties of the reaction wave. Radulescu et al. [49] showed that a resolution of about 10^4 grid points per induction length is necessary to fully resolve the detonation regime, which implies extremely high computational cost. Other studies, such as our present work, focus on the prediction of the larger scales of deflagration and detonation structures. Mazaheri et al. [50] demonstrate that for low activation energy mixtures, such as hydrogen-oxygen, good accuracy of the detonation structure reproducing the essential properties of detonation waves can be achieved by grid resolution with 25 cells per half reaction length, which corresponds to the grid resolution employed here. Furthermore, the resolution at the interface, where flame-vortex interaction will occur, is adequate. Di Sarli et al. [51] investigated flame-vortex interaction and showed very good agreement between their simulations and experimental data using a grid by more than factor of 10 coarser than the grid of the present work.

4. Results and discussion

For the simulation of RSBI, three different initial pressures are chosen: $p_{1_0} = 0.25$ atm, $p_{2_0} = 0.50$ atm and $p_{3_0} = 0.75$ atm. Over this pressure range different types of gas mixture self-ignition are obtained. The initial temperature is set to $T_0 = 350$ K, and the shock wave Mach number is $Ma = 2.30$. The pressure sensitivity of the chemical reactions leads to a deflagration at an initial pressure of p_{1_0} and to detonation for p_{2_0} and p_{3_0}. The different propagation

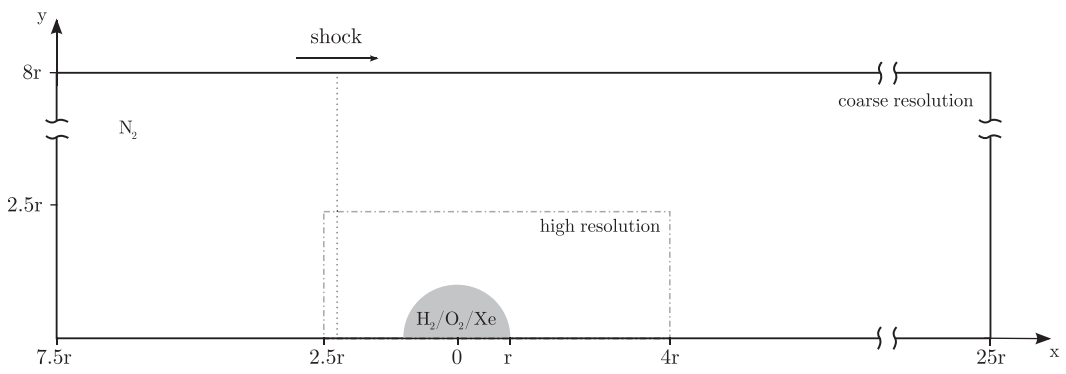

Fig. 5. Schematic of the computational domain of the RSBI, $r = 0.02$ m.

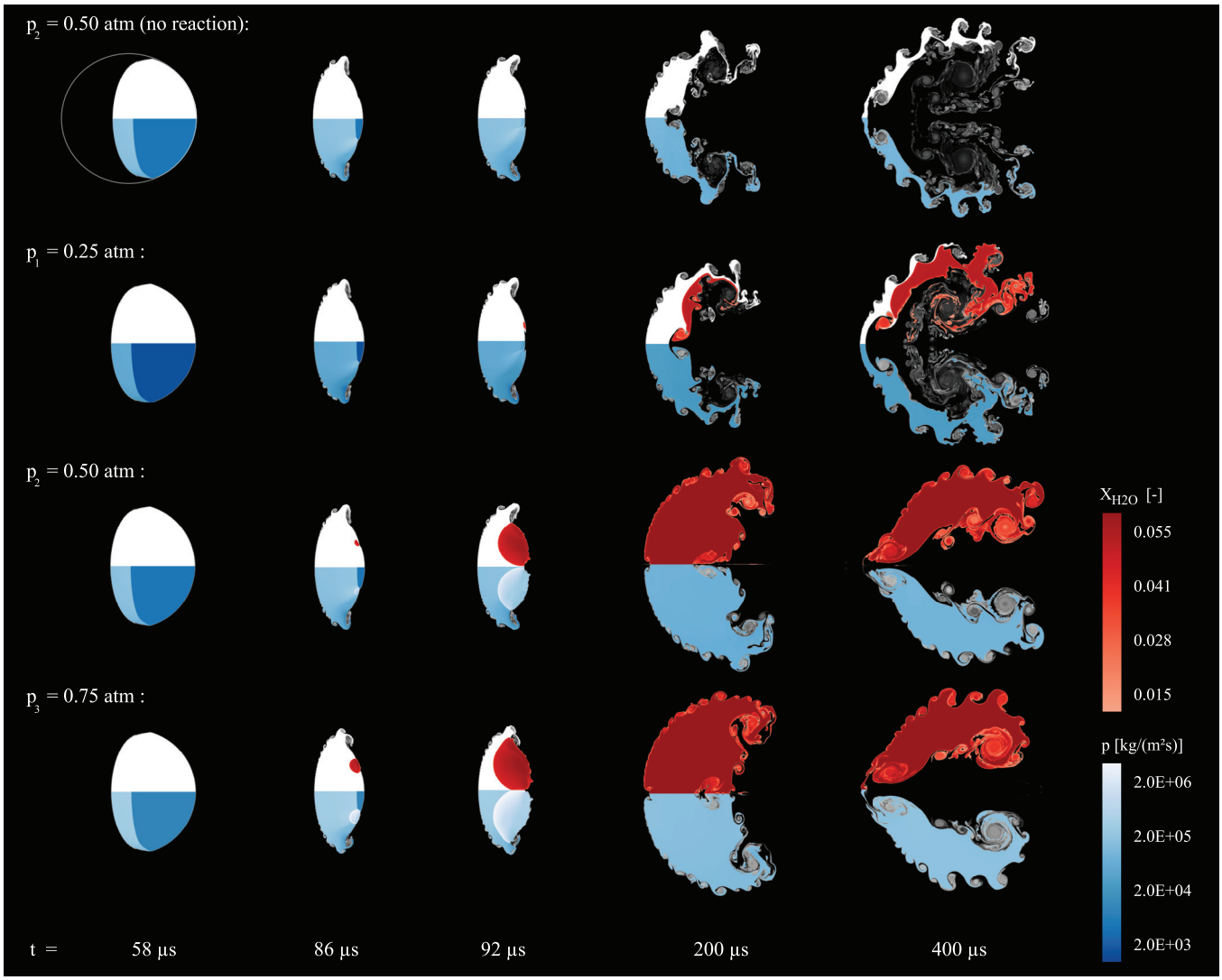

Fig. 6. Chemical kinetics in RSBI: Upper part shows mass fraction of the inert gas *Xe* (gray scale) and the product H_2O (red color scale), illustrating the reaction wave. Lower part depicts the pressure distribution. (For interpretation of the references to color in this figure legend, the reader is referred to the web version of this article).

velocities of the reaction waves have a crucial influence on the temporal and spatial bubble evolution as well as on the mixing process.

4.1. Temporal bubble evolution

Figure 6 shows a visualization of the temporal SBI evolution for all cases. Three different initial pressures are compared to the baseline inert SBI at $p_{2_0} = 0.50$ atm. The contour plots of the mass fraction of *Xe* and H_2O are shown in the upper half of the bubble and the pressure is given in the lower half.

The characteristic stages of the inert bubble evolution are shown in the top row of Fig. 6. At $t = 58$ µs and $t = 86$ µs the shock wave propagates through the bubble and compresses the bubble gas mixture. At $t = 200$ µs the shock wave has passed the bubble and the primary vortex cores form, while secondary instabilities occur due to shear at the material interface. As more and more secondary instabilities develop and the primary vortex cores are advected downstream mixing increases. The contour plots show a high degree of mixing of the bubble gas mixture with the surrounding N_2.

For the reacting SBI the pressure is varied from $p_{1_0} = 0.25$ atm through $p_{2_0} = 0.50$ atm to $p_{3_0} = 0.75$ atm. As the chemical reaction kinetics are strongly sensitive to pressure, initial pressure variations affect the ignition delay time and the subsequent reaction process distinctly. At the lowest pressure, $p_{1_0} = 0.25$ atm, the shock wave ignites the combustible gas mixture at $t \approx 92$ µs in the shock focusing point, similar to the observation of Haehn et al. [19], which is near the downstream pole of the bubble. At the focusing point, temperature and pressure reach a maximum and a deflagration reaction wave is initiated. The deflagration wave propagates at subsonic speed and reaches the upstream pole of the bubble at $t = 500$ µs. The heat release associated with the chemical reaction leads to an expansion of the bubble gas mixture. However, the overall effect of the subsonic deflagration wave on bubble dynamics is small, as one can see from the comparison with the inert baseline case, see Fig. 6.

When the initial pressure is increased to $p_{2_0} = 0.50$ atm, the shock wave ignites the gas mixture slightly earlier at $t = 86$ µs. Instead of a deflagration wave a detonation wave is generated, which propagates within $\Delta t \approx 14$ µs at supersonic speed through the bubble. The detonation reaction wave drives a precursor shock wave, which results in a significant increase in pressure, refer to the pressure contours in Fig. 6. The strong heat release and the pressure increase result in a rapid and significant bubble expansion. When the detonation wave reaches the material interface of the bubble, baroclinic vorticity with opposite sign is generated. This leads to a suppression of secondary instabilities, which develop as a consequence of shear at the material interface, as can be seen in Fig. 6 at $t = 200$ µs and $t = 400$ µs.

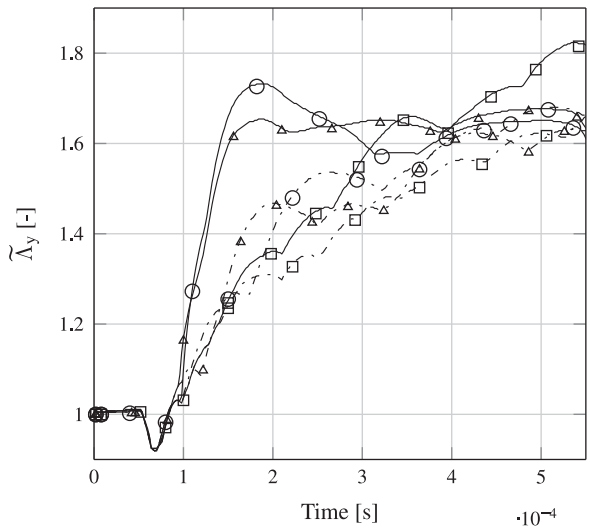

Fig. 7. Normalized transverse bubble diameter for different initial pressures, leading to detonation, respectively deflagration. Solid lines: reaction; Dashed-dotted lines: no reaction; □ $p_{1_0} = 0.25$ atm, ○ $p_{2_0} = 0.50$ atm, △ $p_{3_0} = 0.75$ atm.

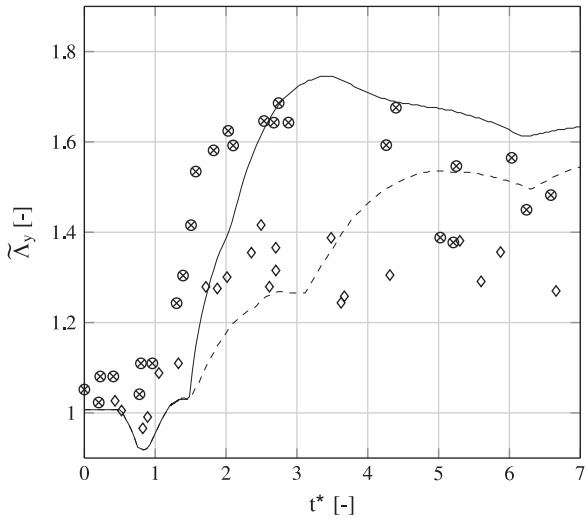

Fig. 8. Normalized transverse bubble diameter as a function of the time t^* normalized by the incident shock wave speed and the initial bubble diameter. Comparison between simulations ($p_{2_0} = 0.50$ atm) and experimental data of Haehn et al. [19]. Reaction: solid line and ⊗; No reaction: dashed line and ◇.

The detonation wave amplifies the N_2-jet that forms at the symmetry plane at the downstream pole of the bubble at $t = 200$ µs. The amplified jet breaks through the bridge at the upstream pole of the bubble which connects the two primary vortices.

A further increase of the initial pressure to $p_{3_0} = 0.75$ atm does not significantly affect the spatial and temporal evolution of the bubble at early times. The gas mixture ignites 2 µs earlier when compared to an initial pressure of $p_{2_0} = 0.50$ atm, and the propagation velocity of the detonation wave is similar. Hence the long-term evolution is nearly unaffected by a further increase of pressure, outlined in the last two rows in Fig. 6. Once a pressure limit is exceeded and transition to detonation is achieved, a further pressure increase shows no significant effect on the evolution of the bubble.

Supplementary to Fig. 6 we provide two videos of the temporal evolution of the RSBI for initial pressures of $p_{1_0} = 0.25$ atm and $p_{2_0} = 0.50$ atm. The multimedia files are published online in the electronic version of this article and can be found at http://www.journals.elsevier.com/combustion-and-flame/.

4.2. Normalized bubble diameter

In their experimental investigation Haehn et al. [19] presented two geometrical length scales, namely the normalized transverse bubble diameter and the normalized vortex ring diameter, for quantifying the impact of chemical reaction processes on the hydrodynamic evolution of the bubble. In the present study the normalized transverse bubble diameter $\widetilde{\Lambda}_y = \Lambda_y / D_0$ is shown in Fig. 7. Note that the roll-up of the primary vortices leads to a wave-like temporal growth of $\widetilde{\Lambda}_y$. Our numerical results are in very good qualitative agreement with the experimental results of Haehn et al. [19]. Li and Zhang [52] emphasize that discrepancies during the linear and intermediate nonlinear stages of RMI between two- and three-dimensional simulations are small. However, as three dimensional RMI shows a larger growth rate, simulations for a detailed quantitative comparison eventually should be performed in a three-dimensional setup. The deflagration wave triggered by an initial pressure of $p_{1_0} = 0.25$ atm shows a minor influence on the bubble dynamics compared to the inert case. This is caused by the low propagation velocity of the reaction wave, compared to the evolution of the hydrodynamic instability. At $p_{2_0} = 0.50$ atm and $p_{3_0} = 0.75$ atm the detonation wave leads to a rapid combustion of the bubble gas mixture and thus to a sudden increase of $\widetilde{\Lambda}_y$ by approximately 70% of the initial bubble diameter. The expansion at $p_{2_0} = 0.50$ atm is stronger because the expansion from detonation pressure to ambient pressure is higher than at $p_{3_0} = 0.75$ atm.

Haehn et al. [19] observed qualitatively the same evolution when they increased the initial shock Mach number from $Ma = 1.34$ to $Ma = 2.83$. Detonation of the bubble gas was observed at the highest shock Mach number of $Ma = 2.83$. Figure 8 compares the normalized transverse bubble diameter of our results at $p_{2_0} = 0.50$ with the experimental data of Haehn et al. [19]. Although the shock Mach numbers differ the following conclusions can be drawn: Detonation type and propagation velocity of the reaction wave are similar and the expansion evolution of the bubble is in very good agreement. The experimental data show a shorter ignition delay time, which can be explained by a higher compression caused by the stronger shock wave. The higher pressure leads to an earlier ignition, an effect that was also observed during our simulation with higher initial pressures. An increase of the initial pressure from $p_{2_0} = 0.50$ atm to $p_{3_0} = 0.75$ atm induces an earlier ignition without affecting the type of the reaction wave type and the propagation velocity, see Fig. 6. In the long-term evolution the normalized transverse bubble diameters of the simulations exceed the experimental data, which is typical for 2D simulations. Wang et al. [53] also observed a higher transverse bubble diameter of 2D SBI compared to their 3D counterpart. We point out that Hejazialhosseini et al. [54] showed that the missing vortex stretching term in 2D may have a significant effect on the spatial expansion in y-direction.

It is important to note that the simulations do not account for three-dimensional effects such as the onset of turbulence. Three-dimensional vortex rings tend to become unstable and vortex stretching may eventually result in broad-band turbulence [55]. This classical production mechanism is suppressed in a two-dimensional setting. The very good agreement between our numerical results and Haehns experimental data [19] shows that turbulence may not have a very important impact on the considered shock-bubble interaction, at least during early stages of evolution. Similar findings have been reported by Miles et al. [56], who also observed no significant differences of the early growth rates of shock-induced instabilities between two- and three-dimensional simulations. Hejazialhosseini et al. [54] underline that vortex stretching affects only the long-term evolution of the mixing rate. We are confident that two-dimensional simulations are sufficient and provide reliable results for the investigation of ignition and reaction wave characteristics during the early stages of evolution.

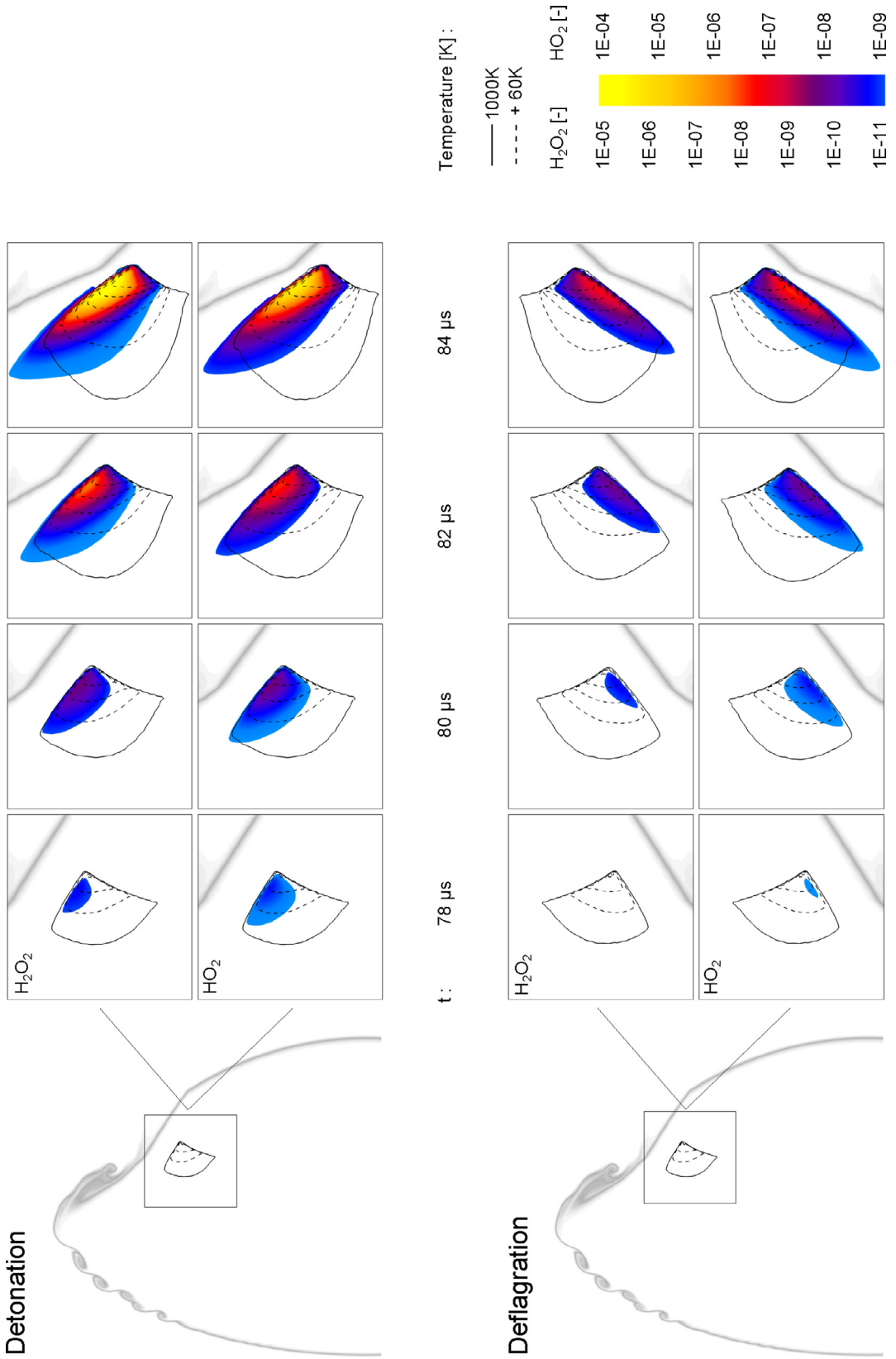

Fig. 9. Temporal evolution of H_2O_2 and HO_2 in the hot spot region, for detonation ($p_{2_0} = 0.50$ atm) and deflagration ($p_{1_0} = 0.25$ atm). Hot spots are localized by temperature isocontours, starting at T = 1000 K.

4.3. Pressure dependency of the reaction wave type

As observed in Fig. 6, an initial pressure of $p_0 \gtrsim p_{2_0} = 0.5$ atm leads to detonation of the gas mixture for a shock Mach number of $Ma = 2.30$, whereas lower initial pressures $p_0 \lesssim p_{1_0} = 0.25$ atm lead to a deflagration reaction wave after a slightly larger ignition delay time. The occurrence of either a detonation or a deflagration reaction wave can be explained by the pressure sensitivity of the H_2-O_2 reaction kinetics. At identical temperatures in the shock focusing point the pressure difference triggers different reaction waves.

The H_2-O_2 reaction is initiated by the formation of H radicals

$$H_2 \longrightarrow H + H, \tag{R.1}$$

which drive the subsequent chemical reactions. The post-shock pressure is crucial for the following branching:

$$H + O_2 + M \longrightarrow HO_2 + M, \tag{R.2}$$

$$H + O_2 \longrightarrow O + OH. \tag{R.3}$$

The ternary collision in reaction (R.2) is proportional to the square of the pressure, the binary collision in reaction (R.3) is only linearly proportional. At lower pressure the chain branching reaction (R.3) dominates, opening the branch that leads to deflagration, including a high concentration of H, O and OH radicals. An increase of the pressure raises the reaction rate of the ternary chain-breaking reaction (R.2). The chain reaction is stopped by the destruction of H into HO_2. In the pressure range between the second and third explosion limit HO_2 is inactive, but becomes active as the third explosion limit is crossed [14]. HO_2 collides with H_2, forming either H_2O or H_2O_2 as an intermediate product that breaks down into OH:

$$HO_2 + H_2 \longrightarrow H_2O + OH, \tag{R.4}$$

$$HO_2 + H_2 \longrightarrow H_2O_2 + H, \tag{R.5}$$

$$H_2O_2 + M \longrightarrow OH + OH + M. \tag{R.6}$$

OH radicals continue the reaction chain by

$$OH + H_2 \longrightarrow H_2O + H. \tag{R.7}$$

The produced chain-carrying radicals accumulate due to insufficient mixing with the surrounding gas. This leads to a further increase of the reaction rate, and finally to chain branching explosion [57]. The detonation above the third explosion limit is characterized by a significant formation of HO_2 and H_2O_2 even before the mixture ignites.

Figures 9 and 10 show the gas composition for detonation and deflagration in RSBI. Figure 9 shows the temporal evolution of HO_2 and H_2O_2 in the hot-spot regions of the bubble gas for both types of ignition. The temperature isocontours are identical during the induction time. However the higher initial pressure leads to a higher formation of HO_2 and H_2O_2 resulting in a detonation of the H_2-O_2 gas mixture.

Figure 10 shows the temporal evolution of the maximum of the five intermediate products. Detonation is accompanied by a higher production of HO_2 and H_2O_2 and a lower formation of H, O and OH radicals. The chain-carrying radicals accumulate until the gas mixture ignites. The influence of the reaction wave type on the global bubble dynamics is determined in the following sections, starting with the Damköhler number.

4.4. Damköhler number

The Damköhler number defines the ratio of the hydrodynamic and chemical reaction time scales

$$Da = \frac{\tau_h}{\tau_r}. \tag{30}$$

$Da < 1$ characterizes a flow field that is dominated by hydrodynamic effects, $Da > 1$ implies a high influence of the chemical reaction on the flow dynamics. We define the two time scales as follows:

$$\tau_h = \frac{1}{|\overline{\omega}|}, \quad \tau_r = \tau_{ign} + \frac{D_0}{V_{RW}}. \tag{31}$$

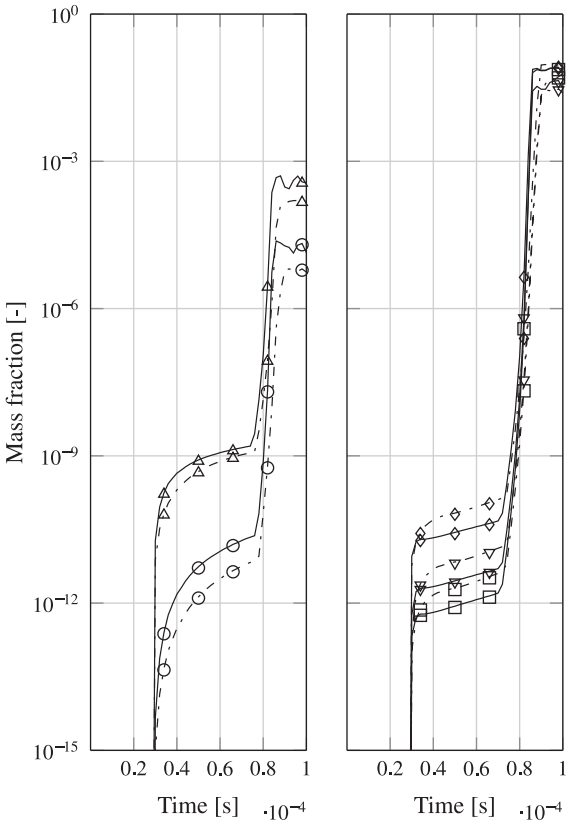

Fig. 10. Maximum of the intermediate products: △ = HO_2, ○ = H_2O_2, □ = OH, ▽ = O, ◇ = H, solid lines: detonation ($p_{2_0} = 0.50$ atm), chain-dotted lines: deflagration ($p_{1_0} = 0.25$ atm).

The characteristic hydrodynamic time scale τ_h is defined by the vorticity, averaged from the first contact of the shock wave with the bubble until the reaction wave has propagated through the bubble. The chemical reaction time scale τ_r consists of two time intervals: τ_{ign} is the period from the first contact of the shock with the bubble until ignition. $D_0/(2V_{RW})$ is the time that it takes for the reaction wave to propagate through half of the initial bubble shape with D_0 as the initial bubble diameter. For detonation the propagation velocity of the reaction wave is determined directly from the simulation. We note that the reaction wave propagates with the typical velocity of a quasi-detonation and much slower than a self-sustaining Chapman–Jouguet detonation. The propagation velocity of the deflagration wave is sensitive to temperature and pressure. This sensitivity is considered by a power law expression introduced by Dehoe [58]

$$V_{RW} = S_{L_0}\left(\frac{T}{T_0}\right)^{\beta_1}\left(\frac{p}{p_0}\right)^{\beta_2}, \tag{32}$$

where S_{L_0} denotes the laminar burning velocity at reference conditions (T_0 and p_0), measured several times and available in the recent literature [58]. The temperature T and the pressure p are taken from the hot spot point shortly before ignition. The parameters β_1 and β_2 are determined by Iijima and Takeno [59] as

$$\begin{aligned}\beta_1 &= 1.54 + 0.026(\Phi - 1),\\ \beta_2 &= 0.43 + 0.003(\Phi - 1).\end{aligned} \tag{33}$$

Dealing with a stoichiometric mixture ($\Phi = 1$) we simplify β_1 and β_2 to $\beta_1 = 1.54$ and $\beta_2 = 0.43$. The Damköhler numbers for the different initial pressures of the RSBI are listed in Table 2.

For the subsonic deflagration wave induced at a low initial pressure of $p_{1_0} = 0.25$ atm we find $Da = 0.4428$. The characteristic time scale of the chemical reaction kinetics τ_r is larger than the hydrodynamic time scale τ_h. Consequently, the flow field is dominated by

Table 2
Damköhler numbers and characteristic time scales for different initial pressures.

p_{x_0} [atm]	τ_h [s]	τ_r [s]	Da [−]
0.25	$0.62893 \cdot 10^{-3}$	$1.42031 \cdot 10^{-3}$	0.4428
0.50	$0.10753 \cdot 10^{-3}$	$0.08278 \cdot 10^{-3}$	1.2990
0.75	$0.11198 \cdot 10^{-3}$	$0.08185 \cdot 10^{-3}$	1.3681
1.00	$0.11111 \cdot 10^{-3}$	$0.08030 \cdot 10^{-3}$	1.3836

hydrodynamic effects. Instabilities at the interface and in the primary vortex regions evolve essentially unaffected from the propagating deflagration wave, as visualized in Fig. 6.

An increase of the initial pressure changes the reaction wave type to a supersonic detonation wave. Due to the fast propagation velocity, the chemical reaction time scale decreases distinctly and becomes smaller than the hydrodynamic time scale. Thus the chemical reaction plays a crucial role for the overall bubble dynamics. This is reflected by an increase of the Damköhler number to $Da = 1.2990$. A further increase of the initial pressure up to $p_{3_0} = 0.75$ atm reduces the induction time slightly by about 2 μs, leading to a Damköhler number of $Da = 1.3681$. For a better classification of the results an additional simulation with $p_{4_0} = 1.00$ atm was performed, again leading to a 2 μs shorter induction time and a higher Damköhler number of $Da = 1.3836$. The similarity of the Damköhler numbers for an initial pressure $p_{x_0} \geq 0.50$ atm indicates that once a critical initial pressure is exceeded the dominant chemical reaction time scale is independent of a further pressure increase. The following analysis of integral quantities supports this observation.

4.5. Enstrophy generation

Baroclinic vorticity production, $(\nabla\rho \times \nabla p)/\rho^2$, sets in when the shock wave reaches the upstream pole of the bubble. If the gas mixture detonates the supersonic reaction wave drives a second shock wave that induces additional vorticity. The enstrophy ε_ρ is used to determine the influence of the different reaction waves on the vorticity production

$$\varepsilon_\rho = \frac{1}{\rho_0}\varepsilon = \frac{1}{\rho_0}\int_S \rho\omega^2 dxdy. \tag{34}$$

As the simulations are initiated with different initial pressures and thus different initial densities, the enstrophy is normalized by the respective initial density ρ_0. Figure 11 shows the temporal evolution of the enstrophy for the simulations of RSBI and their non-reacting counterparts. Vorticity production starts with the first contact of the shock wave with the bubble at $t = 30$ μs and increases during the shock passage. The evolution is identical for the reacting and non-reacting simulations until ignition occurs. Subsequently ($t \approx 86$ μs) the detonation wave induces additional vorticity. The enstrophy peak caused by the detonation of the gas mixture is clearly visible in Fig. 11 and leads to elevated enstrophy levels for about 50 μs. In the long-term evolution the non-reacting SBIs show higher enstrophy levels than the reacting simulations, because of a higher density and pressure gradient in the main vortex region. The deflagration wave has only a small influence on the enstrophy. After the reaction wave has covered a significant fraction of the interface, however the vorticity decays faster compared to the inert counterpart. Again the reason can be found in the decrease of density across the reaction front.

4.6. Suppression of secondary instabilities and mixing

RMI and KHI induce a complex flow field with local hot spots of high mixing. Tomkins et al. [60] observed three main regions of mixing: the vortex core, the outer interface including KHI, and the bridge region, connecting the two main vortices. The latter contributes up to 40% to the mixing. The definition of the molecular mixing fraction (MMF) of Youngs [61]

$$\Theta(t) = \frac{\int_{-\infty}^{\infty} \langle X_{N_2} X_{Xe}\rangle dx}{\int_{-\infty}^{\infty} \langle X_{N_2}\rangle \langle X_{Xe}\rangle dx} \tag{35}$$

is used to estimate the impact of the reaction wave on the mixing. It can be interpreted as the ratio of molecular mixing to large-scale entrainment by convective motion. The temporal evolution of $\Theta(t)$ for the reacting simulations and the non-reacting counterparts is plotted in Fig. 12. The inert simulations show a linear growth over time, irrespective of the initial pressure. The reacting counterpart shows a different behavior. The low pressure simulation diverges only slightly from the inert cases. The mixing in the vortex core region and the outer interface is gradually affected by the deflagration wave. The stretching of the bubble gas around the vortex cores and the interfacial area is less developed, which reduces the mixing. Due to the low propagation velocity of the reaction wave the bridge region at the upstream pole of the bubble, as the main mixing region, is unaffected by the chemical reaction process, reducing the mixing only up to 20%. At higher initial pressure, leading to a detonation wave, we observe

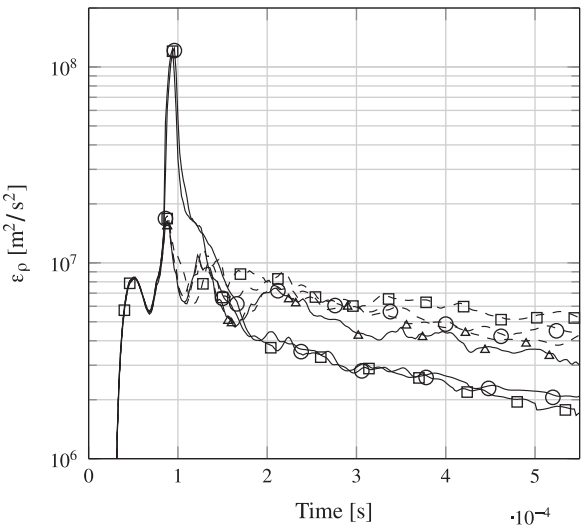

Fig. 11. Enstrophy normalized by the respective initial density. Solid lines: reaction; Dashed lines: no reaction; △ $p_{1_0} = 0.25$ atm, ○ $p_{2_0} = 0.50$ atm, □ $p_{3_0} = 0.75$ atm.

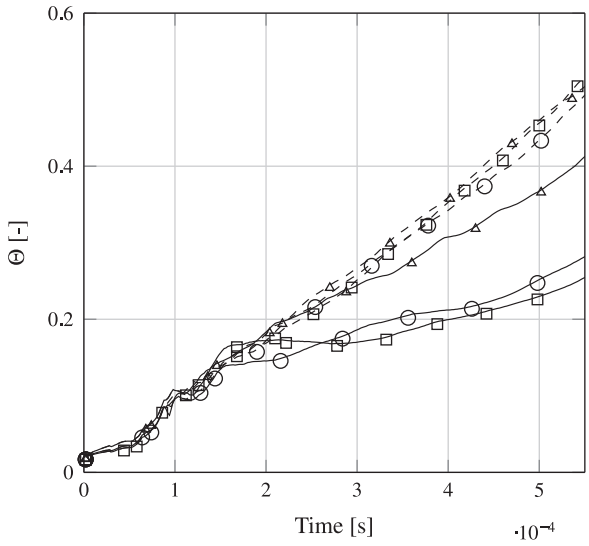

Fig. 12. Molecular mixing fraction. Solid lines: reaction; Dashed lines: no reaction; △ $p_{1_0} = 0.25$ atm, ○ $p_{2_0} = 0.50$ atm, □ $p_{3_0} = 0.75$ atm.

a strong effect of chemical reaction on the MMF. Besides the reduction of the mixing in the vortex core region and at the interface, the bridge region is also highly affected by the reaction wave. The connection of the two main vortices vanishes eventually. Thus the MMF of the high pressure simulations is reduced by up to 50% within the simulations timeframe, see Fig. 12. Again the increase in the initial pressure is only important to obtain detonation. Once the reaction wave propagates with supersonic speed, a further pressure increase shows no significant effect on the MMF. In general MMF is reduced by chemical reaction. In particular the supersonic combustion decreases the mixing distinctly.

5. Conclusion

We have presented results to our knowledge for the first successful numerical simulations of reacting shock-bubble interaction (RSBI) with detailed H_2-O_2 chemical reaction kinetics. We have considered a bubble filled with a stoichiometric gas mixture of H_2, O_2 and Xe, surrounded by pure N_2. A planar shock wave propagates through the domain and interacts with the spherical density inhomogeneity, which leads to Richtmyer–Meshkov instability (RMI). Shock focusing leads to an ignition of the bubble gas. We were able to show that pressure sensitivity of the H_2-O_2 reaction can be used to control the reaction wave type through variation of the initial pressure. A deflagration or a detonation wave can be triggered, which highly affects the efficiency of the mixing process in a RSBI. In a low pressure environment the production of H, O, OH radicals dominates, leading to a subsonic deflagration wave. Higher initial pressures lead to a chemical reaction driven by HO_2 and H_2O_2 resulting in a supersonic detonation wave.

The spatial and temporal evolution of the reacting shock-bubble interaction are strongly affected by the reaction wave type. A subsonic deflagration wave leads to a flow field that is dominated by hydrodynamic effects ($Da \approx 0.44$), and thus the influence of the reaction wave on the global bubble evolution is minor. Secondary instabilities evolve unaffected by the subsonic reaction wave. Hence, mixing decreases by about 20% within the timeframe of the simulation, mainly in the primary vortex core regions. The second reaction wave type, the detonation wave, leads to a flow field that is dominated by chemical reaction time scales ($Da \gtrsim 1.30$). The bubble gas expands quickly due to the supersonic propagation velocity of the reaction wave. Enstrophy production increases distinctly and decays faster. The growth of secondary instabilities is suppressed, and the mixing regions are strongly affected by the chemical reaction. The molecular mixing fraction reduces by up to 50% with respect to the inert case.

Acknowledgment

The authors gratefully acknowledge the Gauss Centre for Supercomputing e.V. (www.gauss-centre.eu) for funding this project by providing computing time on the GCS Supercomputer SuperMUC at Leibniz Supercomputing Centre (LRZ, www.lrz.de).

Supplementary material

Supplementary material associated with this article can be found, in the online version, at 10.1016/j.combustflame.2015.10.016

References

[1] J. Yang, T. Kubota, E.E. Zukoski, Applications of shock-induced mixing to supersonic combustion, AIAA J. 31 (1993) 854–862.
[2] F. Marble, E. Zukoski, J. Jacobs, G. Hendricks, I. Waitz, Shock enhancement and control of hypersonic mixing and combustion, Proceedings of AIAA 26th Joint Propulsion Conference, Orlando, 1990.
[3] R.D. Richtmyer, Taylor instability in shock acceleration of compressible fluids, Commun. Pure Appl. Math. 13 (2) (1960) 297–319.
[4] E.E. Meshkov, Instability of the interface of two gases accelerated by a shock wave, Fluid Dyn. 4 (5) (1969) 101–104.
[5] L. Rayleigh, Investigation of the character of the equilibrium of an incompressible heavy fluid of variable density, Proc. Lond. Math. Soc. 14 (1883) 170–177.
[6] G. Taylor, The instability of liquid surfaces when accelerated in a direction perpendicular to their planes. Part 1. Waves on fluid sheets, Proc. R. Soc. Lond. A Math., Phys. Sci. 201 (1950) 192–196.
[7] M. Brouillette, The Richtmyer-Meshkov Instability, Annu. Rev. Fluid Mech. 34 (2002) 445–468.
[8] N.J. Zabusky, Vortex paradigm for accelerated inhomogeneous flows: visiometrics for the Rayleigh-Taylor and Richtmyer-Meshkov environments, Annu. Rev. Fluid Mech. 31 (1999) 495–536.
[9] W.D. Arnett, The role of mixing in astrophysics, Ap. J. Suppl. 127 (2000) 213–217.
[10] A.M. Khokhlov, E.S. Oran, G.O. Thomas, Numerical simulation of deflagration-to-detonation transition: the role of shock-flame interactions in turbulent flames, Combust. Flame 117 (1-2) (1999) 323–339.
[11] Y. Aglitskiy, A.L. Velikovich, M. Karasik, N. Metzler, S.T. Zalesak, A.J. Schmitt, L. Phillips, J.H. Gardner, V. Serlin, J.L. Weaver, S.P. Obenschain, Basic hydrodynamics of Richtmyer-Meshkov-type growth and oscillations in the inertial confinement fusion-relevant conditions, Phil. Trans. R. Soc. A: Math., Phys. Eng. Sci. 368 (1916) (2010) 1739–1768.
[12] M. Liberman, Introduction to physics and chemistry of combustion: Explosion, flame, Detonation, Springer, 2008.
[13] W. Fickett, W.C. Davis, Detonation: theory and experiment, Detonation: Theory and Experiment, Dover Publications, 2010.
[14] O. Oldenberg, H.S. Sommers, The thermal reaction between hydrogen and oxygen III. The temperature coefficient of the steady thermal reaction, J. Chem. Phys. 9 (5) (1941) 432–438.
[15] X. Wang, K.L. Chung, An analysis of the explosion limits of hydrogen-oxygen mixtures, J. Chem. Phys. 138 (13) (2013) 134305.
[16] J.-F. Haas, B. Sturtevant, Interaction of weak shock waves with cylindrical and spherical gas inhomogeneities, J. Fluid Mech. 181 (1987) 41–76.
[17] J.J. Quirk, S. Karni, On the dynamics of a shock-bubble interaction, J. Fluid Mech. 318 (1996) 129–163.
[18] D. Ranjan, J. Oakley, R. Bonazza, Shock-Bubble interactions, Annu. Rev. Fluid Mech. 43 (1) (2011) 117–140.
[19] N. Haehn, D. Ranjan, C. Weber, J. Oakley, D. Rothamer, R. Bonazza, Reacting shock bubble interaction, Combust. Flame 159 (3) (2012) 1339–1350.
[20] E. Oran, V. Gamezo, Origins of the deflagration-to-detonation transition in gas-phase combustion, Combust. Flame 148 (2007) 4–47.
[21] J.G. Ogilvie, The hydrogen-oxygen second explosion limit. A physical chemistry experiment, J. Chem. Educ. 48 (5) (1971) 342–344.
[22] B.E. Poling, J.M. Prausnitz, J.P. O'Connell, The properties of gases and liquids, McGraw-Hill, 2001.
[23] P.D. Neufeld, A.R. Janzen, R.A. Aziz, Empirical equations to calculate 16 of the transport collision integrals $\Omega^{(l,s)*}$ for the Lennard-Jones (12-6) potential, J. Chem. Phys. 57 (3) (1972) 1100–1102.
[24] A.W. Cook, Enthalpy diffusion in multicomponent flows, Phys. Fluids 21 (2009) 055109.
[25] T. Poinsot, D. Veynante, Theoretical and Numerical Combustion, R T Edwards, 2001.
[26] G. Strang, On the construction and comparison of difference schemes, SIAM Jour. Numer. Anal. 5 (3) (1968) 506–517.
[27] P.L. Roe, Approximate Riemann solvers, parameter vectors, and difference schemes, J. Comput. Phys. 43 (1981) 357–372.
[28] B. Larouturou, L. Fezoui, On the equations of multi-component perfect or real gas inviscid flow, Lect. Notes Math. 1402 (1989) 69–98.
[29] X.Y. Hu, Q. Wang, N.A. Adams, An adaptive central-upwind weighted essentially non-oscillatory scheme, J. Comput. Phys. 229 (23) (2010) 8952–8965.
[30] S. Gottlieb, C.-W. Shu, Total variation diminishing Runge-Kutta schemes, Math. Comput. 67 (1998) 73–85.
[31] V.K. Tritschler, S. Hickel, X.Y. Hu, N.A. Adams, On the Kolmogorov inertial subrange developing from Richtmyer-Meshkov instability, Phys. Fluids 25 (2013) 071701.
[32] V.K. Tritschler, A. Avdonin, S. Hickel, X.Y. Hu, N.A. Adams, Quantification of initial-data uncertainty on a shock-accelerated gas cylinder, Phys. Fluids 26 (2014) 026101.
[33] V.K. Tritschler, B.J. Olson, S.K. Lele, S. Hickel, X.Y. Hu, N.A. Adams, On the Richtmyer-Meshkov instability evolving from a deterministic multimode planar interface, J. Fluid Mech. 755 (2014) 429–462.
[34] D.G. Goodwin, H.K. Moffat, R.L. Speth, Cantera: an object-oriented software toolkit for chemical kinetics, thermodynamics, and transport processes. 2014, Version 2.1.2. http://www.cantera.org, last access: 10/23/2015,
[35] P.N. Brown, G.D. Byrne, A.C. Hindmarsh, VODE: A variable-coefficient ODE solver, SIAM J. Sci. Stat. Comput. 10 (5) (1989) 1038–1051.
[36] E. Oran, J. Boris, Numerical simulation of reactive flow, Cambridge University Press, 2005.
[37] M. Ó. Conaire, H.J. Curran, J.M. Simmie, W.J. Pitz, C.K. Westbrook, A comprehensive modeling study of Hydrogen oxidation, Int. J. Chem. Kinet. 36 (2004) 603–622.
[38] P.J.M. Ferrer, R. Buttay, G. Lehnasch, A. Mura, A detailed verification procedure for compressible reactive multicomponent Navier-Stokes solvers, Comput. Fluids 89 (2014) 88–110.
[39] O.P. Korobeinichev, T.A. Bol'shova, Applicability of Zel'dovich's theory of chain propagation of flames to combustion of hydrogen-oxygen mixtures, Combust., Explos., and Shock Waves 45 (5) (2009) 507–510.
[40] N. Haehn, Experimental investigation of the reactive shock-bubble interaction, University of Wisconsin-Madison, 2012 Ph.D. thesis.

[41] E. Petersen, D. Davidson, M. Röhrig, R. Hanson, Shock-induced ignition of high-pressure H_2-O_2-Ar and CH_4-O_2-Ar mixtures, Proceedings of 31st Joint Propulsion Conference and Exhibit, 1995.
[42] C.J. Jachimowski, An analytical study of the hydrogen-air reaction mechanism with application to scramjet combustion, Technical Report, Langley Research Center, 1988.
[43] S. Bane, J. Ziegler, J. Shepherd, Development of one-step chemistry models for flame and ignition simulation, Technical Report, FM97-3, Graduate Aeronautical Laboratories, Caltech, 2010.
[44] J. Troe, Predictive possibilities of unimolecular rate theory, J. Phys. Chem. 83 (1) (1979) 114–126.
[45] S. Adachi, K. Hayashi, Y. Morii, N. Tsuboi, E. Yamada, Effects of chemical reaction model on H_2/O_2 detonation at high pressures, Proceedings of the 47th AIAA Aerospace Sciences Meeting Including The New Horizons Forum and Aerospace Exposition, Orlando, 2009.
[46] J. Ströhle, T. Myhrvold, An evaluation of detailed reaction mechanisms for hydrogen combustion under gas turbine conditions, Int. J. Hydrogen. Energy 32 (1) (2007) 125–135.
[47] G.P. Smith, D.M. Golden, M. Frenklach, N.W. Moriarty, B. Eiteneer, M. Goldenberg, C.T. Bowman, R.K. Hanson, S. Song, W.C. Gardiner, V.V. Lissianski, Z. Qin, GRI-Mech 3.0, 2014. http://combustion.berkeley.edu/gri-mech/, last access: 10/23/2015.
[48] T. Weydahl, M. Poyyapakkam, M. Seljeskog, N. Haugen, Assessment of existing H_2/O_2 chemical reaction mechanisms at reheat gas turbine conditions, Int. J. Hydrogen Energy 36 (18) (2011) 12025–12034.
[49] M.I. Radulescu, G.J. Sharpe, C.K. Law, J.H.S. Lee, The hydrodynamic structure of unstable cellular detonations, J. Fluid Mech. 580 (2007) 31–81.
[50] K. Mazaheri, Y. Mahmoudi, M.I. Radulescu, Diffusion and hydrodynamic instabilities in gaseous detonations, Combust. Flame 156 (6) (2012) 2138–2154.
[51] V. Di Sarli, A. Di Benedetto, G. Russo, Large eddy simulation of transient premixed flame-vortex interactions in gas explosions, Chem. Eng. Sc. 71 (2012) 539–551.
[52] X.L. Li, Q. Zhang, A comparative numerical study of the Richtmyer-Meshkov instability with nonlinear analysis in two and three dimensions, Phys. Fluids 9 (10) (1997) 3069–3077.
[53] X. Wang, T. Si, X. Luo, J. Yang, Generation of Air/SF6 interface with minimum surface feature by soap film technique, 29th International Symposium Shock Waves 2, Springer International Publishing, 2015, pp. 1065–1070.
[54] B. Hejazialhosseini, D. Rossinelli, P. Koumoutsakos, Vortex dynamics in 3D shock-bubble interaction, Phys. Fluids 25 (2013) 110816.
[55] P.A. Davidson, Turbulence : An introduction for scientists and engineers, Oxford University Press, 2004.
[56] A.R. Miles, B. Blue, M.J. Edwards, J.A. Greenough, J.F. Hansen, H.F. Robey, R.P. Drake, C. Kuranz, D.R. Leibrandt, Transition to turbulence and effect of initial conditions on three-dimensional compressible mixing in planar blast-wave-driven systems, Phys. Plasmas 12 (5) (2005) 056317.
[57] D.P. Mishra, Fundamentals of Combustion, PHI Learning Private Limited, 2013.
[58] A.E. Dahoe, Laminar burning velocities of hydrogen-air mixtures from closed vessel gas explosions, J. Loss Prev. Process Ind. 18 (3) (2005) 152–166.
[59] T. Iijima, T. Takeno, Effects of temperature and pressure on burning velocity, Combust. Flame 65 (1) (1986) 35–43.
[60] C. Tomkins, S. Kumar, G. Orlicz, K. Prestridge, An experimental investigation of mixing mechanisms in shock-accelerated flow, J. Fluid Mech. 611 (2008) 131–150.
[61] D.L. Youngs, Numerical simulation of mixing by Rayleigh-Taylor and Richtmyer-Meshkov instabilities, Laser Part. Beams 12 (1994) 725–750.

B.2. Shock Mach number influence on reaction wave types and mixing in reactive shock-bubble interaction

Combustion and Flame 174 (2016) 85–99

Contents lists available at ScienceDirect

Combustion and Flame

journal homepage: www.elsevier.com/locate/combustflame

Shock Mach number influence on reaction wave types and mixing in reactive shock–bubble interaction

Felix Diegelmann[a,*], Stefan Hickel[a,b], Nikolaus A. Adams[a]

[a] Institute of Aerodynamics and Fluid Mechanics, Technische Universität München, Garching 85748, Germany
[b] Faculty of Aerospace Engineering, TU Delft, 2629 HS Delft, Netherlands

ARTICLE INFO

Article history:
Received 4 March 2016
Revised 3 August 2016
Accepted 13 September 2016

Keywords:
Shock wave
Richtmyer–Meshkov instability
Shock-bubble interaction
Detonation
Deflagration

ABSTRACT

We present numerical simulations for a reactive shock–bubble interaction with detailed chemistry. The convex shape of the bubble leads to shock focusing, which generates spots of high pressure and temperature. Pressure and temperature levels are sufficient to ignite the stoichiometric H_2–O_2 gas mixture. Shock Mach numbers between $Ma = 2.13$ and $Ma = 2.90$ induce different reaction wave types (deflagration and detonation). Depending on the shock Mach number low-pressure reactions or high-pressure chemistry are prevalent. A deflagration wave is observed for the lowest shock Mach number. Shock Mach numbers of $Ma = 2.30$ or higher ignite the gas mixture after a short induction time, followed by a detonation wave. An intermediate shock strength of $Ma = 2.19$ induces deflagration that transitions into a detonation wave. Richtmyer–Meshkov and Kelvin–Helmholtz instability evolutions exhibit a high sensitivity to the reaction wave type, which in turn has distinct effects on the spatial and temporal evolution of the gas bubble. We observe a significant reduction in mixing for both reaction wave types, wherein detonation shows the strongest effect. Furthermore, we observe a very good agreement with experimental observations.

1. Introduction

The interaction between high-speed reactive flows and shock waves is a generic situation present in many combustion systems. Controlled application can promote mixing; uncontrolled interactions, however, can lead to undesirable heat release and thermomechanical loads. Especially in supersonic combustion, where the rapid and efficient mixing of fuel and oxidizer is crucial, as the residence time of the fuel–oxidizer mixture in the combustion chamber is only a few milliseconds [1], mixing can be enhanced sufficiently by shock-induced instabilities. The selected generic configuration of reacting shock–bubble interaction (RSBI) is representative for a large range of hydrodynamic instabilities and different reaction wave types occurring in application, and allows us to study the interaction between different effects in detail.

1.1. Hydrodynamic instabilities

Two hydrodynamic instabilities dominate in a RSBI: the Richtmyer–Meshkov instability (RMI) and the Kelvin–Helmholtz instability (KHI). RMI can enhance mixing in high-speed reactive flows, promote turbulent mixing and thus increase the burning efficiency of supersonic combustion engines [2]. The instability occurs at the interface between two fluids of different densities. Theoretically stated in 1960 by Richtmyer [3] and experimentally verified by Meshkov [4] in 1969, RMI can be considered as the impulsive limit of the Rayleigh–Taylor instability [5,6]. The misalignment of pressure gradient, ∇p, associated with a shock wave and density gradient, $\nabla \rho$, at the material interface causes baroclinic vorticity production at the interface. For comprehensive reviews the reader is referred to Brouillette [7] and Zabusky [8]. RMI occurs on a wide range of highly reactive environments from extremely large scales in astrophysics [9], to intermediate scales in combustion [1,10] and down to very small scales in inertial confinement fusion [11].

RMI induces velocity shear and small perturbations at the interface of the bubble, which are necessary preconditions for KHI [12]. The perturbations are amplified, eventually generating vortices at the interface accompanied by the appearance of smaller scales [7]. KHI drives the breakup of large-scale structures [13] and forces mixing [14]. Both effects are the main hydrodynamic drivers in RSBI.

1.2. Shock-induced ignition and reaction waves

Independently of the scale, RMI is accompanied by a second phenomenon in reactive gas mixtures: the shock-induced variation

* Corresponding author.
E-mail addresses: felix.diegelmann@aer.mw.tum.de, felix.diegelmann@gmail.com (F. Diegelmann).

http://dx.doi.org/10.1016/j.combustflame.2016.09.014

of thermodynamic properties, which can lead to ignition, followed by a reaction wave. Two reaction wave types can be distinguished: deflagration and detonation. Deflagration is a subsonic diffusion-driven reaction wave that propagates through the gas mixture due to direct transfer of chemical energy from burning to unburned gas [15]. Detonation is driven by a fast chemical reaction and the associated large heat release within the reaction wave. A shock wave immediately precedes the detonation wave and preheats the gas mixture by compression [15]. The detonation wave propagates up to 10^8 times faster than the deflagration wave [16]. Due to the large differences in the characteristic reaction time scales, the reaction wave type has a crucial influence on the flow evolution.

Under certain circumstances a deflagration wave can transform into a detonation wave. Deflagration-to-detonation transition (DDT) is one of the most interesting unresolved problems in combustion theory. Generally, a self-propagating deflagration wave is unstable and tends to accelerate. Under specific conditions the continuous acceleration can suddenly transition into a detonation wave [17]. Liberman et al. [18] proposed a mechanism mainly driven by flame acceleration divided into three stages. The reaction front accelerates and produces shock waves far ahead of the flame. Thereafter, the acceleration decreases, shocks are formed on the flame surface and pockets of compressed and heated unburnt gas emerge (preheat zone). In the final stage the transition to detonation happens: the flame propagates into the preheat zone and produces a large amplitude pressure pulse. Increasing pressure enhances reaction rates and the feedback between the pressure peak and the reaction leads to a growth of the pressure peak, which steepens into a strong shock that, coupled with the reaction zone, finally forms an overdriven detonation wave.

Furthermore, the flame front can propagate into regions of gas that already have been compressed and preheated by preceding shock waves such as in shock–bubble interactions (SBI). The reaction rates and the heat release are enhanced in these regions, which in turn increases the pressure pulse and accelerates the transition to detonation. In general, DDT can occur in two regions: it develops from the preheated, compressed gas mixture between the leading shock wave and the flame or it arises from within the flame [19]. The latter transition process is relevant for the presented study as RSBI contains regions of irregular compression by the initial shock wave.

1.3. Reacting shock–bubble interaction

The impact of a shock wave on a reactive gas bubble allows to investigate the interaction between shock-induced hydrodynamic instabilities and ignition. The shock wave triggers RMI and the pressure and temperature increase leads to the formation of radicals, which accumulate until the gas mixture ignites. RMI, due to the misalignment of the pressure and density gradient at the bubble interface, causes the bubble to evolve into a vortex ring. Provided that the initial kinetic-energy input is sufficient, the flow develops a turbulent mixing zone through non-linear interactions of the material interface perturbations [7,8]. Upon contact, the incident shock wave is partially reflected and partially transmitted. For an Atwood number $A = (\rho_1 - \rho_2)/(\rho_1 + \rho_2) < 0$ (the bubble gas is lighter than the ambient gas), the transmitted shock wave propagates faster than the incident shock wave. $A > 0$ shows the converse effect, the transmitted shock wave travels slower than the incident shock wave outside of the bubble. The transmitted shock wave focuses at the downstream pole of the bubble and collapses into a single point (shock-focusing point).

Classical inert SBI was the subject of several studies over the last decades. Haas and Sturtevant [20] investigated the interaction of shock waves propagating in air with a gas bubble filled with either helium or *R*-22. Their experimental results contributed to a better understanding of the temporal bubble evolution under shock acceleration and established a new class of canonical flow configurations. These experimental findings were completed by the investigations of Quirk and Karni [21], providing detailed numerical results of shock–bubble interaction problems. They reproduced the transition from regular to irregular refraction, shock wave focusing and the formation of a jet towards the center of the bubble. For a detailed review of SBI see Ranjan et al. [22].

A new level of complexity can be added to the setup of SBI by replacing the inert gas with a reactive gas mixture. A strong shock wave can ignite the reactive gas mixture directly at the interface, whereas the additional increase of pressure and temperature in the shock-focusing point is required for ignition at lower shock Mach numbers. Two types have to be differentiated: non-premixed and premixed gas mixtures. Reacting SBI of non-premixed gas mixture was studied by Billet et al. [23]. In their setup a H_2 gas bubble surrounded by air is shocked to study the influence of the volume viscosity on the bubble evolution and vorticity production. Attal et al. [24] verified the results of Billet et al. [23] and furthermore observed the formation of a double diffusion flame in the bridge region of the shocked bubble. Attal and Ramaprabhu [25] studied single-mode reacting RM in a non-premixed setup at different interface thicknesses. They observed shock-induced ignition and mixing enhancement by reshocking the propagating flame. Furthermore shock–flame interaction increases the surface area of the flame and the energy release and therefore the burning rate [26]. Massa and Jha [27] showed that small scales are damped by the shock wave and that the growth of RMI and KHI are reduced.

In 2012, Haehn et al. [28] investigated the interaction of a shock wave with a premixed gas bubble, filled with a stoichiometric gas mixture of hydrogen (H_2) and oxygen (O_2), diluted by xenon (Xe). Besides triggering hydrodynamic instabilities, such as RMI, the shock wave also increases the temperature and pressure, which in turn induces faster chemical reaction rates up to the ignition of the gas mixture. Maximum pressures and temperatures are reached when the shock passes the bubble. Subsequently, the gas mixture relaxes and the two main parameters controlling the reaction rate, temperature and pressure, decrease. The experiments of Haehn et al. [28] covered both ignition types deflagration and detonation, by varying the shock wave Mach numbers between $Ma = 1.34$ and $Ma = 2.83$.

A weak shock wave with $Ma = 1.34$ does not ignite the gas mixture within the experimental timeframe. Compression is not sufficient to start a self-sustaining chemical reaction. An increase of the shock strength results in an ignition followed by a deflagration wave. The reaction wave type changes for higher shock Mach numbers; Haehn et al. [28] observed a detonation wave for $Ma = 2.83$, even before the shock wave has reached the shock focusing point. Damköhler numbers between 0.25 ($Ma = 1.65$) and 8.00 ($Ma = 2.83$) were determined. Haehn et al. [28] conclude that heat conduction plays an important role at lower shock Mach numbers, and that the Zeldovich mechanism becomes important at higher shock Mach numbers. Their conclusion is consistent with the two limiting cases of shock-induced combustion, the strong and the weak ignition [19]. Strong ignition results in a detonation essentially initiated directly by the shock wave. Weak ignition is characterized by the appearance of small flames that can undergo transition into detonation waves. Several chemiluminescence exposures are provided by Haehn et al. [28] to depict the qualitative evolution of the bubble and reaction processes. Furthermore, quantitative data for the temporal evolution of the transverse diameter of the bubble as well as for the vortex ring diameter are presented. However, the complex experimental setup implies uncertainties. Haehn et al. [28] estimate the uncertainty of the Damköhler number at the highest shock Mach number ($Ma = 2.83$) of up to 50% ($Da = 8 \pm 4$). At the lowest shock Mach number ($Ma = 1.34$), 30%

of all measurements showed no ignition within the given experimental time frame. Hence, numerical studies of RSBI can provide more certainty and complementary insight into RSBI phenomena that cannot be achieved by purely experimental work.

1.4. Scope of the present work

The present numerical study complements the work of Haehn et al. [28] and continues the first numerical approach to RSBI (Diegelmann et al. [29]). The main emphasis is placed on the general temporal and spatial evolution of RSBI, the comparison with SBI, and the dependence of the bubble evolution on the reaction wave type. In our study, the shock Mach number is varied between $Ma = 2.13$ and $Ma = 2.90$ at a constant initial pressure and temperature. Besides the limiting cases of deflagration and detonation we study two special phenomena in detail, which have not been discussed before: DDT at $Ma = 2.19$ and a double detonation at $Ma = 2.50$. Haehn et al. [28] observed an effect, which they assume is either a double detonation or a reflection of measurement signals, but the experimental measurement technique did not allow a clear identification. Our present numerical study confirms the observed physical effect and gives a deeper insight into the gas composition of the two ignition spots during the induction time. Intentionally, we focus on two-dimensional configurations as they facilitate particular analysis and phenomenological investigation. Moreover, in [29] it was shown that early stages of RSBI can be well reproduced by a two-dimensional approximation.

The chemical reaction rates of most gas mixtures increase with pressure. H_2–O_2 reactions, however, show a different behavior [30]. Some intermediate reaction rates are proportional to the square of the pressure, others are linearly proportional [31]. Hence, the variation of the shock Mach number, or more precisely the post-shock pressure, affects the chemical reaction process and determines the occurrence of either detonation or deflagration.

We structure the paper as follows: Section 2 outlines the governing equations, including molecular transport properties for multicomponent flows and chemical reaction kinetics. Section 3 describes the computational domain and the initial conditions of our setup. General results are discussed in Section 4. The spatial and temporal evolution of the RSBI are presented. The effect of different types of reaction waves on bubble deformation are compared with each other and with their non-reacting counterparts. The chemical reaction process during shock passage until ignition is analyzed in detail. A consistent definition of the dimensionless Damköhler number is used to evaluate whether hydrodynamic or chemical reaction time scales dominate the flow field. Integral quantities, such as enstrophy or the molar mixing fraction, are estimated to assess the effect of the reaction waves on mixing of the bubble gas. In Section 5, we discuss two special cases of RSBI: First the transition of a deflagration into a detonation wave and second a simulation with a simultaneous detonation at two spots. Section 6 presents a comparison to experimental results and a critical discussion. Section 7 summarizes the key findings.

2. Numerical model

2.1. Navier–Stokes equations

We solve the full set of compressible reacting multicomponent Navier–Stokes equations in conservative form

$$\frac{\partial \rho}{\partial t} + \nabla \cdot (\rho \boldsymbol{u}) = 0 \tag{1}$$

$$\frac{\partial \rho \boldsymbol{u}}{\partial t} + \nabla \cdot (\rho \boldsymbol{u}\boldsymbol{u} + p\boldsymbol{\delta} - \boldsymbol{\tau}) = 0 \tag{2}$$

$$\frac{\partial E}{\partial t} + \nabla \cdot [(E + p)\boldsymbol{u}] - \nabla \cdot (\boldsymbol{\tau} \cdot \boldsymbol{u} - \boldsymbol{q_c} - \boldsymbol{q_d}) - \dot{\omega}_T = 0 \tag{3}$$

$$\frac{\partial \rho Y_i}{\partial t} + \nabla \cdot (\rho \boldsymbol{u} Y_i) + \nabla \cdot \boldsymbol{J}_i - \dot{\omega}_i = 0 \tag{4}$$

where ρ is the mixture density and $\boldsymbol{u}$ the velocity vector. The identity matrix is given by $\boldsymbol{\delta}$, total energy by E and pressure by p. Y_i are the mass fraction of species $i = 1, 2, ..., N$, with N being the total number of species. The heat release $\dot{\omega}_T$ and species formation and destruction in terms of individual mass rates $\dot{\omega}_i$ represent the chemical reaction kinetics.

2.2. Caloric and transport properties

The viscous stress tensor $\boldsymbol{\tau}$ for a Newtonian fluid is given by

$$\boldsymbol{\tau} = 2\overline{\mu}\left[\frac{1}{2}\left(\nabla \boldsymbol{u} + (\nabla \boldsymbol{u})^T\right) - \frac{1}{3}\boldsymbol{\delta}(\nabla \cdot \boldsymbol{u})\right], \tag{5}$$

with $\overline{\mu}$ as the mixture viscosity

$$\overline{\mu} = \frac{\sum_{i=1}^{N} \mu_i Y_i / M_i^{1/2}}{\sum_{i=1}^{N} Y_i / M_i^{1/2}}. \tag{6}$$

M_i is defined as the molecular mass of each species i. The calculation of the viscosity of each species μ_i is based on the Chapman–Enskog viscosity model

$$\mu_i = 2.6693 \cdot 10^{-6} \frac{\sqrt{M_i T}}{\Omega_{\mu,i} \sigma_i^2}, \tag{7}$$

where T is the temperature and σ_i the collision diameter. The collision integral $\Omega_{\mu,i}$ [32] is defined as

$$\Omega_{\mu,i} = A(T_i^*)^B + C\exp(DT_i^*) + E\exp(FT_i^*), \tag{8}$$

with $A = 1.16145$, $B = -0.14874$, $C = 0.52487$, $D = -0.7732$, $E = 2.16178$, $F = -2.43787$ and $T_i^* = T/(\epsilon/k)_i$, using the Lennard–Jones energy parameter $(\epsilon/k)_i$ for species i. According to the Fourier law, we define the heat conduction as

$$\boldsymbol{q_c} = -\overline{\kappa}\nabla T, \tag{9}$$

with $\overline{\kappa}$ as the mixture heat conductivity, which is calculated from [33]

$$\overline{\kappa} = \frac{\sum_{i=1}^{N} \kappa_i Y_i / M_i^{1/2}}{\sum_{i=1}^{N} Y_i / M_i^{1/2}}, \tag{10}$$

κ_i is the thermal conductivity of species i. The interspecies diffusional heat flux $\boldsymbol{q_d}$ [34] is given by

$$\boldsymbol{q_d} = \sum_{i=1}^{N} h_i \boldsymbol{J}_i, \tag{11}$$

with h_i as the individual species enthalpy. The species diffusion $\boldsymbol{J}_i$ is modeled as

$$\boldsymbol{J}_i = -\rho\left(D_i \nabla Y_i - Y_i \sum_{j=1}^{N} D_j \nabla Y_j\right). \tag{12}$$

D_i describes the effective binary diffusion coefficient of species i

$$D_i = (1 - X_i)\left(\sum_{j \neq i}^{N} \frac{X_j}{D_{ij}}\right)^{-1}, \tag{13}$$

with X_i as the mole fraction of species i. Eq. (13) ensures that the interspecies diffusion fluxes balance to zero. The constitutive empirical law is used to compute the mass diffusion coefficient of a binary mixture [33]

$$D_{ij} = \frac{0.0266}{\Omega_{D,ij}} \frac{T^{3/2}}{p\sqrt{M_{ij}}\sigma_{ij}^2}, \tag{14}$$

where

$$M_{ij} = \frac{2}{\frac{1}{M_i} + \frac{1}{M_j}} \quad \text{and} \quad \sigma_{ij} = \frac{\sigma_i + \sigma_j}{2}. \tag{15}$$

The collision integral for diffusion $\Omega_{D,\,ij}$ is given by

$$\Omega_{D,ij} = A^*(T_{ij}^*)^{B^*} + C^* \exp(D^* T_{ij}^*) + E^* \exp(F^* T_{ij}^*) + G^* \exp(H^* T_{ij}^*). \tag{16}$$

The parameters are defined as $A^* = 1.06036$, $B^* = -0.1561$, $C^* = 0.19300$, $D^* = -0.47635$, $E^* = 1.03587$, $F^* = -1.52996$, $G^* = 1.76474$, $H^* = -3.89411$, and $T_{ij}^* = T/T_{\epsilon_{ij}}$. $T_{\epsilon_{ij}}$ have been obtained from the Lennard–Jones energy parameters for species i and j as

$$T_{\epsilon_{ij}} = \sqrt{\left(\frac{\epsilon}{k}\right)_i \left(\frac{\epsilon}{k}\right)_j}. \tag{17}$$

2.3. Equation of state

The equation of state for an ideal gas is used to close the equations

$$p(E, Y_i) = (\overline{\gamma} - 1)E. \tag{18}$$

$\overline{\gamma}$ represents the ratio of specific heats of the mixture

$$\overline{\gamma} = \frac{\overline{c_p}}{\overline{c_p} - \overline{R}} \tag{19}$$

with

$$\overline{c_p} = \sum_{i=1}^{N} Y_i c_{p,i}. \tag{20}$$

The specific gas constant of the mixture is defined by $\overline{R} = R/\overline{M}$, with R as the universal gas constant. $\overline{M}$ is the molar mass of the mixture

$$\overline{M} = \left[\sum_{i=1}^{N} \frac{Y_i}{M_i}\right]^{-1} = \sum_{i=1}^{N} X_i M_i. \tag{21}$$

$c_{p,\,i}$ represents the specific heat coefficient

$$c_{p,i} = \frac{\gamma_i}{\gamma_i - 1} R_i. \tag{22}$$

R_i is defined as $R_i = R/M_i$. The temperature is computed from

$$T = \frac{p}{\overline{R}\rho}. \tag{23}$$

2.4. Chemical reaction kinetics

The accurate calculation of chemical reaction kinetics is most important for the precise prediction of combustion effects, such as DDT. The review paper of Oran et al. [19] summarizes several studies about DDT, mainly operating with one-step chemical kinetics. DDT through the Zeldovich gradient mechanism was observed, arising due to the gradient of induction time within the hot spots in front of the flame, where temperature varies in the range of 600 to 800 K. A precise computation of the induction time and the corresponding heat release is therefore essential for an accurate description of DDT [18]. However, it was shown that the induction time of detailed mechanisms is larger than for one-step mechanisms [35] and also larger than the time between flame initiation and transition to detonation, which renders numerical results obtained with simple mechanisms questionable. Furthermore, important quantities of combustion such as detonation initiation and induction time in chain-branching kinetics are not correctly reproduced by one-step mechanisms [36]. Studies of Ivanov et al. [36] reveal significant differences between the temperature gradient that leads to detonation with one-step and detailed mechanisms. For the detailed mechanism a much smaller temperature gradient is sufficient to ignite detonation, which is in accordance with the behavior of real combustible mixtures [18].

Chemical reaction kinetics are expressed by the heat release $\dot{\omega}_T$ and species formation and destruction in terms of individual mass rates $\dot{\omega}_i$. The specific heat release $\dot{\omega}_T$ is defined as

$$\dot{\omega}_T = -\sum_{i=1}^{N} \Delta h_{f,i}^0 \dot{\omega}_i, \tag{24}$$

with $h_{f,i}^0$ as the heat of formation of each species i. Mass rates $\dot{\omega}_i$ for each species are estimated by

$$\dot{\omega}_i = W_i \sum_{r=1}^{N_R} \nu_{ir} \Gamma_r \left(k_{fr} \prod_{j=1}^{N} [X_j]^{\nu'_{jr}} - k_{br} \prod_{j=1}^{N} [X_j]^{\nu''_{jr}} \right), \tag{25}$$

with N_R as the number of reactions, W_i the molecular weight, Γ_r the third body efficiency of reaction r, X_j the molar concentration, and ν'_{ir} and ν''_{ir} the molar stoichiometric coefficients of the reactant and the product of reaction r. ν_{ir} is the net stoichiometric coefficient

$$\nu_{ir} = \nu''_{ir} - \nu'_{ir}. \tag{26}$$

The Arrhenius law is used to calculate the forward and backward reaction rates k_{fr} and k_{br}. The forward reaction rates are defined as

$$k_{fr} = A_{fr} T^{\beta_{fr}} exp\left(\frac{E_{fr}}{RT}\right), \tag{27}$$

where A_{fr} is the pre-exponential factor, E_{fr} is the activation energy, β_{fr} is the temperature exponent for each reaction r [37]. The backward reaction rates are calculated by using the equilibrium constants K_{cr}

$$k_{br} = \frac{k_{fr}}{K_{cr}}. \tag{28}$$

K_{cr} is given by

$$K_{cr} = \left(\frac{p^\circ}{RT}\right)^{\nu_r} exp\left(\frac{\Delta S_{r,i}^\circ}{R} - \frac{\Delta H_{r,i}^\circ}{RT}\right), \tag{29}$$

with p° as a pressure of 1 atm, ν_r as the net change in the number of species in the reaction, $\Delta S_{r,i}^\circ$ as the net change in entropy and $\Delta H_{r,i}^\circ$ as the net change in enthalpy.

Furthermore, pressure dependent and duplicated reactions are considered; for this purpose Eq. (27) is modified. Pressure dependence is taken into account by calculating two forward reaction rates k_{fr_0} and k_{fr_∞} for the high-pressure and for the low-pressure limit, respectively. A blending function composed of these high- and low-pressure Arrhenius rate parameters is applied for a smooth pressure dependence. For more details on the so-called fall-off reactions, the reader is referred to Troe [38]. Duplicated reactions are considered by extending Eq. (27) to

$$k_{fr} = \sum_{i=1}^{2} A_{fr_i} T^{\beta_{fr_i}} exp\left(\frac{E_{fr_i}}{RT}\right), \tag{30}$$

The mechanism, which provides the parameters for the Arrhenius law, is essential for the accuracy of the numerical investigation and has to be chosen carefully. As shown by the authors in a previous publication [29], available mechanisms show large discrepancies in ignition delay time and pressure sensitivity. A certain number of intermediate reactions, third body efficiencies, duplicated and pressure dependent reactions are necessary for the accurate prediction of the reaction kinetics within the wide range of pressures and temperatures considered in this study.

We have chosen the Ó Conaire [39] reaction mechanism for the reaction rate parameters of the Arrhenius law. The mechanism is valid for a wide range of pressures (0.05–87 atm) and temperatures (298–2700 K). $8+N$ species (two reactants: H_2, O_2; 5 chain-carrying intermediates: hydrogen radical (H), oxygen radical (O), hydroxyl radical (OH), hydroperoxyl radical (HO_2), hydrogen peroxid (H_2O_2); the product: hydrogen oxide (H_2O); N inert gases) and 19 intermediate reactions are considered, including duplicated and pressure dependent reactions as well as third-body efficiencies. Third-bodies absorb energy during the two-body recombination reaction and stabilize the final combination. The available modes for energy storage control the energy absorption. The third-body efficiencies of Xe are set identical to argon (Ar), which are provided by Ó Conaire [39]. As the available modes of Ar and Xe are identical, the third-body efficiencies can be assumed to be comparable. Also, the steric factor for monoatomic gases, which accounts for the geometry influence on the collision between molecules, is similar [40].

The mechanism of Ó Conaire [39] has been used widely in the recent years [41,42]. As part of a preceding validation campaign [29], the applied reaction mechanism has been compared to simpler reaction mechanisms. Accurate ignition delay times, crucial for the spatial evolution of the bubble and mixing, can only be achieved with a detailed description of chemistry by a sufficiently complex reaction mechanism.

2.5. Numerical method

The 2nd-order accurate Strang time splitting scheme [43] is used to solve the system of equations (Eq. (1–4)). The Strang splitting scheme separates the stiff terms, containing the chemical reaction kinetics ($\dot{\omega}_T$ and $\dot{\omega}_i$), from the Navier–Stokes equations. This results in a system of partial differential equations (PDE) and in a stiff system of ordinary differential equations (ODE). We use a finite-volume discretization scheme that applies a flux projection onto local characteristics for the hyperbolic part for the PDE system. The Roe matrix required for the projection is calculated for the full multi-species system [44,45]. The numerical fluxes at the cell faces are reconstructed from cell averages by the adaptive central-upwind 6th-order weighted essentially non-oscillatory (WENO-CU6) scheme [46]. The scheme uses a non-dissipative 6th-order central stencil in smooth flow regions and a non-linear convex combination of 3rd-order stencils in regions with steep gradients. Time integration is performed by the 3rd-order strongly stable Runge–Kutta scheme, developed by Gottlieb and Shu [47]. Our numerical model has been tested and validated for shock induced turbulent multi-species mixing problems at finite Reynolds numbers [13,48–50] and for shock–bubble interactions including chemistry [29]. The stiff ODE, governing the specific heat release and mass rates for each species, is separately solved by a variable-coefficient ODE solver using 5th-order backward differentiation formulas [51].

3. Computational setup

We study RSBI within a two-dimensional rectangular domain with a symmetry plane at the center axis of the bubble, see Fig. 1. Inflow boundary conditions are imposed at the left domain boundary and outflow boundary conditions at the right and upper domain boundaries. The domain size is set to 32.5 r × 10.5 r, with r as the initial bubble radius. The distance between the bubble and domain boundaries are chosen sufficiently large to avoid artifacts due to shock reflections. The Cartesian grid in the region of interest is refined by a factor of 25 compared to the coarse outer grid to reduce computational costs. A detailed grid study can be found in our previous paper. We demonstrated grid convergence by comparing four different grid resolutions, with cell sizes of Δ_{xy} = 234, 117, 59 and 29 µm in the high resolution part. The simulations are performed at a CFL-number of 0.3.

The gas bubble is filled with H_2, O_2 and Xe in a stoichiometric composition of 2/1/3.67 mass fractions and surrounded by pure Nitrogen (N_2). The bubble diameter is set to $D = 2r = 0.04$ m. The heavy inert gas Xe is used to increase the density of the bubble, leading to an Atwood number of $A = 0.476$. The gas composition of our domain and the bubble diameter are identical to the experimental setup of Haehn et al. [28]. A sharp and fully resolved interface between the bubble gas and its surrounding is defined in terms of the molar fraction of N_2

$$X_{N_2} = \frac{\tanh((\sqrt{x^2+y^2}-r)\xi)+1}{2}, \tag{31}$$

with r as the radius of the bubble and ξ as parameter for controlling steepness, which is set to ξ = 20,000. The molar fraction ($X = 1 - X_{N_2}$) inside the bubble is distributed among the three gases, ensuring the stoichiometric mixture with a relative composition of 2/1/3.67(H_2/O_2/Xe).

The shock wave is initialized on the left side of the bubble. The pre-shock state is defined by $T_0 = 350$ K and $p_0 = 0.50$ atm. The shock Mach number is varied between $Ma = 2.13$ and $Ma = 2.90$. The post-shock thermodynamics state is given by standard Rankine–Hugoniot conditions

$$\rho'_{N_2} = \rho_{N_2}\frac{(\gamma_{N_2}+1)Ma^2}{2+(\gamma_{N_2}-1)Ma^2}, \tag{32}$$

$$u'_{N_2} = Ma\, c_{N_2}\left(1-\frac{\rho_{N_2}}{\rho'_{N_2}}\right), \tag{33}$$

$$p'_{N_2} = p_0\left(1+2\frac{\gamma_{N_2}}{\gamma_{N_2}+1}(Ma^2-1)\right), \tag{34}$$

where $c_{N_2} = \sqrt{\gamma_{N_2} p_0/\rho_{N_2}}$. Variables indicating post-shock conditions are marked with a prime.

Note that the initial parameters of our setup slightly deviate from the experimental pressure and temperature. To avoid that

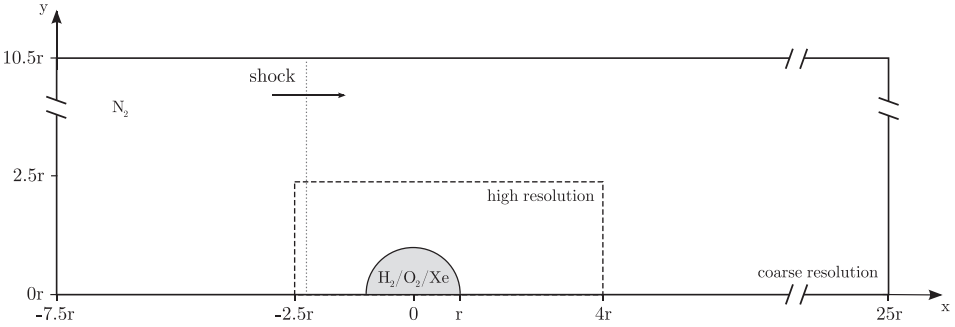

Fig. 1. Computational domain of the RSBI, $r = 0.02$ m.

the pressure peak of the detonation front is outside of the validation range of currently available reaction mechanisms for detailed H_2–O_2 reaction kinetics, we slightly decrease the initial pressure and increase the initial temperature as compared to the experiment to achieve a similar reaction behavior. We believe that it is important for further numerical investigations to operate inside the validated range of the reaction mechanism.

4. Results and discussion

The present numerical investigation of RSBI covers different reaction wave types triggered by shock Mach numbers between $Ma = 2.13$ and $Ma = 2.90$. Deflagration is induced by the lowest shock Mach number of $Ma_1 = 2.13$. Increasing shock strength leads to three different types of supersonic reaction waves: $Ma_2 = 2.19$ induces a deflagration, which transitions to a detonation. $Ma_3 = 2.30$ and $Ma_5 = 2.90$ immediately cause detonations behind the shock wave at the downstream or upstream pole of the bubble, respectively. A shock Mach number of $Ma_4 = 2.50$ leads to a nearly simultaneous double detonation in two bubble regions. Temporal and spatial bubble evolution, enstrophy production and mixing are strongly affected by the reaction wave type, which we discuss comprehensively in the following sections. The simulation with a shock Mach number of $Ma_2 = 2.19$ is excluded from the discussion, as the global bubble dynamics are nearly identical to RSBI at $Ma_3 = 2.30$. The transition process will be discussed in Section 5.1 and the double detonation at $Ma_4 = 2.50$ will be discussed in Section 5.2.

4.1. Global bubble dynamics

The qualitative influence of the chemical reaction kinetics on the temporal evolution of SBI is shown in Fig. 2. The contour plots of the temperature inside the bubble show the compression and propagation of the reaction front. The upper part of each sequence shows the reacting simulation, the lower part provides results for the non-reacting simulation at the same shock Mach number. For clarity we first compare simulations with shock Mach numbers $Ma_1 = 2.13$, $Ma_3 = 2.30$ and $Ma_5 = 2.90$.

We refer to the lower part of the first sequence of contour plots for a general description of the characteristic stages of bubble evolution. At $t = 50$ µs and $t = 86$ µs, the shock wave propagates through the bubble and compresses the gas mixture inside. Before the shock wave has passed, first instabilities on the interface start to arise ($t = 86$ µs). At $t = 120$ µs, the roll-up of the bubble has started, primary vortices form and secondary instabilities grow due to shear at the material interface. Finally at $t = 500$ µs, the bubble gas shows a high degree of mixing with the surrounding gas N_2. The two main vortices are fully developed and connected over the bridge region at the upstream pole of the bubble. Secondary vortex

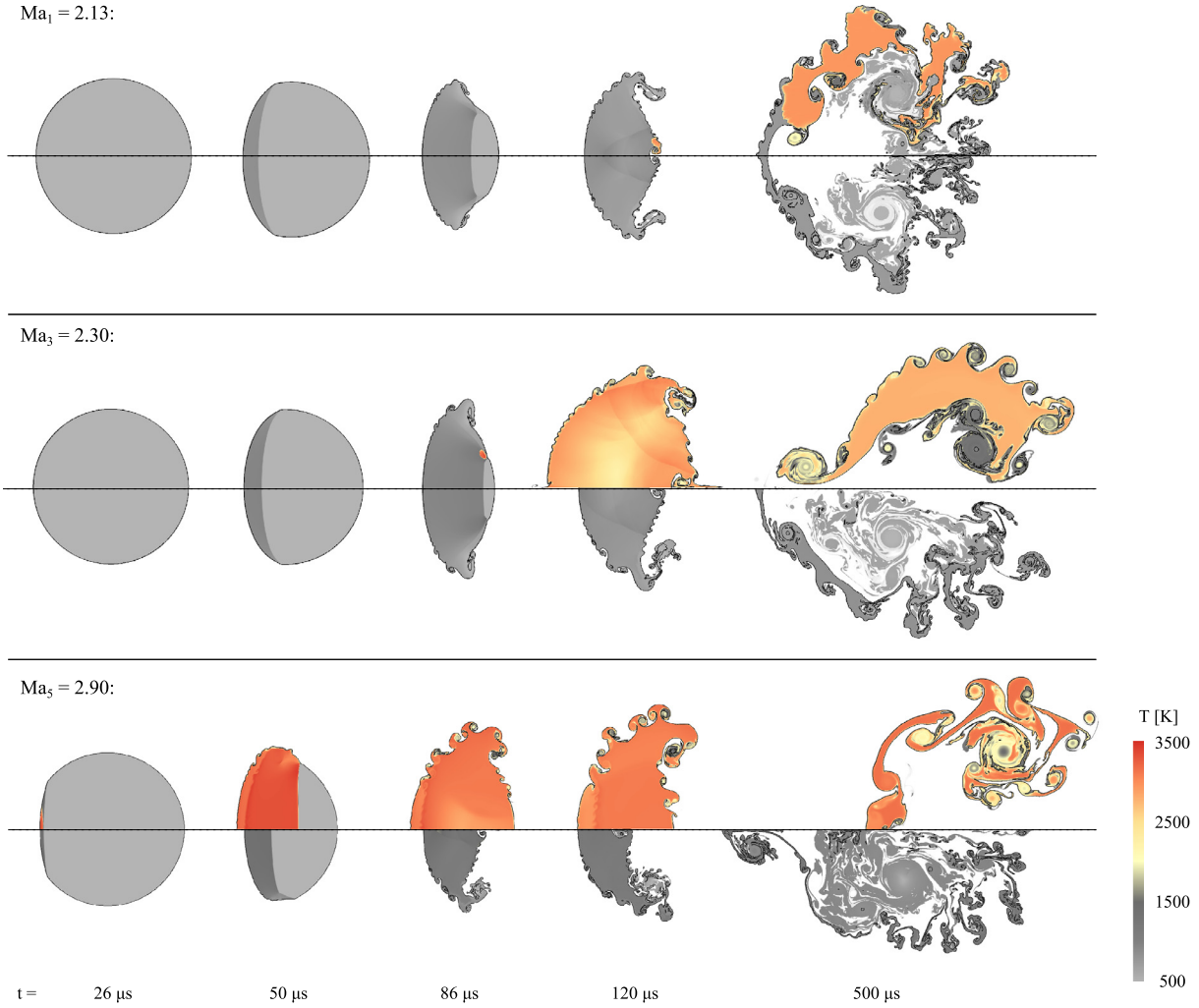

Fig. 2. Temperature contour plots of SBI: upper parts show reacting SBI, lower parts the inert counterparts. $Ma_1 = 2.13$ induces a deflagration wave, $Ma_3 = 2.30$ and $Ma_5 = 2.90$ a detonation wave.

structures are clearly visible at the outer interface. The general evolution of inert SBI and the characteristic stages are similar. The different shock strengths leads to a range of propagation velocities of the shock waves, which in turn shift the overall bubble evolution in time. Furthermore, a higher shock Mach number causes finer structures in the long-term development of the SBI.

Similarity of evolution at different shock Mach numbers cannot be observed when chemical reaction kinetics are taken into account. As the reactions are strongly pressure sensitive, the shock Mach number affects the induction time and the subsequent reaction process. The first and weakest shock wave ($Ma_1 = 2.13$) leads to deflagration. The gas mixture is ignited shortly before $t = 120\,\mu s$, as shown in the upper row of Fig. 2. The reaction front propagates slowly through the bubble gas; even at $t = 500\,\mu s$ the reaction front has not yet reached the upstream pole. Thus bubble structures of reacting and non-reacting SBI are still similar, especially the outer interfaces with evolving Kelvin–Helmholtz instabilities show the same characteristics. Merely, the overall bubble expansion increases due to isobaric heating over the reaction front.

When we increase the shock Mach number to $Ma_3 = 2.30$, the bubble dynamic changes distinctly. The reactive gas mixture ignites earlier, followed by a detonation wave, depicted in the second row of Fig. 2. The supersonic reaction wave propagates within approximately $\Delta t = 10\,\mu s$ through the bubble. Strong heat release and density decrease result in a rapid and significant bubble expansion. When the detonation wave reaches the interface of the bubble, vorticity is generated, with the opposite sign compared to the vorticity induced by the initial shock wave. As a consequence, the growth of the secondary instabilities is decelerated, which has a significant effect on mixing. The contour plots at $t = 120\,\mu s$ and $t = 500\,\mu s$ show the bubble after the reaction wave has propagated through the reactive gas mixture. Comparison with the inert counterpart reveals different growth rates and characteristics. Furthermore, the detonation wave amplifies the N_2-jet at the symmetry plane at the downstream pole of the bubble. Hence the bridge region, connecting the two main vortices, vanishes completely.

A further increase of the shock Mach number to $Ma_5 = 2.90$ shortens the induction significantly. The strong shock ignites the gas mixture directly at the upstream pole of the bubble, followed by a detonation wave. The detonation wave merges with the initial shock wave inside the bubble and subsequently propagates through the unshocked gas mixture. Comparison with the inert counterpart shows that the detonation wave propagates more than twice as fast as the initial shock wave, which significantly influences the spatial bubble evolution. Similarly to the simulation with $Ma_3 = 2.30$, some of the secondary instabilities are suppressed; however, the N_2-jet is less amplified and the bridge region is preserved even in the long-term evolution. The bubble is penetrated by a single detonation wave, whereas the lower shock Mach number of $Ma_3 = 2.30$ induces a detonation wave that propagates in upstream direction through the pre-shock gas mixture. The interface differs from the other simulations, the KHI are not aligned along the outer interface. Furthermore, the timestep at $t = 120\,\mu s$ shows secondary RMI arising from the KHI. Different evolution of primary and secondary instabilities, the bridge region, and the spatial bubble expansion have a significant effect on integral quantities, such as mixing and enstrophy production.

The vortex Reynolds number $Re_\Gamma = \Gamma_0/\nu$, defined by Glezer [52], where Γ_0 is the initial deposition of vorticity and ν the kinematic viscosity of the interface, amounts to 1.4×10^5 for $Ma = 2.13$ and increases with higher shock Mach numbers up to 2.4×10^5 ($Ma = 2.90$). The critical Reynolds number for transition from laminar to turbulent flow is 10^4 to 2×10^4 (Dimotakis [53]). All configurations exceed this mixing-transition Reynolds number by at least one order of magnitude.

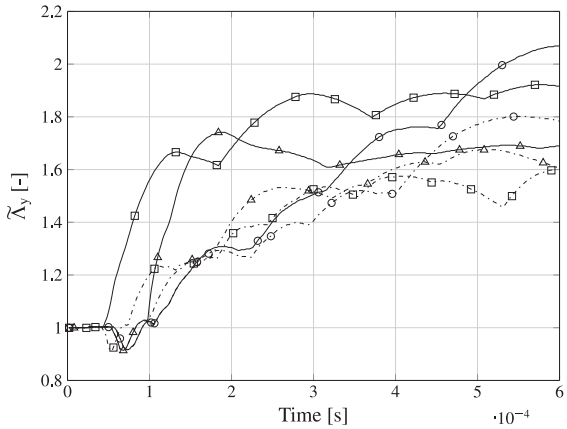

Fig. 3. Normalized transverse bubble diameter for different shock Mach numbers. — : reaction; – : no reaction; ◯ : $Ma_1 = 2.13$, △ : $Ma_3 = 2.30$, □ : $Ma_5 = 2.90$.

4.2. Transverse bubble diameter

The transverse bubble diameter $\tilde{\Lambda}_y = \Lambda_y/D_0$ normalized by the initial bubble diameter D_0 is used to measure the impact of chemical reaction processes on the large-scale evolution of the bubble. The bubble diameter Λ_y is measured based on a threshold value of the xenon mass fraction of $Y_{Xe} = 0.01$.

Figure 3 shows the temporal evolution of $\tilde{\Lambda}_y$ for the inert and the reacting simulations at three different shock Mach numbers. For the inert simulations (dashed-dotted lines) we observe a nearly linear increase in the bubble diameter. Some variation can be found in the long-term evolution: the weaker the shock strength the smaller the streamwise expansion, which leads to a slightly larger transverse bubble diameter. At the highest shock Mach number of $Ma_5 = 2.90$, the evolution levels out much earlier than for the other shock Mach numbers. Note that the roll-up of the primary vortices leads to a wave-like temporal growth of $\tilde{\Lambda}_y$. In the long-term evolution the main vortices are fully developed and the bubble gas rotates around the vortex cores, which results in a flattening of the transverse bubble diameter evolution.

The deflagration wave triggered at a shock Mach number of $Ma_1 = 2.13$ affects the normalized transverse bubble diameter only with respect to the long-term evolution. The propagation velocity of the reaction front is low compared to the evolution of the hydrodynamic instabilities. The density increase over the reaction front accompanied by a spatial expansion leads to a slight divergence from the inert counterpart after $t = 300\,\mu s$. Simulations with shock Mach numbers of $Ma_3 = 2.30$ and $Ma_5 = 2.90$ exhibit supersonic detonation waves, which have a significantly stronger effect on the normalized transverse bubble diameter. The rapid reaction leads to an instantaneous expansion of the reacted gas and a sudden increase of $\tilde{\Lambda}_y$ up to 175% of the initial bubble diameter. The detonation wave at $Ma_3 = 2.30$ propagates in upstream and orthogonal direction of the flow field. Thus, an overshoot in the transverse bubble diameter is visible at $t = 180\,\mu s$, which decreases over time to a slightly lower value. The higher shock Mach number of $Ma_5 = 2.90$ shows an earlier increase of the transverse bubble diameter and levels out at a higher value compared to the simulation with a shock Mach number of $Ma_3 = 2.30$. The higher compression leads to a higher temperature and therefore to a larger spatial expansion of the bubble gas.

4.3. Identification of the reaction wave type

To outline the different features of deflagration and detonation waves we analyze the evolution of characteristic parameters across

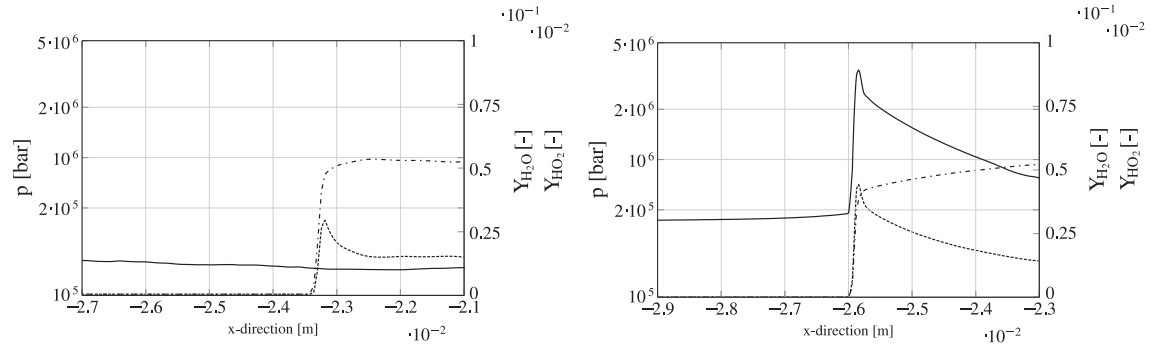

(a) $Ma_1 = 2.13$ (deflagration) (b) $Ma_3 = 2.30$ (detonation)

Fig. 4. Pressure and gas composition across the fully developed reaction wave front. — : pressure; – : Y_{H_2O}; — : Y_{HO_2}.

the reaction front. Figure 4 shows the pressure and the mass fractions of the radical HO_2 and the product gas H_2O across the reaction waves for $Ma_1 = 2.13$ (deflagration) and $Ma_3 = 2.30$ (detonation) at a time and position, when the reaction wave is fully developed and the initial shock wave has passed the bubble. ($t = 90\,\mu s$ for the detonation wave and $t = 300\,\mu s$ for the deflagration wave.)

Figure 4 (a) shows data for the deflagration reaction wave. The reaction front propagates from right to left and its location coincides with the peaks of the HO_2 mass fraction. Accompanied by the peak a rapid increase of the product gaseous H_2O is apparent. The pressure is not affected by the chemical reaction and remains constant across the reaction front.

A different evolution is observed for the supersonic reaction wave at $Ma_3 = 2.30$, see Fig. 4(b). In addition to the increase of the product gaseous H_2O and the intermediate species HO_2 across the reaction front, also the pressure exhibits a pronounced peak, which is caused by the shock wave preceding the detonation wave. The pressure decreases behind the shock wave but levels out at a larger value compared to the deflagration wave. Moreover, the amplitudes of the HO_2 mass fraction peaks in the reaction zone differ. The detonation wave shows a significantly higher amount of HO_2 and a breakdown across the reaction zone indicating that the third explosion limit is crossed and high-pressure reactions dominate [54]. Both reaction waves result in the same amount of the product gas H_2O.

Figure 5 shows the mass fraction of H_2O_2 for the two different reaction wave types. The spatial coordinate ξ denotes the distance from the reaction front, which propagates from right to left. The peak of $Y_{H_2O_2}$ indicates a reaction above the third explosion limit.

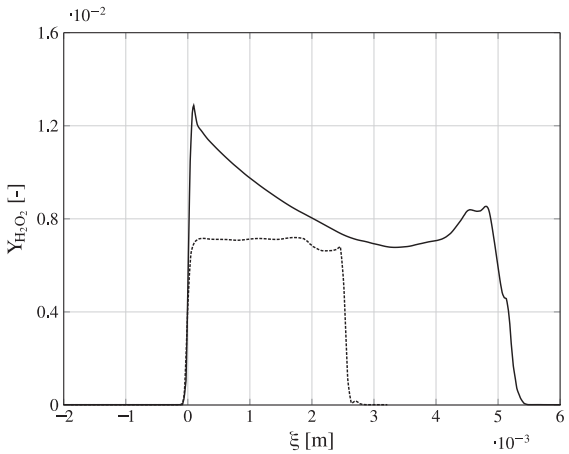

Fig. 5. H_2O_2 mass fraction across the fully developed reaction front. — : $Ma_1 = 2.13$ (deflagration) and — $Ma_3 = 2.30$ (detonation).

HO_2 collides with H_2 forming either H_2O_2 or directly H_2O. [54]. The strong reduction of $Y_{H_2O_2}$ on the right side of the plot identifies the bubble interface and consequently the boundary of the reaction zone.

4.4. Damköhler number

The flow field of RSBI is affected by hydrodynamic effects and chemical reaction kinetics. The Damköhler number, defined as the ratio of the hydrodynamic and chemical reaction time scales,

$$Da = \frac{\tau_h}{\tau_r}, \tag{35}$$

indicates which effect dominates. $Da > 1$ characterizes a flow field mainly driven by chemical reactions, $Da < 1$ implies a domination of the hydrodynamic effects. The two time scales are defined as follows:

$$\tau_h = \frac{1}{|\overline{\omega}|}, \tag{36}$$

$$\tau_r = \tau_{ign} + \frac{D_0}{2V_{RW}}. \tag{37}$$

The characteristic hydrodynamic time scale τ_h is defined by the total vorticity $\overline{\omega}$, averaged from the first contact of the shock wave with the bubble until the reaction wave has propagated through the bubble. The chemical reaction time scale τ_r consists of two time intervals: τ_{ign} is the period from the first contact of the shock with the bubble until ignition, and $D_0/(2V_{RW})$ is the time the reaction wave needs to propagate through half of the initial bubble shape with D_0 as the initial bubble diameter. The propagation velocity of the deflagration wave is sensitive to temperature and pressure, considered by a power law expression as introduced by Dehoe [55]

$$V_{RW} = S_{L_0}\left(\frac{T}{T_0}\right)^{\beta_1}\left(\frac{p}{p_0}\right)^{\beta_2}, \tag{38}$$

with S_{L_0} denoting the laminar burning velocity at reference conditions (T_0 and p_0), available in recent literature [55]. Temperature T and pressure p are taken from the hot spot shortly before ignition. The parameters β_1 and β_2 are 1.54 and 0.43, respectively, as we are dealing with a stoichiometric mixture [56]. We also computed the propagation velocity directly from the simulation and found good agreement to the literature. As the varying temperature and pressure distributions inside the bubble lead to a range of different propagation velocities, we decided to use the velocity calculated from Eq. (38). The obtained velocity proved to be a reasonable estimated value for the propagation velocity. For detonation the propagation velocity of the reaction wave is more stable and therefore determined directly from the simulation. Table 1 provides

Table 1
Damköhler numbers and characteristic time scales for different shock Mach numbers.

Ma [−]	τ_h [s]	τ_r [s]	Da [−]
2.13	4.926×10^{-4}	1.739×10^{-3}	0.283
2.19	1.227×10^{-4}	9.291×10^{-5}	1.321
2.30	1.094×10^{-4}	8.278×10^{-5}	1.322
2.50	1.286×10^{-4}	7.499×10^{-5}	1.715
2.90	3.086×10^{-4}	4.499×10^{-5}	6.859

the Damköhler numbers for the different initial shock Mach numbers, including the ones for $Ma_2 = 2.19$ and $Ma_4 = 2.50$, which are discussed in Section 5.

The deflagration wave induced at a low shock Mach number of $Ma_1 = 2.13$ leads to a Damköhler number of $Da = 0.283$. The hydrodynamic time scale dominates the flow field, bubble evolution and the growth of secondary instabilities are mainly driven by hydrodynamic effects. As shown in Fig. 2, the influence of the reaction front is minor.

At higher shock Mach numbers, chemical reactions start to play a crucial role for the overall bubble dynamics. The fast propagation velocity of the detonation wave shortens the chemical reaction time scale τ_r and leads to a Damköhler number of $Da = 1.322$ for a shock Mach number of $Ma_3 = 2.30$. The primary vortex region and the growth of secondary instabilities are directly affected by the detonation wave. At the highest shock Mach number of $Ma_5 = 2.90$, evolution is entirely dominated by the detonation wave. After it merges with the initial shock wave, it determines the spatial evolution of the gas bubble. RMI, the primary vortices and the secondary instabilities emerge under the influence of the reaction wave. The ignition at the upstream pole of the bubble shortens the reaction time scale. The single reaction wave reduces the vorticity production compared to the detonation wave, which originates at the downstream pole of the bubble and therefore increases the hydrodynamic time scale. The reaction wave dominates the flow field, which finds expression in a significant increase of the Damköhler number up to $Da = 6.859$. At a lower shock Mach number of $Ma_3 = 2.30$, the early RMI evolves in the unburnt gas mixture of the bubble, which leads to a lower Damköhler number compared to the simulation at $Ma_5 = 2.90$.

4.5. Enstrophy generation

We use the enstrophy

$$\varepsilon = \int_S \omega^2 \mathrm{d}x\mathrm{d}y \tag{39}$$

to determine the influence of the different reaction waves on the vorticity production. Figure 6 outlines the enstrophy over time for reacting and inert SBI. The enstrophy is zero until the shock wave reaches the upstream pole of the bubble. Baroclinic vorticity production leads to an increase during the shock wave passage. A first local maximum in enstrophy is reached after the shock has passed half of the bubble, an effect that can be observed for all simulations. Thereafter, a slight decay is visible, followed by another increase due to shock focusing and shock reflections at the interface. The enstrophy gradually decays after the passage of the shock. The same pattern is observed for all inert simulations, independently of the shock Mach number; only overall enstrophy levels differ as stronger shock waves generate more enstrophy.

The deflagration wave induced by a shock Mach number of $Ma_1 = 2.13$ has no noticeable influence on the enstrophy, the variation between the reacting and inert simulations is negligible. The detonation waves induced by a shock Mach number of $Ma_3 = 2.30$ produce significant amounts of additional vorticity, which leads to a distinct enstrophy peak, see Fig. 6. The elevated enstrophy levels persist for about 50 µs. The highest shock Mach number of $Ma_5 = 2.90$ shows a different behavior. As the ignition spot is located at the upstream pole of the bubble and as the mixture ignites immediately after the first contact of the shock wave, enstrophy production is dominated by the detonation wave. Therefore, we have two enstrophy peaks of similar magnitude, one during the shock wave passage of the upstream part of the bubble and one during the passage of the downstream part. Thereafter, similar to the simulation at $Ma_3 = 2.30$, the enstrophy decays faster compared to their inert counterparts. The inert SBI, shown in the contour plots in Fig. 2, is characterized by several small vortices at the outer interface, even in the long-term evolution. The reacting SBI shows a much smoother flow field with fewer vortices. The detonation waves of reacting SBIs decelerate the growth of secondary instabilities and reduces the appearance of smaller vortices as it induces vorticity with opposite sign compared to the vorticity produced by the initial shock wave. Furthermore the increased diffusion across the reaction front damps the growth rate of secondary instabilities. The shock wave Mach number of $Ma_5 = 2.90$ reveals an additional effect: enstrophy production during the first half of the shock wave passage for the reacting SBI is higher than for the inert SBI. Parts of the detonation wave are reflected, when it merges with the initial shock wave. The reflected wave produces additional vorticity at the internal interface inside the bubble. During the second half of the shock wave passage, the inert SBI shows a larger enstrophy production. The density gradient across the shock wave is higher than the gradient across the detonation wave, leading to a higher enstrophy production. The vorticity of the reflected shock wave in a reacting SBI, increasing the enstrophy during the first part of the shock wave passage, has already decayed at this stage of SBI.

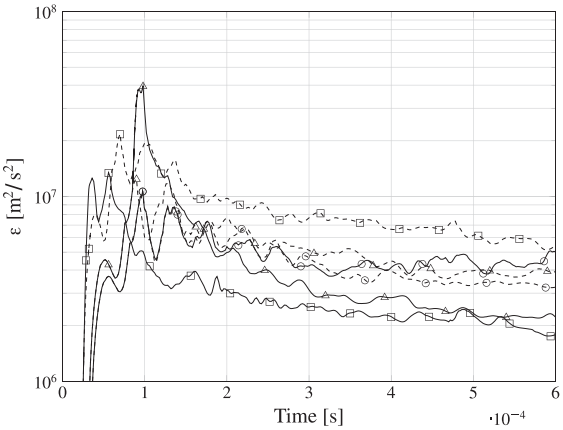

Fig. 6. Enstrophy. — : reaction; — : no reaction; ◯ : $Ma_1 = 2.13$, △ : $Ma_3 = 2.30$, □ : $Ma_5 = 2.90$.

4.6. Mixing in RSBI

The shock–bubble interaction provides a complex flow field, where RMI and KHI induce local spots of high mixing rates. Tomkins et al. [57] identified three main regions of mixing: the main vortices, the outer interface including KHI and the bridge region, which connects the two main vortices. The latter contributes up to 40% to the mixing. To estimate the impact of the reaction waves on the mixing, we use the molecular mixing fraction (MMF), defined by Danckwerts [58] as

$$\Theta(t) = \frac{\int_{-\infty}^{\infty} \langle X_{\mathrm{N_2}} X_{\mathrm{Xe}} \rangle \mathrm{d}x}{\int_{-\infty}^{\infty} \langle X_{\mathrm{N_2}} \rangle \langle X_{\mathrm{Xe}} \rangle \mathrm{d}x} \,. \tag{40}$$

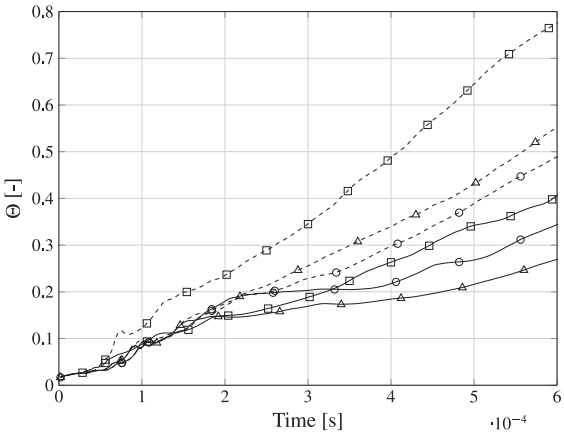

Fig. 7. Molecular mixing fraction. — : reaction; — : no reaction; ◯ : $Ma_1 = 2.13$, △ : $Ma_3 = 2.30$, □ : $Ma_5 = 2.90$.

The molar mixing fraction can be interpreted as the ratio of molecular mixing to large-scale entrainment by convective motion. We plot the temporal evolution of $\Theta(t)$ for reacting and inert simulations in Fig. 7.

The inert simulations show a linear growth of the molar mixing fraction, the slope increases with higher shock Mach number. An increase in shock strength leads to higher enstrophy production and faster growth of secondary instabilities, which enhance mixing. The reacting counterparts show a different behavior. In general, the mixing is reduced by the reaction waves, independent of their type. The deflagration wave induced by the lowest shock Mach number leads to a decrease of up to 30%. Mixing is affected after approximately $t = 270$ µs, when the reaction wave reaches parts of the interface and the main vortices. However, the bridge region remains unaffected, as the propagation velocity of the deflagration wave is too low.

The detonation wave affects all three main mixing regions. The MMF is reduced by up to 50% for $Ma_3 = 2.30$ as well as for $Ma_5 = 2.90$. Besides the reduction of mixing in the region of the main vortices and at the interface, which are already affected by a deflagration wave at a lower shock Mach number, the bridge region is also influenced by the detonation wave. The detonation waves decelerate the growth of secondary instabilities. Especially the bubble evolution at the highest shock Mach number, see Fig. 2, shows damping of fine structures, which explains the higher reduction of the MMF.

Figure 8 outlines the mixing progress in the long-term evolution at $t = 500$ µs for three different shock Mach numbers. The inert SBIs show already a high degree of mixing, whereas the reacting SBIs are characterized by large areas of unmixed bubble gas. The inert SBIs show higher mixing for increasing shock Mach number, which is in accordance to the MMF plotted in Fig. 7. The reacting SBIs follow a similar trend: For low shock Mach numbers of $Ma = 2.13$ (Fig. 8(a)) and $Ma = 2.30$ (Fig. 8(b)) we observe larger areas of unmixed bubble gas, whereas the highest shock Mach number of $Ma = 2.90$ (Fig. 8(c)) shows a higher degree of mixing.

5. Special cases

Two simulations of RSBI contain hydrodynamic and chemical features that have to be discussed in detail. We observed DDT for $Ma_2 = 2.19$ and a double detonation with different reaction branches for $Ma_4 = 2.50$.

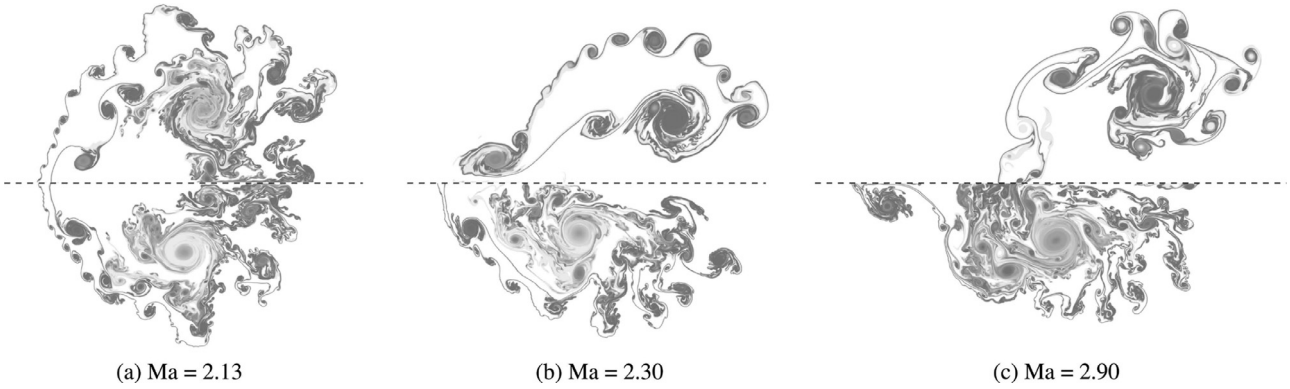

Fig. 8. Mixing of N_2 and Xe for inert and reacting SBI at $t = 500$ µs for different shock Mach numbers. Upper parts show the reacting SBI, lower parts the inert counterpart.

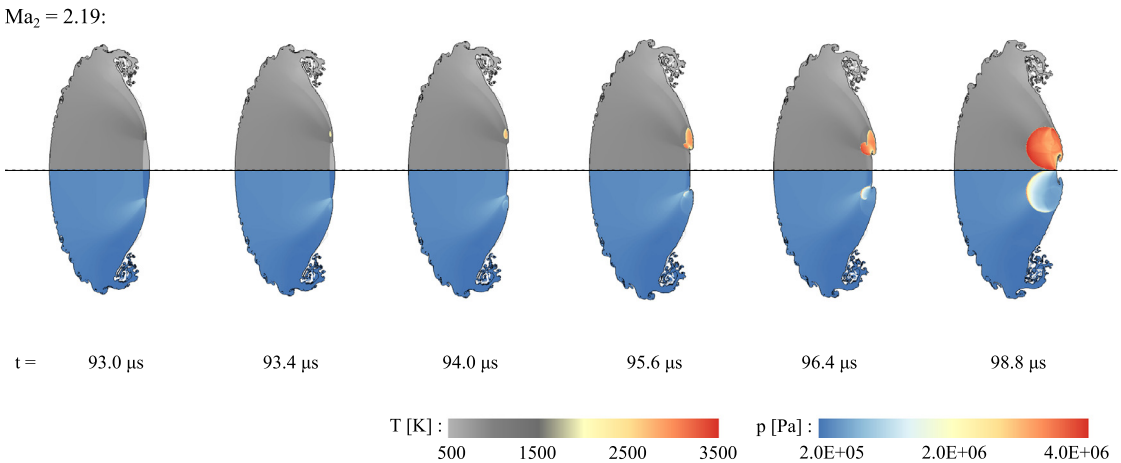

Fig. 9. Contour plots of RSBI at $Ma_2 = 2.19$ during deflagration-to-detonation transition: upper parts shows the temperature, lower parts the pressure.

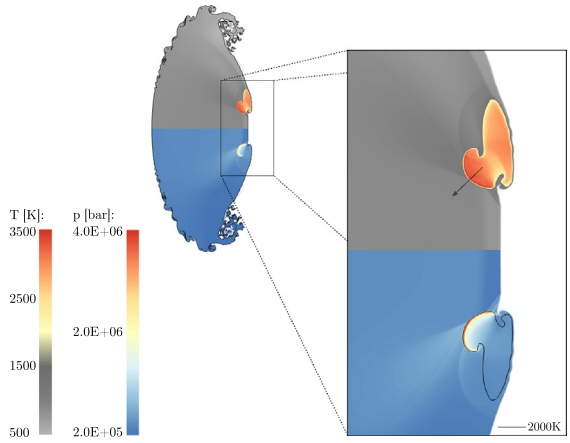

Fig. 10. Detailed contour plot of RSBI at $Ma_2 = 2.19$ shortly after DDT: upper part shows the temperature, lower part the pressure. The arrow shows the line slice for the data of Fig. 11.

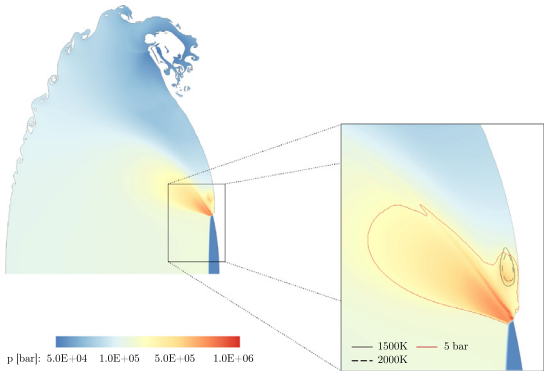

Fig. 12. Reaction front marked by black temperature isocontour, shortly before transition to detonation. High-pressure region denoted by red isocontour ($p > 5$ bar).

5.1. Deflagration-to-detonation transition ($Ma_2 = 2.19$)

Figure 9 shows contour plots for $Ma_2 = 2.19$ during the early stage of ignition. Temperature (upper part of the plot) and pressure (lower part) are parameters that illustrate the ignition and transition process. At $t = 93.0$ µs the shock wave still propagates through the bubble gas, and instabilities at the interface start to grow. The gas mixture ignites near the downstream pole of the bubble at approximately $t = 93.2$ µs. A subsonic deflagration wave propagates through the bubble gas until $t = 94.9$ µs. At $t = 94.9$ µs the transition into a detonation wave starts in the lower region of the reaction front. The remaining contour plots shows a fast growth of the supersonic detonation wave out of the deflagration front and a characteristic steep pressure peak across the detonation reaction wave.

Detailed contour plots to illustrate how the detonation wave evolves from the deflagration wave are outlined in Fig. 10. The upper part of the figure shows the temperature and the lower part the pressure. A temperature isoline ($T = 2000$ K) visualizes the reaction front.

The temporal evolution of the characteristic thermodynamic properties during the transition is plotted in Fig. 11. The plots show the variations of pressure, the radical H concentration (Fig. 11(a)) and the temperature (Fig. 11(b)) for seven timesteps from $t = 94.6$ µs until $t = 96.0$ µs. The coordinate ξ is obtained by a rotation of the original coordinate system. As a result of the transformation ξ coincides with the propagation direction of the reaction wave. The reaction wave propagates from the right to the left. We observed an increase of the pressure peak accompanied by a decrease of H in the reaction zone, which is characteristic for DDT. The H radical appears within the deflagration wave, following the detonation wave. The peak of H can be found behind the shock wave, after the sudden increase in temperature and pressure. Furthermore, DDT can be identified by the steepening of the temperature profile, its peak at the reaction front and the higher temperature of the product gas. These findings are consistent with observations of Ivanov et al. [36] and Liberman et al. [15,18].

The deflagration front propagates in semicircular direction through the bubble gas, hence the question arises why the transition to detonation occurs at specific areas of the reaction front. The reason can be found by the detailed analysis of the pressure distribution in front of the reaction front, where DDT occurs. Figure 12 shows the reaction front shortly before the transition to detonation. The reaction zone is indicated by two black isocontours, the red isocontour depicts the region of high pressure. Due to shock focusing of the initial shock wave at the downstream pole of the bubble, a region of high pressure ($p > 5$ bar) exists. The reaction front propagates into this region and high-pressure reactions are promoted, which support the transition to detonation.

As the deflagration wave persists only for a few microseconds, the overall bubble evolution of the RSBI at $Ma_2 = 2.19$ is similar to that at a shock wave Mach number of $Ma_3 = 2.30$. The normalized transverse bubble diameter, the enstrophy production and the molar mixing fraction are nearly identical. The Damköhler numbers

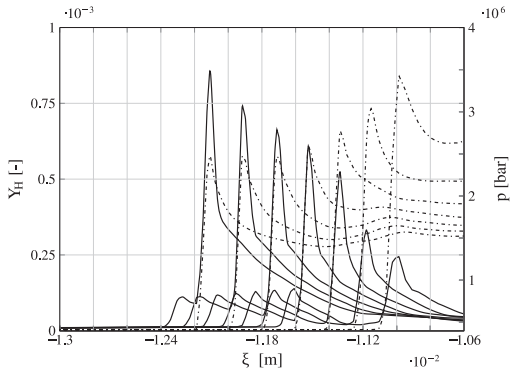

(a) —— : Pressure; -·- : radical H concentration

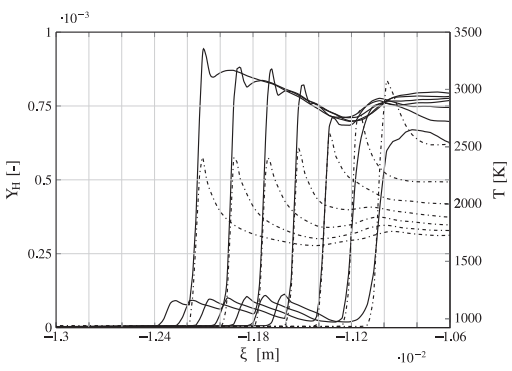

(b) —— : Temperature; -·- : radical H concentration

Fig. 11. Pressure, temperature and radical H concentration in the reaction front during the transition to detonation for seven conservative time steps with $\Delta t = 0.2$ µs starting at $t = 94.6$ µs.

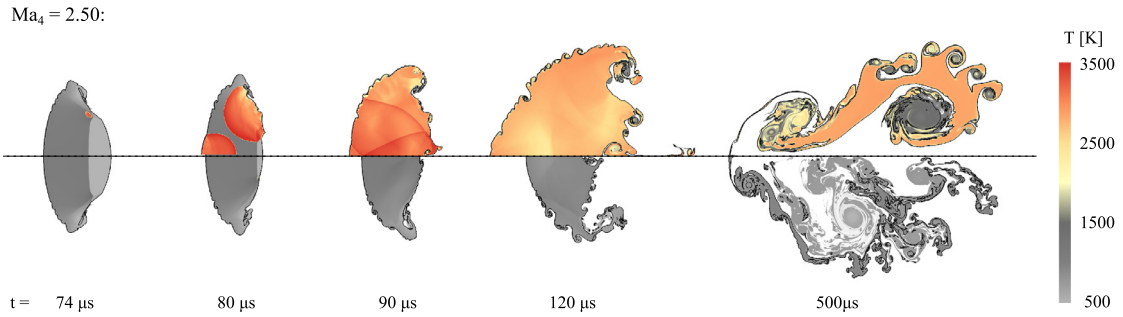

Fig. 13. Contour plots of RSBI at $Ma_4 = 2.50$: upper parts shows the reacting SBI, lower parts the inert SBI.

amount to $Da = 1.321$ ($Ma_2 = 2.19$) and $Da = 1.322$ ($Ma_3 = 2.30$) indicating a chemically dominated flow field. To ensure that the observed DDT is not caused by numerical artifacts, the RSBI with a shock Mach number of $Ma_2 = 2.19$ was repeated at a coarsened and refined grid resolution. We used the same grids that were already applied for the grid convergence study in our previous paper [29] with cell sizes of $\Delta_{xy} = 234$, 117 and 59 µm. All simulations show the same induction time, ignition spot and location of DDT.

5.2. Double detonation ($Ma_4 = 2.50$)

The shock wave of $Ma_4 = 2.50$ induces two detonation waves. One originates near the downstream pole of the bubble and one at the upstream pole. Figure 13 shows the ignition spots, the propagation and interaction of the detonation waves. The two reaction waves propagate towards each other, which leads to a rapid consumption of the reactive bubble gas. The reaction time scale is significantly shortened, leading to an increase of the Damköhler number to $Da = 1.715$, see Table 1. Specific conditions have to be satisfied to cause a double detonation: The ignition delay time in the first reaction spot at the upstream pole of the bubble has to be longer than in the second spot near the downstream pole. However, the ignition has to be nearly simultaneous in the absolute timeframe.

The reaction region at the upstream pole is characterized by a slow increase of the intermediate gas mass fractions directly behind the shock wave, beginning at $t = 28$ µs. After an induction time of about 47 µs the gas mixture ignites and forms a detonation wave. The second ignition spot shows a different behavior; a strong reaction is directly induced after the shock wave has passed at $t = 68$ µs. The induction time only amounts to $t = 6$ µs, which is much shorter than for the first ignition spot. The higher compression and temperature at the downstream pole of the bubble lead to a faster ignition. In the absolute timeframe both spots trigger ignition, followed by a detonation wave at approximately the same time, which leads to a double detonation.

Figure 14 outlines the temporal evolution of the intermediate species H, O, OH during the induction time in the two reaction zones. The solid lines denote the ignition spot at the upstream pole of the bubble, the dashed lines show data for the downstream pole. As the chemical reactions are highly pressure sensitive the higher temperature and pressure at the downstream pole leads to a faster production of the radicals and to a shorter ignition delay time, compared to the upstream pole.

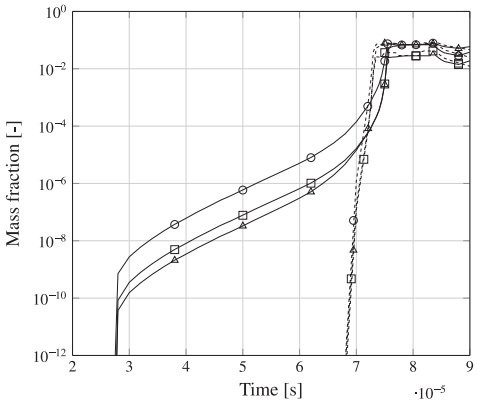

Fig. 14. Maximum mass fraction of intermediate products inside the two ignition spots. ◯ = *H*, □ = *O*, △ = *OH*. – : 1st ignition spot at the upstream pole; – : 2nd ignition spot at the downstream pole.

6. Discussion

6.1. Transverse bubble diameter

Our setup is based on the experimental investigation of Haehn et al. [28]. They observed, similarly to our work, different reaction wave types by varying the shock Mach number between $Ma = 1.34$ and $Ma = 2.83$. In the following section, we compare the results of the two studies. We are well aware that a comparison of two-dimensional simulations with the experiment of Haehn et al. [28] is only reasonable along early stages of evolution [29]. Haehn et al. [28] provide the Damköhler number, the transverse normalized bubble and the main vortex diameter for several experimental setups. We will use the transverse bubble diameter to compare the general evolution of the bubble and the influence of the reaction waves. The experiments exhibit deflagration for shock Mach numbers of $Ma = 1.63$ and $Ma = 2.07$ and detonation for a shock Mach number of $Ma = 2.83$. Haehn et al. [40] also observed detonations for shock Mach numbers smaller than $Ma = 2.83$, however, without providing quantitative data. We compare the experimental results for $Ma_{exp} = 2.07$ and $Ma_{exp} = 2.83$ with our results obtained at $Ma_{num} = 2.13$ and $Ma_{num} = 2.90$. Figure 15 shows the evolution of the normalized transverse bubble diameter for a RSBI with either a deflagration wave (a) or a detonation wave (b). The normalized time t^* follows the definition of Haehn et al. [40]

$$t^* = \frac{t}{\tau_n}, \tag{41}$$

where t is the time measured from the first contact of the shock wave with the bubble. τ_n is defined as D_0/W_i, with W_i as the incident shock wave speed.

As discussed in Section 4.2, the slowly propagating deflagration wave leads only to a slight increase of the bubble diameter. Inert and reacting SBI show a similar evolution, confirmed by the experimental as well as the numerical results in Fig. 15(a) . The numerical data show a larger normalized bubble diameter in the long-term evolution, which is attributed to two-dimensional effects.

Also the data for SBIs, which induce a detonation wave, are in very good agreement. The propagation velocity of the reaction wave, the spatial expansion of the bubble and the peak of the

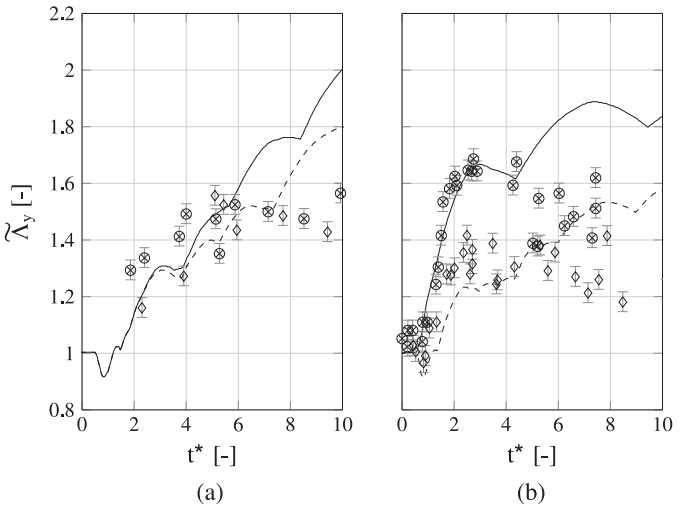

Fig. 15. Normalized transverse bubble diameter. Comparison between simulations and experimental data of Haehn et al. [28]. Reaction: — and ⊗; No reaction: — and ◇. (a) Deflagration $Ma = 2.13/2.07$ [28], (b) Detonation $Ma = 2.90/2.83$ [28].

transverse bubble diameter are nearly identical. Figure 15(b) reveals a good match of the steep bubble diameter increase, indicating that the propagation of the reaction wave inside the gas bubble is well reproduced by the two-dimensional simulations. Similarly to the deflagration setup, the bubble expansion differs from the experimental results in the long-term evolution.

6.2. Double detonation

As mentioned before, Haehn et al. [28] also performed experiments at intermediate shock strengths. For one specific setup, their chemiluminescence signal showed two bright spots, indicating two ignition points. They provided two explanations. The first one suggests that the second bright spot may be a reflection of the first initial combustion signal from the downstream surface of the unshocked bubble interface. The second explanation assumes that simultaneous detonations at two specific points in the compressed bubble are possible as the induction time of the second reaction spot is shortened by the higher compression of the shock focusing. A proper combination of induction times thus can lead to simultaneous ignitions. Our numerical results for $Ma_4 = 2.50$ support this latter hypothesis.

6.3. Limitations and critical discussion

The comparison of our two-dimensional simulations with the experimental data of Haehn et al. [28] has some limitations with respect to the bubble evolution.

As shown in Fig. 15, the transverse expansion of the bubble gas deviates from the experimental results in the long-term evolution. Recent studies of Wang et al. [59] observe the same with respect to the transverse bubble diameter of two- and three-dimensional SBIs in their experiments. The vortex stretching term of the vorticity equation vanishes for a two-dimensional simulation. The missing of this term affects the expansion and increases the transverse expansion in the long-term evolution [60], which explains the deviation of the transverse bubble diameter for $t^* \gtrsim 6$. Hejazialhosseini et al. [60] investigated the vortex dynamics in three-dimensional inert SBI and showed that the growth rate of the vortex stretching term increases significantly in the long-term evolution and contributes to a decrease of the transverse bubble diameter, an effect missing in two-dimensional simulations.

Furthermore, the shock-focusing in three dimensions is stronger, which shortens the ignition delay time. To compensate for this effect, we simulate RSBI at a slightly higher shock Mach number to achieve the same ignition delay time. The validity of two-dimensional simulations containing shock-induced instabilities has also been shown by Peng et al. [61] in their study of vortex-accelerated secondary baroclinic vorticity deposition. Klein et al. [62] investigated the interaction between a sphere and a shock wave at high shock Mach numbers. They compared the two-dimensional results with experimental data and observed good accordance in the radial and axial width of the shocked sphere. Both studies achieved very good agreement between two-dimensional RMI and experiments, even in the long-time dynamics.

Nevertheless some effects are not resolved by our simulation such as the onset of turbulence. Three-dimensional vortex rings tend to become unstable and vortex stretching may eventually result in broad-band turbulence [63]. This production mechanism is suppressed in a two-dimensional simulation. Three-dimensional effects cannot be neglected, however they become important only in the long-term evolution. Niederhaus et al. [64] studied SBIs and showed that three-dimensional effects affect the total enstrophy only at late times. Miles et al. [65] support this assumption, as they also observed no significant differences of the early growth rates of shock-induced instabilities between three- and two-dimensional simulations. Further studies report that vortex stretching affects only the long-term evolution of the mixing rate [60]. These observations support the integrity of our results, as the chemical reaction and its interaction with the hydrodynamic instabilities occur in the early stage of SBI. The very good agreement between our numerical results and the experimental data of Haehn et al. [28] indicate that three-dimensional effects may not be very significant for the specific phenomena considered here. Hence, we are confident to provide valid and reliable results for the investigation of reaction wave characteristics and its influence on the global bubble dynamics. In particular the good agreement of the normalized transverse bubble diameter for the detonating RSBI with experimental data indicates that essential mechanisms are reproduced. Furthermore, the detection and analysis of a double detonation in the simulations supports the experimental observations of Haehn et al. [28].

7. Conclusion

We have presented results of a reacting shock–bubble interaction at different shock Mach numbers with detailed H_2–O_2 chemical reaction kinetics. A gas bubble filled with a reactive stoichiometric gas mixture of H_2, O_2 and Xe is penetrated by a shock wave with Mach numbers between $Ma = 2.13$ and $Ma = 2.90$. The planar shock wave propagates through the domain and interacts with the cylindrical density inhomogeneity, inducing Richtmyer–Meshkov instabilities. The convergent shape of the bubble focuses the shock, which triggers ignition of the bubble gas. Depending on the shock Mach number, the pressure sensitive H_2–O_2 gas mixture shows different induction times, ignition spots and reaction wave types, which strongly affect the spatial bubble evolution and the mixing process. A weak shock wave induces a deflagration wave, higher shock Mach numbers drive high-pressure reactions, resulting in a detonation wave.

We showed that the variation of the shock Mach number covers several reaction wave types with different impact on the mixing process. A deflagration wave has a minor influence on the global bubble evolution and leads to a flow field dominated by hydrodynamic effects ($Da \approx 0.28$). The growth of secondary instabilities is partially affected, which decreases mixing by about 30%. Higher shock Mach numbers and the subsequent detonation waves lead to a chemically driven flow field ($Da \gtrsim 1.32$). The supersonic reaction

wave propagates rapidly through the reactive gas mixture and affects all bubble regions. Secondary instabilities are suppressed, the bridge region is disturbed and mixing is reduced by up to 50%. The detonation wave induces an additional peak in the enstrophy production, followed by a faster decay.

A shock Mach number $Ma = 2.50$ reveals a particular phenomenon. The bubble gas ignites simultaneously at two spots, leading to two detonation waves that propagate towards each other. At an intermediate shock Mach number of $Ma = 2.19$, we observe a deflagration wave that transitions into a detonation wave shortly after ignition. Comparison with experimental data shows a very good agreement in terms of spatial expansion, reaction wave types and propagation velocities.

Acknowledgment

The authors gratefully acknowledge the Gauss Centre for Supercomputing e.V. (http://www.gauss-centre.eu) for funding this project by providing computing time on the GCS Supercomputer SuperMUC at Leibniz Supercomputing Centre (LRZ, http://www.lrz.de).

This project has received funding from the European Research Council (ERC) under the European Union's Horizon 2020 research and innovation programme (grant agreement No 667483).

Supplementary material

Supplementary material associated with this article can be found, in the online version, at 10.1016/j.combustflame.2016.09.014

References

[1] J. Yang, T. Kubota, E. Zukoski, Applications of shock-induced mixing to supersonic combustion, AIAA J. 31 (1993) 854–862.
[2] F. Marble, E. Zukoski, J. Jacobs, G. Hendricks, I. Waitz, Shock enhancement and control of hypersonic mixing and combustion, AIAA 26th Joint Propulsion Conference (1990).
[3] R.D. Richtmyer, Taylor instability in shock acceleration of compressible fluids, Commun. Pure Appl. Math. 13 (1960) 297–319.
[4] E.E. Meshkov, Instability of the interface of two gases accelerated by a shock wave, Fluid Dyn. 4 (1969) 101–104.
[5] L. Rayleigh, Investigation of the character of the equilibrium of an incompressible heavy fluid of variable density, Proc. Lond. Math. Soc. 14 (1883) 170–177.
[6] G. Taylor, The instability of liquid surfaces when accelerated in a direction perpendicular to their planes. Part 1. Waves on fluid sheets, Proc. R. Soc. Lond. A Math., Phys. Sci. 201 (1950) 192–196.
[7] M. Brouillette, The Richtmyer-Meshkov Instability, Annu. Rev. Fluid Mech. 34 (2002) 445–468.
[8] N.J. Zabusky, Vortex paradigm for accelerated inhomogeneous flows: visiometrics for the Rayleigh-Taylor and Richtmyer–Meshkov environments, Annu. Rev. Fluid Mech. 31 (1999) 495–536.
[9] W.D. Arnett, The role of mixing in astrophysics, Ap. J. Suppl. 127 (2000) 213–217.
[10] A.M. Khokhlov, E.S. Oran, G.O. Thomas, Numerical simulation of deflagration-to-detonation transition: the role of shock-flame interactions in turbulent flames, Combust. Flame 117 (1999) 323–339.
[11] R.S. Craxton, K.S. Anderson, T.R. Boehly, V.N. Goncharov, D.R. Harding, J.P. Knauer, R.L. McCrory, P.W. McKenty, D.D. Meyerhofer, J.F. Myatt, A.J. Schmitt, J.D. Sethian, R.W. Short, S. Skupsky, W. Theobald, W.L. Kruer, Direct-drive inertial confinement fusion: a review, Phys. Plasmas 22 (2015).
[12] P.G. Drazin, Introduction to hydrodynamic stability, Cambridge University Press, 2002.
[13] V.K. Tritschler, S. Hickel, X.Y. Hu, N.A. Adams, On the Kolmogorov inertial subrange developing from Richtmyer–Meshkov instability, Phys. Fluids 25 (2013) 071701.
[14] E. Oran, J. Boris, Numerical simulation of reactive flow, Cambridge University Press, 2005.
[15] M.A. Liberman, Introduction to physics and chemistry of combustion: explosion, flame, detonation, Springer, 2008.
[16] W. Fickett, W.C. Davis, Detonation: theory and experiment, Dover Publications, 2010.
[17] J.H.S. Lee, The detonation phenomenon, Cambridge University Press, 2008.
[18] M.A. Liberman, M.F. Ivanov, A.D. Kiverin, M.S. Kuznetsov, A.A. Chukalovsky, T.V. Rakhimova, Deflagration-to-detonation transition in highly reactive combustible mixtures, Acta Astronaut. 67 (2010) 688–701.
[19] E. Oran, V. Gamezo, Origins of the deflagration-to-detonation transition in gas-phase combustion, Combust. Flame 148 (2007) 4–47.
[20] J.-F. Haas, B. Sturtevant, Interaction of weak shock waves with cylindrical and spherical gas inhomogeneities, J. Fluid Mech. 181 (1987) 41–76.
[21] J.J. Quirk, S. Karni, On the dynamics of a shock-bubble interaction, J. Fluid Mech. 318 (1996) 129–163.
[22] D. Ranjan, J. Oakley, R. Bonazza, Shock-bubble interactions, Annu. Rev. Fluid Mech. 43 (2011) 117–140.
[23] G. Billet, V. Giovangigli, G. de Gassowski, Impact of volume viscosity on a shock-hydrogen-bubble interaction, Comb. Theory Model. 12 (2008) 221–248.
[24] N. Attal, P. Ramaprabhu, J. Hossain, V. Karkhanis, M. Uddin, J. Gord, S. Roy, Development and validation of a chemical reaction solver coupled to the flash code for combustion applications, Comput. Fluids 107 (2015) 59–76.
[25] N. Attal, P. Ramaprabhu, Numerical investigation of a single-mode chemically reacting Richtmyer–Meshkov instability, Shock Waves 25 (2015) 307–328.
[26] A.M. Khokhlov, E.S. Oran, A.Y. Chtchelkanova, J.C. Wheeler, Interaction of a shock with a sinusoidally perturbed flame, Combust. Flame 117 (1999) 99–116.
[27] L. Massa, P. Jha, Linear analysis of the Richtmyer–Meshkov instability in shock–flame interactions, Phys. Fluids 24 (2012) 056101.
[28] N. Haehn, D. Ranjan, C. Weber, J. Oakley, D. Rothamer, R. Bonazza, Reacting shock bubble interaction, Combust. Flame 159 (2012) 1339–1350.
[29] F. Diegelmann, V. Tritschler, S. Hickel, N. Adams, On the pressure dependence of ignition and mixing in two-dimensional reactive shock-bubble interaction, Combust. Flame 163 (2016) 414–426.
[30] J.G. Ogilvie, The hydrogen–oxygen second explosion limit. A physical chemistry experiment, J. Chem. Educ. 48 (1971) 342–344.
[31] B. Lewis, G. von Elbe, Combustion, flames and explosions of gases, Academic Press, Inc., 1987.
[32] P.D. Neufeld, A.R. Janzen, R.A. Aziz, Empirical equations to calculate 16 of the transport collision integrals omega(l,s)* for the Lennard–Jones (12–6) potential, J. Chem. Phys. 57 (1972) 1100–1102.
[33] B.E. Poling, J.M. Prausnitz, J.P. O'Connell, The properties of gases and liquids, McGraw-Hill, 2001.
[34] A.W. Cook, Enthalpy diffusion in multicomponent flows, Phys. Fluids 21 (2009) 055109.
[35] M. Kuznetsov, M.A. Liberman, I. Matsukov, Experimental study of the preheat zone formation and deflagration to detonation transition, Combust. Sci. Technol. 182 (2010) 1628–1644.
[36] M.F. Ivanov, A.D. Kiverin, M.A. Liberman, Hydrogen–oxygen flame acceleration and transition to detonation in channels with no-slip walls for a detailed chemical reaction model, Phys. Rev. E 83 (2011) 056313.
[37] T. Poinsot, D. Veynante, Theoretical and numerical combustion, R T Edwards, 2001.
[38] J. Troe, Predictive possibilities of unimolecular rate theory, J. Phys. Chem. 83 (1979) 114–126.
[39] M. Ó Conaire, H.J. Curran, J.M. Simmie, W.J. Pitz, C.K. Westbrook, A comprehensive modeling study of hydrogen oxidation, Int. J. Chem. Kinet. 36 (2004) 603–622.
[40] N.S. Haehn, Experimental investigation of the reactive shock-bubble interaction, University of Wisconsin-Madison, 2012 Ph.D. thesis.
[41] P.J.M. Ferrer, R. Buttay, G. Lehnasch, A. Mura, A detailed verification procedure for compressible reactive multicomponent Navier–Stokes solvers, Comput. Fluids 89 (2014) 88–110.
[42] O.P. Korobeinichev, T.A. Bol'shova, Applicability of Zel'dovich's theory of chain propagation of flames to combustion of hydrogen–oxygen mixtures, Combust., Explos., Shock Waves 45 (2009) 507–510.
[43] G. Strang, On the construction and comparison of difference schemes, SIAM J. Numer. Anal. 5 (1968) 506–517.
[44] P.L. Roe, Approximate Riemann solvers, parameter vectors, and difference schemes, J. Comput. Phys. 43 (1981) 357–372.
[45] B. Larouturou, L. Fezoui, On the equations of multi-component perfect or real gas inviscid flow, Lecture notes in mathematics, 1402, Springer Berlin Heidelberg, 1989, pp. 69–98.
[46] X.Y. Hu, V.K. Tritschler, S. Pirozzoli, N.A. Adams, Dispersion–dissipation condition for finite difference schemes, arXiv:1204.5088 (2012).
[47] S. Gottlieb, C.-W. Shu, Total variation diminishing Runge–Kutta schemes, Math. Comput. 67 (1998) 73–85.
[48] V.K. Tritschler, A. Avdonin, S. Hickel, X.Y. Hu, N.A. Adams, Quantification of initial-data uncertainty on a shock-accelerated gas cylinder, Phys. Fluids 26 (2014a) 026101.
[49] V.K. Tritschler, B.J. Olson, S.K. Lele, S. Hickel, X.Y. Hu, N.A. Adams, On the Richtmyer–Meshkov instability evolving from a deterministic multimode planar interface, J. Fluid Mech. 755 (2014b) 429–462.
[50] V.K. Tritschler, M. Zubel, S. Hickel, N.A. Adams, Evolution of length scales and statistics of Richtmyer–Meshkov instability from direct numerical simulations, Phys. Rev. E 90 (2014c) 063001.
[51] P.N. Brown, G.D. Byrne, A.C. Hindmarsh, VODE: a variable-coefficient ODE solver, SIAM J. Sci. Stat. Comput. 10 (1989) 1038–1051.
[52] A. Glezer, The formation of vortex rings, Phys. Fluids 31 (1988) 3532–3542.
[53] P.E. Dimotakis, The mixing transition in turbulent flows, J. Fluid Mech. 409 (2000) 69–98.
[54] O. Oldenberg, H.S. Sommers, The thermal reaction between hydrogen and oxygen III. The temperature coefficient of the steady thermal reaction, J. Chem. Phys. 9 (1941) 432–438.
[55] A.E. Dahoe, Laminar burning velocities of hydrogen–air mixtures from closed vessel gas explosions, J. Loss Prev. Process Ind. 18 (2005) 152–166.

[56] T. Iijima, T. Takeno, Effects of temperature and pressure on burning velocity, Combust. Flame 65 (1986) 35–43.
[57] C. Tomkins, S. Kumar, G. Orlicz, K. Prestridge, An experimental investigation of mixing mechanisms in shock-accelerated flow, J. Fluid Mech. 611 (2008) 131–150.
[58] P.V. Danckwerts, The definition and measurement of some characteristics of mixtures, Ap. Sci. Res., Sect. A 3 (1952) 279–296.
[59] X. Wang, T. Si, X. Luo, J. Yang, Generation of air/SF6 interface with minimum surface feature by soap film technique, 29th International Symposium on Shock Waves 2 (2015), pp. 1065–1070.
[60] B. Hejazialhosseini, D. Rossinelli, P. Koumoutsakos, Vortex dynamics in 3D shock-bubble interaction, Phys. Fluids 25 (2013) 110816.
[61] G. Peng, N.J. Zabusky, S. Zhang, Vortex-accelerated secondary baroclinic vorticity deposition and late-intermediate time dynamics of a two-dimensional Richtmyer–Meshkov interface, Phys. Fluids 15 (2003) 3730–3744.
[62] R. Klein, K.S. Budil, T.S. Perry, D.R. Bach, The interaction of supernova remnants with interstellar clouds: experiments on the nova laser, Astrophys. J. 583 (2003) 245–259.
[63] P.A. Davidson, Turbulence: an introduction for scientists and engineers, Oxford University Press, 2004.
[64] J.H. Niederhaus, J.A. Greenough, J.G. Oakley, D. Ranjan, M.H. Anderson, R. Bonazza, A computational parameter study for the three-dimensional shock--bubble interaction, J. Fluid Mech. 594 (2008) 85–124.
[65] A.R. Miles, B. Blue, M.J. Edwards, J.A. Greenough, J.F. Hansen, H.F. Robey, R.P. Drake, C. Kuranz, D.R. Leibrandt, Transition to turbulence and effect of initial conditions on three-dimensional compressible mixing in planar blast-wave-driven systems, Phys. Plasmas 12 (2005) 056317.

B.3. Three-dimensional reacting shock-bubble interaction

Combustion and Flame 181 (2017) 300–314

Contents lists available at ScienceDirect

Combustion and Flame

journal homepage: www.elsevier.com/locate/combustflame

Three-dimensional reacting shock–bubble interaction

Felix Diegelmann[a,*], Stefan Hickel[a,b], Nikolaus A. Adams[a]

[a] Institute of Aerodynamics and Fluid Mechanics, Technische Universität München, Garching 85748, Germany
[b] Faculty of Aerospace Engineering, TU Delft, Delft 2629 HS, Netherlands

ARTICLE INFO

Article history:
Received 29 December 2016
Revised 8 March 2017
Accepted 27 March 2017

keywords:
Shock-bubble interaction
Shock-induced ignition
Shock wave
Detonation
Shock-induced mixing
Richtmyer-Meshkov instability

ABSTRACT

We investigate a reacting shock–bubble interaction through three-dimensional numerical simulations with detailed chemistry. The convex shape of the bubble focuses the shock and generates regions of high pressure and temperature, which are sufficient to ignite the diluted stoichiometric H_2–O_2 gas mixture inside the bubble. We study the interaction between hydrodynamic instabilities and shock-induced reaction waves at a shock Mach number of $Ma = 2.83$. The chosen shock strength ignites the gas mixture before the shock-focusing point, followed by a detonation wave, which propagates through the entire bubble gas. The reaction wave has a significant influence on the spatial and temporal evolution of the bubble. The misalignment of density and pressure gradients at the bubble interface, caused by the initial shock wave and the subsequent detonation wave, induces Richtmyer–Meshkov and Kelvin–Helmholtz instabilities. The growth of the instabilities is highly affected by the reaction wave, which significantly reduces mixing compared to an inert shock–bubble interaction. A comparison with two-dimensional simulations reveals the influence of three-dimensional effects on the bubble evolution, especially during the late stages. The numerical results reproduce experimental data in terms of ignition delay time, reaction wave speed and spatial expansion rate of the bubble gas. We observe only a slight divergence of the spatial expansion in the long-term evolution.

1. Introduction

The interaction between a shock wave and a density inhomogeneity induces Richtmyer–Meshkov instability (RMI). The baroclinic vorticity production mechanism and subsequent Kelvin–Helmholtz instabilities (KHI) result in a complex turbulent flow field. The shock–bubble interaction (SBI) is a common setup to study this interaction, which has been done intensively for several decades [1]. An additional degree of complexity can be added by replacing the inert bubble gas by a reactive gas mixture. In the generic configuration of a reacting shock–bubble interaction (RSBI), the increase of pressure and temperature across the shock wave accelerates the chemical reactions. Depending on the shock strength, the stimulation of the reaction kinetics can be sufficient to ignite the reactive bubble gas. The subsequent reaction wave interacts with the hydrodynamic instabilities and affects integral properties of the flow field. By three-dimensional numerical simulation we investigate RSBI of a gas bubble filled with hydrogen (H_2) and oxygen (O_2), diluted with xenon (Xe) in a pure nitrogen (N_2) environment at a shock Mach number of $Ma = 2.83$. The setup is motivated by previous works of the authors [2,3], where the ignition behavior and the early stage bubble evolution of RSBI in two dimensions was investigated. Specific reaction wave types and ignition spots were triggered by the variation of the initial pressure or the shock strength. The subsequent mixing processes and the bubble evolution, including the spatial expansion and the growth of instabilities, showed a high dependence on the reaction wave type. Three-dimensional effects, which are relevant for the long-term evolution are the focus of the current work.

Shock-accelerated flows in reactive environments involve a wide range of scales, from extremely large scales in astrophysics [4], intermediate scales in combustion engines [5], down to very small scales in inertial confinement fusion [6]. Independent of the scale, the misalignment of the pressure gradient, ∇p, associated with the shock wave, and the density gradient, $\nabla \rho$, across a material interface, produces baroclinic vorticity ($\nabla p \times \nabla \rho$) and induces Richtmyer–Meshkov instability (RMI) [7,8], the impulsive limit of the Rayleigh–Taylor instability [9,10]. The RMI promotes turbulent mixing and increases the burning efficiency [11,12]. For a comprehensive review on RMI, the reader is referred to Brouillette [13]. Furthermore, the instability induces velocity shear and small perturbations at the interface of the bubble, which are, besides the initial density mismatch, necessary preconditions for the

* Corresponding author.
E-mail address: felix.diegelmann@aer.mw.tum.de (F. Diegelmann).

http://dx.doi.org/10.1016/j.combustflame.2017.03.026

Kelvin–Helmholtz instability (KHI) [14]. The perturbations are amplified and generate vortices at the interface accompanied by the appearance of smaller scales [13]. The breakup of large-scale structures is driven by the KHI [15,16] and forces mixing.

1.1. Shock–bubble interaction

The classical inert shock–bubble interaction (ISBI) describes the hydrodynamic effects induced by a planar shock wave propagating through a gas bubble. Upon contact, the incident shock wave is partially reflected and partially transmitted. For an Atwood number $A = (\rho_1 - \rho_2)/(\rho_1 + \rho_2) < 0$ (the bubble gas is lighter than the ambient gas), the transmitted shock wave propagates faster than the incident shock wave. $A > 0$ shows the converse effect: the transmitted shock wave travels slower than the incident shock wave outside the bubble. The transmitted shock wave focuses at the downstream pole of the bubble and collapses into a single shock-focusing point. RMI, due to the misalignment of the pressure and density gradient at the bubble interface, causes the bubble to evolve into a vortex ring. Provided that the initial kinetic-energy input is sufficient, the flow develops a turbulent mixing zone through non-linear interactions of the material interface perturbations [13,17].

ISBI was intensively studied over the last decades. The first detailed experimental investigations were performed by Haas and Sturtevant [18] in 1987. They studied gas bubbles filled with either helium or chlorodifluoromethane (R22), surrounded by air, and contributed with their results to a better understanding of the temporal bubble evolution under shock acceleration and established a new class of canonical flow configurations. Quirk and Karni [19] complemented these experimental findings by their detailed numerical results of shock–bubble interaction problems. Shock wave focusing, formation of a jet towards the center of the bubble and the transition from regular to irregular refraction were reproduced. For a detailed review of ISBI the reader is referred to Ranjan et al. [1].

1.2. Reacting shock–bubble interaction

The classical setup of ISBI can be extended replacing the inert bubble gas by a reactive gas mixture. Thus, the compression and temperature increase across the shock wave induce an additional effect: the chemical reaction rates are elevated, radicals form and accumulate. For sufficiently strong shock waves, the mixture ignites and reaction waves propagate through the reactive bubble gas.

Two reaction wave types have to be distinguished: deflagration and detonation. Deflagration is a subsonic diffusion-driven reaction wave that propagates through the gas mixture due to the direct transfer of thermal energy from burning to unburned gas [20]. Detonation is driven by a fast chemical reaction and the associated large heat release within the reaction wave. A shock wave immediately precedes the detonation wave and preheats the gas mixture by compression [20]. Detonation waves propagate up to 10^8 times faster than deflagration waves [21]. The latter reaction wave is observed and studied in our numerical investigation of RSBI.

First experimental studies of RSBI were performed by Haehn et al. [22] in 2012. In their setup, a gas bubble filled with a stoichiometric mixture of H_2 and O_2, diluted by xenon (Xe) is penetrated by a shock wave with shock Mach numbers between $Ma = 1.34$ and $Ma = 2.83$. A weak shock wave with $Ma = 1.34$ does not ignite the gas mixture within the experimental timeframe. Compression is not sufficient to start a self-sustaining chemical reaction. An increase of the shock strength results in ignition, followed by a deflagration wave. The reaction wave type changes for higher shock Mach numbers; Haehn et al. [22] observed a detonation wave for $Ma = 2.83$, even before the shock wave has reached the shock focusing point. They conclude, that the post-shock thermodynamic conditions are near the ignition limits. Several chemiluminescence exposures are provided by Haehn et al. [22] to depict the qualitative evolution of the bubble and the reaction processes. The reaction wave has propagated through the bubble gas before the formation of the vortex ring is initiated. Furthermore quantitative data for the temporal evolution of the transverse diameter of the bubble as well as for the vortex ring diameter are presented. However, the complex experimental setup implies uncertainties. Haehn et al. [22] estimate the uncertainty of the Damköhler number at the highest shock Mach number ($Ma = 2.83$) of up to 50% ($Da = 8 \pm 4$). At the lowest shock Mach number ($Ma = 1.34$) 30% of all measurements showed no ignition within the given experimental time frame. Numerical studies are necessary to obtain a deeper understanding of the physics and reaction kinetics of RSBI. Accurate numerical simulations can provide detailed insight into induction times, gas compositions and mixing processes during the shock–bubble interaction.

We presented first numerical results for two-dimensional RSBI [2,3]. Pressure dependent ignition and reaction waves were in agreement with experiments of Haehn et al. [22]. Despite the missing spatial dimension, the simulations reproduced bubble expansion, ignition location and reaction wave types, and explained experimentally particularities, such as the transition from deflagration to detonation and a double detonation. Nevertheless, some important effects, especially for the long-term evolution, were suppressed as the vortex stretching term is absent in two dimensions. The two-dimensional vortex cores remain stable, whereas three-dimensional vortex rings become unstable and may break up into three-dimensional turbulence [23]. In order to obtain accurate predictions for the mixing processes in the long-term evolution of RSBI, an extension to three-dimensional simulations is needed.

1.3. Scope of the present work

The present numerical investigation extends our previous work on two-dimensional RSBI [2,3] and complements the experimental results of Haehn et al. [22] by three-dimensional RSBI simulations with detailed H_2–O_2 chemistry. At a shock Mach number of $Ma = 2.83$ the mixture ignites ahead of the shock-focusing point. Ignition is followed by a detonation wave that has a distinct effect on the hydrodynamic evolution of the RSBI. We also present results for ISBI to study the influence of the reaction wave on the mixing process, on the vortex ring and on the spatial and temporal bubble evolution. By comparison with two-dimensional simulations, we are able to show how three-dimensional phenomena, such as the decaying vortex ring, destabilized by Widnall-type instabilities, influence the long-term evolution of SBI. The experimental findings of Haehn et al. [22] are confirmed and important quantities such as the ignition delay time, the reaction wave speed, and the spatial and temporal bubble evolution are correctly reproduced.

This paper is structured as follows: Section 2 summarizes the governing equations for fluid dynamics and chemical reaction kinetics. Initial conditions and the computational domain are presented in Section 3. Section 4.1 outlines the results of the three-dimensional simulations, followed by a comparison with two-dimensional data in Section 4.2. In Section 4.3, we compare our results with the experimental work of Haehn et al. [22]. The final Section 5 summarizes the key findings.

2. Numerical model

2.1. Governing equations

We solve the full set of compressible reacting multi-component Navier–Stokes equations in conservative form

$$\frac{\partial \boldsymbol{U}}{\partial t} + \nabla \cdot \boldsymbol{F}(\boldsymbol{U}) = \nabla \cdot \boldsymbol{F}_v(\boldsymbol{U}) + \boldsymbol{S}, \tag{1}$$

with

$$\boldsymbol{U} = \begin{pmatrix} \rho \\ \rho \boldsymbol{u} \\ E \\ \rho Y_i \end{pmatrix}, \quad \boldsymbol{F}(\boldsymbol{U}) = \begin{pmatrix} \rho \boldsymbol{u} \\ \rho \boldsymbol{u}\boldsymbol{u} + p\boldsymbol{\delta} \\ (E+p)\boldsymbol{u} \\ \rho \boldsymbol{u} Y_i \end{pmatrix},$$
$$\boldsymbol{F}_v(\boldsymbol{U}) = \begin{pmatrix} 0 \\ \boldsymbol{\tau} \\ \boldsymbol{\tau} \cdot \boldsymbol{u} - \boldsymbol{q_c} - \boldsymbol{q_d} \\ \boldsymbol{J_i} \end{pmatrix} \quad \text{and} \quad \boldsymbol{S} = \begin{pmatrix} 0 \\ \boldsymbol{0} \\ \dot{\omega}_T \\ \dot{\omega}_i \end{pmatrix}. \tag{2}$$

The solution vector $\boldsymbol{U}$ consists of mass density ρ, momentum $\rho\boldsymbol{u}$, total energy E and the mass fractions Y_i of species $i = 1, 2, \ldots, N$, with N being the total number of species. The identity matrix is given by $\boldsymbol{\delta}$ and pressure by p. $\boldsymbol{q_c}$ represents the heat conduction, $\boldsymbol{q_d}$ the interspecies diffusional heat flux and $\boldsymbol{J}_i$ the species diffusion. The heat release $\dot{\omega}_T$ and species formation and destruction in terms of individual mass rates $\dot{\omega}_i$ represent the chemical reaction kinetics.

The viscous stress tensor $\boldsymbol{\tau}$ for a Newtonian fluid is given by

$$\boldsymbol{\tau} = 2\overline{\mu}\left[\frac{1}{2}\left(\nabla \boldsymbol{u} + (\nabla \boldsymbol{u})^T\right) - \frac{1}{3}\boldsymbol{\delta}(\nabla \cdot \boldsymbol{u})\right], \tag{3}$$

with $\overline{\mu}$ as the mixture viscosity. We define the heat conduction according to the Fourier law as

$$\boldsymbol{q_c} = -\overline{\kappa}\nabla T, \tag{4}$$

where $\overline{\kappa}$ is the mixture heat conductivity. The interspecies diffusional heat flux $\boldsymbol{q_d}$ [24] is defined as

$$\boldsymbol{q_d} = \sum_{i=1}^{N} h_i \boldsymbol{J}_i, \tag{5}$$

with h_i as the individual species enthalpy. The inclusion of interspecies diffusional heat flux is important to prevent anomalous temperature gradients and spurious pressure oscillations, especially in combustion processes [24]. The species diffusion $\boldsymbol{J}_i$ is given by

$$\boldsymbol{J}_i = -\rho\left(D_i \nabla Y_i - Y_i \sum_{j=1}^{N} D_j \nabla Y_j\right). \tag{6}$$

D_i describes the effective binary diffusion coefficient of species i. For a detailed description of the equations and methods used to calculate caloric and transport properties, the reader is referred to our previous papers [2,3].

We close the equations by the equation of state for an ideal gas

$$p = \rho \overline{R} T \tag{7}$$

and

$$p = (\overline{\gamma} - 1)E. \tag{8}$$

$\overline{\gamma}$ represents the ratio of specific heats of the mixture

$$\overline{\gamma} = \frac{\overline{c_p}}{\overline{c_p} - \overline{R}}, \tag{9}$$

with

$$\overline{c_p} = \sum_{i=1}^{N} Y_i c_{p,i}. \tag{10}$$

The specific gas constant of the mixture is defined by $\overline{R} = R/\overline{M}$, with R as the universal gas constant. $\overline{M}$ is the molar mass of the mixture

$$\overline{M} = \left[\sum_{i=1}^{N} \frac{Y_i}{M_i}\right]^{-1} = \sum_{i=1}^{N} X_i M_i, \tag{11}$$

where X_i is the mole fraction and M_i the molar mass of species i. $c_{p,\,i}$ represents the specific heat coefficients at constant pressure.

2.2. Reaction kinetics

Chemical reaction kinetics are represented by the source term in Eq. (1), containing the heat release $\dot{\omega}_T$ and species formation and destruction in terms of individual mass rates $\dot{\omega}_i$. The specific heat release $\dot{\omega}_T$ is defined as

$$\dot{\omega}_T = -\sum_{i=1}^{N} \Delta h^0_{f,i} \dot{\omega}_i, \tag{12}$$

where $\Delta h^0_{f,i}$ is the heat of formation of each species i. The mass rates $\dot{\omega}_i$ for each species are calculated by

$$\dot{\omega}_i = W_i \sum_{r=1}^{N_R} \nu_{ir} \Gamma_r \left(k_{fr} \prod_{i=1}^{N} [X_i]^{\nu'_{ir}} - k_{br} \prod_{i=1}^{N} [X_i]^{\nu''_{ir}}\right). \tag{13}$$

N_R is the number of reactions, W_i the molecular weight, Γ_r the third body efficiency of reaction r, X_i the molar concentration, and ν'_{ir} and ν''_{ir} the molar stoichiometric coefficients of the reactant and the product of reaction r. The net stoichiometric coefficient ν_{ir} is calculated by

$$\nu_{ir} = \nu''_{ir} - \nu'_{ir}. \tag{14}$$

The forward and backward reaction rates k_{fr} and k_{br} are calculated by the Arrhenius law,

$$k_{fr} = A_{fr} T^{\beta_{fr}} exp\left(\frac{E_{fr}}{RT}\right). \tag{15}$$

A_{fr} is the pre-exponential factor, E_{fr} is the activation energy and β_{fr} is the temperature exponent for each reaction r [25]. The equilibrium constants K_{cr} is used to estimate the backward reaction rates

$$k_{br} = \frac{k_{fr}}{K_{cr}}. \tag{16}$$

We calculate the equilibrium K_{cr} from

$$K_{cr} = \left(\frac{p^\circ}{RT}\right)^{\nu_r} exp\left(\frac{\Delta S^\circ_{r,i}}{R} - \frac{\Delta H^\circ_{r,i}}{RT}\right), \tag{17}$$

where p° is a pressure of 1 atm, ν_r the net change in the number of species in the reaction, $\Delta S^\circ_{r,i}$ the net change in entropy and $\Delta H^\circ_{r,i}$ the net change in enthalpy.

Specific intermediate reactions have to be treated as duplicated reactions, by extending Eq. (15) to

$$k_{fr} = \sum_{i=1}^{2} A_{fr_i} T^{\beta_{fr_i}} exp\left(\frac{E_{fr_i}}{RT}\right). \tag{18}$$

One reaction consists of two sets of Arrhenius rate parameters, which lead to two forward reaction rates. The sum of both reactions result in the forward reaction rates k_{fr} of reaction r.

Furthermore, pressure dependence of specific intermediate reactions is considered by the calculation of two forward reaction rates for one reaction. k_{fr_0} for the high-pressure and k_{fr_∞} for the low-pressure limit. A blending function composed of these high- and low-pressure Arrhenius rate parameters is applied for a smooth pressure dependence. For more details on the so-called fall-off reactions the reader is referred to Troe [26].

The accuracy of the reaction kinetics depends on the choice of the reaction mechanism, which provides the parameters of the

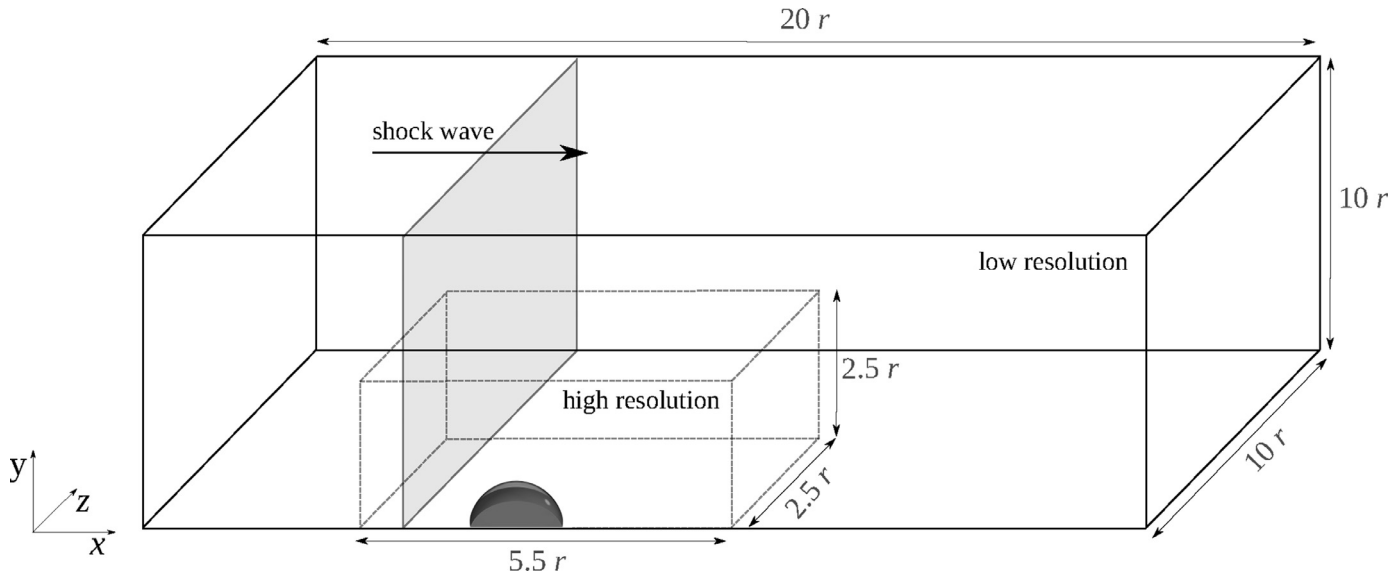

Fig. 1. Schematic of the computational domain with quarter-spherical bubble, filled with H_2, O_2 and Xe, surrounded by pure N_2.

Arrhenius law. Available mechanisms show large discrepancies in the number of reactions and species and in the consideration of third body efficiencies, duplicated and pressure dependent reactions. In RSBI, a setup which exhibits a wide pressure and temperature range, accurate results can only be achieved with a precise prediction of the ignition delay time. Therefore, utilization of a complex mechanism is inevitable, third body efficiencies, duplicated and pressure dependent reactions have to be considered. In a previous study [2], the necessity for a complex mechanism was shown. Simpler mechanisms were not able to predict the correct ignition delay time with a deviation of up to several magnitudes.

The Ó Conaire [27] reaction mechanism is applied in the presented work. The mechanism is validated for temperatures between 298 and 2700 K and a pressure range from 0.05 to 87 atm. Eight species participate in the reaction of H_2 and O_2 (two reactants: H_2, O_2; 5 chain-carrying intermediates: hydrogen radical (H), oxygen radical (O), hydroxyl radical (OH), hydroperoxyl radical (HO_2), hydrogen peroxide (H_2O_2); the product: hydrogen oxide (H_2O) and 19 intermediate reactions are considered, including duplicated and pressure dependent reactions as well as third-body efficiencies. The two-body recombination reaction is stabilized by the absorption of energy by the third-bodies. The third-body efficiencies of Xe are set as the same as for argon (Ar), which are given by Ó Conaire [27]. The available modes, controlling the energy absorption, of Ar and Xe are identical, hence the third-body efficiencies can be assumed to be comparable. Also the steric factor for monoatomic gases, accounting for the geometry influence on the collision between molecules, is similar [28].

2.3. Numerical method

We apply the 2nd-order accurate Strang time splitting scheme [29] to solve the compressible reacting multi-component Navier–Stokes equations (Eq. (1)). The splitting scheme separates the stiff terms, containing the chemical reaction kinetics ($\dot{\omega}_T$ and $\dot{\omega}_i$), from the Navier–Stokes equations. The resulting system of partial differential equations (PDE) and the stiff system of ordinary differential equations (ODE) is solved separately. The PDE system is solved by the 3rd-order Runge–Kutta time-marching scheme of Gottlieb and Shu [30] with a finite-volume discretization scheme that applies a flux projection onto local characteristics for the hyperbolic part. The Roe matrix required for the projection is calculated for the full multi-species system [31,32]. The numerical fluxes at the cell faces are reconstructed from cell averages by a central-upwind 6th-order weighted essentially non-oscillatory (WENO-CU6) scheme [33]. The scheme uses a non-dissipative 6th-order central stencil in smooth flow regions and a non-linear convex combination of 3rd-order stencils in regions with steep gradients. The characteristic flux reconstruction with general multi-component Roe-average [34] has been found necessary to avoid spurious pressure and temperature oscillations at material interfaces, which are a common problem in multi-species flows at material interfaces in general [35] and in the interaction between material interfaces and shock waves [36]. Previous studies have proven the capability for shock induced turbulent multi-species mixing problems of our scheme at finite Reynolds numbers [15,16,37,38] and for shock–bubble interactions including complex chemistry [2,3]. The stiff ODE system, containing the specific heat release and mass rates for each species is solved by a variable-coefficient ODE solver using 5th-order backward differentiation formulae [39].

3. Computational setup

3.1. Computational domain

RSBI is studied on a Cartesian grid in a three-dimensional domain with a quarter-spherical bubble, shown in Fig. 1. We impose inflow boundary conditions at the left domain boundary and outflow boundary conditions at the right, rear and upper domain boundaries. Symmetry boundary conditions are applied at the two cut surfaces of the bubble. The domain size is set to 20 r × 10 r × 10 r, with r as the initial bubble radius. The distance to the boundaries is chosen sufficiently large to avoid artifacts due to shock reflections. Grid resolution is increased around the bubble, regions outside of this area have a coarser resolution to reduce computational costs. The simulations are performed at a resolution of 140 points per radius (ppr) in the fine region, which amounts to a total number of 115 million cells.

The gas bubble is placed in a pure nitrogen (N_2) environment and contains a stoichiometric mixture of H_2, O_2 and Xe in a composition of 2 / 1 / 3.67 mole fractions. The heavy inert gas Xe increases the Atwood number to $A = 0.476$. The bubble radius is set to $r = 0.02$ m. A sharp and fully resolved interface between the bubble gas and the surrounding is defined in terms of the molar

fraction of N_2

$$X_{N_2} = \frac{\tanh((\sqrt{x^2+y^2+z^2} - r)\,\xi) + 1}{2}, \tag{19}$$

with r as the radius of the bubble and ξ as the parameter controlling steepness, which is set to $\xi = 20.000\ \mathrm{m}^{-1}$. The molar fraction ($X = 1 - X_{N_2}$) inside the bubble is distributed among the three gases, ensuring the stoichiometric mixture with a relative composition of 2 / 1 / 3.67 (H_2 / O_2 / Xe).

The shock wave propagates from the left to the right and is initialized near the upstream pole of the bubble. The pre-shock state is defined by $T_0 = 295$ K and $p_0 = 1.0$ atm. The shock Mach number is set to $Ma = 2.83$. The post-shock thermodynamics state is defined by standard Rankine–Hugoniot conditions

$$\rho'_{N_2} = \rho_{N_2} \frac{(\gamma_{N_2}+1)Ma^2}{2 + (\gamma_{N_2}-1)Ma^2}, \tag{20}$$

$$u'_{N_2} = Ma\, c_{N_2} \left(1 - \frac{\rho_{N_2}}{\rho'_{N_2}}\right), \tag{21}$$

$$p'_{N_2} = p_0 \left(1 + 2\frac{\gamma_{N_2}}{\gamma_{N_2}+1}(Ma^2 - 1)\right), \tag{22}$$

with $c_{N_2} = \sqrt{\gamma_{N_2} p_0 / \rho_{N_2}}$, which defines the speed of sound in nitrogen. Variables indicating post-shock conditions are marked with a prime. Initial data are set as the nominal conditions of the experimental setup of Haehn et al. [22].

3.2. Convergence study

We have performed an extensive grid resolution study to establish that our simulation results are grid-converged in terms of quantities of interest. We define the resolution in points per radius (ppr) of the gas bubble. Previous studies of ISBI showed convergence between 100 and 134 ppr. Niederhaus et al. [40] simulated ISBI at 128 ppr and resolved the initial bubble interface with 2 cells. Further studies of Ranjan et al. [41] achieved a converged solution with 134 ppr at similar shock Mach numbers as applied in our investigation. Hejazialhosseini et al. [42] showed converged integral quantities at 100 ppr. Even at high shock Mach numbers of $Ma = 10$, a resolution of 120 ppr was sufficient to resolve the quantities of interest according to Nakamura et al. [43].

For our grid resolution study, we analyze the error of the molar mixing fraction Θ (MMF) for the mixing between the inert bubble gas Xe and the surrounding gas N_2. MMF can be interpreted as the ratio of molecular mixing to large-scale entrainment by convective motion and is defined by Danckwerts [44] as

$$\Theta(t) = \frac{\int_{-\infty}^{\infty}\int_{-\infty}^{\infty} \langle X_{N_2} X_{Xe}\rangle dxdz}{\int_{-\infty}^{\infty}\int_{-\infty}^{\infty} \langle X_{N_2}\rangle \langle X_{Xe}\rangle dxdz}. \tag{23}$$

The angle brackets, $\langle X_{N_2} X_{Xe}\rangle$, $\langle X_{N_2}\rangle$ and $\langle X_{Xe}\rangle$, indicate the averaging of the respective mass fractions in y-direction. The error $\Delta\,\Theta_N$ at a resolution of N ppr is defined as the difference between Θ_N and Θ_{160}, normalized by Θ_{160},

$$\Delta\Theta_N = \frac{|\Theta_N - \Theta_{160}|}{|\Theta_{160}|}. \tag{24}$$

We compare six resolutions, $N = \{50, 80, 100, 120, 140, 160\}$ ppr, where the highest resolution serves as reference. The shock Mach number, the thermodynamic initial conditions and the bubble diameter are set identical to the main simulations of the presented work. Figure 2 shows the error of the MMF for each resolution. The mixing is one of the main quantities of interest, hence the error due to spatial resolution should be reduced to a minimum. The largest discrepancy can be found during the shock wave passage in the early stage of the interaction ($t < 100$ µs). The lowest resolution of 50 ppr shows an error margin of up to 100%. The increase

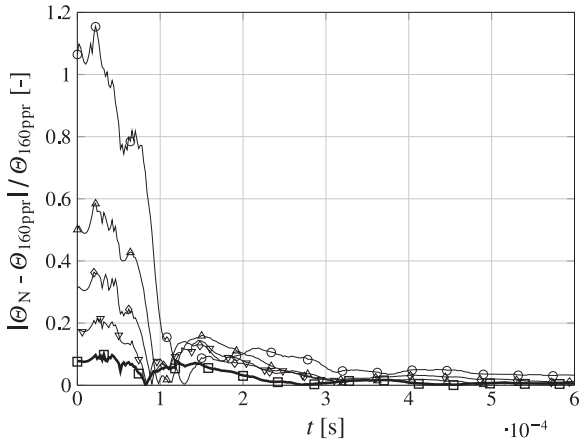

Fig. 2. Convergence of MMF. ◯ : 50 ppr, △ : 80 ppr, ◇ : 100 ppr, ▽ : 120 ppr, □: 140 ppr.

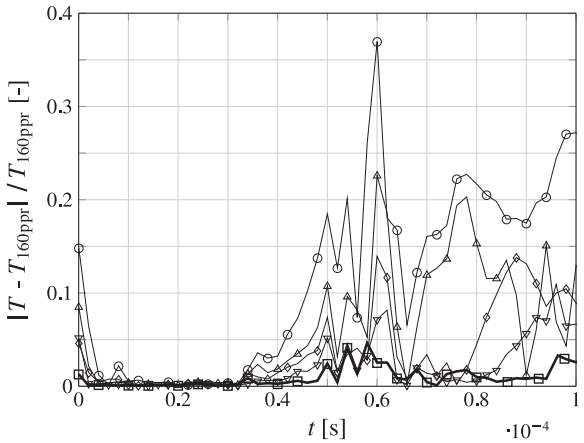

Fig. 3. Convergences of maximum temperature during shock wave passage. ◯ : 50 ppr, △ : 80 ppr, ◇ : 100 ppr, ▽ : 120 ppr, □ : 140 ppr.

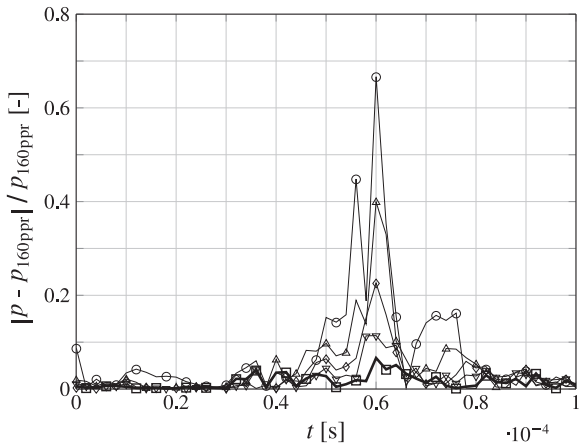

Fig. 4. Convergence of maximum pressure during shock wave passage. ◯ : 50 ppr, △ : 80 ppr, ◇ : 100 ppr, ▽ : 120 ppr, □ : 140 ppr.

of ppr leads to a successive reduction of the error. At a resolution of 140 ppr the error is reduced to less than 10% in the early stage and less than 1% in the long-term evolution of MMF, where the main emphasis of our study lays.

Besides the accurate prediction of MMF, the correct calculation of the pressure and temperature peak during the shock wave passage is important. Especially for RSBI, these two data determine the ignition delay time and the ignition spot. Figures 3 and 4 show the error of the maximum temperature and pressure during the

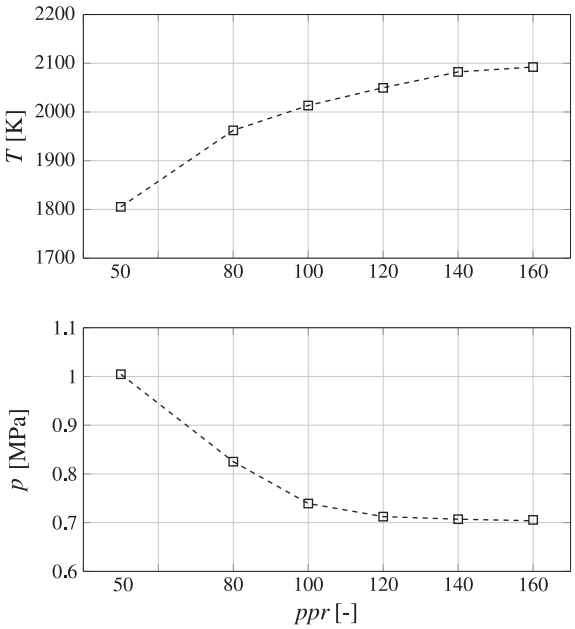

Fig. 5. Temperature and pressure peak for different resolutions at the downstream pole of the bubble during shock focusing.

shock wave passage ($t < 100$ µs). During the shock focusing at $t \approx 60$ µs a precise prediction of temperature and pressure is crucial. Similar to the earlier observation for the MMF, the coarse resolution fails in the correct prediction and an increase of ppr reduces the error significantly. At a resolution of 140 ppr, the remaining deviation amounts to only 6% of the maximum pressure and 2.5% of the temperature peak. Figure 5 shows the temperature and pressure peak for the different resolutions at the downstream pole of the bubble during shock-focusing. Both data exhibit convergent behavior.

Furthermore, the ignition delay time and the location of ignition show convergence at this resolution. The position inside of the bubble where the gas mixture ignites is not affected by a further increase in resolution. In accordance to previous studies, we choose a resolution of 140 ppr for our main simulations of RSBI, which is a higher ppr than used in all previous studies. The important parameters in the field of RSBI, the temperature and pressure peak as well as the molar mixing fraction, show convergence at a resolution of 140 ppr.

4. Results and discussion

In the following section, we present the results of the RSBI at a shock Mach number of $Ma = 2.83$. First we discuss the three-dimensional ISBI and RSBI in detail. We emphasize the effect of the reaction wave by analyzing the spatial and temporal evolution as well as integral quantities. Thereafter the results are compared with results of two-dimensional simulations to quantify the influence of three-dimensional effects on SBI. Finally we compare our results to the experimental data of Haehn et al. [22].

4.1. Three-dimensional RSBI

4.1.1. Inert bubble dynamics

Figure 6 shows surface plots at characteristic time instances of an ISBI evolution to illustrate the hydrodynamic effects induced by the interaction between the shock wave and the gas bubble. Isosurfaces of the mass fraction of xenon are shown in gray and isosurfaces of the vorticity magnitude are shown in red.

The first plot at $t = 26$ µs, Fig. 6(a), shows the bubble during the shock wave passage. Vorticity is produced at the outer interface by the misalignment of the pressure and density gradients

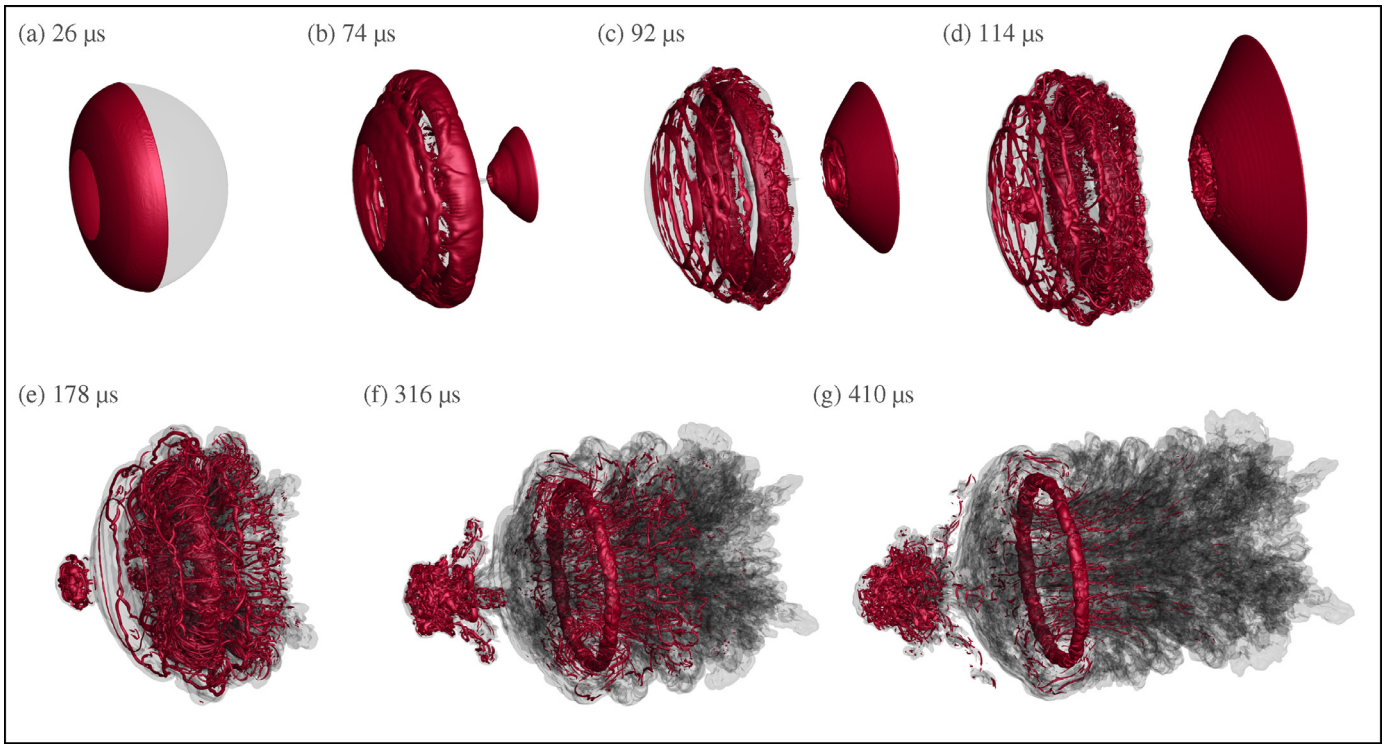

Fig. 6. Bubble evolution for ISBI at $Ma = 2.83$. The gray translucent isosurface indicates a specific mass fraction of xenon ($Y_{Xe} = 0.1$). The red colored isosurface represents a characteristic value of the vorticity magnitude ($|\omega| = 400000\ s^{-1}$) to visualize the evolution of the main vortex ring. (For interpretation of the references to color in this figure legend, the reader is referred to the web version of this article.)

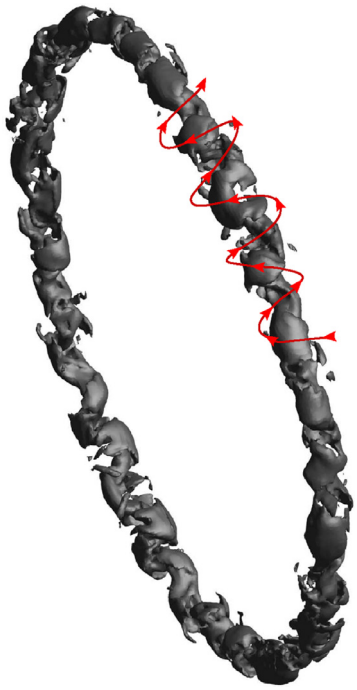

Fig. 7. Vortex ring with Widnall-type instability in the long-term evolution of ISBI ($Ma = 2.83$) at $t = 600$ μs.

(baroclinic vorticity). Figure 6(b) depicts the growth of instabilities at the interface of the bubble at $t = 74$ μs. The vorticity isosurface rings indicate regions where the roll-up of the bubble gas is initiated. Already at this early stage of ISBI, the inner vortex ring is visible. This main vortex ring is preserved throughout the entire simulation time range and shows only a slow decay. At late stages of ISBI, shown in Fig. 6(f) and (g), the vortex ring is still visible, whereas the finer vorticity structures at the outer interface have already vanished.

The surface plots at the intermediate stage of ISBI between $t = 92$ μs, Fig. 6(c), and $t = 178$ μs, Fig. 6(e), are characterized by finer filaments of vorticity, indicating the breakup of the large-scale structures at the bubble interface into smaller vortices. RMI and KHI are fully evolved, which leads to an increase in mixing, amplified by the further roll-up of the shocked bubble gas. Fine filaments of vorticity indicate regions of high vortex stretching and nonlinear energy transfer. Figure 6(e) outlines the filaments inside the roll-ups of the bubble. We also observe the formation and stretching of elongated hairpin-like structures in the azimuthal direction of the vortex core, an effect that can only be resolved in three-dimensional computations. Same observations have been made by Hejazialhosseini et al. [42] in their study of three-dimensional ISBI. Furthermore, as the bubble moves upstream, small ring-like structures are transported into the downstream direction and a jet of the surrounding N_2 transports high density fluid from the downstream pole into the core of the bubble, which ejects a mushroom-like structure of bubble gas. The blow-out structures are in very good agreement with the experimental results of Ranjan et al. [45], who accelerated a bubble, filled with Ar and surrounded by pure N_2, with a shock wave with $Ma = 2.88$ and observed the same mushroom-like structure at the upstream pole of the bubble.

We observe that the main vortex ring becomes unstable at late stages. Figure 7 shows the vortex ring at $t = 600$ μs, destabilized by azimuthal bending modes. Our observations are in very good agreement with the results of Klein et al. [46]. They also observed that their shocked sphere undergoes an azimuthal bending mode instability, which is analogous to the Widnall instability [47]. An unstable vortex ring due to the growth of azimuthal modes is also reported by Niederhaus et al. [40] in their investigation of vorticity evolution in two- and three-dimensional simulations of ISBI, as well as in the study of Hejazialhosseini et al. [42], analyzing the vortex dynamics in three-dimensional ISBI. Furthermore they observed a restriction for the growth of Widnall-type instabilities: the Atwood numbers has to be larger than 0.2 to induce the azimuthal instability, which is fulfilled in our setup with an Atwood number of $A = 0.476$. The destabilized vortex ring significantly affects the mixing process at late stages of evolution.

4.1.2. Chemically reacting bubble dynamics

The consideration of chemical reaction kinetics in RSBI changes the spatial and temporal bubble evolution significantly. The stoichiometric H_2–O_2 gas mixture is compressed and heats up during the shock-wave passage. The convex shape of the bubble increases this effect by shock focusing. The mixture ignites, if at a certain point a sufficient amount of radicals has been formed. Depending on the shock strength, the ignition point moves from the shock-focusing point at the downstream pole of the bubble for low shock Mach numbers up to the upstream pole for high shock Mach numbers [3].

The ignition spot and the propagation of the reaction wave is shown in Fig. 8. Each set of isosurface and isocontour plots contains a two-dimensional slice and a three-dimensional rendering of the RSBI. Figure 8(a) shows the bubble shortly after ignition. The solid line represents the initial shock wave, propagating from left to right. The gas mixture is ignited directly behind the shock wave after a short induction time and propagates as a combustion ring through the bubble gas. At the early stage of combustion the reaction wave spreads radially in all spatial directions, see Fig. 8(b). After approximately 10 μs, the reaction wave has consumed most of the bubble gas and a torus-like region of burned gas is formed, which is outlined in Fig. 8(c). The last set of isosurface and isocontour plots in Fig. 8(d) shows the RSBI at $t = 100$ μs. The H_2–O_2 mixture has been burned, shock reflections cause a complex temperature field inside the bubble and the roll-up with the formation of the main vortex ring is initiated. The propagation of the detonation wave towards the shock-focusing point and the subsequent blow out of bubble gas leads to a characteristic jellyfish-like structure of three-dimensional RSBI.

For the investigation of the induction and ignition process, we analyze the accumulation of radicals during the shock wave passage, shown in Fig. 9. Exemplary for the five intermediate species, we plot the maximum concentration of the radicals HO_2 and H_2O_2 and the temperature in the early stage of RSBI ($t < 100$ μs). The maximum temperature in the flow field serves as an indicator for the ignition. First radicals are formed directly after the shock wave impacts the bubble ($t = 2$ μs). Thereafter the mass fractions of HO_2 and H_2O_2 increase slightly until $t = 38$ μs, however the production rates are insufficient to ignite the gas mixture or to start a chain reaction. At $t = 38$ μs, the initial shock wave reaches the ignition point and the induction phase starts. We observe a sudden increase in the formation of the radicals accompanied by a slight temperature rise. The chain reaction starts and finally ignites the gas mixture at $t = 42$ μs. The following reaction wave propagates through the bubble gas and has burned the stoichiometric mixture at $t = 56$ μs. The slight decline of the maximum temperature indicates the termination of the main reaction. Further fluctuations of the radicals and the temperature are caused by shock waves, which re-induce some weak reactions to sustain the chemical equilibrium.

Figure 10 compares the spatial and temporal bubble evolution between three-dimensional RSBI (left column) and ISBI (right column). The slices depict the density in the upper parts and the mix-

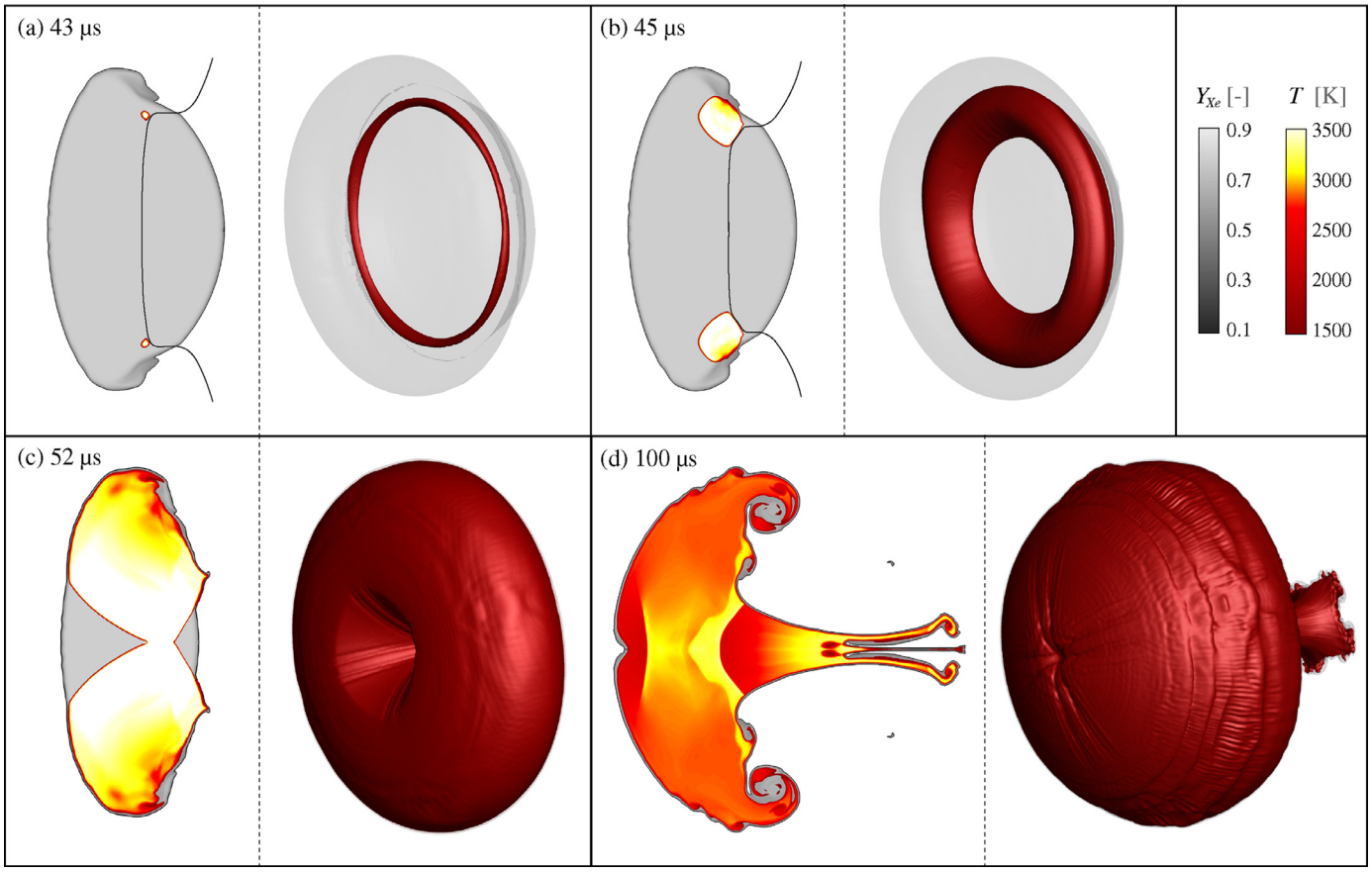

Fig. 8. Ignition and detonation wave propagation in a RSBI with a shock Mach number of $Ma = 2.83$. For two-dimensional plots: Gray color scale shows the xenon mass fraction, red–yellow color scale the temperature with a cutoff at $T = 1500$ K. Black lines in (a) and (b) depict the initial shock wave, propagating from left to right. For three-dimensional plots: red isosurface depicts the temperature at cutoff level of $T = 1500$ K, gray isosurface illustrates the bubble shape ($Y_{Xe} = 0.1$). (For interpretation of the references to color in this figure legend, the reader is referred to the web version of this article.)

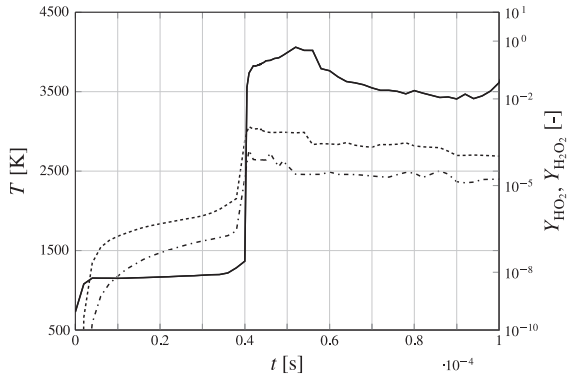

Fig. 9. Maximum temperature and radical mass fractions during the early stage of RSBI, including induction time, ignition and reaction wave propagation. ——: temperature; ……: Y_{HO_2}; - - - -: $Y_{H_2O_2}$.

ing between the inert gas Xe and the surrounding gas N_2 in the lower part ($Y_{N_2} \cdot Y_{Xe}$). The bubble gas is highly mixed with the surrounding gas in dark colored zones and less mixed in regions with lighter color. In addition the mass fraction peak of hydroperoxyl radicals illustrate the reaction wave front. During the compression and ignition stage of the RSBI, outlined in Fig. 10(a), no influence of the chemical reaction kinetics on the bubble evolution is visible. The spatial expansion is initially influenced after the reaction wave reaches the interface, see Fig. 10(b). Thereafter, the growth of secondary instabilities is significantly affected. Figure 10(c) shows the early growth stage of KHI at the outer interface for the ISBI, whereas the RSBI lags of these instabilities. The detonation wave damps the growth of KHI as well as the formation of the vortex core. There are two reasons for this deceleration: The detonation wave induces vorticity with opposite sign compared to the vorticity produced by the initial shock wave and thus reduces the total vorticity at the interface. Additionally, increased molecular diffusion across the reaction wave reduces the growth rate of the instabilities. The temperature increase across the reaction front and the spatial expansion decreases the density and increases the viscosity of the bubble gas. The fourth contour plot, Fig. 10(d), shows that the density of the bubble gas is even lower than the surrounding gas, which is in contrast to the inert SBI, where the density of the bubble gas is significantly higher than the density of the surrounding N_2. Figure 10(c) and (d) illustrate the blow-out of bubble gas and the formation of the jellyfish-like structure of RSBI, characterized by a smoother, less mixed, interface compared to the inert SBI. The last set of contour plots (e) at $t = 450$ µs shows the long-term spatial evolution of the inert and reacting bubble. The two simulations clearly differ: RSBI on the left side is characterized by the blow-out of large amounts of bubble gas in downstream direction, forming a nozzle-like structure. Surrounding gas is transported along the center axis in upstream direction and penetrates the gas bubble. Strong mixing takes place near the vortex ring and in the upstream region. However, most of the bubble gas in the downstream region is nearly unmixed. The ISBI shows a different evolution, large areas of the bubble are mixed with the surrounding. The unimpeded growth of instabilities accelerates the mixing especially in the downstream part and in the blow-out region at

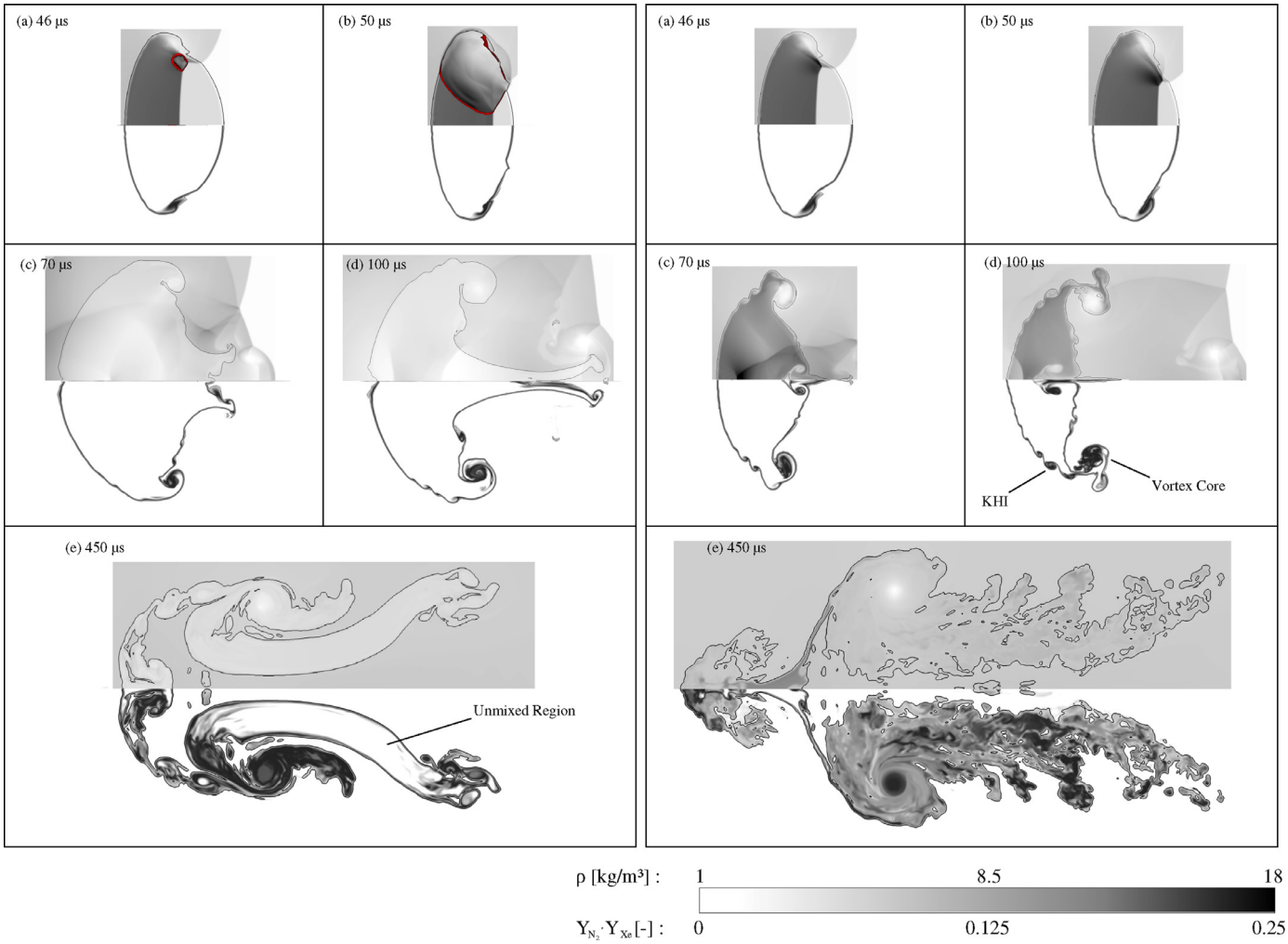

Fig. 10. Evolution of three-dimensional RSBI (left) and ISBI (right). Isolines of $Y_{Xe} = 0.1$ outlines the bubble interface. The contour plot shows density (top) and mixing of the two inert gases (bottom) for five instants. The reaction wave front is indicated by the peak of Y_{HO_2} in red color scale (first two contour plots on the left side). (For interpretation of the references to color in this figure legend, the reader is referred to the web version of this article.)

the upstream pole of the bubble, only the throat region exhibits small amounts of unmixed bubble gas.

Figure 11 shows the temporal evolution of regions with high vorticity in the RSBI at four characteristic time steps. In contrast to the ISBI shown in Fig. 6, which is characterized by a highly mixed bubble gas with a large number of fine filaments of vorticity, the surface plots of the RSBI show that vorticity is concentrated inside the bubble in form of several distinct vortex rings. Despite the chemical reaction and the different spatial bubble evolution, we observe a similar main vortex ring as in ISBI, however, with a slightly smaller diameter. Beside the main vortex ring, the RSBI shows three additional vortex rings (Fig. 11(b)), whereas the one with the largest diameter shows a highly unstable behavior already at $t = 300$ µs. The three additional vortex rings are transported downstream and circulate around the main vortex ring. They are characterized by a successive decay, the largest vortex ring has vanished completely at $t = 450$ µs, see Fig. 11(c). Figure 11(d) shows the vortex rings at $t = 580$ µs; the tail of the shocked bubble is transported further downstream and the additional vortex rings are dispersed into small filaments of vorticity. Only the main vortex ring persists, however, with a strongly disturbed structure. Furthermore, we observe a roll-up of the bubble gas around the vortex ring (illustrated with a set of arrows in Fig. 11(c)) and the growth of instabilities in the upstream region around the vortex ring. The animation available with the online version of the paper shows the rotation of the smaller vortex rings around the main vortex ring and clarifies the temporal decay.

4.1.3. Transverse bubble diameter

The reaction wave has a distinct influence on the spatial expansion of the bubble. To quantify the impact of the chemical reaction, we analyze the normalized transverse bubble diameter (TBD), which is defined as $\widetilde{\Lambda}_y = \Lambda_y / D_0$. The TBD describes the maximum spatial expansion of the bubble gas in transverse direction (Λ_y), normalized by the initial bubble diameter D_0 . The bubble diameter Λ_y is measured based on a threshold value of the xenon mass fraction of $Y_{Xe} = 0.01$. Figure 12 depicts the temporal evolution of TBD for ISBI (solid line) and RSBI (dashed line). Contour plots of the bubble at three characteristic time steps are plotted in Fig. 13, showing the mass fraction of Xe to illustrate the different shape of ISBI and RSBI. The bubble diameters of the two simulations are identical at the early stage of the evolution. The shock wave compresses the bubble gas and hence the TBD is reduced. At $t = 42$ µs the reactive gas mixture is ignited and the subsequent reaction wave leads to a significant expansion of the bubble gas. The first contour plots (a) in Fig. 13 show the expansion at $t = 100$ µs. The point in time where the RSBI shows the highest $\widetilde{\Lambda}_y$. The temperature rise and density decrease across the reaction front leads to a higher bubble volume, compared to the ISBI. Thereafter, the TBD of the RSBI decreases and large compact parts of the bubble gas are

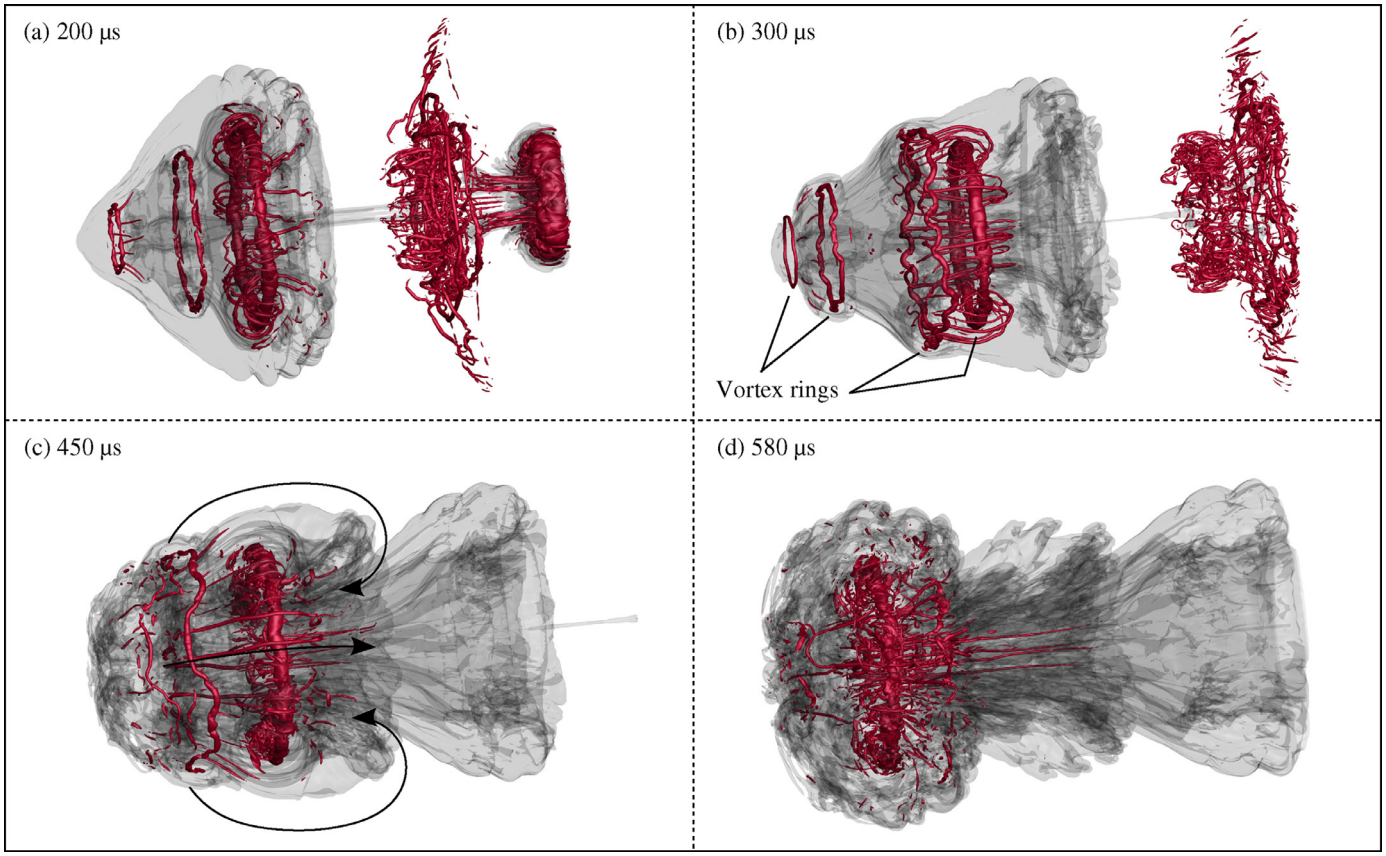

Fig. 11. Vortex ring evolution for RSBI at four characteristic timesteps. Gray translucent isosurface shows a specific mass fraction of xenon (Y_{Xe} = 0.1). The red isosurface represents a characteristic value of the vorticity magnitude ($|\omega|$ = 400,000 s^{-1}) to visualize the evolution of the vortex structure, including the main vortex ring. (For interpretation of the references to color in this figure legend, the reader is referred to the web version of this article.)

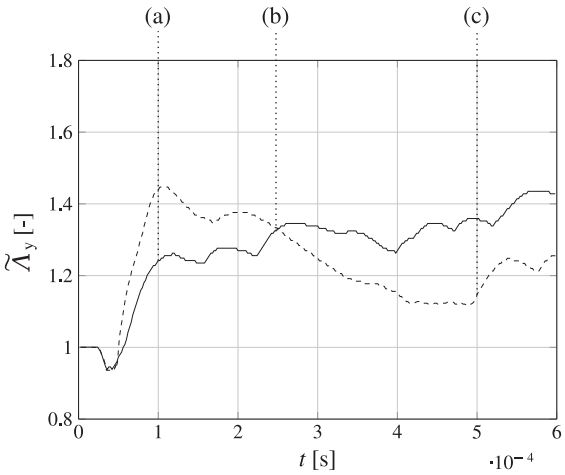

Fig. 12. Normalized transverse bubble diameter for three-dimensional ISBI and RSBI. ——: non reacting; ……: reacting.

transported downstream. In contrast, the TBD of the ISBI shows a different behavior: Figure 12 shows a continuous increase of the bubble diameter over time, the high vorticity leads to a successive expansion in transverse and downstream direction. The inert and reacting TBDs intersect at $t = 244$ µs. The contour plots, Fig. 13 (b), reveal that the vortex ring of the ISBI is more outbound and developed than the reacting counterpart. In the long-term evolution, Fig. 13(c) at $t = 500$ µs, the ISBI shows a highly mixed bubble gas, which has spread in the streamwise as well as in the transverse

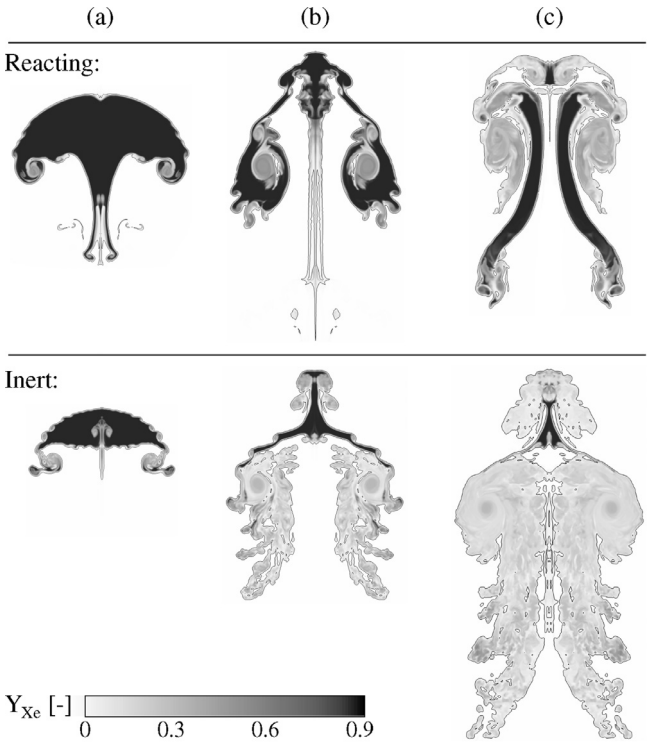

Fig. 13. Characteristic contour plots for three-dimensional ISBI and RSBI. Gray color scale indicates the mass fraction of Xe (Y_{Xe}). (a): $t = 100$ µs; (b): $t = 244$ µs; (c): $t = 500$ µs.

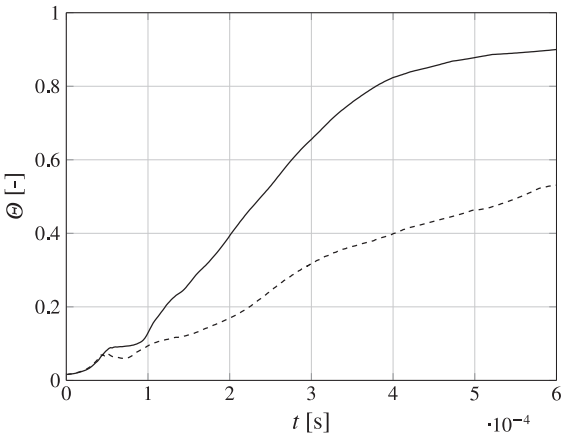

Fig. 14. Molar mixing fraction for three-dimensional ISBI and RSBI. ____: inert; .....: reacting.

direction. The RSBI shows a more complex behavior: the TBD is reduced until $t = 400$ µs, the diameter of the main vortex ring decreases and determines the maximum spatial expansion. Thereafter, the diameter of the vortex ring is smaller than the diameter of the nozzle-like structure in the downstream part of the bubble for approximately 100 µs. This structure remains stable and therefore the TBD stays nearly constant. However, after $t = 500$ µs the roll-up of the bubble gas around the vortex ring leads to a spatial expansion and an increase of the TBD. We outline both stages; Fig 11(c) shows the RSBI before the roll-up with a maximum TBD in the nozzle-like region and Fig 11(d) during the roll-up of the bubble gas and the subsequent increase in the diameter at the upstream regions of the shocked bubble.

4.1.4. Mixing in RSBI

The results shown in Figs. 10–13 have indicated distinct deviations in the mixing behavior of the bubble gas between ISBI and RSBI. For quantification, we analyze the temporal evolution of the molar mixing fraction (MMF) in Fig. 14, as defined in Eq. (23) in Section 3.2. During the early stage of the simulations, the MMF shows the same increase for both cases. The molar mixing fraction differs only after the ignition of the bubble gas. The MMF of the ISBI increases during the shock wave passage and levels for approximately $\Delta t = 40$ µs. Within this period, the shock-induced secondary instabilities start to evolve. After their formation, they contribute significantly to the MMF, which increases linearly for the next 250 µs, followed by a leveling at approximately $\Theta = 0.9$. This integral quantity confirms the observation of a highly mixed bubble gas, based on the three-dimensional isosurface plots of the ISBI in Fig. 6. The RSBI shows a different evolution: after ignition, the subsequent detonation wave flattens the bubble interface and decreases the MMF slightly. Thereafter, mixing increases, but with a significant lower rate compared to the inert counterpart. Similarly to ISBI, secondary instabilities act as a main driver of mixing, however, due to the detonation wave, these instabilities exhibit a different evolution. As shown in the contour plots in Fig. 10, the growth of instabilities is decelerated by the reaction wave, leading to a lower MMF the RSBI. At the end of the simulated time range, the RSBI MMF amounts to approximately $\Theta = 0.53$. Large regions of unmixed bubble gas remain, especially in the nozzle-like structure in the downstream region. In total, mixing is reduced by up to 40% compared to the inert case.

4.2. Comparison with two-dimensional simulations

In the following section, we compare the three-dimensional results to two-dimensional simulations at the same shock Mach number of $Ma = 2.83$. We use the same grid resolution for both simulations. Differences are expected, particularly at late stages of SBI evolution. Figure 15 shows contour plots at characteristic stages; the left box contains the two-dimensional plots and the right box the three-dimensional results. The isocontour lines of $Y_{Xe} = 0.1$ illustrate the bubble interface and indicate the interface deformation pattern. The upper parts of Fig. 15 outline the density, the lower part the vorticity magnitude. The first plots (a) show no differences between two- and three-dimensional simulations during the shock wave passage at $t = 66$ µs. During the growth stage of the KHI, annotated in the second contour plots (b), no three-dimensional effects can be observed at the outer interface. First differences become visible during the intermediate ISBI stage, see Fig. 15(c) and (d). The vorticity in the two-dimensional simulation coalesces in a compact vortex ring. A vortex pair propagates in the upstream direction, followed by a jet of N_2 in the center axis of the bubble. The N_2-jet is shown in the magnified sections in Fig. 15(c), detail and Fig. 15(d), detail (left column). The three-dimensional simulation shows a different evolution: The vortex ring is in a more outbound position and less compact. We observe a higher degree in mixing already in the intermediate stage of ISBI and the growth rates of the KHI are decelerated. Furthermore, the N_2-jet is absent; however, a jet of bubble gas is formed and propagates in the upstream direction, resulting in a mushroom-like structure in the long-term evolution, see Fig. 15(e). The missing jet was also reported by Giordano and Burtschell [48] in their study of RMI in two- and three-dimensional ISBIs. The long-term evolution is dominated by the effect of the vortex stretching term, which is absent in two-dimensional simulations. Vortex stretching leads to an elongation of the bubble gas in streamwise direction. The contour plots emphasize the different evolution of two- and three-dimensional simulations in the late stage of ISBI. The flow field shows large discrepancies in terms of spatial expansion and mixing. The isocontour lines of xenon show a cloud of mixed bubble gas for the three-dimensional domain, containing complex turbulent structures. The two-dimensional simulation preserves a sharp interface between the shocked bubble and the surrounding, especially at the outer interface. Obviously two-dimensional simulations cannot reproduce Widnall-type instabilities, which are responsible for the destabilization of the vortex ring in the long-term evolution [49]. This results in a less mixed structure of the shocked bubble at the late stages of two-dimensional SBI.

The normalized bubble diameters for ISBI and RSBI calculated from two- and three-dimensional simulations are plotted in Fig. 16 and support the observation from the contour plots in Fig. 15. The diameters for the inert simulations (◯) are nearly identical until $t = 70$ µs, thereafter the evolution differs. Both diameters increase in time, however with different slopes: The three-dimensional SBI (solid line) is characterized by a lower slope compared to the two-dimensional setup (dashed line), which leads to a successive divergence of the bubble diameters. This observation is in accordance with previous studies: Wang et al. [50] also measured a smaller bubble diameter in their study of three-dimensional ISBI in comparison with two-dimensional ISBI. These differences are caused by the missing vortex stretching in two dimensions, which reduces the spanwise expansion in the long-term evolution. Hejazialhosseini et al. [42] examined the vorticity growth rates during ISBI at different shock Mach numbers and also emphasized the importance of the vortex stretching term for the expansion in the long-term evolution. The TBD confirms the qualitative analysis of the spatial and temporal bubble evolution in Fig. 15.

RSBI (□) also show a different evolution in two-dimensional and three-dimensional simulations. The bubble diameter evolves similarly at the early stage and exhibits the same ignition delay time, which confirms that the induction time is not significantly affected by three-dimensional effects. However, the subsequent

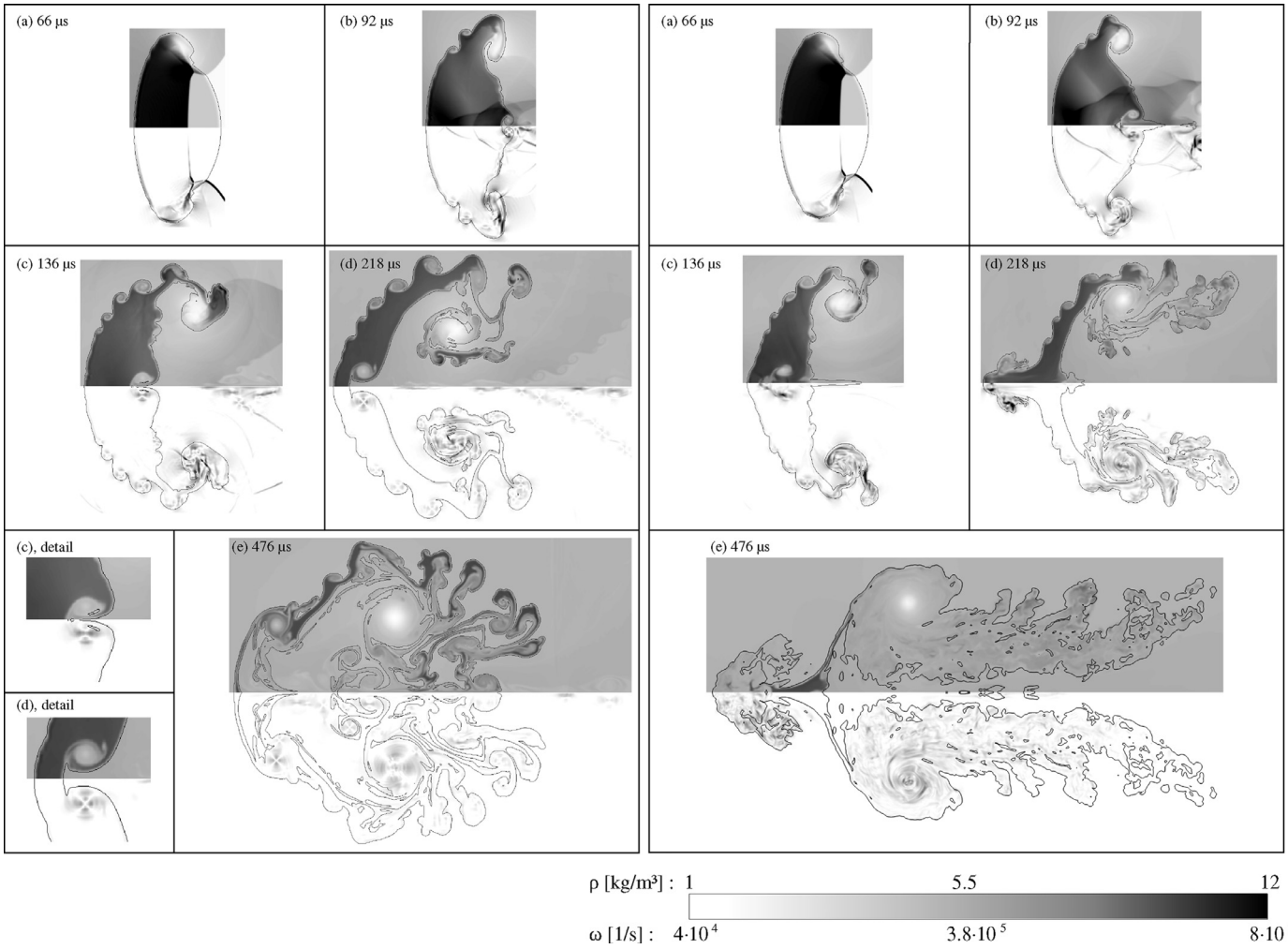

Fig. 15. Bubble evolution of two-dimensional (left) and three-dimensional (right) simulations of ISBI at a shock Mach number of Ma = 2.83. Isocontours of $Y_{Xe} = 0.1$ outlines the bubble interface. Density (top) and vorticity magnitude (bottom) show different evolution at five time steps. N_2-jet is illustrated in the magnified sections in (c), detail and (d), detail.

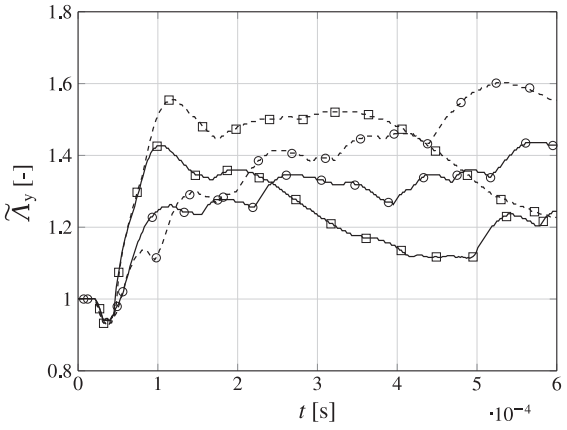

Fig. 16. Comparison of TBD for two- and three-dimensional SBI. ——: three-dimensional simulations; ……: two-dimensional simulations; ○: ISBI; □: RSBI.

expansion of the reacted bubble gas differs: the two-dimensional simulations leads to a 10% higher expansion. The following temporal evolution is similar, both TBD decrease. However, the two-dimensional RSBI shows a slower reduction, which increases the divergence until $t = 400$ µs. Thereafter, the TBD is constant and increases again after $t = 500$ µs, caused by the roll-up of the bubble gas around the main vortex ring. This effect is absent in two dimensions, see Section 4.1.2. Similarly to the inert simulations, the missing vortex stretching term causes a different spatial evolution. Especially between $t = 40$ and 120 µs, where the TBD diverges, the vortex stretching term exhibits the highest magnitude in the three-dimensional simulation.

The influence of the additional dimension on the mixing is shown in Figure 17 for the MMF of ISBI and RSBI. The mixing is highly influenced by the additional dimension for both cases. The inert simulations show an increase in mixing during the early stages of the shock wave passage, $t < 50$ µs, and leveling during the shock focusing. Then the mixing raises again, where the three-dimensional ISBI shows a much higher slope than the two-dimensional ISBI, which leads to a higher overall mixing. In the long-term evolution of the three-dimensional ISBI, the bubble is highly mixed and eventually levels out at a MMF of about 90%. The two-dimensional ISBI shows a mixing of approximately 70% at the end of the simulated timeframe, still exhibiting a positive slope, which indicates that the mixing may further increase in time. The better mixing can be explained by the instability of the vortex ring, which contributes to an enhancement in mixing. This effect was also observed by Klein et al. [46] in their investigation of the interaction of strong shock waves with interstellar clouds. Furthermore, the three-dimensional stretching term increases the spanwise

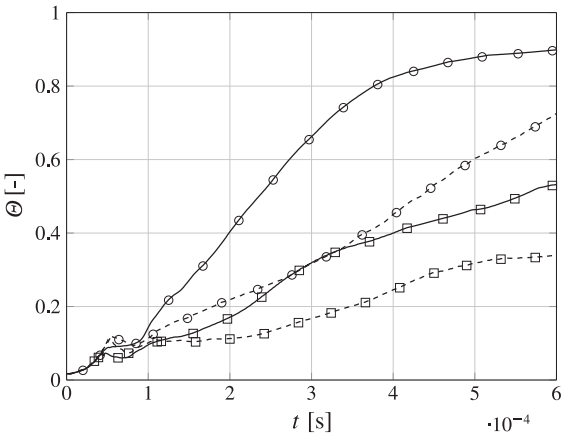

Fig. 17. Comparison of MMF for two- and three-dimensional SBI. ——: three-dimensional simulations; ……: two-dimensional simulations; ○: ISBI; □: RSBI.

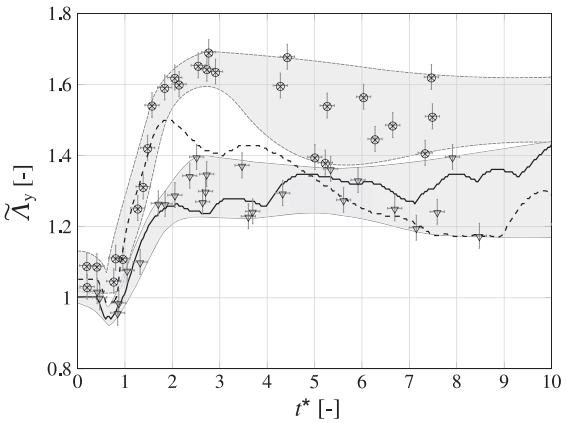

Fig. 18. Comparison of TBD for three-dimensional SBI and experimental data. ——: ISBI; ……: RSBI; ▽: ISBI; ⊗: RSBI.

expansion of the bubble gas and contributes to the higher degree in mixing. RSBI shows only weak similarity to the inert counterpart: the three-dimensional simulation shows also a higher mixing than the two-dimensional RSBI. At the end of the simulated timeframe the mixing of the three-dimensional simulation amounts to approximately 53%, which is lower than for the three-dimensional ISBI. The MMF of the two-dimensional RSBI amounts only to about 35% and starts to level at the end of the simulated timeframe.

4.3. Comparison with experimental data

We compare simulation data with experimental results of Haehn et al. [22]. The nominal initial conditions of their experiments are identical to our numerical setup. Figure 18 shows the TBD for the inert and reacting simulation and the experimental data. The experimental data are provided with the normalized time, $t^* = (tW_i)/D_0$, which is retained for the plots in Fig. 18 and Fig. 19. The normalization uses the hydrodynamic time scale τ_H, which is defined as $\tau_H = D_0/W_i$, with the initial bubble diameter D_0 and the incident shock wave speed W_i. The experimental data contain large uncertainties in time and space and are an ensemble average from several realizations. The scattering between the different experiments is indicated by the gray shaded area. The inert simulation (solid line) agrees well with the experimental data (▽). The decrease of the bubble diameter by the compression of the shock wave at $t^* \approx 0.8$ is resolved as well as the subsequent expansion of the bubble gas in spanwise direction. After $t^* > 2$ the main expansion is completed and the TBD increases only slightly

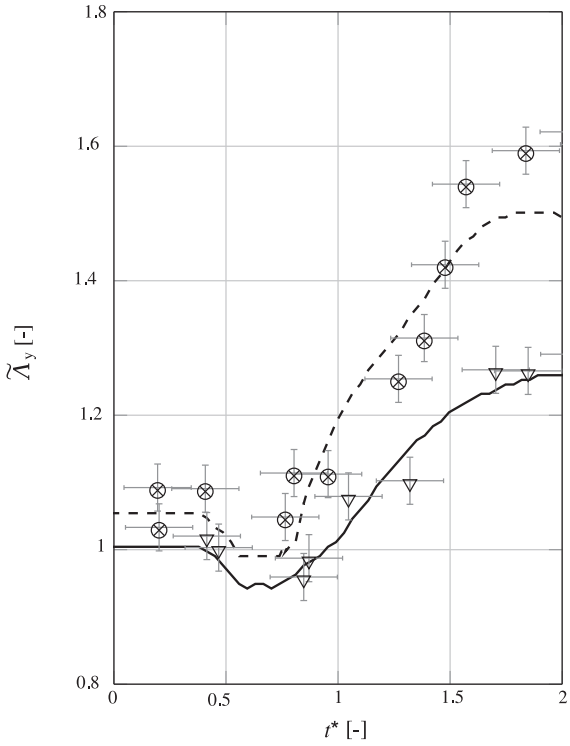

Fig. 19. Detailed section of the early stage of TBD for three-dimensional SBI and experimental data. ——: ISBI; ……: RSBI; ▽: ISBI; ⊗: RSBI.

in time, which also is in good agreement with the measured spanwise length of the bubble.

The comparison of the TBD for the RSBI is less conclusive. The experimental pre-shock bubble diameter deviates up to 9% from the nominal diameter. Hence, we adjusted our initial bubble diameter to the average of the measured values of Haehn et al. [22]. The sudden expansion in the early stage until $t^* = 2$, induced by the detonation wave, shows very good agreement. Figure 19 outlines the ignition and expansion stage in detail. The slope of the diameter increase agrees very well, which indicates that the propagation velocity of the reaction waves are identical. Thereafter, the increase of the experimentally measured TBD continues, whereas the numerical simulation predicts a slight decrease. Unfortunately, the available data of Haehn et al. [22] do not include the roll-up stage of the RSBI, $t^* > 9$. The deviation of the RSBI bubble diameter may be attributed to several reasons. The challenging experimental measurement of the spanwise length of the reacted bubble gas leads to a high scattering. Besides the deviation of the pre-shock bubble diameter of up to 9% from the nominal value, the burned bubble gas shows a large scatter on the long-term evolution, which can be explained by the sensitivity of the chemical reaction kinetics on the gas composition and on the shock Mach number. Haehn et al. [22] quantified the uncertainty of the initial shock Mach number to ± 0.03 and the uncertainty in the gas mixture composition to ± 3%. Both variations influence the ignition delay and, more importantly, the ignition location significantly. Tritschler et al. [37] performed a detailed uncertainty analysis of two-dimensional ISBI and showed that already small deviations in the initial gas composition highly affect the bubble evolution. Furthermore, the deviation from the nominal initial bubble diameter influences the SBI. Zou et al. [51] studied different bubble aspect ratios in a ISBI and revealed a distinct impact on the spatial bubble evolution, the vorticity production and the vortex ring diameter. Similar observation have been made by Georgievskiy et al. [52].

They studied spherical and slightly stretched bubbles and observed a distinct influence on the thermodynamic post shock properties.

The position of the ignition and the resulting direction of the detonation wave influence the spatial expansion of the bubble significantly. We assume that the ignition in our simulation occurs at a slightly different position than in the experiment, which leads to a small deviation in the propagation direction. The detonation wave of the experimental RSBI spreads partially in the transverse direction, whereas the reaction wave in our simulations mainly propagates in the streamwise direction, which leads to a lower TBD in the simulations. We believe that the TBD has a high sensitivity to the ignition spot, respectively to the shock Mach number and the bubble shape. A set of two-dimensional simulations with slightly different shock Mach numbers confirms this assumption. Deviations of the shock strength in the range of $Ma \pm 0.03$, which is within the nominal uncertainty of the experimental data, have a strong effect on the TBD. A detailed uncertainty quantification is beyond the scope of the presented work and recommended for prospective investigations. Nevertheless, the reaction wave speed and the spatial bubble expansion of ISBI confirm the very good overall agreement of our simulation with the experimental data.

5. Conclusion

We have presented three-dimensional numerical simulations of a reacting shock–bubble interaction (RSBI) with detailed H_2-O_2 chemical reaction kinetics. A shock wave with a Mach number of $Ma = 2.83$ accelerates a gas bubble, filled with a stoichiometric gas mixture of H_2 and O_2, diluted by Xe. During the shock wave passage, the initial shock wave is reflected, transmitted and diffracted, which triggers the Richtmyer–Meshkov and secondary instabilities. Furthermore, the passage of the shock leads to a compression of the bubble gas and a sudden jump in the thermodynamic properties, sufficient to ignite the reactive gas mixture. The following reaction wave in turn interacts with the bubble interface and affects the spatial and temporal evolution as well as the mixing of the bubble gas.

Ignition of the bubble gas is observed upstream of the downstream pole of the bubble. The shock wave is sufficiently strong to ignite the mixture without additional compression in the shock-focusing point. The following reaction wave is a supersonic detonation wave, which suppresses the growth of secondary instabilities and reduces mixing by up to 40% compared to the inert simulation. Furthermore, the reaction wave decreases the spatial expansion in the transverse as well as in the streamwise direction.

The comparison of three- and two-dimensional RSBI reveals the distinct influence of three dimensional effects on the bubble evolution. We observed differences in the long-term evolution: the two-dimensional vortex core remains stable, whereas the three-dimensional vortex ring is destabilized by Widnall-type instabilities. The vortex stretching term, which is absent in two-dimensional simulations, increases the spatial bubble expansion of the three-dimensional simulation in the streamwise direction. Both effects, the breakdown of the vortex ring and the vortex stretching, increase the mixing significantly. Furthermore, comparison with experimental data showed very good agreement in terms of ignition delay time, reaction wave propagation velocity and spatial expansion rate. While a detailed quantification of parametric uncertainties was not the goal of this paper, we recommend further exploration of the effect of initial-data uncertainties on the long-term evolution for future work.

Acknowledgment

The authors gratefully acknowledge the Gauss Centre for Supercomputing e.V. (http://www.gauss-centre.eu) for funding this project by providing computing time on the GCS Supercomputer SuperMUC at Leibniz Supercomputing Centre (LRZ, http://www.lrz.de).

This project has received funding from the European Research Council (ERC) under the European Union's Horizon 2020 research and innovation programme (grant agreement No 667483).

Supplementary material

Supplementary material associated with this article can be found, in the online version, at 10.1016/j.combustflame.2017.03.026.

References

[1] D. Ranjan, J. Oakley, R. Bonazza, Shock–bubble interactions, Annu. Rev. Fluid Mech. 43 (1) (2011) 117–140.
[2] F.R. Diegelmann, V. Tritschler, S. Hickel, N.A. Adams, On the pressure dependence of ignition and mixing in two-dimensional reactive shock–bubble interaction, Combust. Flame 163 (2016) 414–426.
[3] F.R. Diegelmann, S. Hickel, N.A. Adams, Shock Mach number influence on reaction wave types and mixing in reactive shock-bubble interaction, Combust. Flame 174 (2016) 085–099.
[4] W.D. Arnett, The role of mixing in astrophysics, Astrophys. J. Suppl. 127 (2000) 213–217.
[5] A.M. Khokhlov, E.S. Oran, G.O. Thomas, Numerical simulation of deflagration-to-detonation transition: the role of shock-flame interactions in turbulent flames, Combust. Flame 117 (1–2) (1999) 323–339.
[6] R.S. Craxton, K.S. Anderson, T.R. Boehly, V.N. Goncharov, D.R. Harding, J.P. Knauer, R.L. McCrory, P.W. McKenty, D.D. Meyerhofer, J.F. Myatt, A.J. Schmitt, J.D. Sethian, R.W. Short, S. Skupsky, W. Theobald, W.L. Kruer, Direct-drive inertial confinement fusion: a review, Phys. Plasmas 22 (11) (2015) 110501.
[7] R.D. Richtmyer, Taylor instability in shock acceleration of compressible fluids, Commun. Pure Appl. Math. 13 (2) (1960) 297–319.
[8] E.E. Meshkov, Instability of the interface of two gases accelerated by a shock wave, Fluid Dyn. 4 (5) (1969) 101–104.
[9] L. Rayleigh, Investigation of the character of the equilibrium of an incompressible heavy fluid of variable density, Proc. Lond. Math. Soc. 14 (1883) 170–177.
[10] G. Taylor, The instability of liquid surfaces when accelerated in a direction perpendicular to their planes. Part 1. Waves on fluid sheets, Proc. R. Soc. Lond. A Math., Phys. Sci. 201 (1950) 192–196.
[11] F. Marble, E. Zukoski, J. Jacobs, G. Hendricks, I. Waitz, Shock enhancement and control of hypersonic mixing and combustion, AIAA 26th Joint Propulsion Conference (1990).
[12] E. Oran, J. Boris, Numerical simulation of reactive flow, Cambridge University Press, 2005.
[13] M. Brouillette, The Richtmyer–Meshkov instability, Annu. Rev. Fluid Mech. 34 (2002) 445–468.
[14] P.G. Drazin, Introduction to hydrodynamic stability, Cambridge University Press, 2002.
[15] V.K. Tritschler, S. Hickel, X.Y. Hu, N.A. Adams, On the Kolmogorov inertial subrange developing from Richtmyer–Meshkov instability, Phys. Fluids 25 (2013) 071701.
[16] V.K. Tritschler, M. Zubel, S. Hickel, N.A. Adams, Evolution of length scales and statistics of Richtmyer–Meshkov instability from direct numerical simulations, Phys. Rev. E 90 (2014) 063001.
[17] N.J. Zabusky, Vortex paradigm for accelerated inhomogeneous flows: visiometrics for the Rayleigh–Taylor and Richtmyer–Meshkov environments, Annu. Rev. Fluid Mech. 31 (1999) 495–536.
[18] J.-F. Haas, B. Sturtevant, Interaction of weak shock waves with cylindrical and spherical gas inhomogeneities, J. Fluid Mech. 181 (1987) 41–76.
[19] J.J. Quirk, S. Karni, On the dynamics of a shock–bubble interaction, J. Fluid Mech. 318 (1996) 129–163.
[20] M.A. Liberman, Introduction to physics and chemistry of combustion: explosion, flame, detonation, Springer, 2008.
[21] W. Fickett, W.C. Davis, Detonation: theory and experiment, Dover Publications, 2010.
[22] N.S. Haehn, D. Ranjan, C. Weber, J. Oakley, D. Rothamer, R. Bonazza, Reacting shock bubble interaction, Combust. Flame 159 (3) (2012) 1339–1350.
[23] A.R. Miles, B. Blue, M.J. Edwards, J.A. Greenough, J.F. Hansen, H.F. Robey, R.P. Drake, C. Kuranz, D.R. Leibrandt, Transition to turbulence and effect of initial conditions on three-dimensional compressible mixing in planar blast-wave-driven systems, Phys. Plasmas 12 (5) (2005) 056317.
[24] A.W. Cook, Enthalpy diffusion in multicomponent flows, Phys. Fluids 21 (2009) 055109.
[25] T. Poinsot, D. Veynante, Theoretical and numerical combustion, R T Edwards, 2001.
[26] J. Troe, Predictive possibilities of unimolecular rate theory, J. Phys. Chem. 83 (1) (1979) 114–126.

[27] M. Ó Conaire, H.J. Curran, J.M. Simmie, W.J. Pitz, C.K. Westbrook, A comprehensive modeling study of hydrogen oxidation, Int. J. Chem. Kinet. 36 (2004) 603–622.
[28] N.S. Haehn, Experimental investigation of the reactive shock–bubble interaction, University of Wisconsin-Madison, 2012 Ph.D. thesis.
[29] G. Strang, On the construction and comparison of difference schemes, SIAM J. Numer. Anal. 5 (3) (1968) 506–517.
[30] S. Gottlieb, C.-W. Shu, Total variation diminishing Runge–Kutta schemes, Math. Comput. 67 (1998) 73–85.
[31] P.L. Roe, Approximate Riemann solvers, parameter vectors, and difference schemes, J. Comput. Phys. 43 (1981) 357–372.
[32] B. Larouturou, L. Fezoui, On the equations of multi-component perfect or real gas inviscid flow, Lect. Notes Math. 1402 (1989) 69–98.
[33] X.Y. Hu, V.K. Tritschler, S. Pirozzoli, N.A. Adams, Dispersion–dissipation condition for finite difference schemes, ArXiv e-prints (2012) arXiv:1204.5088.
[34] V.K. Tritschler, X.Y. Hu, S. Hickel, N.A. Adams, Numerical simulation of a Richtmyer–Meshkov instability with an adaptive central-upwind 6th-order WENO scheme, Phys. Scr. T155 (2013) 014016.
[35] R. Abgrall, S. Karni, Computations of compressible multifluids, J. Comput. Phys. 169 (2001) 594–623.
[36] E. Johnsen, F. Ham, Preventing numerical errors generated by interface-capturing schemesin compressible multi-material flows, J. Comput. Phys. 231 (2012) 5705–5717.
[37] V.K. Tritschler, A. Avdonin, S. Hickel, X.Y. Hu, N.A. Adams, Quantification of initial-data uncertainty on a shock-accelerated gas cylinder, Phys. Fluids 26 (2014) 026101.
[38] V.K. Tritschler, B.J. Olson, S.K. Lele, S. Hickel, X.Y. Hu, N.A. Adams, On the Richtmyer–Meshkov instability evolving from a deterministic multimode planar interface, J. Fluid Mech. 755 (2014) 429–462.
[39] P.N. Brown, G.D. Byrne, A.C. Hindmarsh, VODE: a variable-coefficient ODE solver, SIAM J. Sci. Stat. Comput. 10 (5) (1989) 1038–1051.
[40] J.H. Niederhaus, J.A. Greenough, J.G. Oakley, D. Ranjan, M.H. Anderson, R. Bonazza, A computational parameter study for the three-dimensional shock–bubble interaction, J. Fluid Mech. 594 (2008) 85–124.
[41] D. Ranjan, J.H.J. Niederhaus, J.G. Oakley, M.H. Anderson, J.A. Greenough, R. Bonazza, Experimental and numerical investigation of shock-induced distortion of a spherical gas inhomogeneity, Phys. Scr. T132 (2008) 014020.
[42] B. Hejazialhosseini, D. Rossinelli, P. Koumoutsakos, Vortex dynamics in 3D shock-bubble interaction, Phys. Fluids 25 (2013) 110816.
[43] F. Nakamura, C.F. McKee, R.I. Klein, R.T. Fisher, On the hydrodynamic interaction of shock waves with interstellar clouds. II. The effect of smooth cloud boundaries on cloud destruction and cloud turbulence, Astrophys. J. Suppl. Ser. 164 (2) (2006) 477.
[44] P.V. Danckwerts, The definition and measurement of some characteristics of mixtures, Appl. Sci. Res. Sect. A 3 (4) (1952) 279–296.
[45] D. Ranjan, M. Anderson, J. Oakley, R. Bonazza, Experimental investigation of a strongly shocked gas bubble, Phys. Rev. Lett. 94 (2005) 184507.
[46] R. Klein, K.S. Budil, T.S. Perry, D.R. Bach, The interaction of supernova remnants with interstellar clouds: experiments on the Nova laser, Astrophys. J. 583 (2003) 245–259.
[47] S.E. Widnall, D.B. Bliss, C.-Y. Tsai, The instability of short waves on a vortex ring, J. Fluid Mech. 66 (1974) 35–47.
[48] J. Giordano, Y. Burtschell, Richtmyer–Meshkov instability induced by shock--bubble interaction: numerical and analytical studies with experimental validation, Phys. Fluids 18 (3) (2006) 036102.
[49] J.F. Hansen, H.F. Robey, R.I. Klein, A.R. Miles, Experiment on the mass-stripping of an interstellar cloud in a high Mach number post-shock flow„ Phys. Plasmas 14 (5) (2007) 056505.
[50] X. Wang, T. Si, X. Luo, J. Yang, Generation of Air/SF6 interface with minimum surface feature by soap film technique, 29th International Symposium on Shock Waves 2, 2015, pp. 1065–1070.
[51] L. Zou, S. Liao, C. Liu, Y. Wang, Z. Zhai, Aspect ratio effect on shock-accelerated elliptic gas cylinders, Phys. Fluids 28 (3) (2016) 036101.
[52] P.Y. Georgievskiy, V.A. Levin, O.G. Sutyrin, Interaction of a shock with elliptical gas bubbles, Shock Waves 25 (4) (2015) 357–369.

C. Reaction mechanism

	Reaction	A	n	E_a	Ref.
	H_2/O_2 Chain Reactions				
1	$H + O_2 = O + OH$	$1.915 \cdot 10^{14}$	0.00	$1.644 \cdot 10^{02}$	[1]
	Reversed:	$5.481 \cdot 10^{11}$	0.39	$-2.930 \cdot 10^{02}$	
2	$O + H_2 = H + OH$	$5.080 \cdot 10^{04}$	2.67	$6.292 \cdot 10^{03}$	[2]
	Reversed:	$2.667 \cdot 10^{04}$	2.65	$4.880 \cdot 10^{03}$	
3	$OH + H_2 = H + H_2O$	$2.160 \cdot 10^{08}$	1.51	$3.43 \cdot 10^{03}$	[3]
	Reversed:	$2.298 \cdot 10^{09}$	1.40	$1.832 \cdot 10^{04}$	
4	$O + H_2O = OH + OH$	$2.970 \cdot 10^{06}$	2.02	$1.340 \cdot 10^{04}$	[4]
	Reversed:	$1.465 \cdot 10^{05}$	2.11	$-2.904 \cdot 10^{03}$	
	H_2/O_2 Dissociation/Recombination Reactions				
5	$H_2 + M = H + H + M$	$4.577 \cdot 10^{19}$	-1.40	$1.044 \cdot 10^{05}$	[5]
	Reversed:	$1.146 \cdot 10^{20}$	-1.68	$8.200 \cdot 10^{02}$	
	TBE: H_2 : 2.50, H_2O : 12.00				
6	$O_2 + M = O + O + M$	$4.515 \cdot 10^{17}$	-0.64	$1.189 \cdot 10^{05}$	[5]
	Reversed:	$6.165 \cdot 10^{15}$	-0.50	$0.000 \cdot 10^{00}$	
	TBE: H_2 : 2.50, H_2O : 12.00, Ar : 0.83				
7	$OH + M = O + H + M$	$9.880 \cdot 10^{17}$	-0.74	$1.021 \cdot 10^{05}$	[5]

	Reversed:	$4.718 \cdot 10^{18}$	-1.00	$0.000 \cdot 10^{00}$	
	TBE: $H_2 : 2.50$, $H_2O : 12.00$, $Ar : 0.75$				
8	$H_2O + M = H + OH + M$	$1.912 \cdot 10^{23}$	-1.83	$1.185 \cdot 10^{05}$	[5] ·2.00
	Reversed:	$4.500 \cdot 10^{22}$	-2.00	$0.000 \cdot 10^{00}$	
	TBE: $H_2 : 0.73$, $H_2O : 12.00$, $Ar : 0.38$				
	Formation and consumption of HO_2				
9	$H + O_2 + M = HO_2 + M$	$1.475 \cdot 10^{12}$	0.60	$0.000 \cdot 10^{00}$	[6]
	Low:	$3.482 \cdot 10^{16}$	-0.41	$-1.115 \cdot 10^{03}$	
	Troe: $\alpha : 0.5$, $T^{***} : 1.0 \cdot 10^{-30}$, $T^{*} : 1.0 \cdot 10^{30}$, $T^{**} : 1.0 \cdot 10^{100}$				
	TBE: $H_2 : 1.30$, $H_2O : 14.00$, $Ar : 0.67$				
	Reaction	**A**	**n**	**E_a**	**Ref.**
10	$HO_2 + H = H_2 + O_2$	$1.660 \cdot 10^{13}$	0.00	$8.230 \cdot 10^{02}$	[7]
	Reversed:	$3.164 \cdot 10^{12}$	0.35	$5.551 \cdot 10^{04}$	
11	$HO_2 + H = OH + OH$	$7.079 \cdot 10^{13}$	0.00	$2.950 \cdot 10^{02}$	[7]
	Reversed:	$2.027 \cdot 10^{10}$	0.72	$3.684 \cdot 10^{04}$	
12	$HO_2 + O = OH + O_2$	$3.250 \cdot 10^{12}$	0.33	$0.000 \cdot 10^{00}$	[8]
	Reversed:	$3.252 \cdot 10^{12}$	0.33	$5.328 \cdot 10^{04}$	
13	$HO_2 + OH = H_2O + O_2$	$2.890 \cdot 10^{13}$	0.00	$-4.970 \cdot 10^{02}$	[8]
	Reversed:	$5.861 \cdot 10^{13}$	0.24	$6.908 \cdot 10^{04}$	
	Formation and Consumption of H_2O_2				
14	$H_2O_2 + O_2 = HO_2 + HO_2$	$4.634 \cdot 10^{16}$	-0.35	$5.067 \cdot 10^{04}$	[9]
	Reversed:	$4.200 \cdot 10^{14}$	0.00	$1.198 \cdot 10^{04}$	
	Duplicated:				
	$H_2O_2 + O_2 = HO_2 + HO_2$	$1.434 \cdot 10^{13}$	-0.35	$3.706 \cdot 10^{04}$	
	Reversed:	$1.300 \cdot 10^{11}$	0.00	$-1.629 \cdot 10^{03}$	
15	$H_2O_2 + M = OH + OH + M$	$2.951 \cdot 10^{14}$	0.00	$4.843 \cdot 10^{04}$	[10]
	Low:	$1.202 \cdot 10^{17}$	0.00	$4.450 \cdot 10^{04}$	
	Troe: $\alpha : 0.5$, $T^{***} : 1.0 \cdot 10^{-30}$, $T^{*} : 1.0 \cdot 10^{30}$, $T^{**} : 1.0 \cdot 10^{100}$				
	TBE: $H_2 : 2.50$, $H_2O : 12.00$, $Ar : 0.64$				
16	$H_2O_2 + H = H_2O + OH$	$2.410 \cdot 10^{13}$	0.00	$3.970 \cdot 10^{03}$	[5]
	Reversed:	$1.269 \cdot 10^{08}$	1.31	$7.141 \cdot 10^{04}$	
17	$H_2O_2 + H = H_2 + HO_2$	$6.025 \cdot 10^{13}$	0.00	$7.950 \cdot 10^{03}$	[5] ·1.25
	Reversed:	$1.041 \cdot 10^{11}$	0.70	$2.395 \cdot 10^{04}$	
18	$H_2O_2 + O = OH + HO_2$	$9.550 \cdot 10^{06}$	2.00	$3.970 \cdot 10^{03}$	[5]
	Reversed:	$8.660 \cdot 10^{03}$	2.68	$1.856 \cdot 10^{04}$	
19	$H_2O_2 + OH = H_2O + HO_2$	$1.000 \cdot 10^{12}$	0.00	$0.000 \cdot 10^{00}$	
	Reversed:	$1.838 \cdot 10^{10}$	0.59	$3.089 \cdot 10^{04}$	[11]
	Duplicated:				
	$H_2O_2 + OH = H_2O + HO_2$	$5.800 \cdot 10^{14}$	0.00	$9.557 \cdot 10^{03}$	

Reversed:	$1.066 \cdot 10^{13}$	0.59	$4.045 \cdot 10^{04}$

Table C.1.: H_2-O_2 reaction mechanism; units: cm^3, mol, s, kcal, K (Ó Conaire et al., 2004), [1] Pirraglia et al. (1989), [2] Sutherland et al. (1988), [3] Michael and Sutherland (1988), [4] Sutherland et al. (1991), [5] Tsang and Hampson (1986), [6] Mueller et al. (1998), [7] Mueller et al. (1999), [8] Baulch et al. (1994), [9] Hippler et al. (1990), [10] Warnatz (1984), [11] Hippler and Troe (1992).

D. Bibliography

Y. Aglitskiy, A. L. Velikovich, M. Karasik, N. Metzler, S. T. Zalesak, A. J. Schmitt, L. Phillips, J. H. Gardner, V. Serlin, J. L. Weaver, and S. P. Obenschain. Basic hydrodynamics of Richtmyer-Meshkov-type growth and oscillations in the inertial confinement fusion-relevant conditions. *Phil. Trans. R. Soc. A: Math., Phys. Eng. Sci.*, 368 (1916):1739–1768, 2010.

W. D. Arnett. The Role of Mixing in Astrophysics. *Ap. J. Suppl.*, 127:213–217, 2000.

U. M. Ascher and L. R. Petzold. *Computer Methods for Ordinary Differential Equations and Differential-Algebraic Equations.* Soc. Ind. Appl. Math., Philadelphia, PA, USA, 1998.

D. L. Baulch, C. J. Cobos, R. A. Cox, P. Frank, G. Hayman, T. Just, J. A. Kerr, T. Murrells, M. J. Pilling, J. Troe, R. W. Walker, and J. Warnatz. Evaluated kinetic data for combustion modeling. Supplement I. *J. Phys. Chem. Ref. Data*, 23:847–848, 1994.

M. Brouillette. The Richtmyer-Meshkov Instability. *Annu. Rev. Fluid Mech.*, 34:445–468, 2002.

P. N. Brown, G. D. Byrne, and A. C. Hindmarsh. VODE: A Variable-coefficient ODE Solver. *SIAM J. Sci. Stat. Comput.*, 10(5):1038–1051, 1989.

C. Charignon and J.-P. Chiéze. Deflagration-to-detonation transition by amplification of acoustic waves in type Ia supernovae. *Astron. Astrophys.*, 550(A105), 2013.

A. W. Cook. Enthalpy diffusion in multicomponent flows. *Phys. Fluids*, 21:055109, 2009.

R. S. Craxton, K. S. Anderson, T. R. Boehly, V. N. Goncharov, D. R. Harding, J. P. Knauer, R. L. McCrory, P. W. McKenty, D. D. Meyerhofer, J. F. Myatt, A. J. Schmitt, J. D. Sethian, R. W. Short, S. Skupsky, W. Theobald, and W. L. Kruer. Direct-drive inertial confinement fusion: A review. *Phys. Plasmas*, 22(11), 2015.

P. A. Davidson. *Turbulence: An Introduction for Scientists and Engineers.* Oxford University Press, 2004.

F. R. Diegelmann. Numerical simulation of a reacting shock-bubble interaction. Master's thesis, TU Darmstadt, 2013.

F. R. Diegelmann, V. K. Tritschler, S. Hickel, and N. A. Adams. On the pressure dependence of ignition and mixing in two-dimensional reactive shock-bubble interaction. *Combust. Flame*, 163:414–426, 2016a.

F. R. Diegelmann, S. Hickel, and N. A. Adams. Shock Mach number influence on reaction wave types and mixing in reactive shock-bubble interaction. *Combust. Flame*, 174: 085–099, 2016b.

F. R. Diegelmann, S. Hickel, and N. A. Adams. Three-dimensional reacting shock-bubble interaction. *Combust. Flame*, 181:300–314, 2017.

P. E. Dimotakis and R. Samtaney. Planar shock cylindrical focusing by a perfect-gas lens. *Phys. Fluids*, 18(3), 2006.

P. G. Drazin. *Introduction to Hydrodynamic Stability.* Cambridge University Press, 2002.

S. Dutta, J. Glimm, J. W. Grove, D. H. Sharp, and Y. Zhang. Spherical Richtmyer-Meshkov Instability for Axisymmetric Flow. *Math. Comput. Simul.*, 65(4-5), 2004.

P. J. M. Ferrer, R. Buttay, G. Lehnasch, and A. Mura. A detailed verification procedure for compressible reactive multicomponent Navier-Stokes solvers. *Comput. Fluids*, 89: 88–110, 2014.

W. Fickett and W. C. Davis. *Detonation: Theory and Experiment.* Dover Publications, 2010.

P. Y. Georgievskiy, V. A. Levin, and O. G. Sutyrin. Interaction of a shock with elliptical gas bubbles. *Shock Waves*, 25(4):357–369, 2015.

J. Giordano and Y. Burtschell. Richtmyer-Meshkov instability induced by shock-bubble interaction: Numerical and analytical studies with experimental validation. *Phys. Fluids*, 18(3):036102, 2006.

D. G. Goodwin, H. K. Moffat, and R. L. Speth. Cantera: An Object-oriented Software Toolkit for Chemical Kinetics, Thermodynamics, and Transport Processes. http://www.cantera.org, 2014. Version 2.1.2.

S. Gottlieb and C.-W. Shu. Total variation diminishing Runge-Kutta schemes. *Math. Comput.*, 67:73–85, 1998.

J.-F. Haas and B. Sturtevant. Interaction of weak shock waves with cylindrical and spherical gas inhomogeneities. *J. Fluid Mech.*, 181:41–76, 1987.

N. S. Haehn. *Experimental investigation of the reactive shock-bubble interaction.* PhD thesis, University of Wisconsin-Madison, 2012.

N. S. Haehn, D. Ranjan, C. Weber, J. Oakley, D. Rothamer, and R. Bonazza. Reacting shock bubble interaction. *Combust. Flame*, 159(3):1339–1350, 2012.

J. F. Hansen, H. F. Robey, R. I. Klein, and A. R. Miles. Experiment on the mass-stripping of an interstellar cloud in a high Mach number post-shock flow. *Phys. Plasmas*, 14(5), 2007.

D. A. Hardy. https://www.york.ac.uk/news-and-events/news/2013/research/exploding-stars/gallery/, last access: 31/03/2017, Science and Technology Facilities Council, 2017.

A. Harten, B. Engquist, S. Osher, and S. R. Chakravarthy. Uniformly High Order Accurate Essentially Non-oscillatory Schemes. *J. Comput. Phys.*, 71(2):231–303, 1987.

B. Hejazialhosseini, D. Rossinelli, and P. Koumoutsakos. Vortex dynamics in 3D shock-bubble interaction. *Phys. Fluids*, 25:110816, 2013.

H. Hippler and J. Troe. Rate constants of the reaction HO + H_2O_2 → HO_2 + H_2O at T ≥ 1000 K. *Chem. Phys. Lett.*, 192:333–337, 1992.

H. Hippler, J. Troe, and J. Willner. Shock wave study of the reaction HO_2 + HO_2 = H_2O_2 + O_2 : Confirmation of a rate constant minimum near 700 K. *J. Chem. Phys.*, 93:1755–1760, 1990.

X. Y. Hu and N. A. Adams. Scale separation for implicit large eddy simulation. *J. Comput. Phys.*, 230(19):7240–7249, 2011.

X. Y. Hu, Q. Wang, and N. A. Adams. An adaptive central-upwind weighted essentially non-oscillatory scheme. *J. Comput. Phys.*, 229(23):8952–8965, 2010.

M. F. Ivanov, A. D. Kiverin, and M. A. Liberman. Hydrogen-oxygen flame acceleration and transition to detonation in channels with no-slip walls for a detailed chemical reaction model. *Phys. Rev. E*, 83:056313, 2011.

R. J. Kee, M. E. Coltrin, and P. Glarborg. *Chemically Reacting Flow: Theory and Practice.* John Wiley & Sons, Inc., 2003.

A. M. Khokhlov, E. S. Oran, and G. O. Thomas. Numerical simulation of deflagration-to-detonation transition: the role of shock-flame interactions in turbulent flames. *Combust. Flame*, 117(1-2):323–339, 1999.

R. Klein, K. S. Budil, T. S. Perry, and D. R. Bach. The Interaction of Supernova Remnants with Interstellar Clouds: Experiments on the Nova Laser. *Astrophys. J.*, 583:245–259, 2003.

R. I. Klein, H. F. Robey, T. S. Perry, K. J. O., J. A. Greenough, and M. Marinak. The Interaction of Supernova Blast Waves with Interstellar Clouds: Experiments on the Omega Laser. In *2nd International Conference on Inertial Fusion Science Applications, Kyoto, Japan*, 2001.

O. P. Korobeinichev and T. A. Bol'shova. Applicability of Zel'dovich's theory of chain propagation of flames to combustion of hydrogen-oxygen mixtures. *Combust., Explos., Shock Waves*, 45(5):507–510, 2009.

S. Kumar, P. Vorobieff, G. Orlicz, A. Palekar, C. Tomkins, C. Goodenough, M. Marr-Lyon, K. Prestridge, and R. Benjamin. Complex flow morphologies in shock-accelerated gaseous flows. *Physica D Nonlinear Phenom.*, 235(1-2):21–28, 2007.

M. Kuznetsov, M. A. Liberman, and I. Matsukov. Experimental study of the preheat zone formation and deflagration-to-detonation transition. In *Proceedings of the 22nd ICDERS*, 2009.

M. Kuznetsov, M. A. Liberman, and I. Matsukov. Experimental Study of the Preheat Zone Formation and Deflagration to Detonation Transition. *Combust. Sci. Technol.*, 182(11-12):1628–1644, 2010.

B. Larouturou and L. Fezoui. On the equations of multi-component perfect or real gas inviscid flow. *Lecture Notes Math.*, 1402:69–98, 1989.

J. H. S. Lee. *The Detonation Phenomenon.* Cambridge University Press, 2008.

M. A. Liberman. *Introduction to Physics and Chemistry of Combustion: Explosion, Flame, Detonation.* Springer, 2008.

M. A. Liberman, M. F. Ivanov, A. D. Kiverin, M. S. Kuznetsov, A. A. Chukalovsky, and T. V. Rakhimova. Deflagration-to-detonation transition in highly reactive combustible mixtures. *Acta Astronaut.*, 67(78):688–701, 2010.

X.-D. Liu, S. Osher, and T. Chan. Weighted Essentially Non-oscillatory Schemes. *J. Comput. Phys.*, 115(1):200 – 212, 1994.

F. Marble, E. Zukoski, J. Jacobs, G. Hendricks, and I. Waitz. Shock Enhancement and Control of Hypersonic Mixing and Combustion. *AIAA 26th Joint Propuls. Conf. (1990)*, 1990.

E. E. Meshkov. Instability of the interface of two gases accelerated by a shock wave. *Fluid Dyn.*, 4(5):101–104, 1969.

J. Michael and J. W. Sutherland. Rate constant for the reaction of H with H_2O and OH with H_2 by the flash photolysis-shock tube technique over the temperature range 1246-2297 K. *J. Phys. Chem.*, 92:3853–3857, 1988.

A. R. Miles, B. Blue, M. J. Edwards, J. A. Greenough, J. F. Hansen, H. F. Robey, R. P. Drake, C. Kuranz, and D. R. Leibrandt. Transition to turbulence and effect of initial conditions on three-dimensional compressible mixing in planar blast-wave-driven systems. *Phys. Plasmas*, 12(5):056317, 2005.

D. Mishra. *Fundamentals of Combustion.* PHI Learning Private Limited, 2013.

M. Mueller, R. Yetter, and F. Dryer. Measurement of the rate constant of H + O_2 + M = HO_2 + M (M = N_2, Ar) using kinetic modeling of the high pressure H_2 / O_2 / NO_x reaction. In *27th Symposium (International) on Combustion*, 1998.

M. Mueller, R. Yetter, and F. Dryer. Flow reactor and kinetic modeling studies of the H_2 / O_2 reaction. *Int. J. Chem. Kinet.*, 31:113–125, 1999.

P. D. Neufeld, A. R. Janzen, and R. A. Aziz. Empirical Equations to Calculate 16 of the Transport Collision Integrals Omega(l,s)* for the Lennard-Jones (12-6) Potential. *J. Chem. Phys.*, 57(3):1100–1102, 1972.

J. H. Niederhaus, J. A. Greenough, J. G. Oakley, D. Ranjan, M. H. Anderson, and R. Bonazza. A computational parameter study for the three-dimensional shock–bubble interaction. *J. Fluid Mech.*, 594:85–124, 2008.

M. Ó Conaire, H. J. Curran, J. M. Simmie, W. J. Pitz, and C. K. Westbrook. A comprehensive modeling study of Hydrogen oxidation. *Int. J. Chem. Kinet.*, 36:603–622, 2004.

O. Oldenberg and H. S. Sommers. The Thermal Reaction Between Hydrogen and Oxygen III. The Temperature Coefficient of the Steady Thermal Reaction. *J. Chem. Phys.*, 9 (5):432–438, 1941.

E. Oran and J. Boris. *Numerical Simulation of Reactive Flow.* Cambridge University Press, 2005.

E. Oran and V. Gamezo. Origins of the Deflagration-to-Detonation Transition in Gas-Phase Combustion. *Combust. Flame*, 148:4–47, 2007.

G. Peng, N. J. Zabusky, and S. Zhang. Vortex-accelerated secondary baroclinic vorticity deposition and late-intermediate time dynamics of a two-dimensional Richtmyer-Meshkov interface. *Phys. Fluids*, 15(12):3730–3744, 2003.

A. N. Pirraglia, J. V. Michael, J. W. Sutherland, and R. B. Klemm. A flash photolysis-shock tube kinetic study of the hydrogen atom reaction with oxygen: H + O_2 $\rightleftharpoons$ OH + O (962K $\leq$ T $\leq$ 1705K) and H + O_2 + Ar $\rightarrow$ HO_2 + Ar (746K $\leq$ T $\leq$ 987K). *J. Phys. Chem.*, 93:282–291, 1989.

T. Poinsot and D. Veynante. *Theoretical and Numerical Combustion.* R T Edwards, 2001.

B. E. Poling, J. M. Prausnitz, and J. P. O'Connell. *The Properties of Gases and Liquids.* McGraw-Hill, 2001.

J. J. Quirk and S. Karni. On the dynamics of a shock-bubble interaction. *J. Fluid Mech.*, 318:129–163, 7 1996.

D. Ranjan, M. Anderson, J. Oakley, and R. Bonazza. Experimental Investigation of a Strongly Shocked Gas Bubble. *Phys. Rev. Lett.*, 94:184507, 2005.

D. Ranjan, J. Oakley, and R. Bonazza. Shock-Bubble Interactions. *Annu. Rev. Fluid Mech.*, 43(1):117–140, 2011.

L. Rayleigh. Investigation of the character of the equilibrium of an incompressible heavy fluid of variable density. *Proc. Lond. Math. Soc.*, 14:170–177, 1883.

R. D. Richtmyer. Taylor instability in shock acceleration of compressible fluids. *Commun. Pure Appl. Math.*, 13(2):297–319, 1960.

H. F. Robey, T. S. Perry, R. I. Klein, J. O. Kane, J. A. Greenough, and T. R. Boehly. Experimental Investigation of the Three-Dimensional Interaction of a Strong Shock with a Spherical Density Inhomogeneity. *Phys. Rev. Lett.*, 89:085001, 2002.

P. L. Roe. Approximate Riemann solvers, parameter vectors, and difference schemes. *J. Comput. Phys.*, 43:357–372, 1981.

C.-W. Shu. Essentially Non-Oscillatory and Weighted Essentially Non-Oscillatory Schemes for Hyperbolic Conservation Laws. Technical report, Division of Applied Mathematics - Brown University, 1997.

K. K. So. *Uncertainty Analysis of Shock-Bubble Interaction.* PhD thesis, Technische Universität München, 2013.

G. Sod. Survey of several finite difference methods for systems of nonlinear hyperbolic conservation laws. *J. Comput. Phys.*, 26:4, 1978.

G. Strang. On the Construction and Comparison of Difference Schemes. *SIAM Jour. Numer. Anal.*, 5(3):506–517, 1968.

E. Süli and D. F. Mayers. *An Introduction to Numerical Analysis.* Cambridge Univ. Press, 2003.

J. Sutherland, J. Michael, A. Pirraglia, F. Nesbitt, and R. Klemm. Rate constant for the reaction of $O(^3P)$ with H_2 by the flash photolysis-shock tube and flash photolysis-resonance fluorescence techniques; 504 K $\leq$ T $\leq$ 2495 K. *Symp. (Int.) Comb.*, 21: 929–941, 1988.

J. W. Sutherland, P. M. Patterson, and R. B. Klemm. Rate constants for the reaction, $O(^{3P})$ + $H_2O \rightleftharpoons$ OH + OH, over the temperature range 1053 K to 2033 K using two direct techniques. *Symp. (Int.) Comb.*, 23:51–57, 1991.

E. M. Taylor, M. Wu, and M. P. Martin. Optimization of nonlinear error for weighted essentially non-oscillatory methods in direct numerical simulations of compressible turbulence. *J. Comput. Phys.*, 223(1):384 – 397, 2007.

G. Taylor. The instability of liquid surfaces when accelerated in a direction perpendicular to their planes. Part 1. Waves on fluid sheets. *Proc. R. Soc. Lond. A Math., Phys. Sci.*, 201:192–196, 1950.

C. Tomkins, K. Prestridge, P. Rightley, M. Marr-Lyon, P. Vorobieff, and R. Benjamin. A quantitative study of the interaction of two Richtmyer-Meshkov-unstable gas cylinders. *Phys. Fluids*, 15:986–1004, 2003.

C. Tomkins, S. Kumar, G. Orlicz, and K. Prestridge. An experimental investigation of mixing mechanisms in shock-accelerated flow. *J. Fluid Mech.*, 611:131–150, 2008.

E. F. Toro. *Riemann solvers and numerical methods for fluid dynamics*. Springer Berlin, 2009.

V. K. Tritschler, S. Hickel, X. Y. Hu, and N. A. Adams. On the Kolmogorov inertial subrange developing from Richtmyer-Meshkov instability. *Phys. Fluids*, 25:071701, 2013.

V. K. Tritschler, A. Avdonin, S. Hickel, X. Y. Hu, and N. A. Adams. Quantification of initial-data uncertainty on a shock-accelerated gas cylinder. *Phys. Fluids*, 26:026101, 2014a.

V. K. Tritschler, B. J. Olson, S. K. Lele, S. Hickel, X. Y. Hu, and N. A. Adams. On the Richtmyer-Meshkov instability evolving from a deterministic multimode planar interface. *J. Fluid Mech.*, 755:429–462, 2014b.

V. K. Tritschler, M. Zubel, S. Hickel, and N. A. Adams. Evolution of length scales and statistics of Richtmyer-Meshkov instability from direct numerical simulations. *Phys. Rev. E*, 90:063001, 2014c.

J. Troe. Predictive possibilities of unimolecular rate theory. *J. Phys. Chem.*, 83(1): 114–126, 1979.

W. Tsang and R. F. Hampson. Chemical kinetic data base for combustion chemistry. part I. Methane and related compounds. *J. Phys. Chem. Ref. Data*, 15:1087–1279, 1986.

X. Wang and K. L. Chung. An analysis of the explosion limits of hydrogen-oxygen mixtures. *J. Chem. Phys.*, 138(13):134305, 2013.

X. Wang, T. Si, X. Luo, and J. Yang. Generation of Air/SF6 Interface with Minimum Surface Feature by Soap Film Technique. *29th Int. Symp. Shock Waves 2*, pages 1065–1070, 2015.

J. Warnatz. *Combustion chemistry - Critical survey of elementary reaction rate coefficients on the C/H/O system*. Springer-Verlag, 1984.

S. E. Widnall, D. B. Bliss, and C.-Y. Tsai. The instability of short waves on a vortex ring. *J. Fluid Mech.*, 66:35–47, 1974.

J. Yang, T. Kubota, and E. Zukoski. Applications of shock-induced mixing to supersonic combustion. *AIAA J.*, 31:854–862, 1993.

N. J. Zabusky. Vortex paradigm for accelerated inhomogeneous flows: visiometrics for the Rayleigh-Taylor and Richtmyer-Meshkov environments. *Annu. Rev. Fluid Mech.*, 31:495–536, 1999.

Y. B. Zel'dovich. Flame propagation in a substance reacting at initial temperature. *Comb. Flame*, 39(3):219–224, 1980.

Y. B. Zel'dovich, V. B. Librovich, G. Makhviladze, and G. I. Sivashinsky. On the development of detonation in a non-uniformly preheated gas. *Acta Astronaut.*, 15:313–321, 1970.

Z.-G. Zhai, T. Si, L.-Y. Zou, and X.-S. Luo. Jet formation in shock-heavy gas bubble interaction. *Acta Mech. Sin.*, 29(1):24–35, 2013.

L. Zou, S. Liao, C. Liu, Y. Wang, and Z. Zhai. Aspect ratio effect on shock-accelerated elliptic gas cylinders. *Phys. Fluids*, 28(3):036101, 2016.